SAE Aerospace
An SAE International Group

AEROSPACE INFORMATION REPORT

SAE AIR1168/11

Issued 2008-02

Spacecraft Boost and Entry Heat Transfer

PREFACE

This document is one of 14 Aerospace Information Reports (AIR) of the Third Edition of the SAE Aerospace Applied Thermodynamics Manual. The manual provides a reference source for thermodynamics, aerodynamics, fluid dynamics, heat transfer, and properties of materials for the aerospace industry. Procedures and equations commonly used for aerospace applications of these technologies are included.

In the Third Edition, no attempt was made to update material from the Second Edition nor were SI units added. However, all identified errata were corrected and incorporated and original figure numbering was retained, insofar as possible.

The SAE AC-9B Subcommittee originally created the SAE Aerospace Applied Thermodynamics Manual, and, for the Third Edition, used a new format consisting of AIR1168/1 through AIR1168/10. AIR1168/11 through AIR1168/14 were created by the SAE SC-9 Committee.

The AIRs comprising the Third Edition are shown below. Applicable sections of the Second Edition are shown parenthetically in the third column.

AIR1168/1	Thermodynamics of Incompressible and Compressible Fluid Flow	(1A,1B)
AIR1168/2	Heat and Mass Transfer and Air-Water Mixtures	(1C,1D,1E)
AIR1168/3	Aerothermodynamic Systems Engineering and Design	(3A,3B,3C,3D)
AIR1168/4	Ice, Rain, Fog, and Frost Protection	(3F)

TO PLACE A DOCUMENT ORDER:
Tel: 877-606-7323 (inside USA and Canada)
Tel: 724-776-4970 (outside USA)
Fax: 724-776-0790
Email: CustomerService@sae.org
SAE WEB ADDRESS: http://www.sae.org

PREFACE (Continued)

AIR1168/5	Aerothermodynamic Test Instrumentation and Measurement	(3G)
AIR1168/6	Characteristics of Equipment Components, Equipment Cooling System Design, and Temperature Control System Design	(3H,3J,3K)
AIR1168/7	Aerospace Pressurization System Design	(3E)
AIR1168/8	Aircraft Fuel Weight Penalty Due to Air Conditioning	(3I)
AIR1168/9	Thermophysical Properties of the Natural Environment, Gases, Liquids, and Solids	(2A,2B,2C,2D)
AIR1168/10	Thermophysical Characteristics of Working Fluids and Heat Transfer Fluids	(2E,2F)
AIR1168/11	Spacecraft Boost and Entry Heat Transfer	(4A,4B)
AIR1168/12	Spacecraft Thermal Balance	(4C)
AIR1168/13	Spacecraft Equipment Environmental Control	(4D)
AIR1168/14	Spacecraft Life Support Systems	(4E)

F.R. Weiner, formerly of Rockwell International and past chairman of the SAE AC-9B Subcommittee, is commended for his dedication and effort in preparing the errata lists that were used in creating the Third Edition.

TABLE OF CONTENTS

TABLE OF CONTENTS (Continued)

TABLE OF CONTENTS (Continued)

LIST OF FIGURES

LIST OF FIGURES (Continued)

LIST OF FIGURES (Continued)

LIST OF FIGURES (Continued)

LIST OF FIGURES (Continued)

LIST OF FIGURES (Continued)

LIST OF FIGURES (Continued)

LIST OF FIGURES (Continued)

LIST OF TABLES

NOMENCLATURE FOR SECTIONS A AND B:

a	=	Velocity of sound, ft/s
A, B, C	=	Constants
A	=	Area, in^2, ft^2
a_e	=	Thermal accommodation coefficient (defined by Equation 257)
B_s	=	Measure of the eccentricity of the conic section, dimensionless
C	=	Constant of integration, dimensionless
C	=	Concentration, mol/g
C_A	=	Nose drag coefficient, dimensionless
C_D	=	Drag coefficient, dimensionless
C_f	=	Skin friction coefficient, dimensionless
C_g	=	Specific heat capacity of gas, Btu/lb-°R
C_H	=	Heat transfer coefficient, lb/ft^2-s
C_l	=	Lift coefficient, dimensionless
c_p	=	Specific heat capacity, constant pressure, Btu/lb-°R
C_p	=	Pressure coefficient, dimensionless
c_v	=	Specific heat capacity, constant volume, Btu/lb-°R
D	=	Diameter, ft, in
D	=	Drag, lb
D	=	Protuberance width or diameter, ft
d	=	Section thickness, ft
E	=	Arrhenius constant activation energy, Btu/lb-mole, Kcal/mole
E	=	Energy, Btu/ft^2-s
E_b	=	Re-emitted energy of incident molecules, if they had a Maxwellian velocity distribution, Btu/ft^2-s
E_i	=	Incident energy, Btu/ft^2-s
E_r	=	Reflected or re-emitted energy, Btu/ft^2-s
E_t	=	Radiation intensity of shock layer, watts/cm^3
f	=	Defined in Figure 75
F_c	=	Centrifugal force, lb
g	=	Gravitational constant at sea level (32.17), ft/s^2
gρ or ρg	=	Specific weight (density), lb/ft^3 (NOTE: gρ and ρg are used interchangeably)
h or H	=	Altitude, ft
h	=	Heat transfer coefficient, Btu/ft^2-s-°R
h	=	Specific enthalpy, Btu/lb
H	=	Altitude ratio, dimensionless
ΔH	=	Latent heat of melting, Btu/lb
H_{gf}	=	Heat of gas formation, Btu/lb
H_k	=	Heat of cracking, Btu/lb
i	=	Specific enthalpy, Btu/lb
i	=	Orbit inclination angle, deg
J	=	Mechanical equivalent of heat, 778 ft-lb/Btu
k	=	Thermal conductivity, Btu-ft/ft^2-h-°F, Btu-ft/ft^2-s-°R
K	=	Reaction rate or collision frequency, 1/s
K	=	Hypersonic similarity parameter or shock wave parameter ($K = M \tan \theta$)

NOMENCLATURE FOR SECTIONS A AND B (Continued):

k	=	Nose drag term, dimensionless
k	=	0, one-dimensional body
k	=	1, axisymmetric body
K_1, K_2, K_3, K_4	=	Shock shape constants, dimensionless
K_o	=	Effective collision frequency, 1/s
L	=	Characteristic body length, ft
L	=	Latent heat, Btu/lb
L	=	Lift, lb
L	=	Protuberance height, ft
L_q	=	Leeward heat flux ratio, $\dot{q}/\dot{q}_\alpha = 0$
M	=	Mach number, dimensionless
m	=	Vehicle mass, lb-s^2/ft
$\dot{m}$	=	Mass injection or loss rate per unit area, lb/ft^2-s
$\overline{M}$	=	Average molecular weight, mole/g-mole
M	=	Molecular weight, g/mole
n	=	Order of reaction, dimensionless
N	=	Kinetic order of the reaction, dimensionless
N_a	=	Number of atoms in compound
N_{Kn}	=	Knudsen number (λ/L), dimensionless
N_{Le}	=	Lewis number (h/ks), dimensionless
N_{Nu}	=	Nusselt number (hD/k or $\dot{q}N_{Pr}s/\mu_e(h_r - h_w)$), dimensionless
N_{Pr}	=	Prandtl number ($\mu g c_p/k$), dimensionless
N_{Re}	=	Reynolds number ($VD\rho g/\mu$), dimensionless
$N_{Re,s}$	=	Reynolds number based on wetted length ($u_e s\rho g/\mu_e$), dimensionless
$N_{Re,\theta}$	=	Reynolds number based on momentum thickness ($u_e\theta\rho g/\mu_e$), dimensionless
N_{St}	=	Stanton number ($(N_{Nu})/(N_{Re}\,N_{Pr}) = h/\rho g V c_p$), dimensionless
P	=	Pressure, lb/ft^2
$P_{o_2,w}$	=	Partial pressure of oxygen at wall, lb/ft^2
$\dot{q}$	=	Heat flux, Btu/ft^2-s
q	=	Dynamic (impact) pressure, lb/ft^2
Q_c	=	Net heat conducted into element, Btu/ft^2
Q_k	=	Heat absorbed in cracking of recombination, Btu/ft^2
Q_r	=	Heat absorbed in reaction, Btu/ft^2
Q_{sg}	=	Heat stored in gas, Btu/ft^2
Q_{ss}	=	Heat stored in solid, Btu/ft^2
Q*	=	Effective heat of ablation, Btu/lb
Q_H^*	=	Heat sink effectiveness (defined by Equation 125), dimensionless
Q_v^*	=	Effective heat of vaporization (defined by Equation 126), Btu/lb
r	=	Recovery factor, dimensionless
r	=	Radius, ft, in

NOMENCLATURE FOR SECTIONS A AND B (Continued):

R	=	Gas constant, ft-lb/lb-°R
R	=	Universal gas constant, Btu/mole-°R
r_b	=	Base radius, ft
r_c	=	Radius of flight path, ft
r_n	=	Nose radius, ft
r_o	=	Radius of earth, ft
R_s or r_s	=	Radius of curvature of bow shock at the axis (r_s = o), ft
S	=	Area, ft^2
s	=	Distance along body surface, ft
S	=	Entropy, Btu/lb, Btu/mole-°R
$\dot{S}$	=	Recession rate, ft/s
$S_{\dot{q}}$	=	Side ray heat flux ratio $(\dot{q} / \dot{q}_{\alpha=o})$, dimensionless
T	=	Temperature, °R
t	=	Thickness, ft, in
U	=	Velocity, ft/s
U_∞	=	Freestream velocity, ft/s
u	=	Boundary layer velocity, ft/s
u_e	=	Velocity at edge of boundary layer, ft/s
V	=	Velocity, ft/s
V_e	=	Entry velocity, ft/s
$\overline{V}_e$	=	Velocity ratio (V/V_e), dimensionless
V_f	=	Final or impact velocity, ft/s
V_i	=	Inertial velocity, ft/s
V_s	=	Satellite velocity, ft/s
W	=	Weight, lb
$W_{\dot{q}}$	=	Windward ray heat flux ratio $(\dot{q} / \dot{q} = o)$
W/C_DA	=	Ballistic coefficient, lb/ft^2
x	=	Characteristic dimension, ft
x	=	Axial length or station, ft
x	=	Wetted length from stagnation point, ft
Y	=	Compressibility factor ($Y = \rho ghJ/3.5P$), dimensionless
y	=	Distance normal to surface, ft
Z	=	Arrhenius constant, collision frequency, 1/s
Z	=	Compressibility factor ($Z = P/g\rho RT$), dimensionless
α	=	Angle-of-attack, deg
α	=	Shock wave angle, rad. or deg
α	=	Degree of dissociation, dimensionless
α	=	Thermal diffusivity, ft^2/s
α	=	Coefficient of linear expansion, dimensionless
β	=	Ballistic coefficient (W/C_DA), dimensionless
β	=	Stagnation point velocity gradient, 1/s
β	=	Constant, dimensionless
β	=	Solid area/(solid area + porous area),dimensionless

NOMENCLATURE FOR SECTIONS A AND B (Continued):

β_1	=	Constant = 1/22,000 ft
β	=	Defined by Equation 348
Γ	=	Defined by the title of Figure 152
Γ	=	Ratio of vaporization to melting, dimensionless
γ	=	Specific heat ratio (c_p/c_v), dimensionless
$\bar{\gamma}$	=	Specific heat ratio (for ionized gases), dimensionless
Δb	=	Radial distance from afterbody to dividing streamline, ft
ΔT	=	Temperature rise, °R
ΔX	=	Stagnation point shock stand-off distance, ft
δ	=	Flow deflection angle, rad. or deg
δ	=	Velocity boundary layer thickness, ft
δ	=	Cone angle, rad. or deg
δ^*	=	Boundary layer displacement thickness, ft
ε	=	Emissivity, emittance, dimensionless
ε	=	Quantity defined by (γ-1)/(γ+1), Equation 149
ε_H	=	Quantity defined by Equation 312
θ	=	Flow inclination angle, deg
θ	=	Momentum boundary layer thickness, ft
θ	=	Body angle, deg
θ	=	Deflection angle = angle of attack + half wedge angle, deg
θ	=	Polar angle, deg
θ_c	=	Half cone angle, deg
θ_e	=	Entry angle, deg
θ_s	=	Shock angle, deg
Λ	=	Sweep angle, deg
λ	=	Free mean path length, ft
μ	=	Viscosity, lb/s-ft for N_{Re} and many other uses, lb-s/ft^2 in a few uses
ν	=	Prandtl-Meyer function, dimensionless
ν	=	Heat sink efficiency, dimensionless
ν	=	Poisson's ratio, dimensionless
ρ	=	Mass density, lb-s^2/ft^4 = slugs/ft^3 = ($g\rho$)/32.2
ρg or $g\rho$	=	Specific weight (density), lb/ft^3
σ	=	Stefan-Boltzmann constant (4.81 x 10^{-13}), Btu/ft^2-s-°R^4
τ	=	Shear stress, lb/ft^2
τ	=	Time, s, h
$\bar{\tau}$	=	Total heating time, s, h
ϕ	=	Bank angle, deg
ϕ	=	Circumferential angle, deg
ϕ	=	Meridian angle, deg
ϕ_o	=	Defined by Equation 364
$\bar{\chi}$	=	Interaction parameter, dimensionless

NOMENCLATURE FOR SECTIONS A AND B (Continued):

ψ	=	Inertial heating angle, deg
ω	=	Angular velocity of earth, rad./s

Subscripts:

A	=	Air
a	=	Ablation
adw or aw	=	Adiabatic wall
axi	=	Axisymmetric
B	=	Blasius
b	=	Base
b	=	Blunt or normal shock conditions
b	=	Body
b	=	Properties determined along dividing streamline
c	=	Char
c	=	Cold
c	=	Conduction
D	=	Diffusion controlled
d	=	Degradation zone
d	=	Dissociation
e	=	Local boundary layer edge conditions
e	=	Re-entry conditions
eq	=	Equilibrium
f	=	Final
g	=	Gas
H	=	Heat sink
i	=	Based on enthalpy
i	=	Interface, at gas-liquid
i	=	Incompressible flow
i	=	Initial
i	=	Gaseous mixture
iso	=	Isothermal
L	=	Laminar
l	=	Leading edge
l	=	Lower
l	=	Receiver
l	=	Local boundary layer edge
max	=	Maximum
N	=	Nitrogen
n	=	Nose
o	=	Reference value
O	=	Oxygen
O	=	Virgin or original plastic

NOMENCLATURE FOR SECTIONS A AND B (Continued):

P	=	Pointed cone
p	=	Conical shock conditions
R	=	Reaction
r	=	Recovery conditions
rad	=	Radiation
rad.	=	Radians
S	=	Schultz-Grunow
s	=	Shock
s	=	Wetted length
s	=	Stagnation point
T	=	Tangency point
T	=	Turbulent
t	=	Total
t	=	Stagnation point or total conditions behind a normal shock
u	=	Upper
w	=	Wall
wc	=	Adiabatic wall temperature (cold wall)
α	=	Angle-of-attack
Λ	=	Sweep angle
o	=	Sea level conditions
1	=	Upstream of shock
2	=	Downstream or behind normal shock
2-dim	=	Two-dimensional
∞	=	Freestream conditions

Superscripts:

*	=	Evaluated at reference temperature or enthalpy conditions
*	=	Reference conditions
o	=	Stagnation point
2	=	After shock

COMMON ABBREVIATIONS FOR SECTIONS A AND B:

Abs	=	Absolute
Abs	=	Absorbed
AEDC	=	Arnold Engineering Development Center
Aero.	=	Aeronautical
AIAA J.	=	American Institute of Aeronautics and Astronautics Journal.
Alt	=	Altitude
ARAP	=	Aeronautical Research Associates of Princeton
ARDC	=	Atmospheric Research Development Council
ARL	=	Aeronautical Research Laboratory
ARS	=	American Rocket Society
atm	=	Atmosphere
axi	=	Axisymmetric
BF	=	Back face
BL	=	Boundary layer
B_2O_3	=	Boric oxide
Btu	=	British thermal unit
C	=	Carbon
cm	=	Centimeter
CN	=	Cyano radial
CO_2	=	Carbon dioxide gas
CO	=	Carbon monoxide gas
Co.	=	Company
conf	=	Configuration
Const	=	Constant
convec	=	Convection
cps	=	Cycles per second
deg	=	Degree(s)
dia	=	Diameter
dim	=	Dimensional
Div	=	Division
E	=	Elastic modulus
Eng	=	Engineering
Eq.	=	Equation
°F	=	Degrees Fahrenheit
Fe	=	Iron
FF	=	Front face
FPRE	=	Flat plate reference enthalpy
ft/s, FT/S	=	Feet per second
ft	=	Feet
ft-lb	=	Foot-pound
g	=	Gram
gas rad	=	Gas radiation
GE-AETM	=	General Electric Co. - Aerophysics Engineering Technical Memo
GE-MSD	=	General Electric Co. - Missile Systems Division

COMMON ABBREVIATIONS FOR SECTIONS A AND B (Continued):

GE-RSD	=	General Electric Co. - Re-entry Systems Division
Hemi	=	Hemisphere
Hg	=	Mercury
H_2O	=	Water
h	=	Hour
Hz	=	Hertz
I_2	=	Iodide
IAS	=	Institute of the Aerospace Sciences (now AIAA, American Institute of Aeronautics and Astronautics)
in	=	Inch
iso	=	Isothermal
J.	=	Journal
K	=	Degrees Kelvin
K	=	Potassium
Lab.	=	Laboratory
lb	=	Pound
lb/ft^3	=	Pounds per cubic foot
Li	=	Lithium
LMSD	=	Lockheed Missiles and Space Division
ln	=	Logarithm, natural
log	=	Logarithm to the base 10
Mg	=	Magnesium
Mass.	=	Massachusetts
Max, max	=	Maximum
Mo	=	Molybdenum
MSSD	=	Missiles and Space Systems Division
MSVD	=	Missiles and Space Vehicle Division
N	=	North
Na	=	Sodium
NACA	=	National Advisory Committee for Aeronautics
NASA	=	National Aeronautics and Space Administration
NBS	=	National Bureau of Standards
Ni	=	Nickel
No., no.	=	Number
N_2	=	Nitrogen gas
O_2	=	Oxygen gas
p.	=	Page
pp.	=	Pages
°R	=	Degrees Rankine
rad.	=	Radians
rad (RAD.)	=	Radiation or radiative heating
s	=	Second
S	=	Sulfur
SiC	=	Silicon carbide

COMMON ABBREVIATIONS FOR SECTIONS A AND B (Continued):

SiO_2	=	Silica
Tech.	=	Technical
TGA	=	Thermogravimetric analysis
Ti	=	Titanium
TIS	=	Technical Information Series
TN	=	Technical Note
TR	=	Technical Report
Vol	=	Volume
WADC	=	Wright Air Development Center
WADD	=	Wright Air Development Division
%	=	Percent
~	=	Proportional to
≅ or ≃	=	Approximately equal to
>>	=	Much greater than

SECTION A - BOOST HEAT TRANSFER

1. INTRODUCTION:

1.1 Scope:

The prediction of vehicle temperatures during ascent through the earth's atmosphere requires an accurate knowledge of the aerodynamic heating rates occurring at the vehicle surface. Flight parameters required in heating calculations include the local airstream velocity, pressure, and temperature at the boundary layer edge for the vehicle location in question. In addition, thermodynamic and transport air properties are required at these conditions.

Both laminar and turbulent boundary layers occur during the boost trajectory. Experience has shown that laminar and turbulent heating are of equivalent importance. Laminar heating predominates in importance in the stagnation areas, but the large afterbody surfaces are most strongly affected by turbulent heating. Once the local flow conditions and corresponding air properties have been obtained, the convective heating rate may be calculated for a particular wall temperature. This assumes that the boundary layer flow regime (that is, turbulent, laminar, or transitory) has also been established, so that a heating theory corresponding to the particular flow conditions may be selected.

This section presents theoretical methods for computing boost vehicle surface aerodynamic heating rates. First, procedures are given for computing the local flow distributions around the vehicle. Second, methods are given for computing the convective heating rates, using the flow parameters found previously.

1.2 Nomenclature:

Refer to the nomenclature list on page 15.

2. FLOW FIELD CALCULATIONS:

Prediction of aerodynamic heat transfer depends first on the determination of the applicable flow field. In practice, knowledge of the surface pressure distribution is essential for heat transfer calculations. Figure 1 is a schematic representation of the flow field about a typical vehicle during supersonic flight. This figure also serves to define flow field terms that will be used consistently throughout this section.

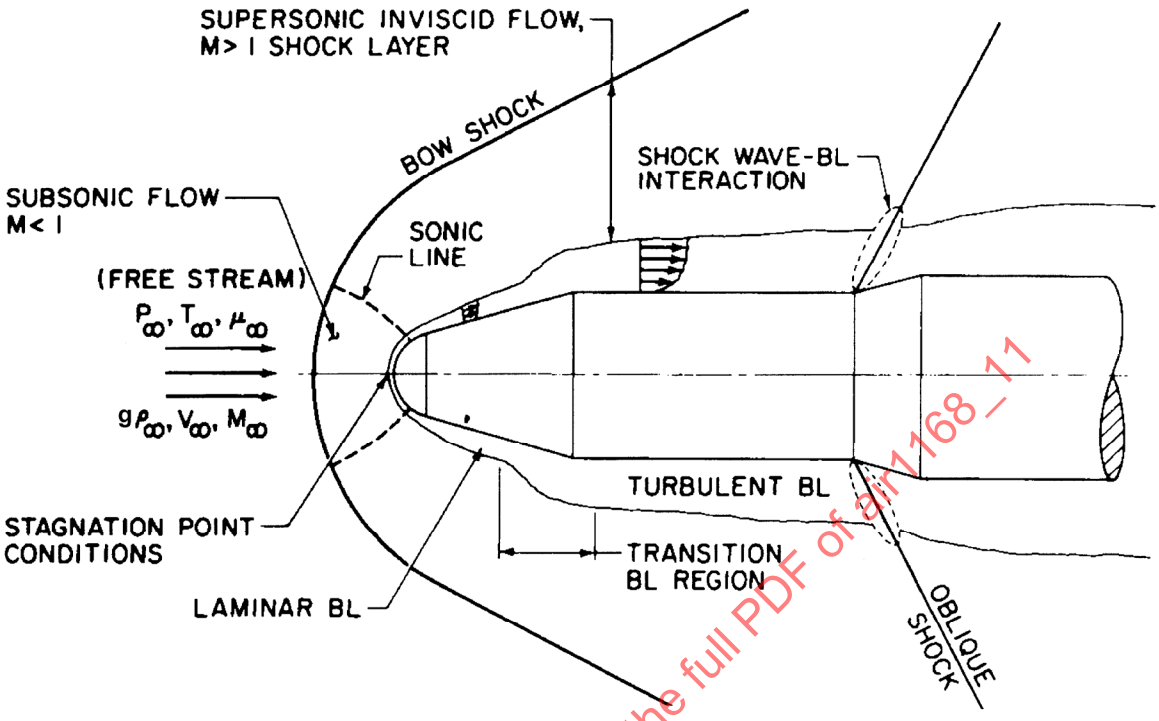

FIGURE 1 - Typical Boost Vehicle Configuration and Flow Field Structure
BL = Boundary Layer

2. (Continued):

In many instances, the concern is with the flow about blunted bodies or about bodies that are sufficiently blunt to produce a detached bow shock. Figure 1 indicates that in addition to the bow shock, other shock waves may be generated as a result of the vehicle geometry. Depending on the configuration, more than one oblique shock may exist.

The region bounded by the shock wave and the outer edge of the boundary layer shown in Figure 1 is called the shock layer. This region is important because its structure determines the distribution of surface pressures on the body. Because of the absence of significant viscous forces in this region, it is also commonly referred to as the inviscid flow field.

The shock layer, or inviscid flow field, is further divided into a subsonic and supersonic region. The subsonic portion exists in the vicinity of the stagnation region, where the local velocities are low (relative to the freestream velocity). Static temperatures are high because of passage of the fluid through the strong, nearly normal shock wave. The combination of the relatively low velocity and high temperature levels leads to local Mach numbers below 1 in this region.

The flow, which is compressed as a result of the strong shock, expands as it moves around the body until a second shock occurs. This expansion increases the velocity, lowers the static temperature, and at some point the local Mach numbers in the shock layer exceed 1. The dividing line between the subsonic and supersonic regions is called the sonic line.

2. (Continued):

Figure 1 also shows the development of a viscous boundary layer on the body. The boundary layer is initiated at the stagnation point, where it is laminar. It remains laminar for some distance downstream of the stagnation point until, at some location, various disturbances may cause the boundary layer to undergo transition from a laminar to a turbulent state. In general, this transition front moves aft on the vehicle during the boost phase of flight.

Configurations of the type shown in Figure 1 may, for the purpose of flow field analysis, be broken down into geometric sections to be solved by various theories. To obtain the pressure distribution on the entire vehicle, it is necessary to match the pressure and pressure gradient at the junction of two theories. Theoretical methods for calculating inviscid flow field quantities are discussed in the following paragraphs. A sample calculation illustrating the application of such theories is presented in Paragraph 8.

2.1 Isentropic Relations:

For the purpose of approximate flow field calculations, it is customary to assume a thermally and calorically perfect gas, that is, $P = \rho g R T$ and c_p = Const, respectively. In addition, with the exception of flow across shock waves, the flow is assumed isentropic. The term “isentropic” denotes a reversible adiabatic process. For these conditions, the following relations apply:

$$\frac{P_1}{P_2} = \left(\frac{g\rho_1}{g\rho_2}\right)^{\gamma} \quad \text{(Eq.1)}$$

$$\frac{T_1}{T_2} = \left(\frac{P_1}{P_2}\right)^{(\gamma-1)/\gamma} \quad \text{(Eq.2)}$$

$$\frac{T_t}{T} = 1 + \frac{\gamma-1}{2}(M^2) \quad \text{(Eq.3)}$$

$$\frac{P_t}{P} = \left[1 + \frac{\gamma-1}{2}(M^2)\right]^{\gamma/(\gamma-1)} \quad \text{(Eq.4)}$$

$$\frac{g\rho_t}{g\rho} = \left[1 + \frac{\gamma-1}{2}(M^2)\right]^{1/(\gamma-1)} \quad \text{(Eq.5)}$$

where:

Subscripts 1 and 2 refer to any two points in the flow

2.1 (Continued):

The total temperature relation, Equation 3, is restricted to adiabatic flow only.

The equations for total temperature, pressure, and density are plotted in Figure 2 for $\gamma = 1.4$. Tabulations of these quantities may also be found in Reference 1.

2.2 Normal Shock Relations:

From the mass, momentum, and energy conservation equations and the perfect gas equation of state, the following useful relations may be obtained for flow across a normal shock wave:

$$\frac{P_2}{P_\infty} = \frac{2\gamma M_\infty^{\,2} - (\gamma - 1)}{\gamma + 1} \tag{Eq.6}$$

$$\frac{g\rho_2}{g\rho_\infty} = \frac{(\gamma + 1)M_\infty^{\,2}}{(\gamma - 1)M_\infty^{\,2} + 2} \tag{Eq.7}$$

$$\frac{T_2}{T_\infty} = \frac{[2\gamma M_\infty^{\,2} - (\gamma - 1)][(\gamma - 1)M_\infty^{\,2} + 2]}{(\gamma + 1)^2 M_\infty^{\,2}} \tag{Eq.8}$$

$$M_2^{\,2} = \frac{(\gamma - 1)M_\infty^{\,2} + 2}{2\gamma M_\infty^{\,2} - (\gamma - 1)} \tag{Eq.9}$$

$$\frac{P_{t2}}{P_\infty} = \left[\frac{(\gamma + 1)M_\infty^{\,2}}{2}\right]^{\gamma/(\gamma-1)} \left[\frac{\gamma + 1}{2\gamma M_\infty^{\,2} - (\gamma - 1)}\right]^{1/(\gamma-1)} \tag{Eq.10}$$

Assuming that $\gamma = 1.4$, the preceding ratios have been computed and are plotted in Figure 3 as a function of freestream Mach number.

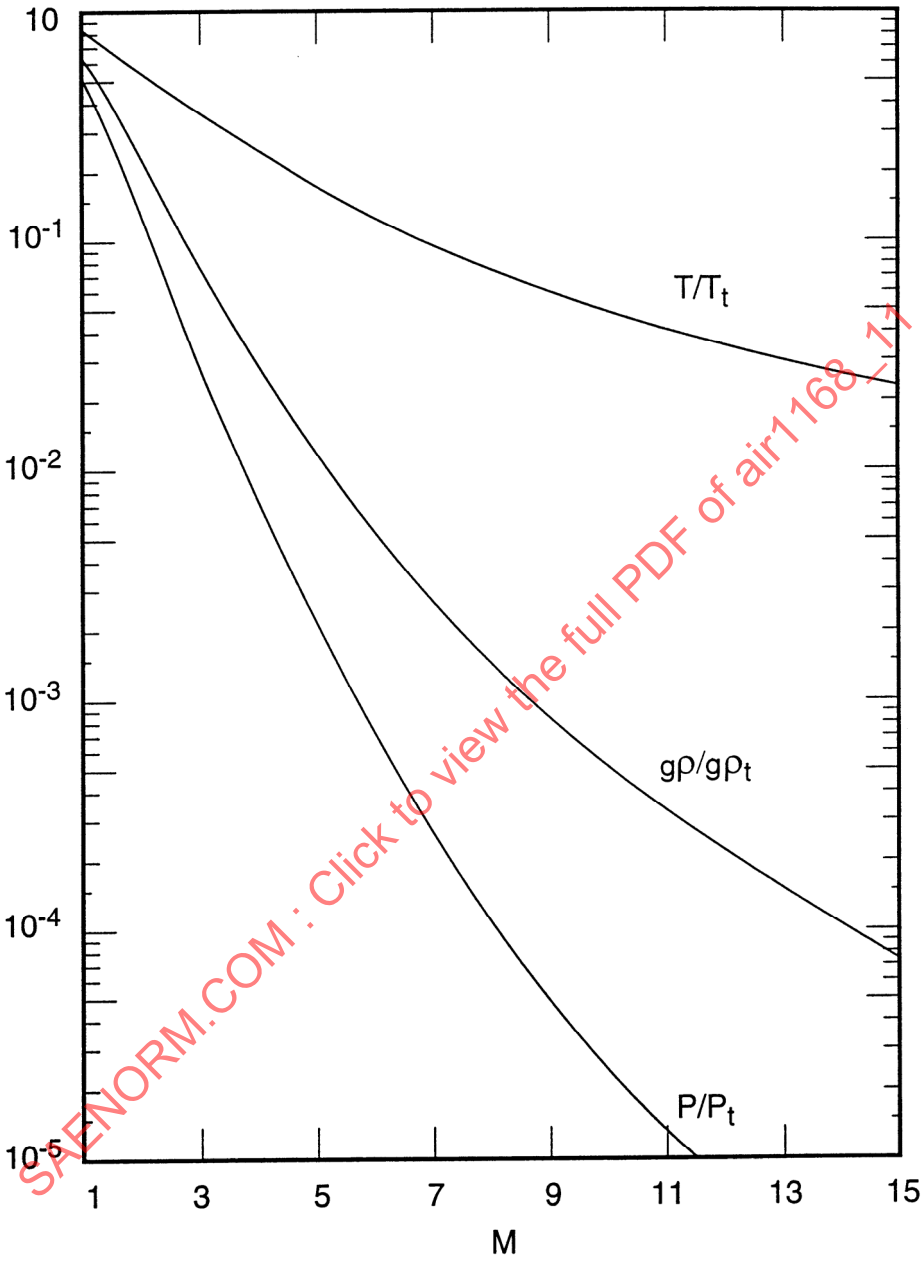

FIGURE 2 - Isentropic Flow Relations

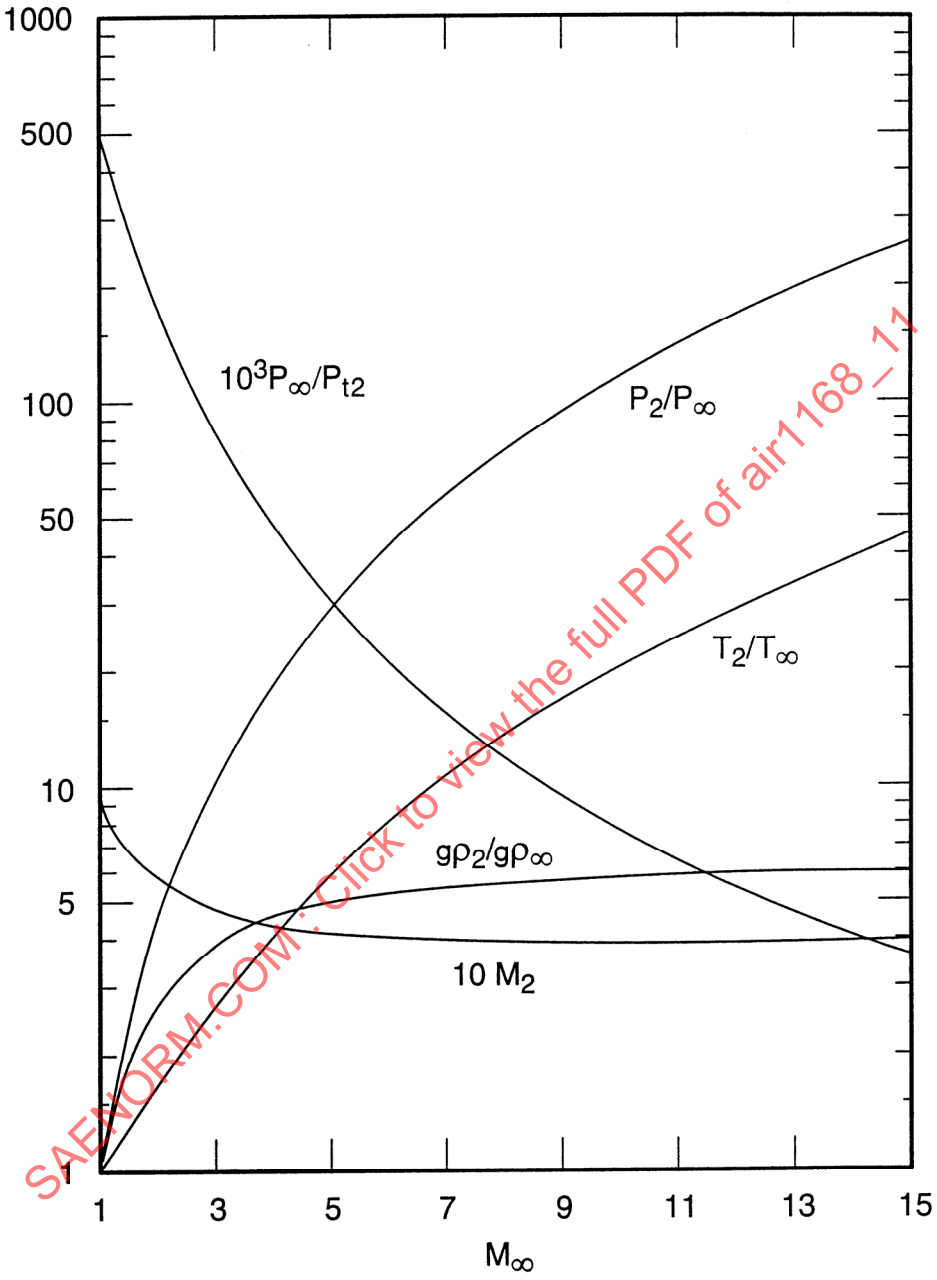

FIGURE 3 - Normal Shock Flow Relations

2.3 Oblique Shock Relations:

With the exception of the static-to-total pressure ratio, the perfect gas normal shock relations tabulated above may be used for oblique shocks if M_∞ and M_2 are replaced by their normal components, $M_\infty \sin \alpha$ and $M_2 (\alpha - \delta)$, where α is the shock wave angle and δ is the flow deflection angle. The application of this technique is also explained in Reference 1, and appropriate charts are provided for the determination of the shock wave angle.

Figures 4 through 6 present the pressure and temperature ratios and the Mach number as functions of the freestream Mach number for various flow deflection angles.

2.4 Normal and Oblique Shock Relations for Real Gas:

At Mach numbers greater than about 6, dissociation effects become significant, and the normal and oblique shock relations for a perfect gas no longer hold. As an example, both temperature and density ratios across a normal shock at $M_\infty = 20$ would be in error by over 100%, using ideal gas shock relations.

Real gas equilibrium quantities as a function of $M_\infty \sin \alpha$, where α is the oblique shock angle, are shown in Figures 7 through 11. These curves are reproduced from Reference 2 and are based on the 1959 ARDC atmosphere. The shock functions shown were calculated for the terminal points of the isothermal atmosphere regions.

For a given freestream Mach number and two-dimensional flow deflection angle (δ), Figure 7 may be used to obtain the shock angle parameter ($M_\infty \sin \alpha$). This quantity and a known altitude allow the ratios T_2/T_∞, P_2/P_∞, $g\rho_2/g\rho_\infty$, V_∞/V_2, and i_2/i_∞ to be read from Figures 8 through 10.

For the real gas case of air in dissociated equilibrium, a useful relation between the pressure ratio and freestream Mach number is given by (Reference 3)

$$\frac{P_{t2}}{P_\infty} = 1.27\, M_\infty^{2.02} \qquad \text{(Eq.11)}$$

For high Mach numbers the perfect gas pressure ratio relation, Equation 10, reduces to

$$\frac{P_{t2}}{P_\infty} = 1.289\, M_\infty^{2} \qquad \text{(Eq.12)}$$

Thus, real gas effects do not significantly change the pressure ratio from the perfect gas value.

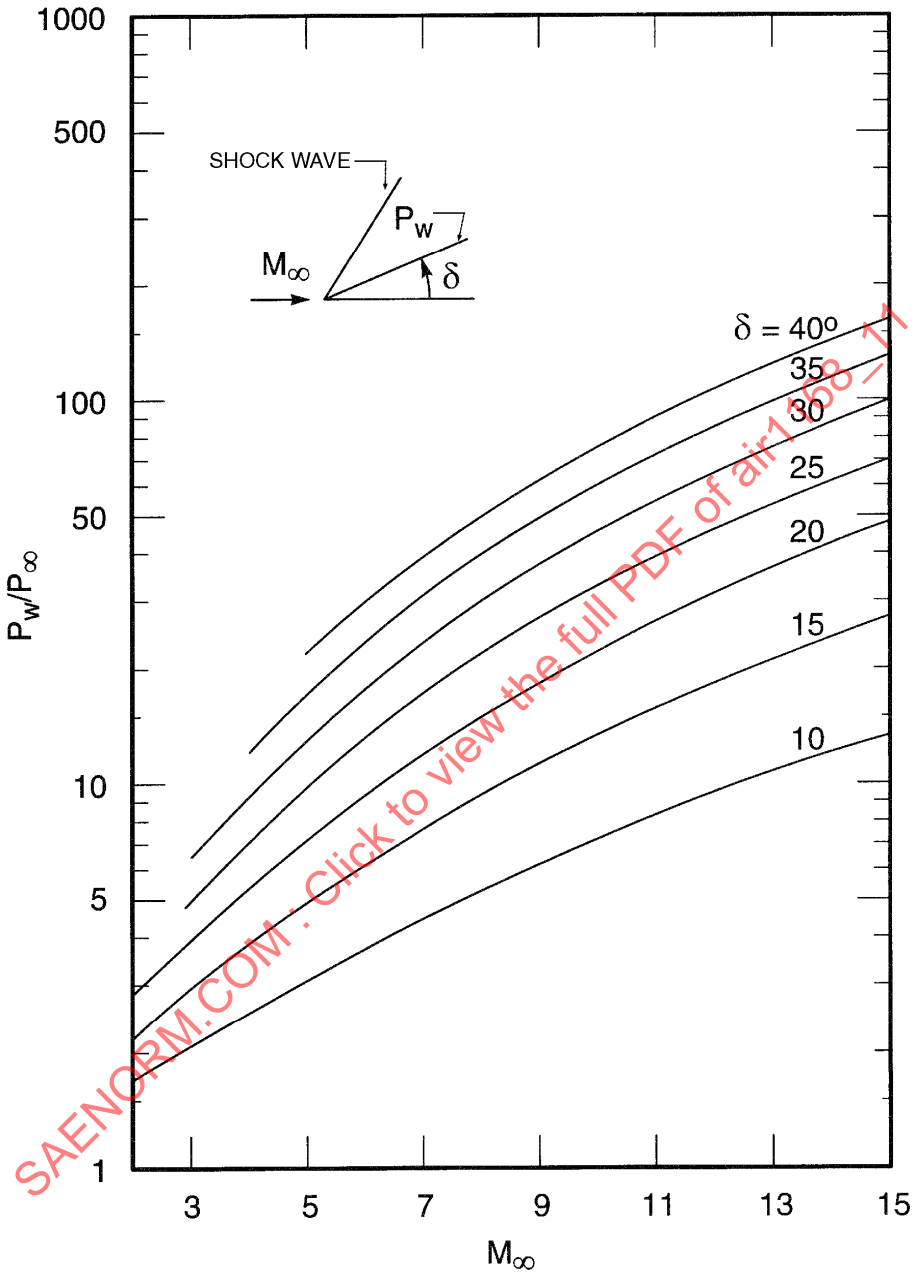

FIGURE 4 - Pressure Ratio Across an Oblique Shock (Perfect Gas, $\gamma = 1.4$)

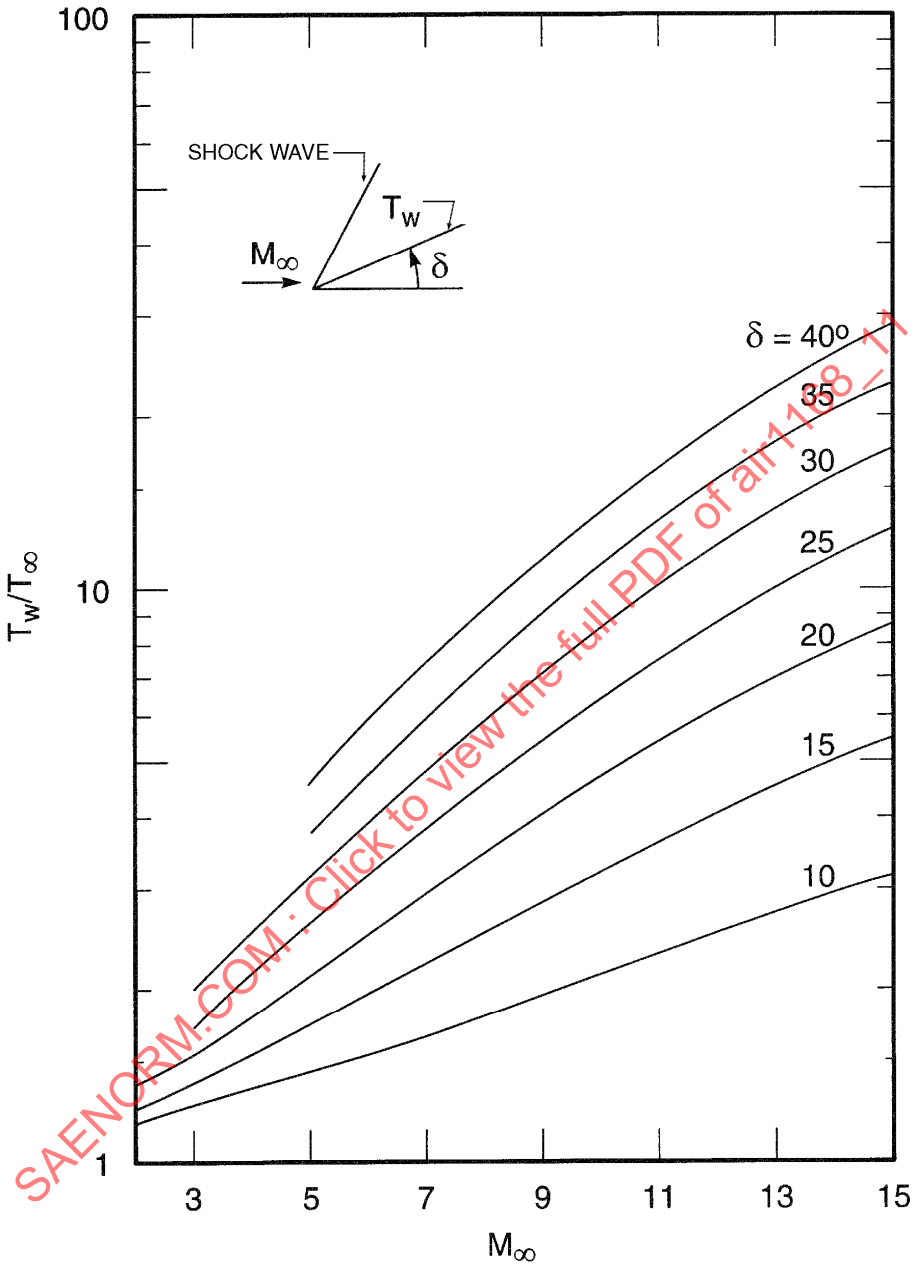

FIGURE 5 - Temperature Ratio Across an Oblique Shock (Perfect Gas, $\gamma = 1.4$)

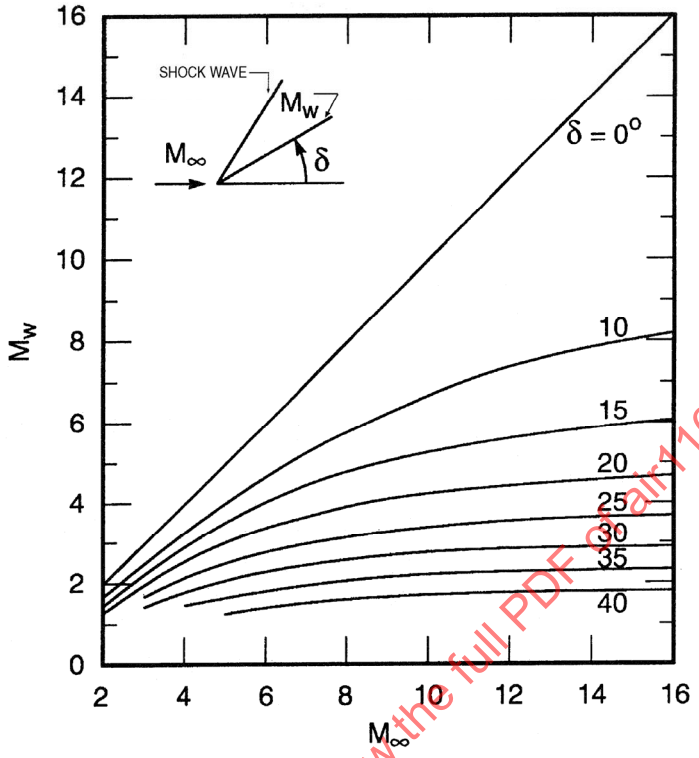

FIGURE 6 - Mach Number Behind an Oblique Shock

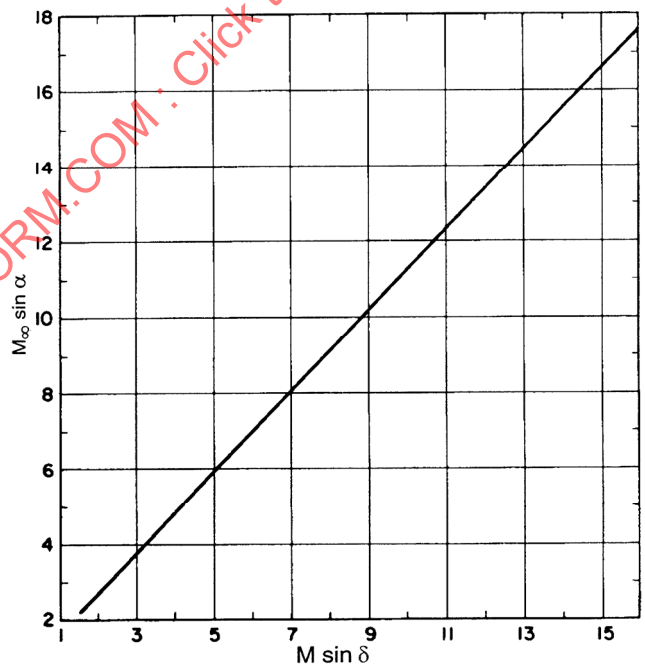

FIGURE 7 - Two-Dimensional Flow Hypersonic Similarity Parameter Versus Shock Angle Parameter

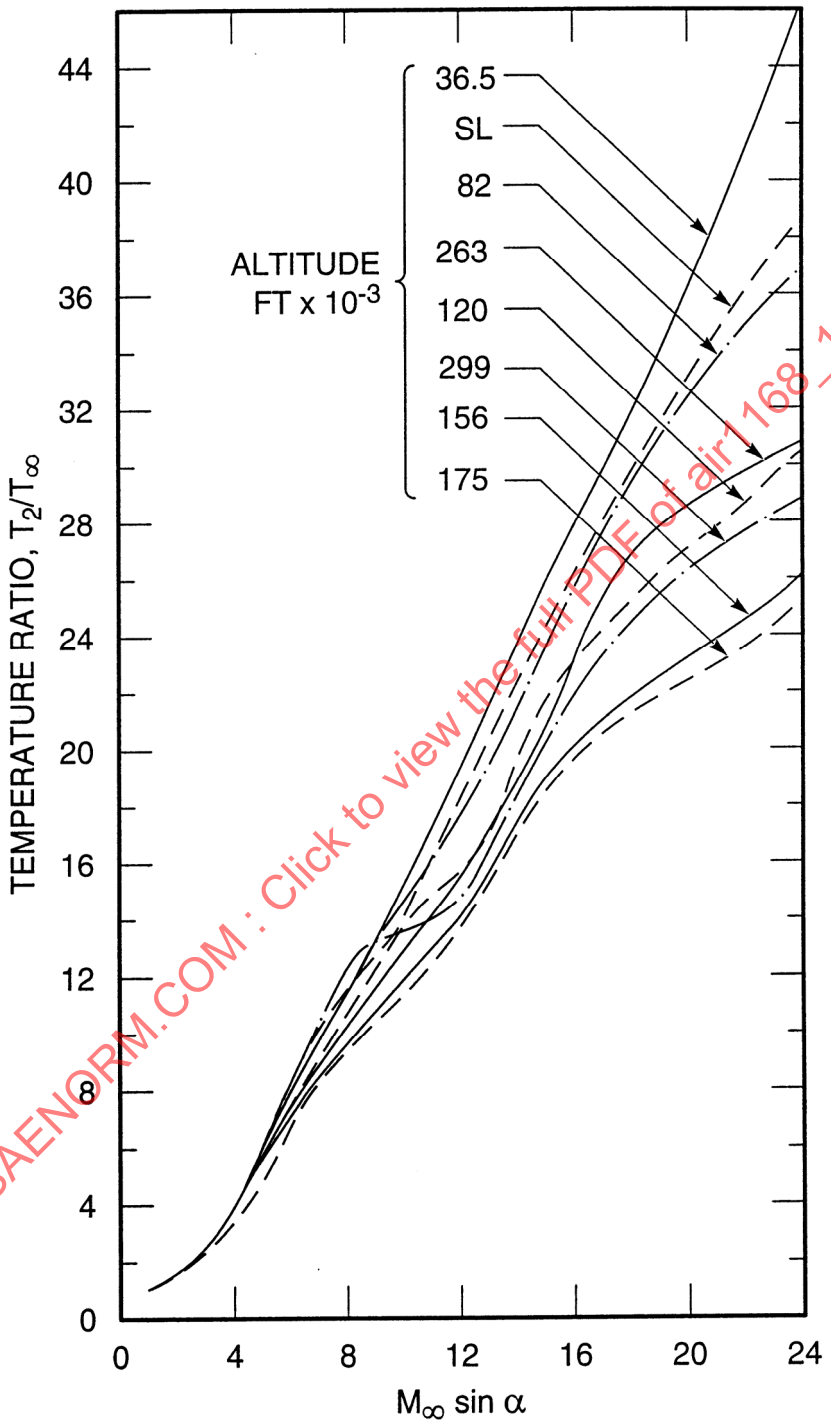

FIGURE 8 - Real Gas Temperature Ratio Across an Oblique Shock

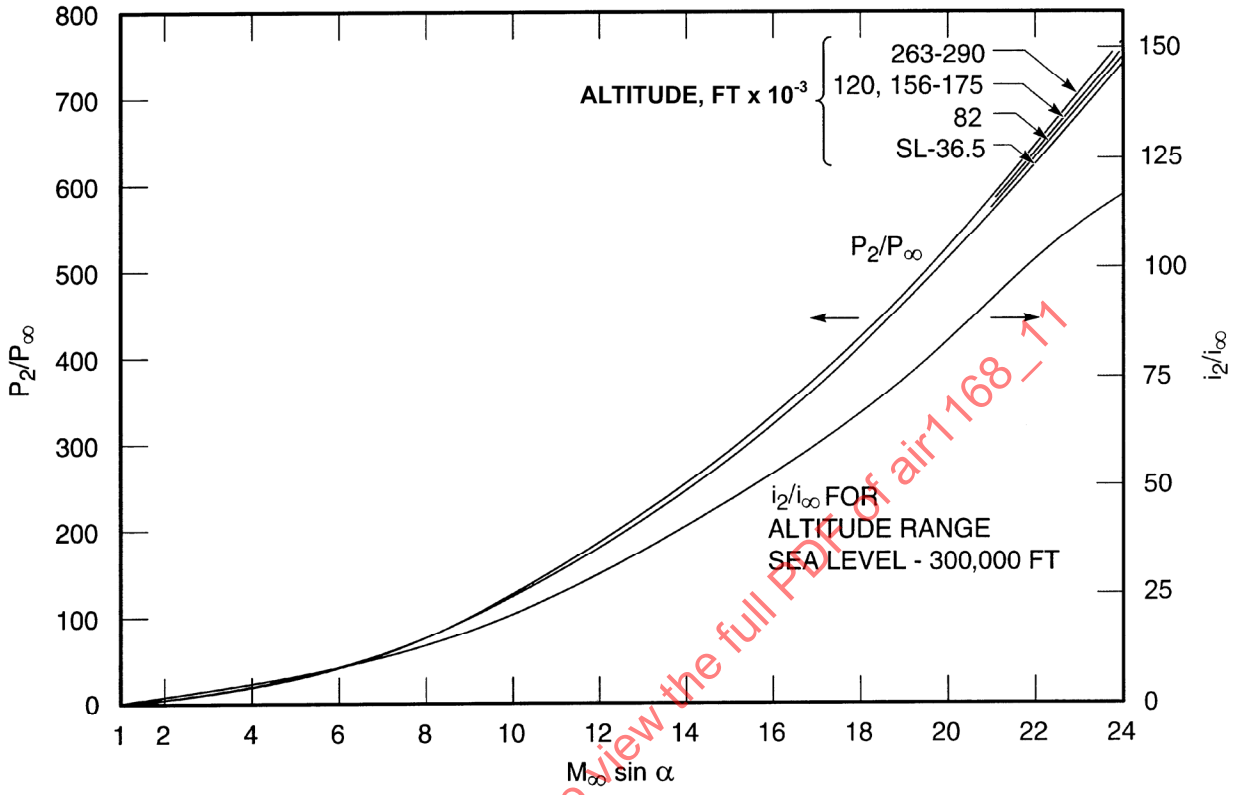

FIGURE 9 - Real Gas Pressure Ratio and Enthalpy Ratio Across an Oblique Shock

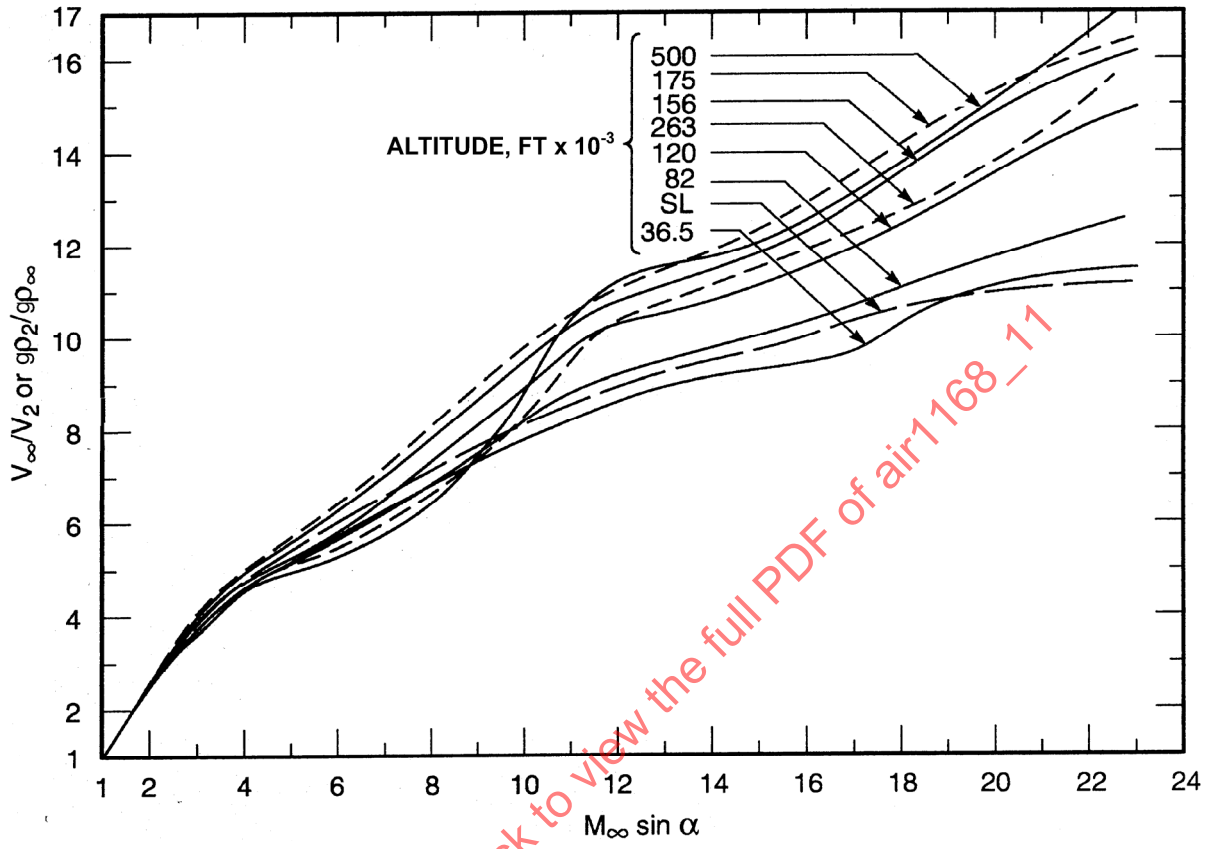

FIGURE 10 - Real Gas Density Ratio and Reciprocal of Velocity Ratio Across an Oblique Shock

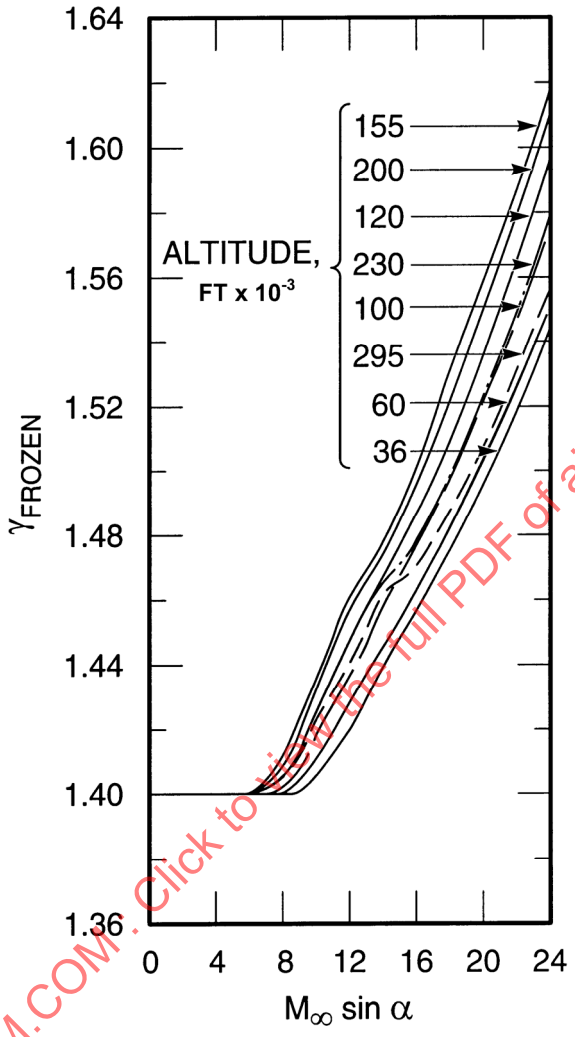

FIGURE 11 - Frozen Flow Specific Heat Ratio

2.4 (Continued):

At higher Mach numbers a finite rate nonequilibrium chemistry will exist which is between the limiting cases of infinite reaction rates (equilibrium) and zero recombination rates (frozen). At flight altitudes below 100,000 ft, the flow will be close to thermochemical equilibrium. It is also a good approximation to assume frozen-flow for the expansion about the body at higher altitudes. For equilibrium, one can use a Mollier diagram by expanding along an isentrope from the conditions behind the shock to the body pressure. For frozen flow, one can use γ_{frozen} from Figure 11 in the isentropic Equations 1 and 2.

2.5 The Newtonian Approximation:

A common method for predicting surface pressure distributions is based on the Newtonian particle model. This model postulates discrete noninteracting particles impacting upon the body surface. The approaching stream loses all its normal momentum component to the body, but the tangential component remains unaltered. A momentum balance for a windward body element results in the following expression for the pressure coefficient:

$$C_p = 2 \sin^2 \delta \qquad \text{(Eq.13)}$$

where:

δ is the angle between the freestream velocity and the local body surface tangent; that is, at the stagnation point, δ = 90 deg

2.6 Modified Newtonian:

Equation 13 is sometimes modified to match experimental data at the stagnation point. The resulting expression is known as the modified Newtonian approximation and is given by

$$\frac{C_p}{C_{p,max}} = \frac{P - P_\infty}{P_{t2} - P_\infty} = \sin^2 \delta \qquad \text{(Eq.14)}$$

where:

$C_{p,max}$ = Pressure coefficient at stagnation point

2.6 (Continued):

This relation has been extensively compared with theory and adequately predicts the pressure in the vicinity of the stagnation point. Assuming the shock layer fluid in the stagnation point vicinity to be incompressible, the normal shock continuity and momentum equations provide an approximation of $C_{p,\,max}$ where

$$C_{p,max} = 2 - \frac{g\rho_1}{g\rho_2} \qquad \text{(Eq.15)}$$

where:

Subscripts 1 and 2 denote conditions upstream and downstream from the detached shock wave, respectively

The modified Newtonian pressure distribution, combined with a Prandtl-Meyer expansion (see 2.7), for a hemisphere is presented in Figure 12.

The derivation of either the Newtonian or modified Newtonian equation makes the assumption that $M_\infty\ \delta >> 1$, where δ is the angle between the surface tangent and the freestream velocity vector. This means that as the velocity decreases or the body becomes parallel to the flow, the method becomes increasingly inaccurate. The modified Newtonian method has, however, given good correlation with other methods even in the low supersonic regime (M = 2).

2.7 Prandtl-Meyer Flow:

A solution for supersonic inviscid flow is available for corner type flows. In such a flow, for given initial conditions, the magnitude of the Mach number at any point depends only on the flow direction at that point. Figure 13 illustrates the Prandtl-Meyer corner flow.

The results of the theory are very simple, since the direction of flow and the upstream Mach number are sufficient to determine the downstream Mach number, which in turn determines all the local point functions of that Mach number.

The relation between the flow inclination θ and the Mach number M in an isentropic two-dimensional compression, or expansion by turning, is

$$-\theta + C = \left(\frac{\gamma+1}{\gamma-1}\right)^{1/2} \tan^{-1}\left[\left(\frac{\gamma-1}{\gamma+2}\right)(M^2-1)\right]^{1/2} - \tan^{-1}(M^2-1)^{1/2} \qquad \text{(Eq.16)}$$

where:

C = Constant of integration

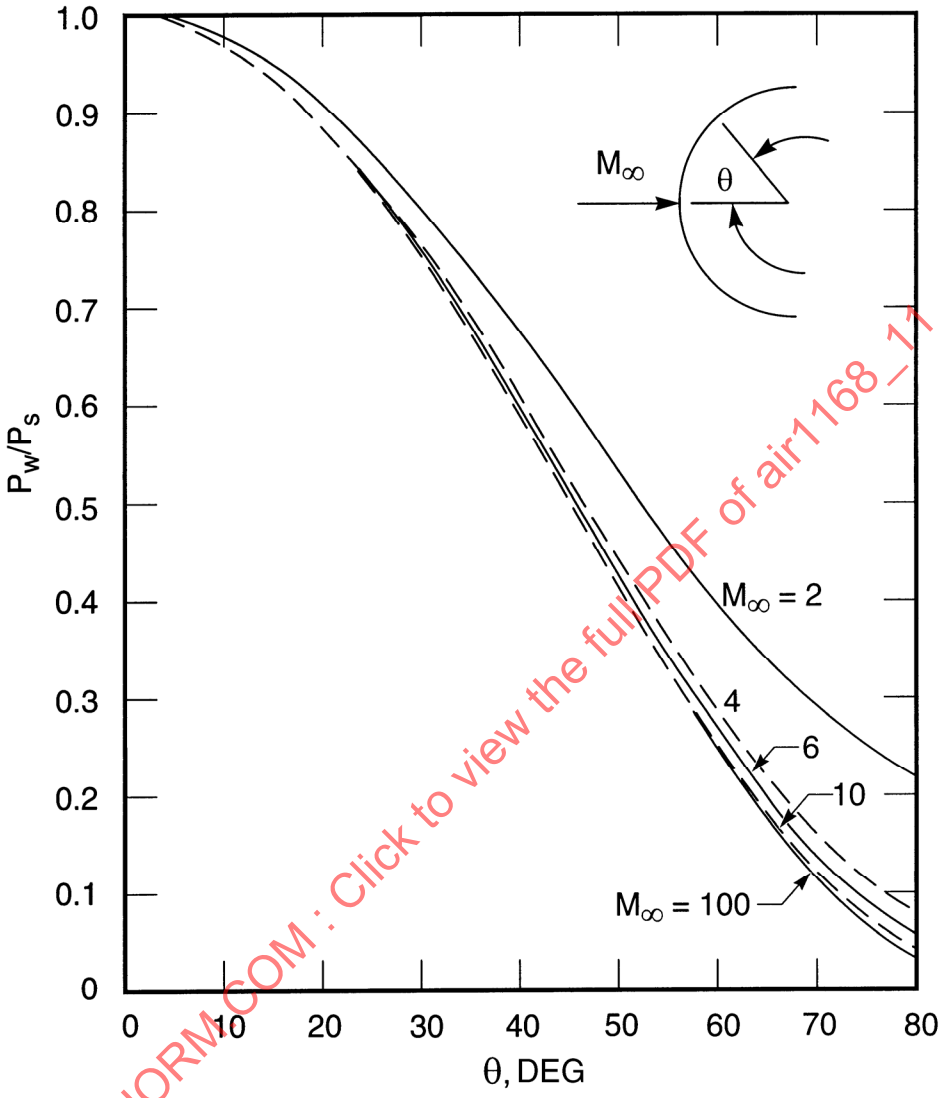

FIGURE 12 - Modified Newtonian-Prandtl-Meyer Pressure Distribution on a Hemisphere

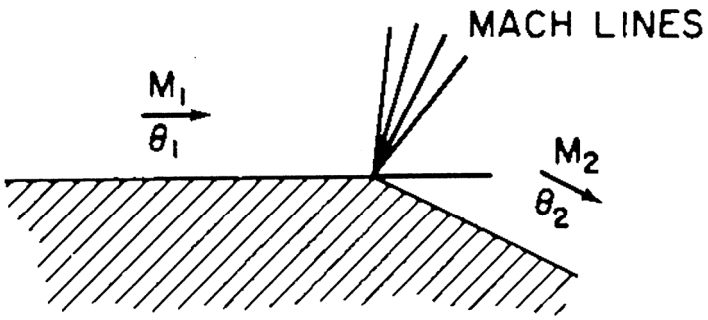

FIGURE 13 - Prandtl-Meyer Expansion

2.7 (Continued):

The right-hand side of Equation 16 is called the Prandtl-Meyer function, $\nu(M)$. The constant of integration is chosen such that $\nu(1) = 0$. The resulting relations between the flow inclination angle θ and the Prandtl-Meyer functions are:

1. For expansion,

$$\nu_2 - \nu_1 = |\theta_2 - \theta_1| \qquad \text{(Eq.17)}$$

2. For compression,

$$\nu_2 - \nu_1 = - |\theta_2 - \theta_1| \qquad \text{(Eq.18)}$$

where:

Subscripts 1 and 2 refer to conditions upstream and downstream from the expansion, respectively

Although the Prandtl-Meyer theory applies only to a single boundary problem, it can be used to construct the flow in any plane symmetric problem by breaking the expansion zones into several regions of constant flow conditions. Each region is assumed to be separated by weak expansion shock boundaries. For a given initial Mach number and change in flow deflection angle, the resulting Mach number may be obtained from tabular values of $\nu(M)$. Such tables are contained in Reference 1 for $\gamma = 1.4$.

It has been demonstrated that the surface pressure distribution for a blunt body can be predicted by combining the modified Newtonian and Prandtl-Meyer expansion methods. The technique is to utilize modified Newtonian theory from the stagnation point to the point where the pressure gradient equals that computed by using the Prandtl-Meyer method. A Prandtl-Meyer solution is then introduced, starting with the Newtonian pressure.

2.8 Taylor-Maccoll Cone Theory:

The inviscid flow around a cone at zero angle of attack is axially symmetric and can, therefore, be described in terms of two independent space coordinates. Because of the axial symmetry, all stream properties are constant on conical surfaces having a common vertex. Taylor and Maccoll derived a nonlinear differential equation describing the flow about a cone. By utilizing the energy equation derived from the mass conservation relations for steady, nonviscous flow, they arrived at the following differential equation:

$$\frac{d^2(V/c)}{d\theta^2}\left[\frac{\gamma+1}{2}\left(\frac{dV/c}{d\theta}\right)^2-\left(\frac{\gamma-1}{2}\right)\left(1-\frac{V^2}{C^2}\right)\right]$$
$$=(\gamma-1)\left(1-\frac{V^2}{C^2}\right)\frac{V}{C}+\frac{\gamma-1}{2}\left(1-\frac{V^2}{C^2}\right)\cot\theta\frac{dV/c}{d\theta}+(-\gamma)\frac{V}{C}\left(\frac{dV/c}{d\theta}\right)^2-\left(\frac{\gamma-1}{2}\right)\cot\theta\left(\frac{dV/c}{d\theta}\right)^3 \quad \text{(Eq.19)}$$

The constant C is the maximum attainable speed for a gas, that is, the speed produced by expansion into a vacuum.

Results of this theory are plotted in Figures 14 through 16. Figures 14 and 15 present the cone surface pressure and temperature, respectively, in ratio to freestream values. Cone surface Mach number variation is illustrated in Figure 16. From these curves, additional conical flow quantities may be determined, using the isentropic flow relations. Additional presentation of the perfect gas results of this theory are contained in References 1 and 4.

For the real gas case of air in dissociated equilibrium, Romig (Reference 5) has calculated the cone flow quantities. These calculations are based on a constant freestream temperature of 490 °R. A portion of Romig's results are plotted in Figures 17 and 18, showing the cone pressure ratio and velocity parameter as functions of the hypersonic similarity parameter $V_\infty \sin\theta_c/10^4$. Approximate relations, valid to about ±2%, are given by:

$$V_\infty{}^2 - V_c{}^2 = 1.131\times10^8\left[\frac{V_\infty \sin\theta_c}{10^4}\right]^{1.93} \quad \text{(Eq.20)}$$

$$\frac{P_c}{P_\infty} = 123.7\left(\frac{V_\infty \sin\theta_c}{10^4}\right)^{1.96} \quad \text{(Eq.21)}$$

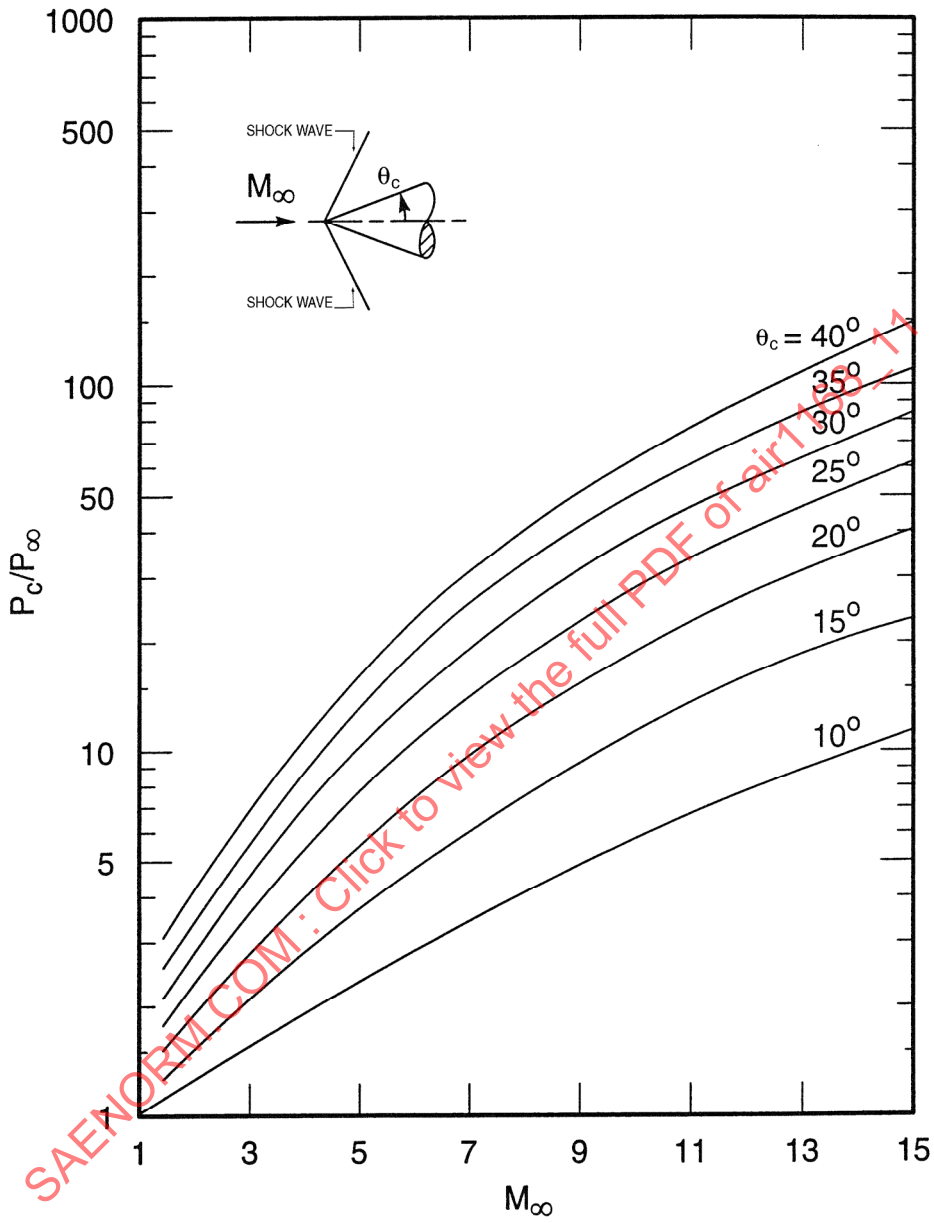

FIGURE 14 - Cone Surface Pressure to Freestream Pressure Ratio (γ = 1.4)

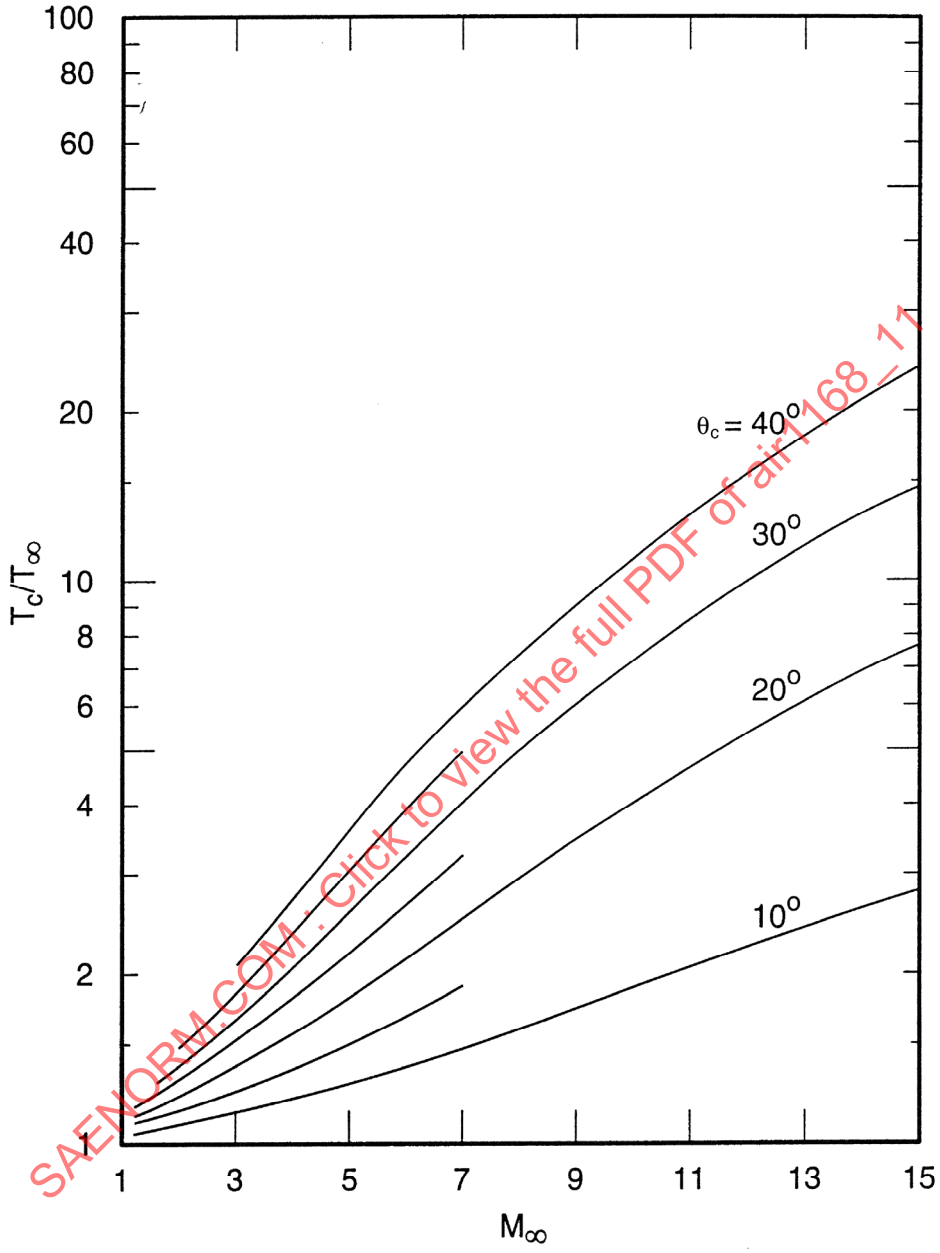

FIGURE 15 - Cone Surface Temperature to Freestream Temperature ($\gamma = 1.4$)

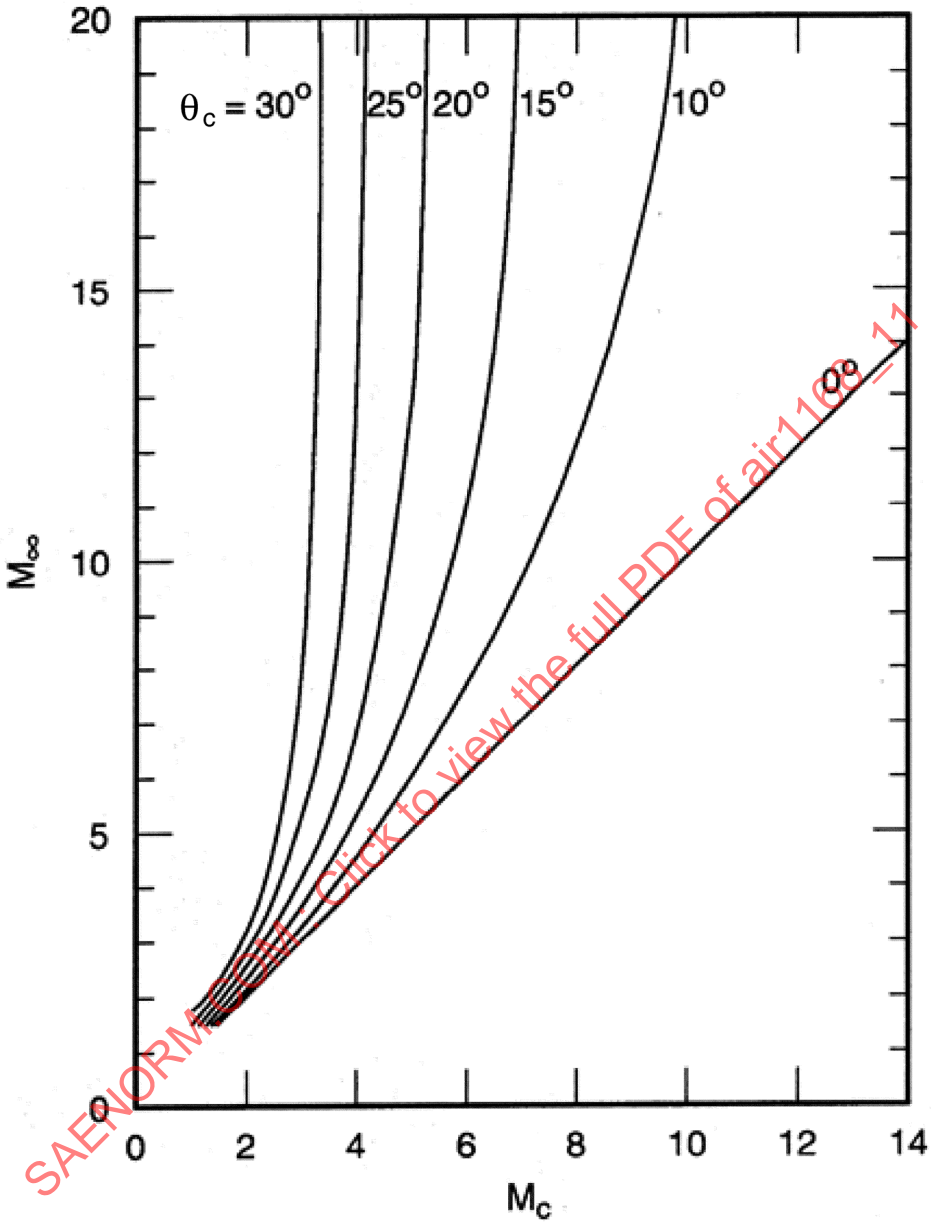

FIGURE 16 - Mach Number at Cone Surface ($\gamma = 1.4$)

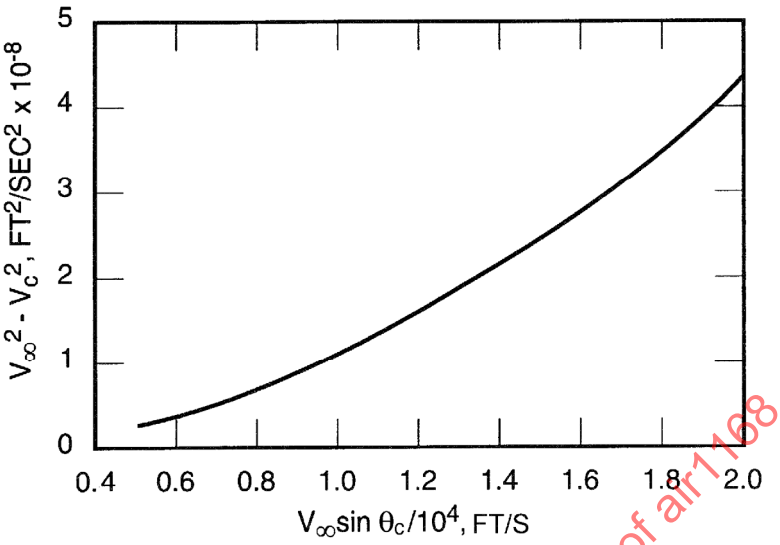

FIGURE 17 - Real Gas Cone Velocity Parameters
(T_∞ = 490 °R, $10^{-4} \leq P_\infty \leq 10^{-1}$ atm)

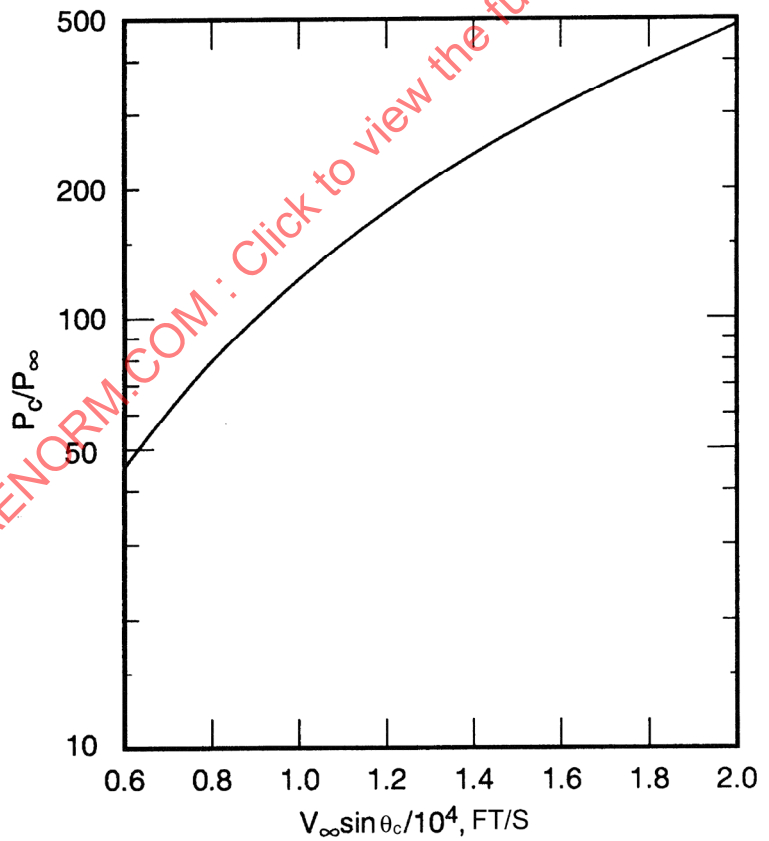

FIGURE 18 - Real Gas Cone Pressure Ratio
(T_∞ = 490 °R, $10^{-4} \leq P_\infty \leq 10^{-1}$ atm)

2.9 Tangent Cone:

The tangent cone approximation states that the pressure at any point on the surface of a body of revolution at arbitrary angles of pitch and yaw is identical with that on a semi-infinite unyawed circular cone of half-angle equal to the local inclination of the streamline with respect to the flight direction.

The equation for the local inviscid pressure is given by

$$\frac{P}{P_\infty} = 1 + \left(\frac{2\gamma}{\gamma+1}\right)(k_s{}^2 - 1) + \gamma(k_s - k_c)^2 \cdot \left[\frac{\gamma+1}{(\gamma-1)+(2/k_s{}^2)}\right] \quad \text{(Eq.22)}$$

where:

$$k_s = \left(\frac{\gamma+1}{\gamma+3}\right)k_c + \left[\left(\frac{\gamma+1}{\gamma+3}\right)^2 k_c{}^2 + \frac{2}{\gamma+3}\right]^{1/2} \quad \text{(Eq.23)}$$

$$k_c = M_\infty\, \theta_c \quad \text{(Eq.24)}$$

This method applies for angles only between 0 and 90 deg. Reference 1 contains graphs and equations of local pressure coefficient based on this method.

2.10 Tangent Wedge:

This method is very similar to the tangent cone method except that the local pressure coefficient calculation is based upon a two-dimensional oblique shock instead of a three-dimensional conical shock. Equations and graphs of local pressure coefficient for the tangent wedge are also found in Reference 1.

2.11 Expansions to Zero Pressure Coefficient:

At many vehicle locations it is possible to assume that the local flow has passed through a normal shock wave and expanded to freestream static pressure; that is,

$$C_p = \frac{P_1 - P_\infty}{\left(\frac{1}{2g}\right) g\rho_\infty V_\infty{}^2} \cong 0 \quad \text{(Eq.25)}$$

2.11 (Continued):

For most blunted vehicles with length-to-diameter ratios of about 5 or less, studies have shown that all fluid in the boundary layer passes through the near normal portion of the shock wave (Reference 6). Zero angle of attack blunted cylinders and flat plates are possible examples of such configurations. For these conditions, it is possible to calculate the inviscid flow quantities using the perfect gas isentropic and normal shock relations discussed previously.

Shown in Figures 19 and 20 are the temperature, Mach number, and Reynolds number ratios for flow through a normal shock and expansion to zero pressure coefficient; that is, $P_1 = P_\infty$. The Reynolds number curve assumes μ is proportional to (defined as ~) $T^{0.7}$.

Expansion to zero pressure coefficient is also frequently assumed for cone-cylinder configurations. Local flow properties on the cylinder surface may be calculated by using the isentropic relations and the cone flow solutions discussed previously. An example of one such calculation for a 15 deg semi-apex angle cone-cylinder is shown in Figure 21.

2.12 Applications:

Various methods for predicting pressure can be used on a single vehicle. To obtain the inviscid pressure distribution on the entire vehicle, it is necessary to match the pressures and slope of the pressure at the junction of the two methods. An example of how a complicated composite body of revolution can be broken into sections to be solved by various methods, and the various methods that can be used for each section, is shown in Figure 22, on which the numerals refer to the following items:

1. Theories that can be used in the stagnation region are the Newtonian and modified Newtonian.

2. Theories that can be used in this region are the Taylor-Maccoll cone solution and the tangent cone.

3. At locations close to cone-frustum-cylinder intersections, the flow tends to overexpand to static pressures less than freestream. A two-dimensional Prandtl-Meyer expansion may be assumed to occur at the cone-cylinder intersection.

4. For cylindrical vehicle sections at zero angle of attack, a common method used in obtaining the local static pressure is to assume a zero pressure coefficient at the location in question. This approximation is usually made at locations downstream from cone-frustum-cylinder intersections so that overexpansions and recompressions of the flow have had sufficient distance to take place.

5. For small expansions, the local problem of having separated flow at the aft end of this region should not affect the pressure obtained by using the Prandtl-Meyer expansion.

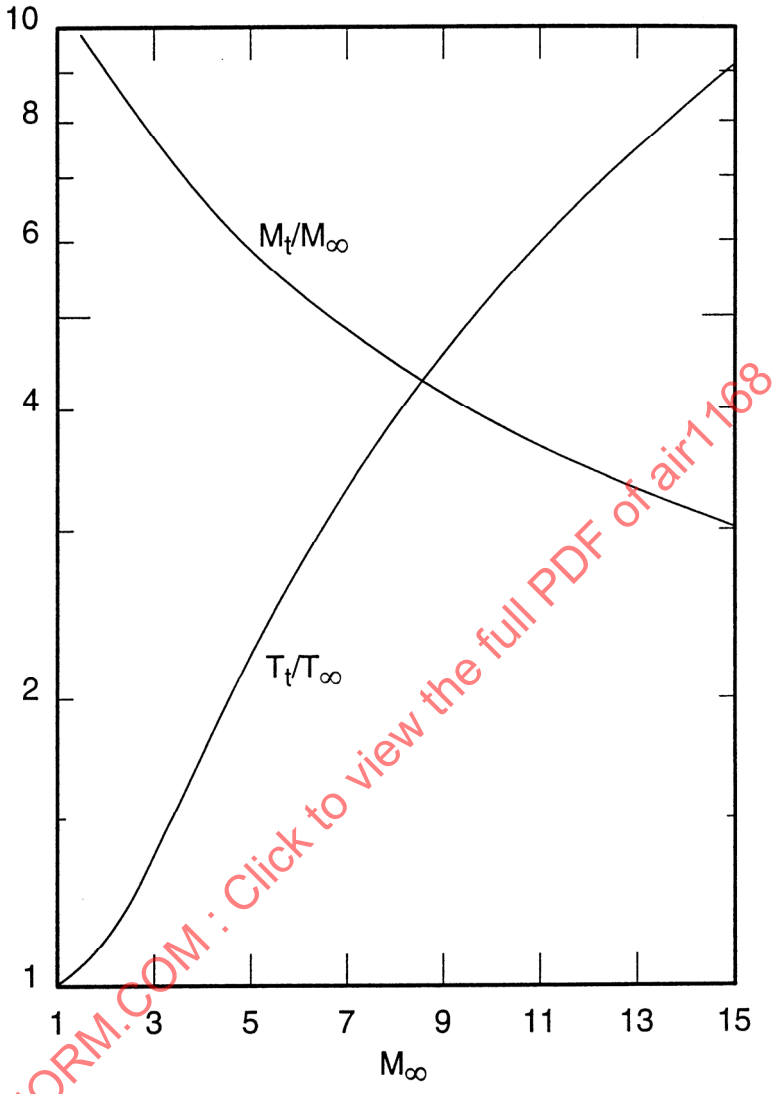

FIGURE 19 - Property Ratios Across a Normal Shock, Expanded to Freestream Pressure

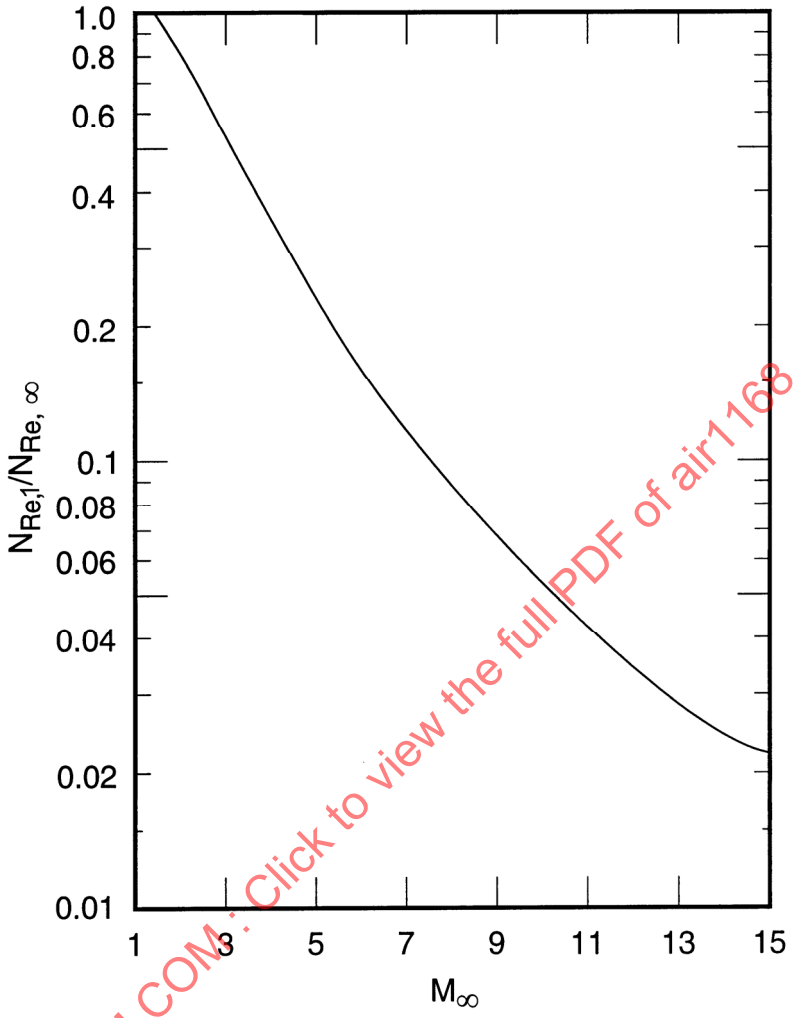

FIGURE 20 - Reynolds Number Ratio Across a Normal Shock, Expanded to Freestream Pressure

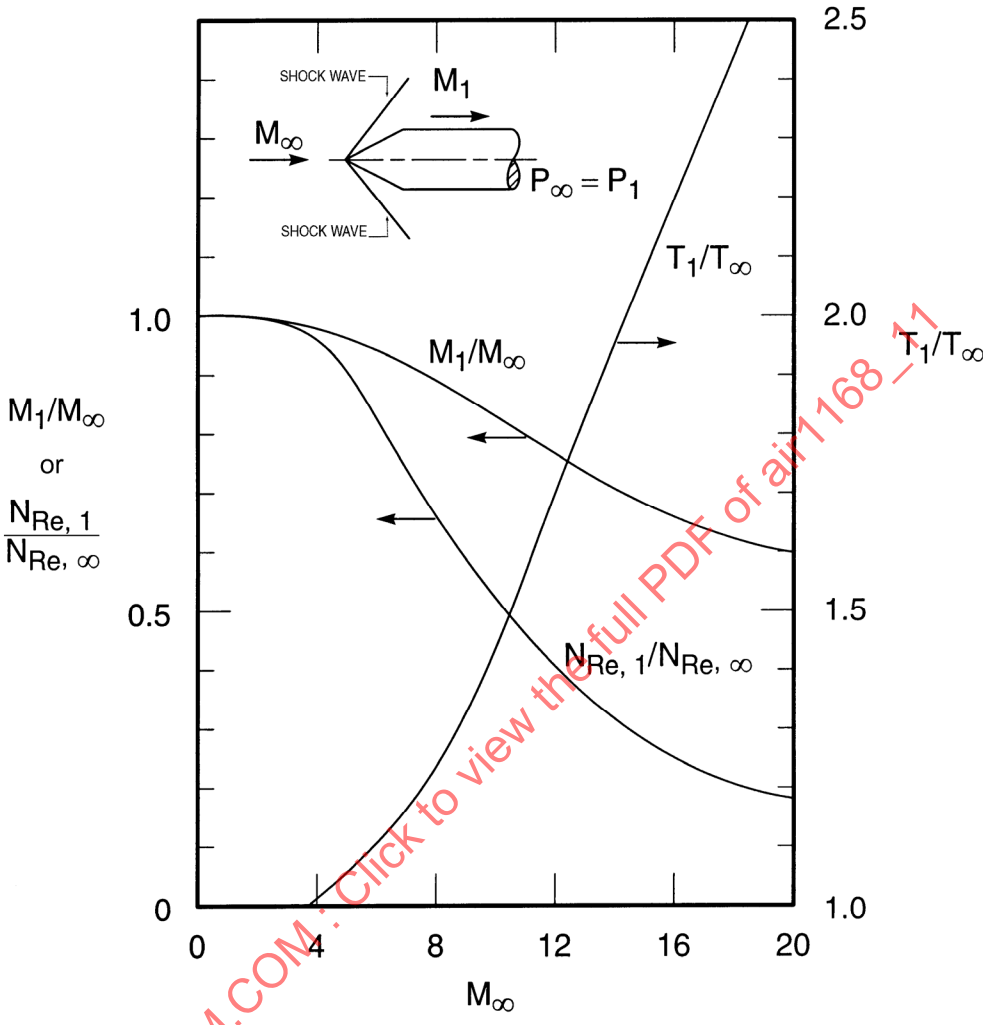

FIGURE 21 - Flow Field Parameters for a 15 deg Half-Angle Sharp Cone, Expanded to Freestream Pressure

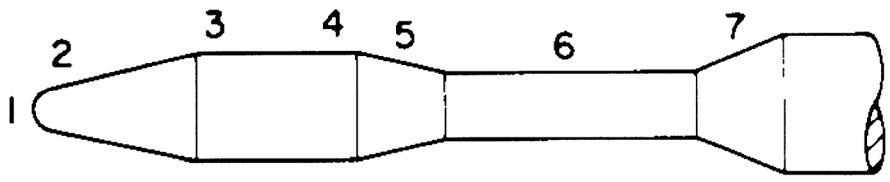

FIGURE 22 - Example of a Body Broken Into Sections for Analysis

2.12 (Continued):

6. The forward portion of this section will be in separated flow, with the flow reattaching somewhat aft of this region. In the region aft of the point of reattachment and in front of the point of separation due to surface 7, the assumption of a zero pressure coefficient is reasonable.

7. At the cylinder-cone-frustum intersection, an oblique shock is generated, owing to the flow compression. Using the flow properties previously obtained for the cylindrical section, it is a simple matter to compute the change in these quantities across the oblique shock. Some variation in the computed properties will result, depending on whether a conical or wedge shock is assumed at the intersection.

In addition to static pressure, a second local flow property is required to determine fully the flow at the location of interest. At locations downstream of the nose shock only (locations 1 through 6), the local total pressure ratio to the freestream total pressure should range between that computed across a normal shock wave and a conical shock generated by a pointed cone equal in cone angle to the nose cone value. The selection of which type shock wave (normal or conical) that most nearly approximates the correct loss in total pressure is dependent on both the nose bluntness ratio and distance downstream from the vehicle nose to the particular location. For length-to-nose diameter ratios of 5 or less, a normal nose shock is usually assumed.

Besides the theories discussed in the previous paragraphs, which permit useful results to be obtained from hand calculations, additional analytical techniques available require the use of digital computers. Examples include the Van Dyke blunt body solution and the well-known method of characteristics. The primary justification for the use of approximate techniques in calculating inviscid flow fields is that results can be achieved in a relatively short time, although with some sacrifice in accuracy.

3. AIR PROPERTY RELATIONS:

Once the velocity, static temperature, and pressure distribution around the body have been determined, boundary layer edge thermodynamic and transport air property values may be obtained. At temperatures below about 3500 °R, air may be considered a thermally perfect gas, obeying the equation of state:

$$P = \rho g R T \qquad \text{(Eq.26)}$$

At higher temperatures, thermodynamic air properties have been tabulated and are presented in Section 2A of AIR 1168/9. For the temperature range 180 to 3600 °R, the well-known Sutherland viscosity relation may be used

$$\mu = 2.27 \times 10^{-8} \frac{T^{3/2}}{T + 198.6} \qquad \text{(Eq.27)}$$

3. (Continued):

This relation is shown in Figure 23. For approximate calculations the viscosity-temperature relation is often taken as $\mu \sim T^{0.7}$. Thermal conductivity values of air for the temperature range 200 to 1800 °R are plotted in Figure 24. A reasonable assumption for the Prandtl number of air for the temperature range 180 to 3600 °R is

$$N_{Pr} \cong \text{Const} = 0.71 \quad \text{(Eq.28)}$$

4. AERODYNAMIC HEATING DEFINITIONS:

4.1 Heat Transfer Coefficient:

Similar to low speed flows, the high velocity convection process is conventionally expressed through a heat transfer coefficient h, which is defined by

$$q = h(T_{aw} - T_w) \quad \text{(Eq.29)}$$

At very high temperatures, where real gas effects become important, enthalpy is a better criterion of the energy potential than is temperature. This fact is accounted for through an alternate definition of the heat transfer coefficient, based on enthalpy difference:

$$q = h_i(i_{aw} - i_w) \quad \text{(Eq.30)}$$

Frequently the heat transfer coefficient is expressed nondimensionally as either a Stanton or Nusselt number:

$$N_{St} = \frac{h}{\rho g V c_p} \quad \text{(Eq.31)}$$

$$N_{Nu} = \frac{hx}{k} \quad \text{(Eq.32)}$$

4.2 Adiabatic Wall Temperature and Enthalpy:

The adiabatic wall temperature and enthalpy are the temperature and enthalpy which the wall surface assumes for zero heat transfer. These qualities are expressed by a dimensionless parameter r, called the recovery factor, and defined as

$$r = \frac{T_{aw} - T_1}{T_t - T_1} = \frac{i_{aw} - i_1}{i_t - i_1} \quad \text{(Eq.33)}$$

where:

Subscript 1 denotes the local (edge of boundary layer) condition

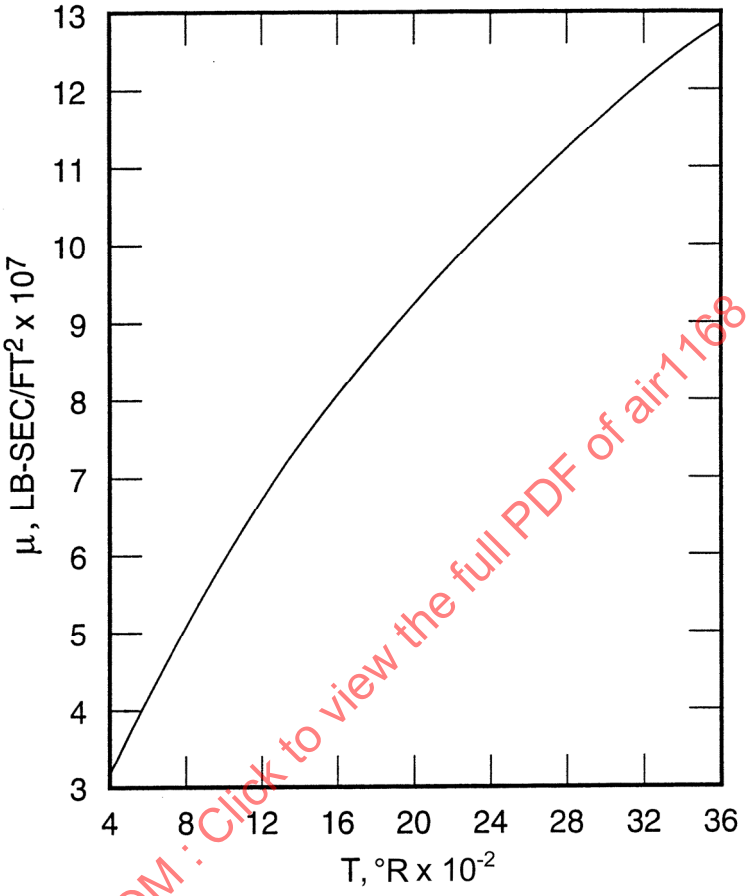

FIGURE 23 - Viscosity of Air (Equation 27)

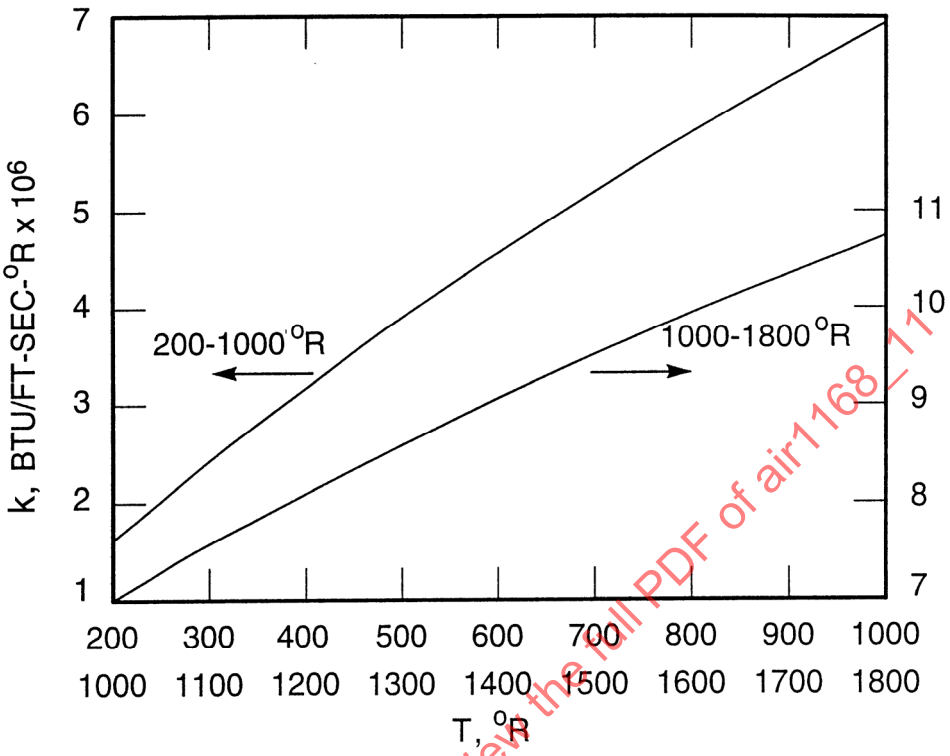

FIGURE 24 - Thermal Conductivity of Air

4.2 (Continued):

From the relations for total temperature and enthalpy, namely,

$$T_t = T_1 + \frac{V_1^2}{2gJc_p} \quad \text{(Eq.34)}$$

$$i_t = i_1 + \frac{V_1^2}{2gJ} \quad \text{(Eq.35)}$$

the expressions for adiabatic wall temperature and enthalpy become

$$T_{aw} = T_1 + r\frac{V_1^2}{2gJc_p} \quad \text{(Eq.36)}$$

$$i_{aw} = i_1 + r\frac{V_1^2}{2gJ} \quad \text{(Eq.37)}$$

4.2 (Continued):

For a perfect gas, the temperature relation is alternatively

$$T_{aw} = T_1\left(1 + r\,\frac{\gamma - 1}{2}M_1^2\right) \qquad \text{(Eq.38)}$$

Generally, the recovery factor for air is taken as

$$r = (N_{Pr})^{1/2} = 0.85 \text{ for laminar flow} \qquad \text{(Eq.39)}$$

$$r = (N_{Pr})^{1/3} = 0.90 \text{ for turbulent flow} \qquad \text{(Eq.40)}$$

Using these values for the recovery factor, perfect gas adiabatic wall temperatures are plotted in Figures 25 and 26 versus freestream Mach number. These curves assume a constant freestream temperature equal to 415 °R, and may be easily corrected for other temperatures. At high velocities these temperature are incorrect because of real gas effects.

4.3 Local Skin Friction Coefficient:

The local skin friction coefficient is, by definition, equal to the ratio of local shearing stress to the dynamic pressure; that is,

$$c_f = \frac{\tau_w}{\left(\frac{1}{2g}\right)g\rho_1 V_1^2} \qquad \text{(Eq.41)}$$

This quantity is of particular interest for heating calculation since it is related to the nondimensional heat transfer coefficient through the modified Reynolds analogy:

$$N_{St} = \frac{h}{(\rho g)_1 V_1 c_p} = \frac{c_f}{2}(N_{Pr})^{-2/3} \qquad \text{(Eq.42)}$$

For incompressible flows, the local skin friction coefficient is a function of the local Reynolds number only, and may be obtained from the following relations:

$$c_f = 0.664\ (N_{Re})^{0.5} \text{ (laminar flow/flat plate)} \qquad \text{(Eq.43)}$$

$$c_f = 0.023\ (N_{Re})^{0.139} \text{ (turbulent flow/flat plate)} \qquad \text{(Eq.44)}$$

The preceding equations are due to Blasius (laminar) and Nikuradse (turbulent).

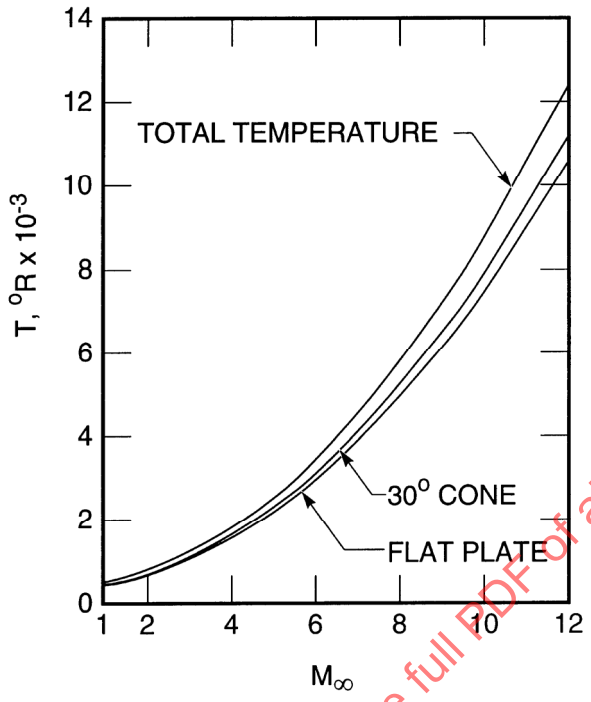

FIGURE 25 - Laminar Adiabatic Wall Temperature (T_∞ = 415 °R)

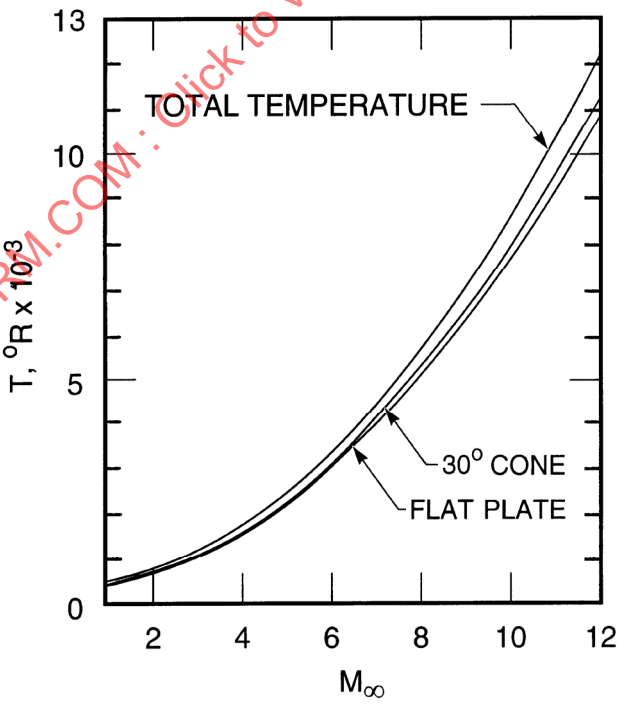

FIGURE 26 - Turbulent Adiabatic Wall Temperature (T_∞ = 415 °R)

5. REFERENCE TEMPERATURE - ENTHALPY CONCEPT:

In addition to Reynolds number, the skin friction coefficient for high velocity flow is a function of both the local Mach number and the wall-to-freestream static temperature ratio. By using a suitably defined reference temperature for evaluating the air flow properties, it is possible to eliminate the dependence of the skin friction coefficient on Mach number and temperature ratio (Reference 7). This temperature allows the incompressible skin friction relations to be employed for high velocity compressible flow.

The reference temperature relation for both laminar and turbulent flow is given by

$$T^* = 0.22T_{aw} + 0.28T_1 + 0.50T_w \quad \text{(Eq.45)}$$

For a perfect gas, Equation 45 may be written in terms of Mach numbers as

$$\frac{T^*}{T_1} = 0.5\left(\frac{T_w}{T_1} + 1\right) + 0.044rM_1^2 \quad \text{(Eq.46)}$$

This relation is shown in Figure 27 for r = 0.85 and 0.9.

When the temperature variation within the boundary layer is so large that the specific heat of the air varies considerably, heating calculations should be based on enthalpies rather than on temperatures. The Stanton number relation becomes

$$N_{St} = \frac{h_i}{\rho g V c_p} \quad \text{(Eq.47)}$$

and a reference enthalpy is used for the property evaluation, given by

$$i^* = 0.22i_{aw} + 0.28i_1 + 0.50i_w \quad \text{(Eq.48)}$$

6. HEATING RELATIONS:

6.1 Flat Plates:

Calculations for laminar, turbulent, and transition flows are given in the paragraphs below.

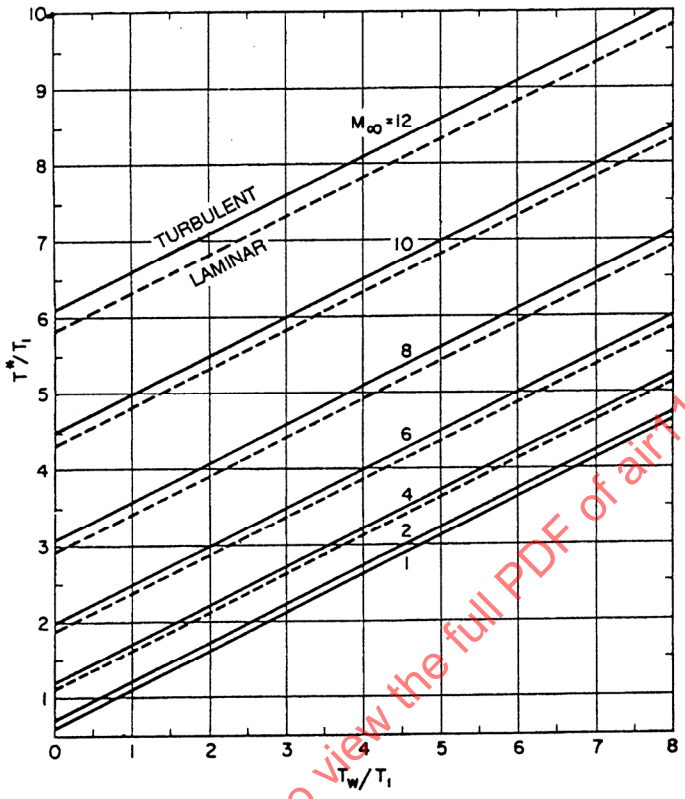

FIGURE 27 - Reference Temperature Versus Boundary Layer Edge Temperature
(Solid Lines are Turbulent Boundary Layers; Dashed Lines are Laminar Boundary Layers)

6.1.1 Laminar Flow: The recommended relation for calculation of laminar heat transfer on a uniform temperature flat plate is obtained from the modified Reynolds analogy and the Blasius equation for skin friction coefficient:

$$N^*_{St} = 0.332(N^*_{Re})^{-1/2}(N_{Pr})^{-2/3} \qquad \text{(Eq.49)}$$

where the Stanton number may be based on either temperature or enthalpy. The asterisk superscripts denote property evaluation at the reference temperature or enthalpy. An alternate expression, in terms of Nusselt number, may be written when the reference temperature is employed:

$$N^*_{Nu} = 0.332(N^*_{Re})^{1/2}(N_{Pr})^{1/3} \qquad \text{(Eq.50)}$$

6.1.1 (Continued):

A single equation, in terms of primary flow variables, for computing laminar flat plate convective heating applicable to flight velocities from 3600 to 36,500 ft/s is given in Reference 8 as

$$q = 1.17 \times 10^4 \left(\frac{1}{x}\frac{V_1}{V_\infty}\frac{g\rho_1}{g\rho_t}g\rho_\infty\right)^{1/2}\left(\frac{T_w}{900}\right)^{-0.051}\left(\frac{V_\infty}{10^4}\right)^{3.21}\left(1-1.2\frac{i_w}{i_t}\right) \quad \text{(Eq.51)}$$

This relation assumes $P_t = \left(\frac{2}{2g}\right) g\rho_\infty V_\infty{}^2$, which is the Newtonian stagnation pressure, neglecting P_∞.

A simplified relation for the heat transfer coefficient valid for the temperature range $100 \le T \le 2000$ °R is given by (Reference 9)

$$h = 2.06 \times 10^{-6}\left(\frac{P_1 V_1}{x}\right)^{1/2} \quad \text{(Eq.52)}$$

Use of Equations 49 to 52 should be restricted to the Reynolds number range, $N^*_{Re} \le 10^5$.

6.1.2 Turbulent Flow: For Reynolds numbers greater than 10^6, the following reference temperature relation is recommended:

$$N^*_{Nu} = 0.0126(N^*_{Re})^{0.861}(N_{Pr})^{0.333} \quad \text{(Eq.53)}$$

This equation has been extensively verified by comparisons with flight data (Reference 10), and is valid for the Mach number range $1 \le M_1 \le 7$.

6.1.3 Transition Flow: For the Reynolds number range $10^5 \le N^*_{Re} \le 10^6$, the boundary layer flow is usually transitory in nature. An equation for heating prediction for this N_{Re} range is given by

$$N^*_{Nu} = 5.85x10^{-5}(N^*_{Re})^{5/4}(N_{Pr})^{1/3} \quad \text{(Eq.54)}$$

The properties in this relation are evaluated at the reference temperature, Equation 45.

Equations 49 to 54 for flat plate heating may also be employed for cylindrical sections as long as the cylinder radius is large in comparison with the boundary layer thickness.

6.2 Cone and Cone Frustums:

For equal boundary layer edge flow conditions, the heating rate to a cone will be higher than to a flat plate, owing to the thinner boundary layer associated with the conical flow. By using a Mangler transformation, it can be shown that the heating rate at a distance x from the apex of a cone with laminar boundary layer is equal to the heating rate at a distance x/3 from the leading edge of a flat plate, flow conditions immediately outside the boundary layer being the same.

With the Blasius laminar skin friction relation, the equation for Stanton number on a cone becomes

$$N^*_{St} = \sqrt{3}[0.332(N^*_{Re})^{-1/2}(N_{Pr})^{-2/3}] \qquad \text{(Eq.55)}$$

The heat transfer rates on a cone for turbulent flow at zero angle of attack can also be determined from flat plate heating formulas. The heating rate at a distance x from the apex of a cone with turbulent boundary layer is equal to the heating rate on a flat plate at a distance x/2 from the leading edge of the plate, flow conditions immediately outside the boundary layer being the same. Thus, any of the formulas for the predicting turbulent flat plate heating rates can be used to predict heating rates on a cone.

6.3 Stagnation Points:

Due to the severity of stagnation heating rates, considerable study has been given to this region. Various relations for computing laminar stagnation heating to bodies of revolution are summarized below.

6.3.1 Fay and Riddell Solution: An exact solution for laminar stagnation point heat transfer was obtained by Fay and Riddell (Reference 11), who considered both equilibrium and frozen flow. Numerical solutions were obtained for the range of variables, $540 \le T_w \le 5400$ °R, $670 \le i_t \le 10{,}400$ Btu/lb (corresponding to $5800 \le V_\infty \le 22{,}800$ ft/s). The actual $g\rho\mu$ variation through the boundary layer was determined. Their numerical solutions correlated to the following equation:

$$q_s = 0.763\,(N_{Pr})^{-0.6}\,(i_1 - i_w)\left(\frac{g\rho_w\mu_w}{g\rho_1\mu_1}\right)^{0.1}(g\rho_1\mu_1\beta)^{1/2}\left[1 + (N^{\alpha}_{Le} - 1)\frac{i_d}{i_t}\right] \qquad \text{(Eq.56)}$$

where:

α = 0.52 for equilibrium flow
α = 0.63 for frozen flow

Although this solution is based on the Sutherland formula for viscosity, a Prandtl number of 0.71 and a Lewis number constant through the boundary layer, the authors note that it should be valid for values of these parameters differing not too markedly from the values employed in the numerical solution.

6.3.2 Lees Solution: Lees (Reference 12) has presented a solution for laminar heat transfer to the stagnation point of a body of revolution for the cases of dissociation equilibrium with unit Lewis number and chemically frozen flow with arbitrary Lewis number. For dissociation equilibrium,

$$q_s = 0.71\ (N_{Pr})^{-2/3}\ i_1\ (g\rho_1\mu_1\beta)^{1/2} \qquad \text{(Eq.57)}$$

and for frozen flow,

$$q_s = 0.71\ (N_{Pr})^{-2/3}\ i_1\ (g\rho_1\mu_1\beta)^{1/2} \left[1 + \left\{(N_{Le})^{2/3} - 1\right\} \frac{i_d}{i_1}\right] \qquad \text{(Eq.58)}$$

Lees assumed $g\rho\mu = g\rho_1\mu_1$ and N_{Pr} = Const = 0.71, viscosity based on Lennard-Jones potential, and a highly cooled wall, so that $i_w << i_{1,t}$.

6.3.3 Romig Solution: Romig (Reference 13) derived a simplified formula, based on the reference enthalpy method, by assuming $M_\infty >> 1$, $N_{Pr} = 1$, $T_\infty = 400\ ^\circ R$, and a highly cooled wall:

$$q_s = 0.0145 M_\infty^{3.1} \left(\frac{P_\infty}{R_N}\right)^{1/2} \qquad \text{(Eq.59)}$$

Although Romig's reference enthalpy equation is an extrapolation of a low-speed solution rather than a solution of the appropriate boundary layer equations, it has been shown to predict heating rates in fairly good agreement with the Fay-Riddell equation (Equation 56).

6.3.4 Hoshizaki Solution: Hoshizaki (Reference 14) has investigated the hypervelocity laminar convective heating to an axisymmetric blunt body for the case of equilibrium boundary layer flow. The effects of dissociation and ionization have been taken into account by means of the total thermodynamic and transport property concept. Heat transfer rates were obtained for $6000 < V_\infty < 50{,}000$ ft/s, $0.001 < P_\infty < 100$ atm, and $540 < T_w < 5400\ ^\circ R$ by solving the momentum and energy equations by successive approximation. Prandtl number and Lewis number were assumed variable.

Hoshizaki's numerical results for heat transfer correlated to the equation

$$q_s = C \left[\beta\rho_w\mu_w \left(\frac{T_w}{900}\right)^{0.4}\right]^{1/2} \left(\frac{V_\infty}{10^4}\right)^{1.69} \left(1 - \frac{i_w}{i_1}\right) \qquad \text{(Eq.60)}$$

where:

$C = 4.32 \times 10^4$ Btu/slug
ρ_w = slugs/ft^3

6.3.4 (Continued):

This equation yields results that differ by less than 6% from the Fay-Riddell equation (Equation 56) for $6000 \le V_\infty \le 26{,}000$ ft/s and is in slightly simpler form for engineering calculations. Below 6000 ft/s the Hoshizaki prediction decreases rapidly in comparison to the Fay-Riddell prediction.

For a modified Newtonian flow, the stagnation point velocity gradient is given by

$$\beta = \frac{1}{R_N}\left[\frac{2(P_t - P_\infty)}{\rho_t}\right]^{1/2} \qquad \text{(Eq.61)}$$

For air at hypervelocities, $N_{Le} \cong 1.4$, i_d is the dissociation enthalpy and may be approximated by (Reference 15)

For $1 \le Z \le 1.21$, $i_d = 8331Z - 8272$ (Eq.62)

For $1.21 \le Z \le Z_e$, $i_d = 14{,}032Z - 15{,}205$ (Eq.63)

where:

Z = Compressibility factor defined by $Z = P/\rho gRT$

The upper limit of applicability of Equation 63, Z_e, is the value of the compressibility factor at the onset of significant ionization (10^{-3} electrons per initial atom). Figure 28 presents Z_e as a function of density ratio $g\rho/g\rho_o$.

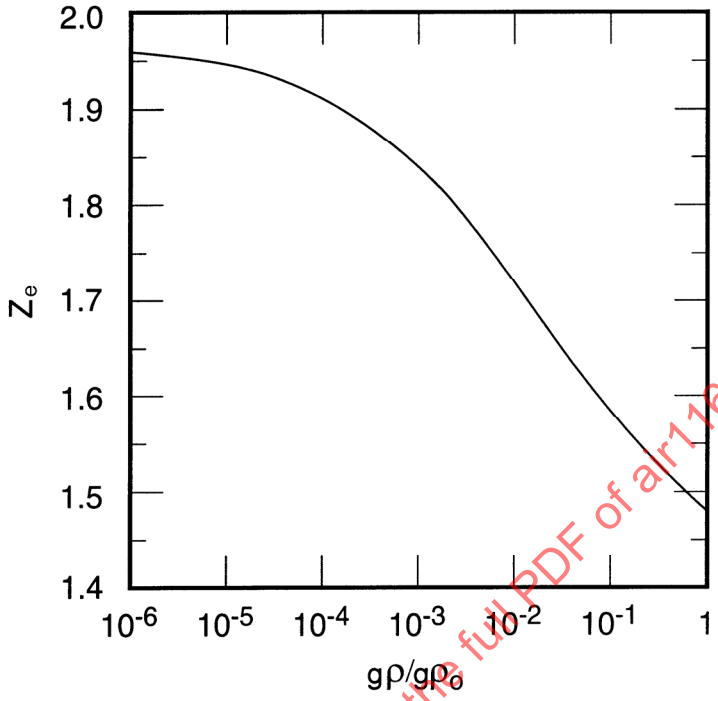

FIGURE 28 - Air Compression Factor at Onset of Ionization
(10^{-3} Electrons/Initial Air Atom); $(\rho g)_o$ = 0.0807 lb/ft^3

6.3.4 (Continued):

The ratio between stagnation point heat transfer to bodies of revolution and two-dimensional bodies can be expressed as follows:

$$\frac{q_{s,axi}}{q_{s,2-dim}} \simeq 2^{1/2} \left(\frac{\beta_{axi}}{\beta_{2-dim}} \right)^{1/2} \qquad \text{(Eq.64)}$$

For bodies of the same nose radius and with freestream Mach numbers greater than approximately 2, Equation 64 reduces to

$$q_{s,axi} \simeq 2^{1/2} \, (q_{s,2\text{-}dim}) \qquad \text{(Eq.65)}$$

Thus, the formulas given above for bodies of revolution may also be employed for two-dimensional bodies.

6.4 Heat Transfer Distribution on a Blunt Body:

The preferred method of calculating laminar boundary layer heat transfer distributions is that suggested by Lees in Reference 12. The fundamental input parameter in the calculation is the surface pressure distribution. Lees' results may be expressed as

$$\frac{q}{q_s} = \frac{(1/2)(P_1/P_t)(V_1/V_\infty)r(R_N)^{1/2}}{\left[\int_o^s (P_1/P_t)(V_1/V_\infty)r^2 ds\right]^{1/2}} \frac{1}{\left[\frac{1}{V_\infty}\left(\frac{dV_1}{d\theta}\right)_s\right]^{1/2}} \quad \text{(Eq.66)}$$

Figure 29 presents the heating distribution on a hemisphere for the case of a modified Newtonian-Prandtl-Meyer pressure distribution with freestream Mach number as a parameter.

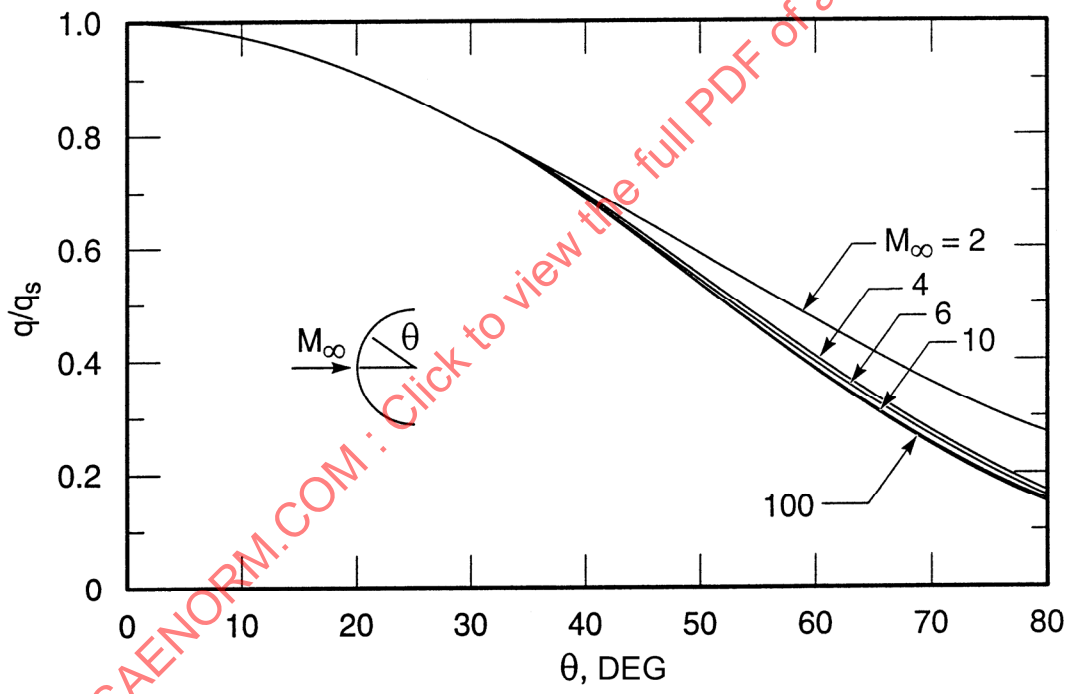

FIGURE 29 - Laminar Heating Distribution on a Hemisphere

Heat transfer distributions for a family of blunted cones are presented in Figures 30 through 34. These calculations utilize the modified Newtonian-Prandtl-Meyer method for estimating pressure variations.

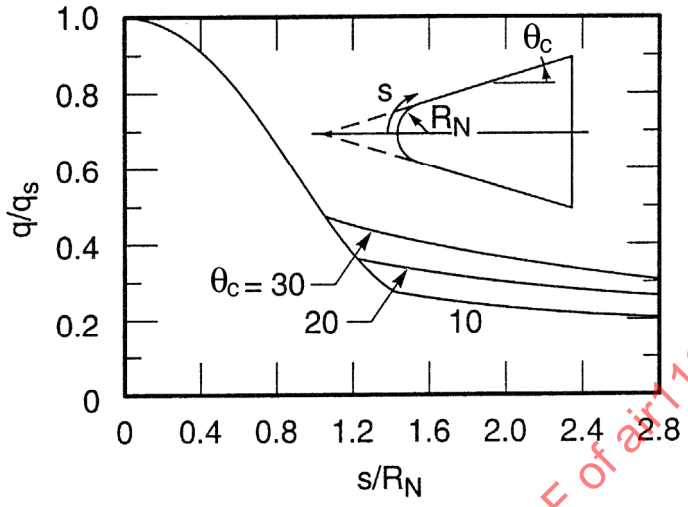

FIGURE 30 - Blunted Cone Laminar Heating Distribution; $M_\infty = 2$

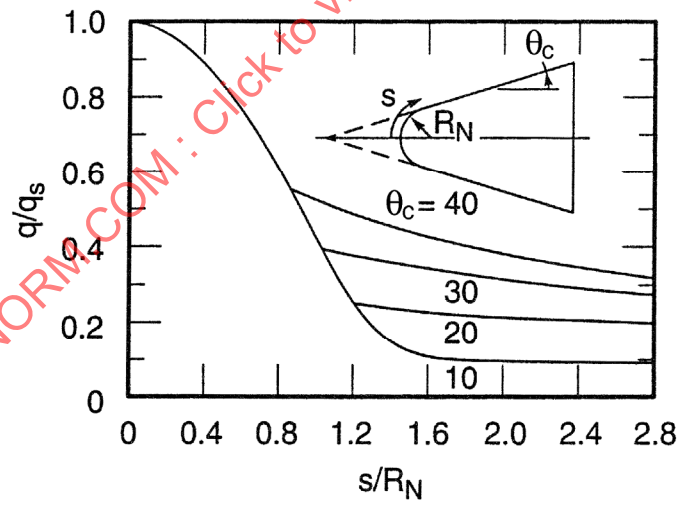

FIGURE 31 - Blunted Cone Laminar Heating Distribution; $M_\infty = 4$

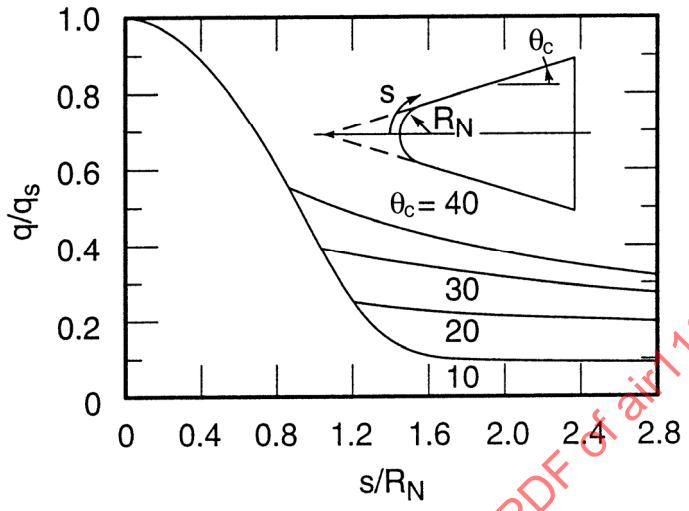

FIGURE 32 - Blunted Cone Laminar Heating Distribution; $M_\infty = 6$

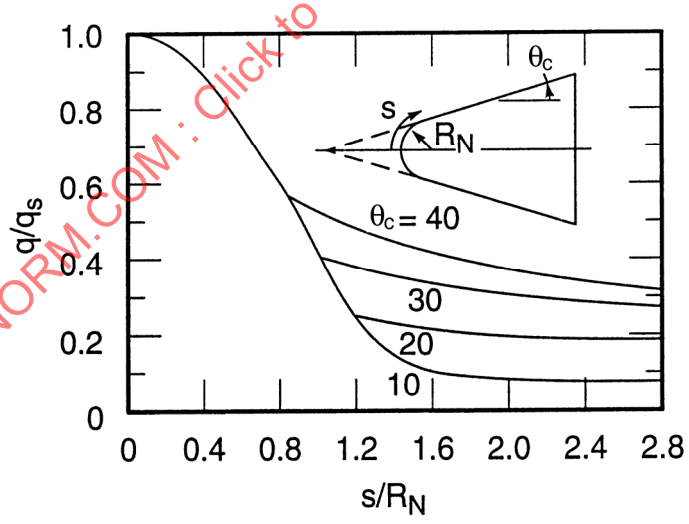

FIGURE 33 - Blunted Cone Laminar Heating Distribution; $M_\infty = 10$

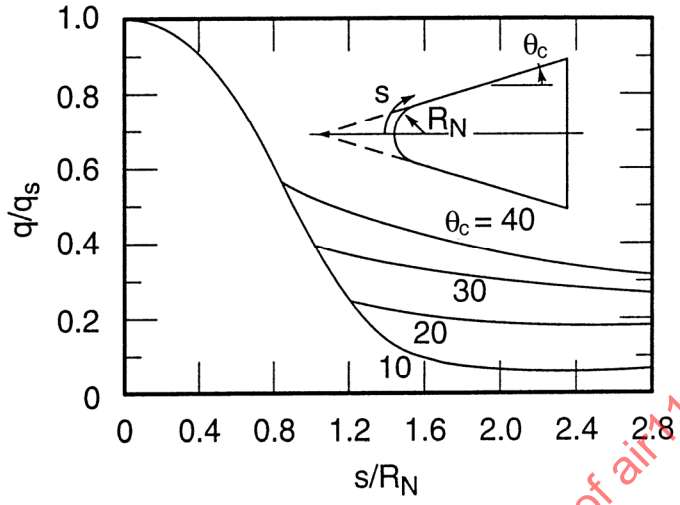

FIGURE 34 - Blunted Cone Laminar Heating Distribution; M_∞ = 100

7. NONISOTHERMAL WALL HEAT TRANSFER:

The equations and methods listed previously have been derived for the case of constant wall temperature. For a continuous wall temperature variation and a constant property boundary layer, the wall heating rate at location x_n may be calculated from the following expression (References 16 and 17):

$$q(x_n) = h_{iso}\left\{\zeta_{w,o} + A(\zeta_{w,n} - \zeta_{w,o}) + B(\Delta x / x)[-\zeta_{w,o} - 2\zeta_{w,1} - 2\zeta_{w,2}\cdots 2\zeta_{w,n-1} + (2n-1)\zeta_{w,n}]\right\} \quad \text{(Eq.67)}$$

In this equation, $\zeta_w = (T_w - T_{aw})$ indicates an arbitrary variation of the temperature potential. The isothermal heat transfer coefficient h_{iso} is given by

$$h_{iso} = C\left(\frac{k}{x}\right)(N_{Re,x})^n (N_{Pr})^{1/3} \quad \text{(Eq.68)}$$

The constants A, B, C, and n are dependent on the flow type (laminar or turbulent) and are tabulated in Table 1.

TABLE 1 - Values of Constants

Flow Type	m	A	B	C	n
Laminar	0	0.895	0.690	0.332	1/2
	1/4	0.837	0.635	0.412	1/2
	1/2	0.840	0.572	0.496	1/2
	1	0.792	0.538	0.560	1/2
Turbulent	0	0.991	0.117	0.0296	0.8

7. (Continued):

The quantity m is dependent on the pressure gradient through the relation

$$V_1 = cx^m \qquad \text{(Eq.69)}$$

For a flat plate, m = 0.

Equation 67 was derived under the assumption that the length x is subdivided into n at equal intervals; that is, Δx = Const. For flows with variable properties, the procedure given above is used in conjunction with the reference temperature method, and all properties appearing in the equations are evaluated at this temperature.

8. SAMPLE CALCULATION:

This section presents a sample calculation that illustrates a portion of the recommended procedures for aerodynamic heating calculation. The vehicle configuration and location selected for this example are shown on the following sketch.

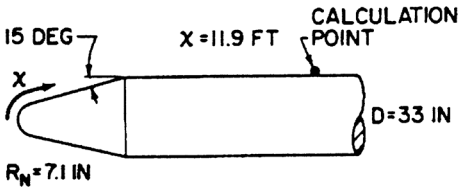

FIGURE 35 - Sketch of Vehicle Configuration

8. (Continued):

The nose configuration consists of a 15 deg blunted cone intersecting a 33 in dia cylinder. At a particular trajectory time point (t = 80 s), the freestream altitude and velocity are 100,000 ft and 6000 ft/s, respectively. The wall temperature at this time is 652 °R. It is desired to calculate the wall heating rate.

Using the 1962 ARDC atmosphere and the trajectory given data above,

$$T_\infty = 408\ ^\circ R \qquad \text{(Eq.70)}$$
$$a_\infty = 991\ ft/s$$

Therefore

$$M_\infty = V/a_\infty = 6000/991 = 6.05 \qquad \text{(Eq.71)}$$

Prior to calculation of the local aerodynamic heating rates, a determination of the inviscid flow parameters (M_1, P_1, T_1) at the boundary layer edge is required. An approximate flow field calculation method is utilized, which assumes that the boundary layer edge streamline passes through a shock wave generated by a 15 deg semi-apex angle sharp cone and expands to zero pressure coefficient along the cylindrical section. Zero angles of attack, pitch, and yaw are assumed in the analysis.

8.1 Inviscid Flow Field Calculation:

The assumed configuration and shock shape used in the analysis is sketched below.

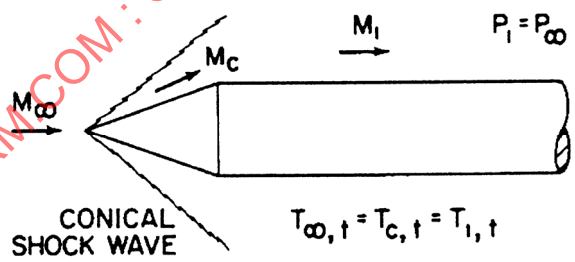

FIGURE 36 - Sketch of Assumed Configuration

The ratios of the local Mach number and static temperature to the corresponding freestream values are plotted in Figure 21. However, to illustrate the computational method, these curves will not be employed. The sharp cone-to-freestream property values are obtained from Figures 14 and 16 as

8.1 (Continued):

$$\frac{P_c}{P_\infty} = 4.80,\ M_c = 4.36 \qquad \text{(Eq.72)}$$

and from Figure 2,

$$\frac{P_c}{P_{c,t}} = 0.00412 \qquad \text{(Eq.73)}$$

The entire flow field downstream of the nose shock is assumed isentropic. Therefore,

$$P_\infty = P_1,\ P_{c,t} = P_{1,t}$$

$$\frac{P_1}{P_{1,t}} = \left(\frac{P_c}{P_{c,t}}\right)\left(\frac{P_\infty}{P_c}\right) = \frac{0.00412}{4.80} = 0.858 \times 10^{-3} \qquad \text{(Eq.74)}$$

Then M_1 is obtained from Figure 2 as

$$M_1 = 5.71$$

$$\frac{T_\infty}{T_{\infty,t}} = 0.120 \qquad \text{(Eq.75)}$$

$$\frac{T_1}{T_{1,t}} = 0.133$$

Since $T_{\infty,t} = T_{1,t}$,

$$T_1 = \frac{T_1}{T_{1,t}}\frac{T_{\infty,t}}{T_\infty}T_\infty = \left(\frac{0.133}{0.120}\right)408 = 452\ ^\circ R \qquad \text{(Eq.76)}$$

8.2 Heating Rate Calculation:

Flat plate heating relations are employed, since the cylinder radius is large compared with the boundary layer thickness. In order to calculate the adiabatic wall temperature, turbulent flow is assumed. This assumption is checked later in the calculations. From Equation 38,

$$T_{aw} = 452\left[1+0.71^{1/3}\left(\frac{1.4-1}{2}\right)(5.71)^2\right] = 3070\ ^\circ R \quad \text{(Eq.77)}$$

This temperature may also be obtained from Figure 26.

According to the Nusselt number definition,

$$h = N^*_{Nu}\left(\frac{k^*}{x}\right) \quad \text{(Eq.78)}$$

The superscript asterisk denotes property evaluation at the reference temperature, given by Equation 45; since T_w = 652 °R,

$$T^* = 0.22(3070)+0.28(452)+0.50(652) = 1127\ ^\circ R \quad \text{(Eq.79)}$$

From Equation 53,

$$h = 0.0126\left(\frac{k^*}{x}\right)(N^*_{Re})^{0.861}(N_{Pr})^{1/3} \quad \text{(Eq.80)}$$

The Reynolds number evaluated at the reference temperature is

$$N^*_{Re} = \frac{V_1\rho^* g x}{\mu^*} \quad \text{(Eq.81)}$$

Using the perfect gas equation of state (P = ρgRT) and the speed of sound relation ($a = \sqrt{g\gamma RT}$), this Reynolds number may be expressed as

$$N^*_{Re} = N_{Re,\infty}\left(\frac{M_1}{M_\infty}\right)\left(\frac{T_1}{T_\infty}\right)^{1/2}\left(\frac{P_1}{P_\infty}\right)\left(\frac{T_1}{T^*}\right)\left(\frac{\mu_\infty}{\mu^*}\right) \quad \text{(Eq.82)}$$

8.2 (Continued):

Assuming a viscosity-temperature relation of the form

$$\mu \sim T^{0.7} \qquad \text{(Eq.83)}$$

and the condition $P_1 = P_\infty$ yields

$$N_{Re}^{*} = N_{Re,\infty}\left(\frac{M_1}{M_\infty}\right)\left(\frac{T_1}{T_\infty}\right)^{1/2}\left(\frac{T_\infty}{T^*}\right)^{1.7} \qquad \text{(Eq.84)}$$

The heat transfer coefficient is then

$$h = \frac{0.0126}{x^{0.139}}\left[k^* N_{Pr}^{1/3}\right]\left[\frac{N_{Re,\infty}}{x}\left(\frac{M_1}{M_\infty}\right)\left(\frac{T_1}{T_\infty}\right)^{1/2}\left(\frac{T_\infty}{T^*}\right)^{0.861}\right] \qquad \text{(Eq.85)}$$

where:

x = Wetted distance from the stagnation point to specified location
$N_{Re,\infty}/x$ = Freestream Reynolds number per foot, a function of vehicle altitude and velocity
k^* = Temperature dependent thermal conductivity of air (from Figure 24)
N_{Pr} = Constant Prandtl number = 0.71, recommended for heating rate calculation

The freestream Reynolds number is, by definition,

$$N_{Re,\infty} = \frac{V_\infty \rho_\infty g x}{\mu_\infty} \qquad \text{(Eq.86)}$$

From the configuration sketch in 8.1, the wetted distance x is given as

$$x = 11.9 \text{ ft} \qquad \text{(Eq.87)}$$

From the 1962 Atmosphere Table at 100,000 ft,

$$\frac{\mu_\infty}{\rho_\infty g} = 9.30 \times 10^{-3} \text{ ft}^2/\text{s} \qquad \text{(Eq.88)}$$

Then

$$N_{Re,\infty} = \frac{(6000)(11.9)}{9.30 \times 10^{-3}} = 7.0 \times 10^{6} \qquad \text{(Eq.89)}$$

8.2 (Continued):

The local Reynolds number, evaluated at T*, is thus

$$N_{Re}^{*} = (7.0 \times 10^{6})\left(\frac{5.71}{6.05}\right)\left(\frac{452}{408}\right)^{0.5}\left(\frac{408}{1127}\right)^{1.7} \quad \text{(Eq.90)}$$
$$= 1.23 \times 10^{6}$$

Since $N_{Re}^{*} > 10^{6}$, the turbulent flow assumption is probably correct. The heat transfer coefficient for turbulent flow is then (from Equation 53)

$$h = 0.0126\,\frac{(7.75 \times 10^{-6})}{11.9}\,(1.23 \times 10^{6})^{0.861}\,(0.71)^{1/3} \quad \text{(Eq.91)}$$
$$= 1.26 \times 10^{-3}\ \text{Btu}/(\text{ft}^2 - \text{s} - {}^{\circ}\text{R})$$

for which k(T*) is obtained from Figure 24.

From Equation 29, the wall heating rate is

$$q_w = 1.26 \times 10^{-3}\,(3070 - 652) \quad \text{(Eq.92)}$$
$$= 3.04\ \text{Btu}/\text{ft}^2 - \text{s}$$

9. REFERENCES:

1. Ames Aeronautic Lab., “Equations, Tables, and Charts for Compressible Flow,” NACA Report 1135, 1953.
2. A. B. Walburn and P. Harner, “Real Gas Oblique Shock Functions for Air in Chemical Equilibrium,” Fairchild Stratos Corp., DM 63-1, December 1962.
3. M. G. Meyer, “Real Gas Equilibrium Properties Behind a Normal Shock in Air,” Lockheed Missiles and Space Co., Report 399791, July 13, 1961.
4. C. L. Dailey and F. C. Wood, "Computation Curves for Compressible Fluid Problems." John Wiley & Sons, Inc., 1949.
5. M. Romig, “On Heat Transfer to Cones at High Velocities,” Convair Lab. Report, August 1958.
6. M. G. Dunn, “Boost-Phase Aerodynamic Heat Transfer Calculation Techniques,” Lockheed Missiles and Space Co., Report A381550, July 1963.
7. E. R. G. Eckert, “Survey of Boundary Layer Heat Transfer at High Velocities and High Temperatures,” Wright Air Development Center, WADC Tech. Report 59-624, April 1960.

9. (Continued):

8. G. M. Hanley, “Hypervelocity Laminar Convective Flat Plate Heating,” ARS J., November 1962.

9. R. R. Gold, “A Note on the Expressions for the Local Heat Transfer Coefficient,” J. Aero. Sciences, Vol. 19, April 1952.

10. F. L. Guard, et al., “Compilation of Structural Inflight Heating Data Applicable to Large Launch Vehicles,” Lockheed-California Co., Report LR 17562, February 1964.

11. J. A. Fay and F. R. Riddell, “Theory of Stagnation Point Heat Transfer in Dissociated Air,” J. Aero. Sciences, February 1958.

12. L. Lees, “Laminar Heat Transfer Over Blunt-Nosed Bodies at Hypersonic Speeds,” Jet Propulsion, April 1956.

13. M. Romig, “Stagnation Point Heat Transfer for Hypersonic Flow,” Jet Propulsion, December 1956.

14. H. Hoshizaki, “Heat Transfer in Planetary Atmospheres at Super-Satellite Speeds,” ARS J., October 1962.

15. J. D. Murphy and R. A. Rindal, “Enthalpy of Dissociation for Air in Thermodynamic Equilibrium,” Vidya Technical Note 2T, Jan. 12, 1962.

16. E. R. G. Eckert, J. P. Hartnett, and R. Birkebak, “Simplified Equations for Calculating Local and Total Heat Flux to Nonisothermal Surfaces,” J. Aero. Sciences, Vol. 24, July 1957.

17. J. P. Hartnett, E. R. G. Eckert, R. Birkebak, and R. L. Sampson, “Simplified Procedures for Calculation of Heat Transfer to Surfaces with Non-Uniform Temperatures,” Wright Air Development Center, WADC Tech. Report, No. 56-373, December 1956.

PART B - ENTRY HEAT TRANSFER

1. INTRODUCTION:

Increasing emphasis on high-speed flight, particularly that associated with spacecraft hypersonic entry into earth and other planet atmospheres, requires that the spacecraft designer be familiar with the technical problems of heat protection subsystem design. As a result of increased launch vehicle propulsion capability and increased entry mission sophistication, a significant broadening of the complexity of the entry problem has developed, from comparatively simple zero lift ballistic entry technology in earth's entry to the more complex lifting systems technology for operation in earth or planetary atmospheres. Heat protection subsystem problems also exist at lower speeds in the form of high structural metal temperatures for the Mach 3 supersonic transport and the long "soak" problem associated with lifting vehicle flight from approximately 50 miles altitude to touchdown.

For preliminary design purposes, approximate methods are adequate to assess the overall entry system thermal environment and heat protection subsystem. However, accurate definition of the type of heat protection subsystem (heat sink, ablative, radiative), its material composition, and its weight and reliability require an accurate definition of the entry thermal environment or heat transfer as well as definition of the material-thermal environment interaction. Further, the necessity of considering "localized" effects induced by the presence of field joints, steps and gaps, protuberances, and so forth on the overall design indicates the need for a design manual in which methods are available for determining the aerothermodynamic environment and heat protection response as well as the extent of these local effects.

The purpose of this section is to describe methods and techniques for the analysis of spacecraft entry heat transfer and heat protection subsystem performance.

1.1 Scope:

In hypersonic flight, the effect of forced convection heat transfer (frequently defined as aerodynamic heating) is a significant consideration for the structural designer. At velocities in excess of Mach 2.5, depending somewhat upon altitude, the problem has been recognized as sufficiently important as to be categorized as a somewhat specialized subsystem of high-speed system design. It is frequently referred to as the heat protection subsystem. The type of heat protection subsystem, its material composition, design, fabrication, and weight are strongly dependent upon the rate of heat application and, for certain systems (such as ablative or mass transfer systems), upon the total heat load and the time of its application.

Aerodynamic heating is the heating of an object as a result of the flow of a gas at high speed about that object. It is a forced convection phenomenon involving the transfer of heat from a fluid to a solid when the relative motion between fluid and solid is due to other than gravitational forces resulting from density variation within the fluid. Friction between the fluid filaments while they stream along the object surface, and compression at and near the stagnation regions of forward surfaces, convert the kinetic energy of motion into heat within the thin layer of air (the boundary layer) which envelopes the body. Such a region is shown in Figure 37. The temperature of this layer increases approximately as the square of the velocity (up to air dissociation and ionization)

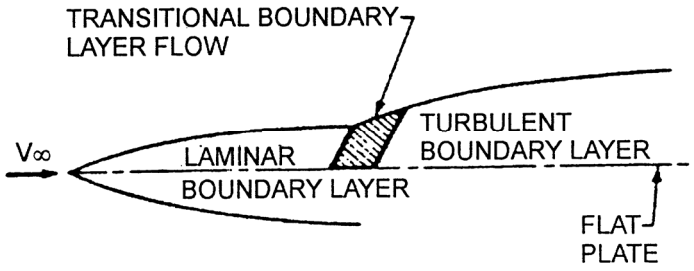

FIGURE 37 - Boundary Layer on a Flat Plate

1.1 (Continued):

so that, at Mach 3, the boundary layer temperature attains a value of about 600 °F. Within the boundary layer the fluid flows at velocities between the limits of that at the outer edge of the boundary layer where the velocity equals the local flow at that point and that at the body surface (for continuum flow) where the velocity is zero. The change of velocity from local to zero takes place in an orderly manner (defined as the velocity distribution). This velocity distribution is a manifestation of the shear forces between the fluid layers within the boundary layer. The reduction of kinetic energy and the energy generated by the viscous forces results in an increase in temperature of the boundary layer. Figure 38 shows typical temperature and velocity variations in the boundary layer for conditions of high and low Mach numbers at the edge of the boundary layer. (The reason for no numbers on the temperature line of the abscissa is that Schlicting intended this figure to be conceptual only, to display the temperature profile in a turbulent bounday layer in a qualitative fashion only.)

At velocities somewhat in excess of earth orbital velocity (approximately 26,000 ft/s), the thermal radiation from the high-temperature gas enclosed within the spacecraft-induced shock system can become a significant portion of the total heat transfer, particularly for large blunted vehicles.

This subsection describes the methods, techniques, and procedures for the prediction of the aerodynamic and thermal radiation heating for typical entry systems and the prediction of heat protection subsystem response.

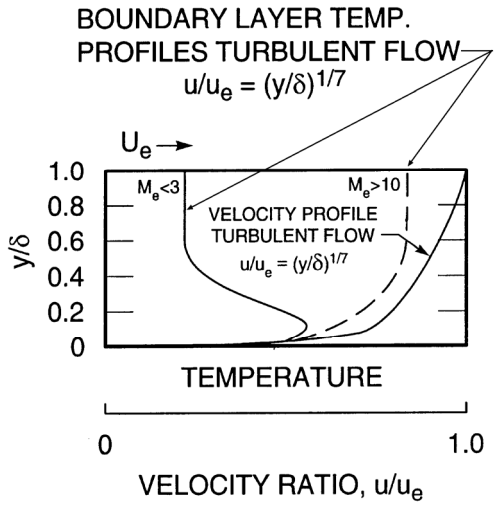

FIGURE 38 - Typical Temperature and Velocity Variations in Boundary Layer Flow (Reference 41)

1.1 (Continued):

The predictive methods and procedures are presented in two general forms: generalized relations, approximate and in curve form for rapid estimation purposes; and detailed, more accurate methods suitable for more precise design. In all cases the designer should examine the mission, anticipated system configuration, flight regimes, and trajectory characteristics to determine those aspects of the entry which are most significant to the design problem.

1.2 Nomenclature:

Refer to the nomenclature list on page 15.

1.3 Generalized Entry Relations:

Generalized equations and curves are presented which establish the fundamental relationships between the entry system, its orientation at entry, its W/C_DA ratio (commonly defined as ballistic parameter), and its heating and loading environment.

1.3.1 Ballistic Entry: The predominant loads and heating for a ballistic vehicle exist during entry into the sensible atmosphere. Evaluation of the loads and heating for various vehicle concepts requires a relationship between the ambient density and velocity. Although the choice of a prime independent variable from among velocity, density or altitude, range, and time is somewhat arbitrary, velocity is preferable because the others intimately involve some aerodynamic characteristic of the vehicle.

1.3.2 Trajectories and Loads: For ballistic entry, the gravitational force is small compared with the aerodynamic drag, and can be disregarded (Reference 1).[1] The flight path of a ballistic vehicle then becomes a straight line, where the air density as a function of altitude may be expressed in terms of the entry velocity ratio as

$$\rho g = \frac{2\beta_1}{g}\frac{W}{C_D A}(\sin\theta_e)\ln\frac{1}{V_e} \qquad \text{(Eq.93)}$$

where:

β_1 = 1/22,000 ft

Entry is assumed to begin at an altitude greater than 40 miles. (A more complete development of the loads and heating relations is contained in Reference 2.) In Equation 93 the density is taken to vary exponentially with altitude, assuming an isothermal atmosphere (see Figure 39). Using Equation 93 with the exponential density model, the altitude trace of a ballistic vehicle is determined. Figure 40 gives ballistic vehicle altitude as a function of entry velocity ratio.

The dynamic pressure may be expressed in terms of entry velocity ratio, using Equation 93. By differentiation, the maximum dynamic pressure may be written as

$$(q_\infty)_{max} = \frac{\beta V_e^{\,2}}{2g}\left(\frac{W}{C_D A}\sin\theta_e\right) \qquad \text{(Eq.94)}$$

which occurs at approximately 60% of the entry velocity (specifically, 0.6065). Deceleration is related to the dynamic pressure through the ballistic coefficient W/C_DA; the maximum deceleration may then be expressed as

$$-\left(\frac{dV/dt}{g}\right)_{max} = \frac{\beta V_e^{\,2}}{2g}\sin\theta_e \qquad \text{(Eq.95)}$$

The maximum deceleration and the maximum dynamic and stagnation pressures are given in Figure 41 as a function of entry angle and velocity. Note from Figure 41 that if man's tolerance to acceleration is limited to 15 g, the entry angle of a ballistic satellite (25,500 ft/s) must be less than 5 deg to the horizontal.

[1] This is also true with reasonable accuracy for the nonlifting satellite entry, provided the entry angle is greater than 2 to 3 deg.

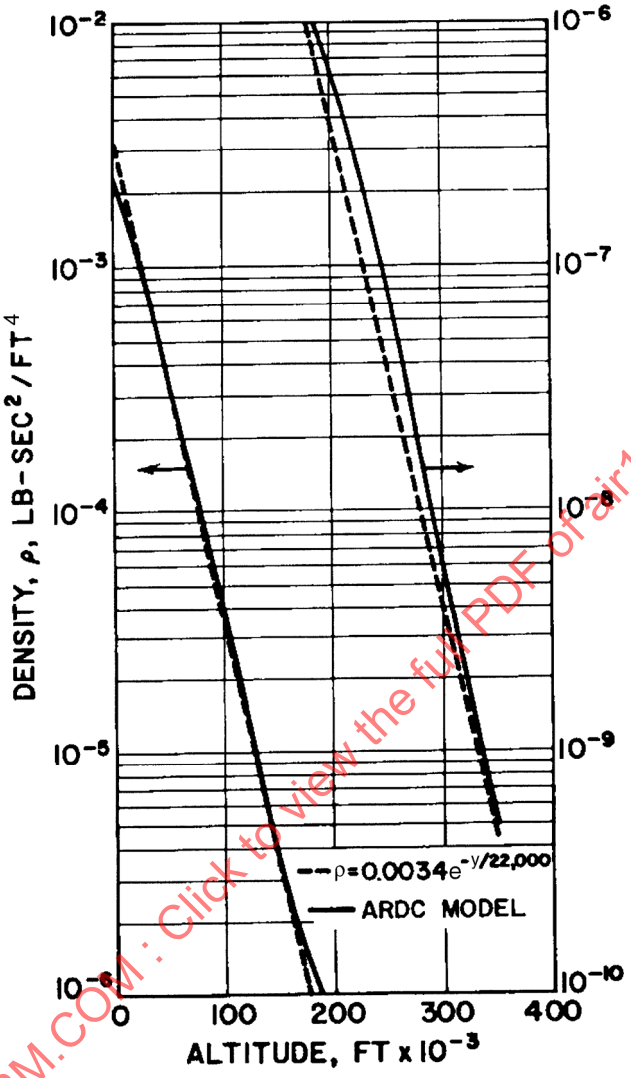

FIGURE 39 - Atmospheric Models

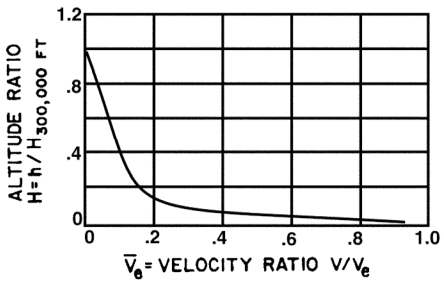

FIGURE 40 - Altitude Ratio as a Function of Velocity Ratio

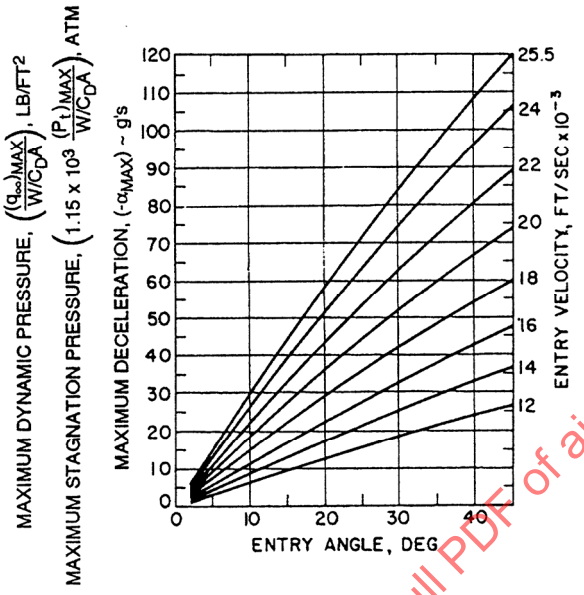

FIGURE 41 - Maximum Pressures and Accelerations for Ballistic Entry

1.3.2 (Continued):

The variation of pressure and deceleration throughout a ballistic entry is plotted in Figure 42 as a function of the entry velocity ratio. This curve should be read from right to left, corresponding to the decreasing velocity of entry. The variation of laminar and turbulent heat transfer is superimposed on Figure 42 for comparison of time of occurrence relative to pressure and deceleration.

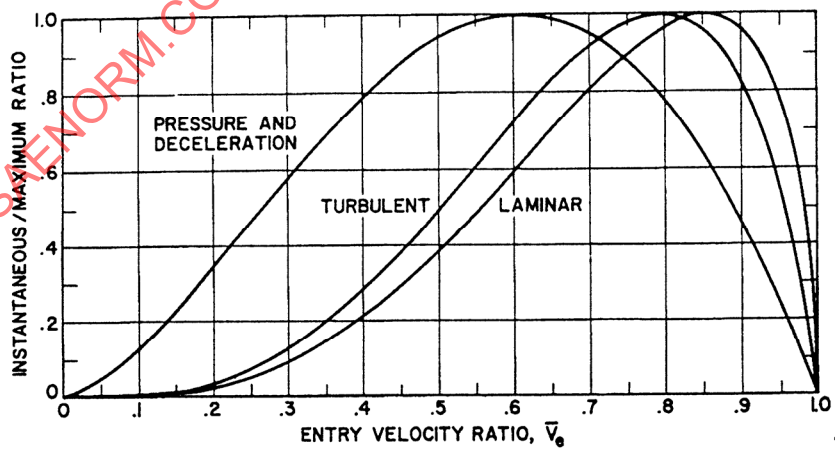

FIGURE 42 - Heat Flux, Pressure, and Deceleration Ratios for Ballistic Entry

1.3.3 Aerodynamic Heating: Many theoretical and experimental methods are available to calculate aerodynamic convective heating. Several will be presented. These methods are given below for the calculation of stagnation heat flux. Their differences are primarily in the choice of the form of variable, such as density and velocity, and corrections for wall temperature.

$$\dot{q}_t = 3.16 \times 10^{-9} \sqrt{\frac{(\rho g)_\infty}{r_n}}\, V^{3.0} \qquad \text{(Eq.96)}$$

$$\dot{q}_t = \frac{17{,}600}{\sqrt{r_n}} \sqrt{\frac{(\rho g)_\infty}{(\rho g)_o}} \left(\frac{V_\infty}{V_s}\right)^{3.15} \left[\frac{h_t - h_w}{h_t - h_{wc}}\right] \qquad \text{(Eq.97)}$$

where:

V_s = Satellite velocity, 26,000 ft/s

$$q_t = 8.147 \times 10^{-10}\, f_s(\bar{\gamma}, M) \sqrt{\frac{(\rho g)_\infty}{r_n}}\, V^{3.2} \qquad \text{(Eq.98)}$$

See Reference 2. The expression $f_s(\bar{\gamma}, M)$ is a correction for real gas dissociation as discussed in the following paragraphs.

From the preceding relations, the maximum stagnation heating for ballistic entry becomes

$$\frac{(\dot{q}_t)_{max} r_n^{0.5}}{f_s(\bar{\gamma}, M)} = 1.866 \times 10^{-12} \left[\frac{W}{C_D A} \sin\theta_e\right]^{0.5} V_e \qquad \text{(Eq.99)}$$

where:

V_e = Entry velocity at 300,000 ft altitude

Results from Equation 99 are given in Figure 43 as a function of the ballistic trajectory parameter $(W/C_DA) \sin\theta_e$ for various entry velocities. For $M_\infty < 5$, $\gamma = 1.4$; for $M_\infty > 10$, use $\gamma = 1.2$. A linear interpolation of these values is usually adequate for $5 \leq M_\infty \leq 10$. Maximum laminar heating rates occur at 85% of the entry velocity.

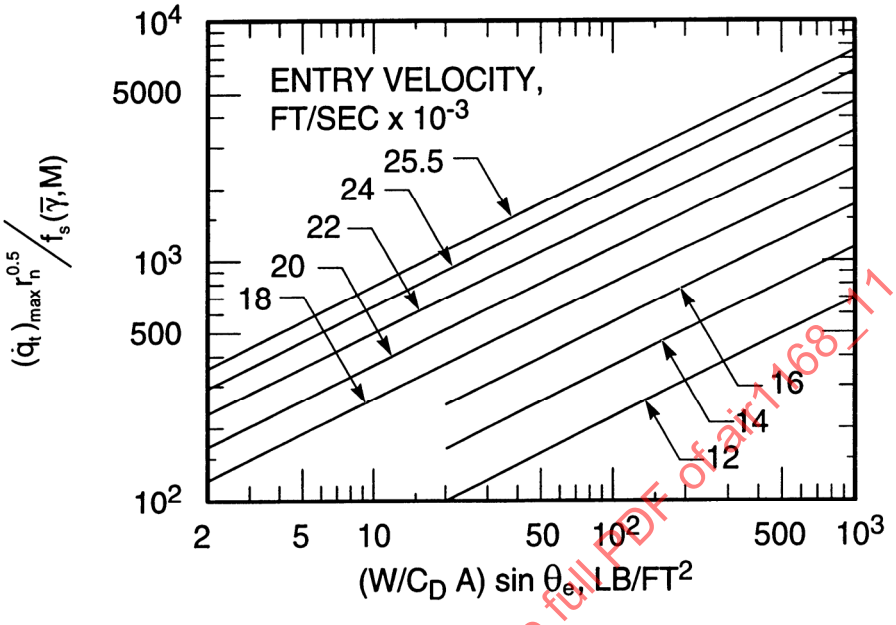

FIGURE 43 - Maximum Laminar Heat Flux, Ballistic, $f(M,\bar{\gamma}) = \frac{[(\bar{\gamma}+3)(\bar{\gamma}-1)]^{1/4}}{\sqrt{2\bar{\gamma}}}$

1.3.3 (Continued):

Maximum turbulent heating is given in Figure 44 as a function of ballistic trajectory parameter $(W/C_DA)\sin\theta_e$ for various entry velocities (Reference 2). The maximum turbulent heat transfer is expressed in its simplest form as

$$(\dot{q}_t s^{0.2})_{max} = 4.26 \times 10^{-8} (g\rho_\infty)^{0.8} V^{3.0} \qquad \text{(Eq.100)}$$

See Paragraph 6. Maximum turbulent heating rate occurs at 77% of the entry velocity. The quantity $f_T(M, \bar{\gamma}, P/P_t)$ is a correction for real gas dissociation effects and for local surface pressure ratio, and is defined in Figure 44. Maximum turbulent heat transfer occurs at a pressure ratio of approximately 0.50.

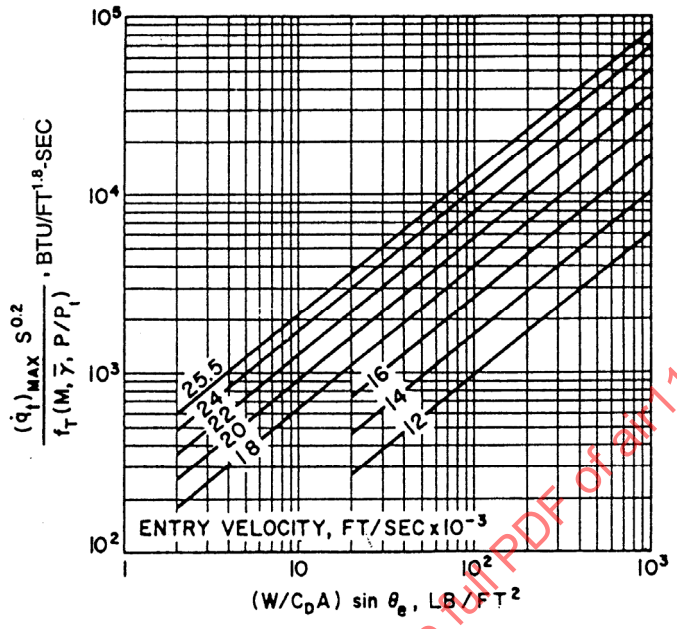

FIGURE 44 - Maximum Turbulent Heat Flux, Ballistic

$$f_T(M, \bar{\gamma}, P/P_t) = \frac{[(\bar{\gamma}+1)/2\bar{\gamma}]^{0.8}\,[P/P_t]^{0.8}\,[1-(P/P_t)^{(\bar{\gamma}-1)/\bar{\gamma}}]^{0.4}}{[1+1.272(P/P_t)^{(\bar{\gamma}-1)/\bar{\gamma}}]^{0.46}}$$

1.3.3 (Continued):

The variation of heat flux during a ballistic entry is given in Figure 42 as a function of entry velocity ratio. Maximum aerodynamic heating will occur at higher velocities and earlier than peak pressures and deceleration. This is significant for controlled ballistic entry missions, since maneuvering may be made during the time of peak heating to minimize the loading at peak dynamic pressure.

Calculation of loads and heating with time requires a relation between time and the velocity. Figure 45 is a curve of the entry velocity ratio as a function of the nondimensional entry time, $\beta V_e \tau \sin \theta_e$. By combining the heating, loads, and time through their relation with velocity, the instantaneous to maximum values are given in Figure 46 versus the nondimensional entry time. Aerodynamic heating reaches a maximum while the pressures are approximately half their maximum; after peak heating this condition is reversed. This can present a serious aerothermodynamic design problem for active heat protection systems, particularly if the application is a control surface where loads are high and may be changing rapidly.

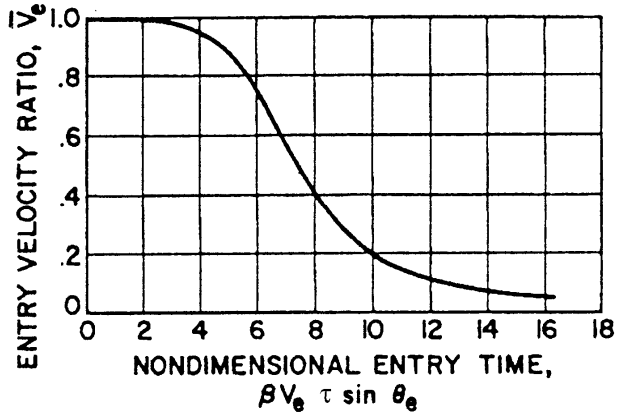

FIGURE 45 - Entry Velocity Ratio Versus Time, Ballistic.
Initial Condition $\tau = 0$ at $\bar{V}_e = 0.999$

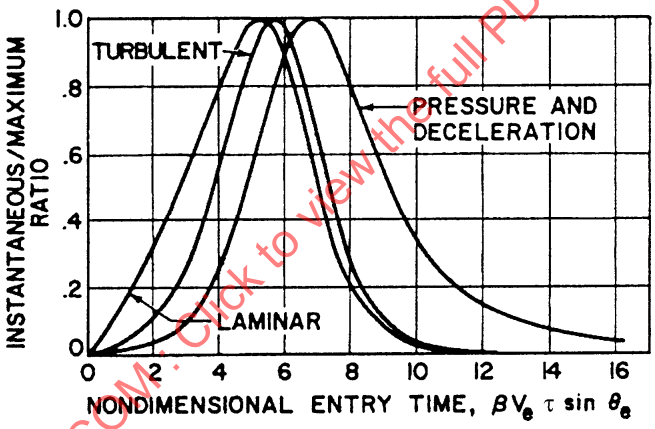

FIGURE 46 - Heat Flux, Pressure, and Deceleration Ratios for Ballistic Entry Versus Time

1.3.4 Glide Vehicle Entry: The loads and heating of a glide vehicle are significantly different from those of a ballistic vehicle, primarily as a result of the difference in trajectories. The ballistic vehicle achieves most of its range in drag-free flight beyond the sensible atmosphere; the glide vehicle relies on aerodynamic lift and may experience loads and heating throughout its entire flight regime for nonorbital missions.

The trajectory and aerodynamic heating for glide vehicle entry account for direction of travel at entry, neglected in Paragraph 1.3.1. The trajectory derivations shown are applicable to ballistic entry when the lift (L) = 0.

1.3.4.1 Trajectories: The flight path for vehicles entering the earth's atmosphere is described by the following equations (see Figure 47):

$$L \cos \phi + F_c - W \cos \theta_e = 0 \qquad \text{(Eq.101)}$$

$$D - W \sin \theta_e + m \frac{dV}{d\tau} = 0 \qquad \text{(Eq.102)}$$

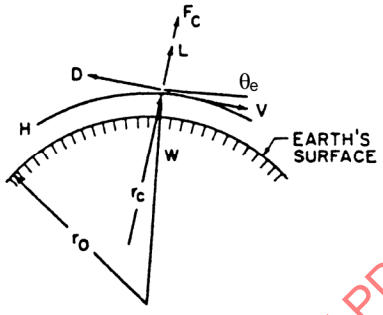

FIGURE 47 - Flight Path Forces

Equations 101 and 102 are the sum of the forces perpendicular and parallel to the flight path.

Vehicles of moderate to large lift coefficients fly at small flight path angles, θ_e. Then for small θ_e, $\cos \theta_e \cong 1$, and $\sin \theta_e \cong 0$,

$$L \cos \phi + F_c - W = 0 \qquad \text{(Eq.103)}$$

$$D + m \frac{dV}{d\tau} = 0 \qquad \text{(Eq.104)}$$

where:

$L = C_L qS$

$D = C_D qS$

$F_e = \dfrac{mV_i^2}{r_c}$

$m = \dfrac{W}{g}$

$r_c \cong r_0 + H$

ϕ = bank angle

1.3.4.1 (Continued):

Substituting into Equations 103 and 104 gives

$$C_l qS \cos\phi + \frac{W}{g}\frac{V_i^2}{r_0 + H} - W = 0 \qquad \text{(Eq.105)}$$

$$C_D qS + \frac{W}{g}\frac{dV}{d\tau} = 0 \qquad \text{(Eq.106)}$$

These equations describe the flight paths of lifting vehicles entering the Earth's atmosphere from near-Earth orbits.

1.3.4.2 Entry Direction: Since θ_e for lifting entry vehicles is small (can be neglected),

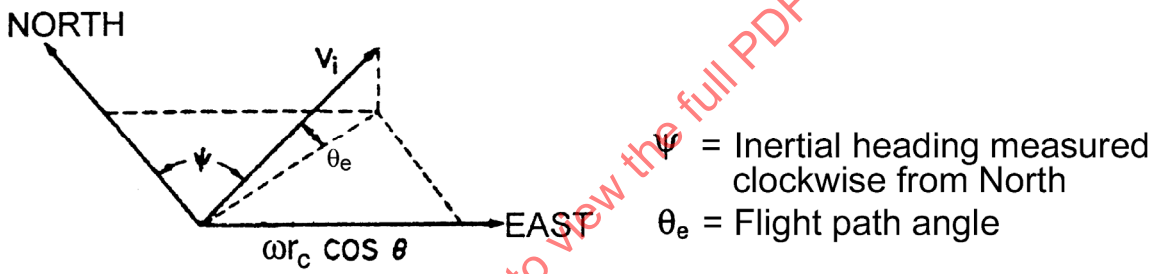

FIGURE 48 - Entry Direction Vectors

$$V^2 = (V_i \sin\psi - \omega r_c \cos\theta_e)^2 + (V_i \cos\psi)^2 \qquad \text{(Eq.107)}$$

or

$$V = V_i\left[\left(\sin\psi - \frac{\omega r_c}{V_i}\cos\theta_e\right)^2 + \cos^2\psi\right]^{1/2} \qquad \text{(Eq.108)}$$

From spherical trigonometry, the inertial headings are expressed in terms of the latitude and orbit inclination. For eastward flight direction

$$\sin\psi = \frac{\cos i}{\cos\theta_e} \qquad \text{(Eq.109)}$$

1.3.4.2 (Continued):

and for westward flight

$$\sin \psi = -\frac{\cos i}{\cos \theta_e} \qquad \text{(Eq.110)}$$

For polar flight, ψ = 0 or 180 deg, and

$$\sin \psi = 0, \qquad \cos^2 \psi = 1 \qquad \text{(Eq.111)}$$

The following are the relationships between relative and inertial velocity for the three flight directions:

Eastward flight:

$$V = V_i \left[\left(\frac{\omega r_c}{V_i} \right)^2 \cos^2 \theta_e - 2 \left(\frac{\omega r_c}{V_i} \right) \cos i + 1 \right]^{1/2} \qquad \text{(Eq.112)}$$

Westward flight:

$$V = V_i \left[\left(\frac{\omega r_c}{V_i} \right)^2 \cos^2 \theta_e + 2 \left(\frac{\omega r_c}{V_i} \right) \cos i + 1 \right]^{1/2} \qquad \text{(Eq.113)}$$

Polar flight:

$$V = V_i \left[\left(\frac{\omega r_c}{V_i} \right)^2 \cos^2 \theta_e + 1 \right]^{1/2} \qquad \text{(Eq.114)}$$

1.3.4.3 Equilibrium Glide Flight: Lifting vehicles entering from near-Earth orbits can rapidly establish equilibrium glide flight. This type of flight is defined by the gravity force being balanced by the aerodynamic lift and centrifugal force:

$$L \cos \phi + F_c = W \qquad \text{(Eq.115)}$$

Solution of Equation 105 gives the required dynamic pressure for equilibrium glide flight:

$$q = \frac{W}{SC_l \cos \phi} \left[\frac{V_i^2}{g r_c} - 1 \right] \qquad \text{(Eq.116)}$$

1.3.4.3 (Continued):

Equation 116 shows that $W/SC_l \cos \phi$ is the only vehicle characteristic required to define the altitude-velocity relationship of an equilibrium glide path. Equilibrium glide velocity and altitude expected design values of $W/SC_l \cos \phi$ and various entry directions are given in Figures 49 and 50.

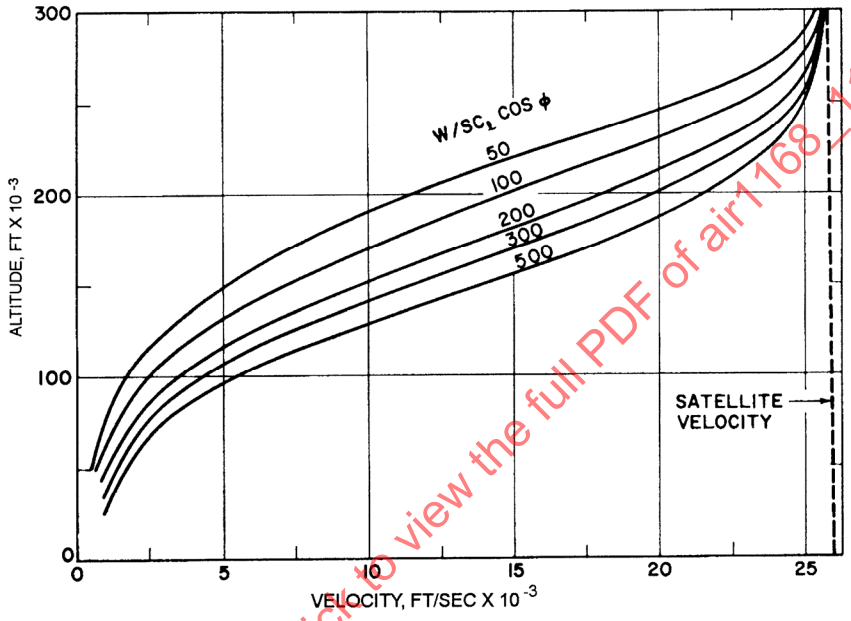

FIGURE 49 - Polar Entry; Equilibrium Glide Paths

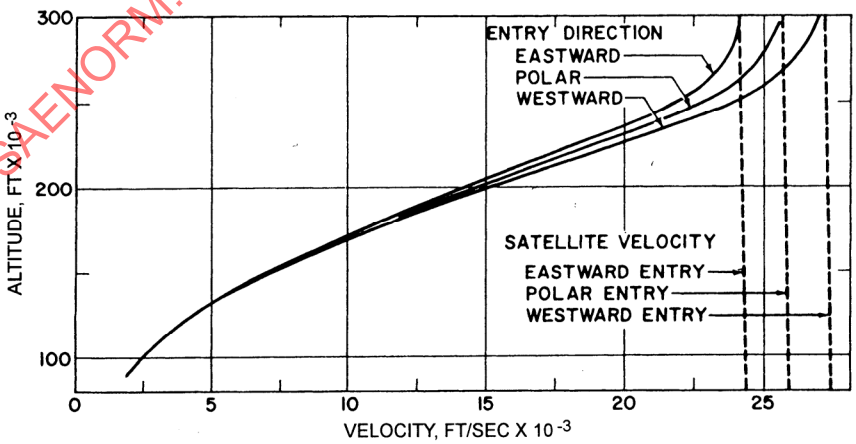

FIGURE 50 - Comparison of Entry Directions, $W/SC_l \cos \phi = 100$

1.3.4.3 (Continued):

Since an equilibrium glide flight path is defined by flying a constant $W/SC_l \cos \phi$, the lift coefficient during entry is also constant. This results from the assumption that the wing loading, W/S, remains constant during entry and that the hypersonic lift coefficient is constant. The typical drag polar for lifting vehicles indicates that when maintaining constant C_l, the drag coefficient is also constant (see Figure 51). Consequently, the L/D during equilibrium glide flight is also constant.

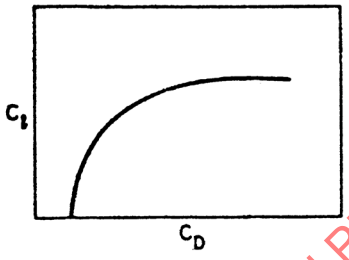

FIGURE 51 - Typical Drag Polar for Lifting Vehicles

Time for flight along equilibrium glide paths can be determined by substituting Equation 105 in Equation 108 and solving for $d\tau/dV$:

$$\frac{d\tau}{dV} = \frac{L}{D} \cos \phi \left[\frac{r_o + H}{V_i^2 - g(r_o + H)} \right] \qquad \text{(Eq.117)}$$

Integration gives

$$\tau = \left(\frac{L}{D} \right) \cos \phi \, \frac{r_o + H}{2\sqrt{g(r_o + H)}} \ln \left[\left(\frac{1 - \overline{V}_f}{1 + \overline{V}_f} \right) \left(\frac{1 + \overline{V}_i}{1 - \overline{V}_i} \right) \right] \qquad \text{(Eq.118)}$$

$$\tau = \left(\frac{L}{D} \right) \cos \phi \, \frac{V_s}{2g} \ln \left[\left(\frac{1 - \overline{V}_f}{1 + \overline{V}_f} \right) \left(\frac{1 + \overline{V}_i}{1 - \overline{V}_i} \right) \right] \qquad \text{(Eq.119)}$$

1.3.4.3 (Continued):

where:

$$\overline{V}_i = \frac{V_i}{V_s} \quad \text{(Eq.120)}$$

$$\overline{V}_f = \frac{V_f}{V_s} \quad \text{(Eq.121)}$$

$$V_s = \sqrt{g\,(r_o + H)} \quad \text{(Eq.122)}$$

$$g = g_o \left(\frac{r_o}{r_o + H} \right)^2 \quad \text{(Eq.123)}$$

Equations 118 and 119 show that the time involved in flying along equilibrium glide paths is only a function of (L/D) cos ϕ and the inertial velocity. Solutions of these equations for eastward, polar, and westward entries are given in Figure 52. The ticks on the curves show the variations in velocity that vehicles having the W/SC$_L$ noted will have when flying equilibrium glide paths at an altitude of 300,000 ft.

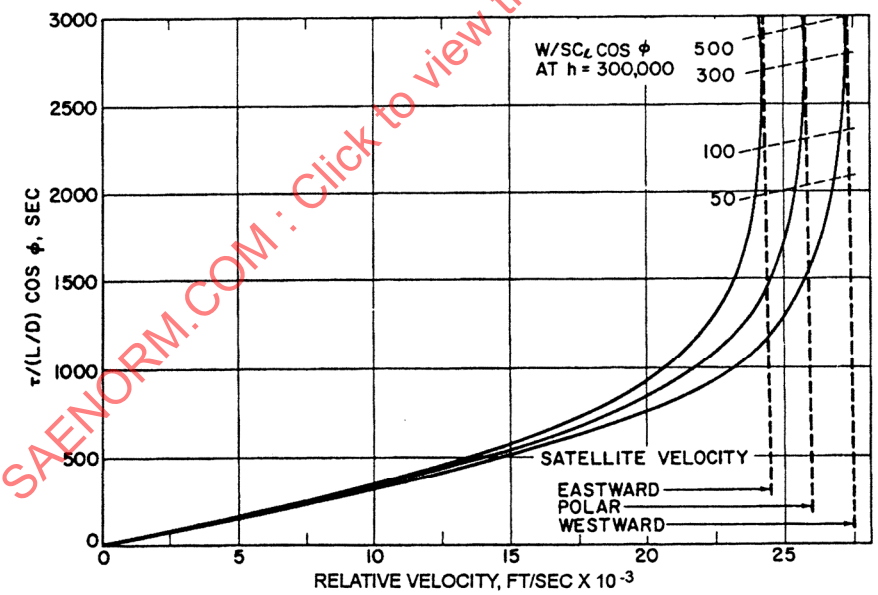

FIGURE 52 - Flight Time Along Equilibrium Flight Paths (Equation 119)

The equations presented show that flight along equilibrium glide paths is uniquely expressed by defining the entry direction, bank angle, L/D, and W/SC$_L$.

1.3.4.4 Aerodynamic Heating: Many theoretical and experimental methods are available to calculate aerodynamic convective heating. Results of these methods can be presented as $q = C_H (h_r - h_w)$ as well as in the more complete forms of Equations 96, 97, and 98. For hypersonic flight the heat transfer coefficient C_H can be essentially considered independent of wall temperature. Therefore it is convenient to deal with the cold wall heat flux $q = C_H h_r$, as it is independent of the wall temperature and thus of the particular material being used.

For a particular vehicle configuration, attitude, location on a vehicle, and type of flow, the cold wall heating rate is a function only of altitude and velocity. For flight along equilibrium glide paths, different values of $W/SC_l \cos \phi$ result in different altitude-velocity profiles. Also, variations in $(L/D) \cos \phi$ directly affect flight time. Thus variations in these aerodynamic parameters produce significantly different thermal environments. This can make preliminary design studies time consuming, since a wide variety of vehicle configurations and flight attitudes must be frequently considered. In addition, the time history of heating to a number of locations on a given vehicle (in a specific attitude) must be calculated to determine overall heat shield weights.

Results of heating analyses show that the time histories of heat transfer coefficient C_H and recovery enthalpy h_r form families of similarly shaped curves for flying equilibrium glide paths with various values of $W/SC_l \cos \phi$. Only absolute values of C_H and time change with different values of $W/SC_l \cos \phi$ and $(L/D) \cos \phi$. Thus, curves of the cold wall heat flux, $C_H h_r$ or $\dot{q}_o$, have similar shapes but different maximum values. Upon normalizing the cold wall heat flux $(\dot{q} / \dot{q}_{max})$ and plotting this versus $\tau/[(L/D) \cos \phi]$, the data essentially produce one curve for laminar flow and another for turbulent flow. These data are shown in Figures 53 through 55 for eastward, polar, and westward flights, respectively. From these data the heat transfer and recovery enthalpy may be normalized to their values at the time when the cold wall heat flux is a maximum. These results are shown in Figures 56 and 57 for polar entry.

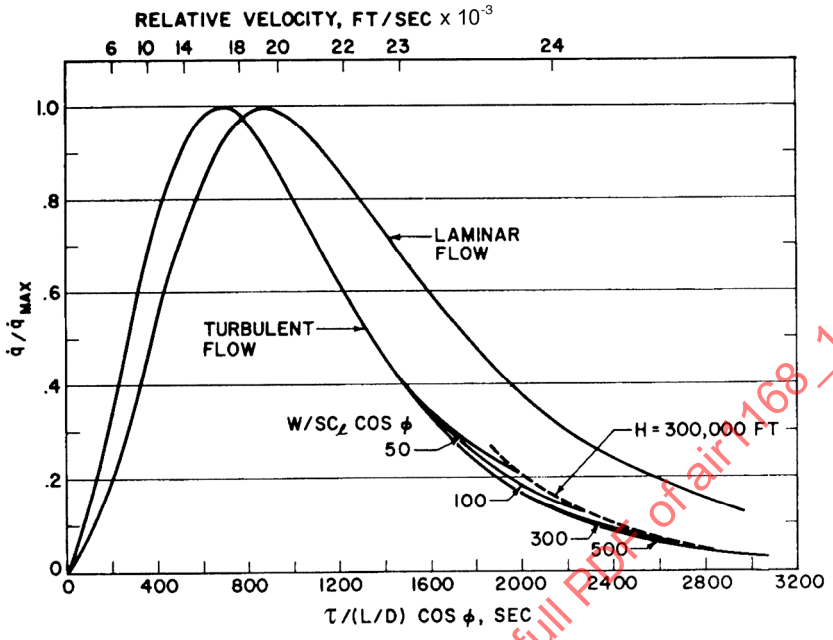

FIGURE 53 - Eastward Entry, Normalized Heat Pulse; τ = Time to Ground (Equilibrium Glide Flight)

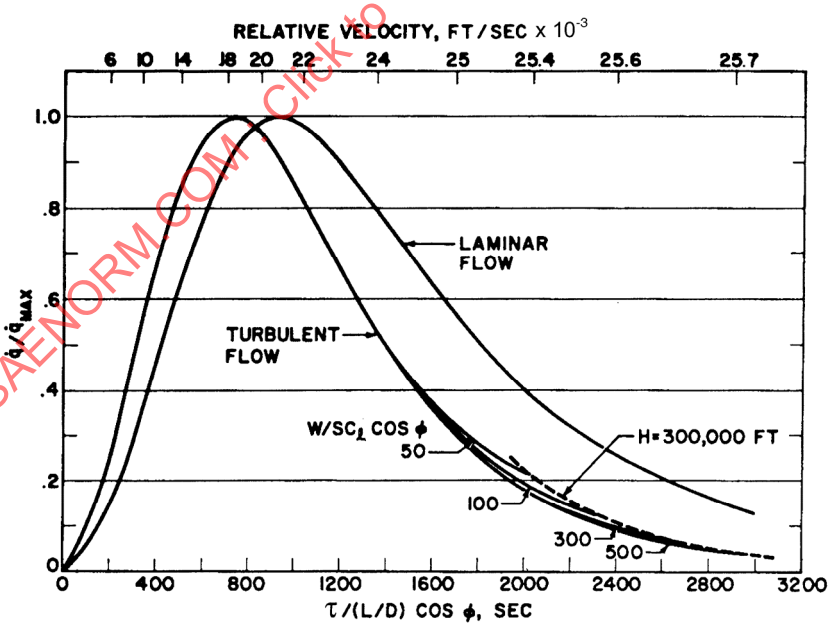

FIGURE 54 - Polar Entry, Normalized Heat Pulse (Equilibrium Glide Flight)

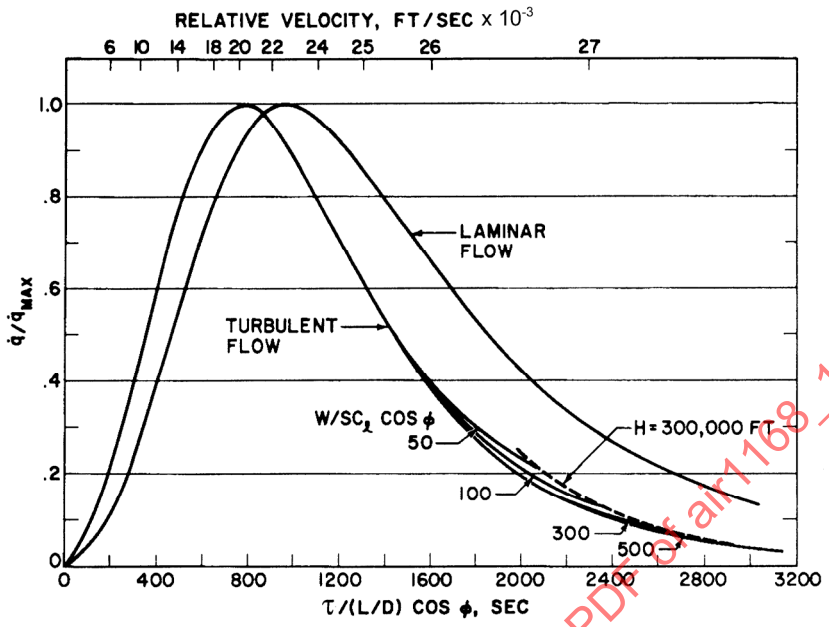

FIGURE 55 - Westward Entry, Normalized Heat Pulse (Equilibrium Glide Flight)

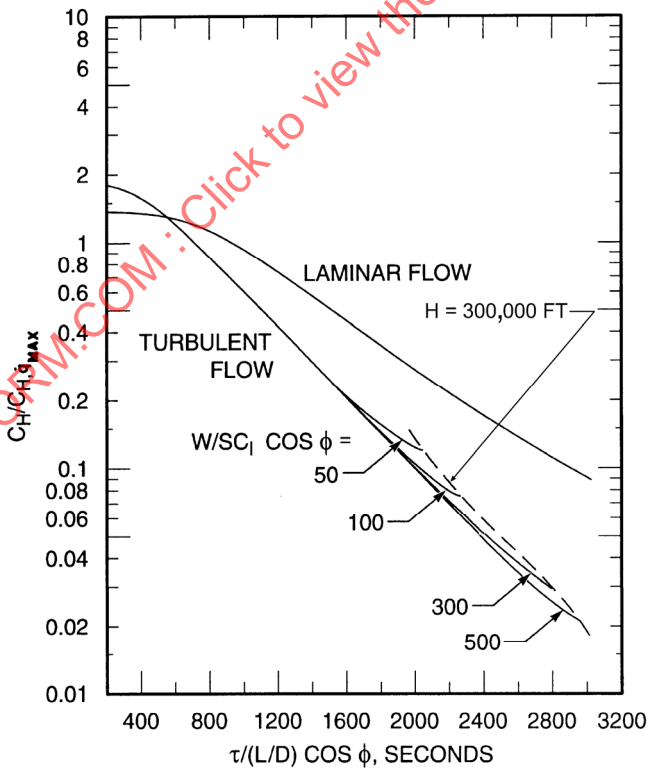

FIGURE 56 - Polar Entry, Normalized Heat Transfer Coefficient; τ = Time to Ground. Turbulent Flow $\dot{q}_{max}$ Occurs at V = 18,500 ft/s; Laminar Flow $\dot{q}_{max}$ Occurs at V = 21,000 ft/s

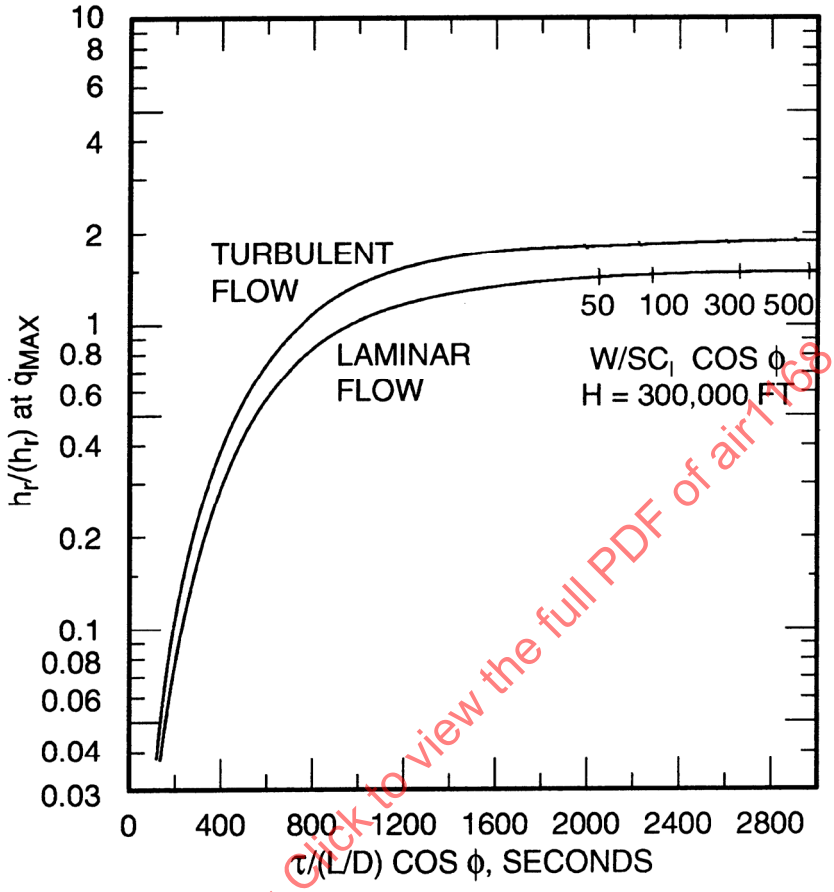

FIGURE 57 - Polar Entry, Normalized Recovery Enthalpy; τ = Time to Ground. Turbulent Flow $\dot{q}_{max}$ Occurs at V = 18,500 ft/s; Laminar Flow $\dot{q}_{max}$ Occurs at V = 21,000 ft/s

1.3.4.4 (Continued):

Normalized heating data presented are for eastward, polar, and westward entry directions. Little difference exists in these data. The inertial velocity for eastward entry is given by $V_i = V + 1524$, while for westward entry, $V_i = V - 1524$. This ± 1524 ft/s creates $\pm 50/[(L/D) \cos \phi]$ seconds in total entry time when flying equilibrium glide paths from an altitude of 300,000 ft to the ground. For preliminary design, this variation in total time is insignificant. Thus, the normalized curves for polar entry are good approximations for any entry direction. The principal effect of variations in entry direction is that of changing the maximum value of the cold wall heat flux. The equilibrium glide paths presented in Figure 50 show that the severity of heating is least for eastward entry and greatest for westward entry. Results, simplified for polar entry, are given in Figures 58 through 61.

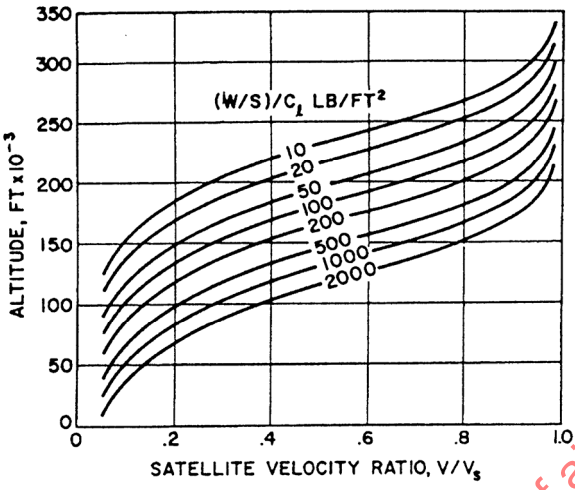

FIGURE 58 - Altitude Variation with Satellite Velocity for Equilibrium Glide Vehicle, Polar Entry

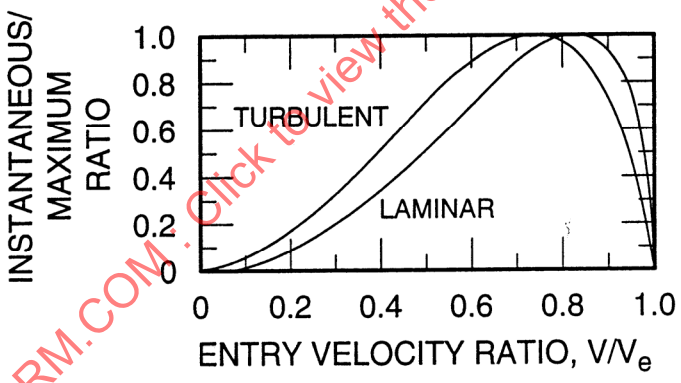

FIGURE 59 - Heat Flux Ratios for Glide Entry Versus Velocity Ratio, Polar Entry

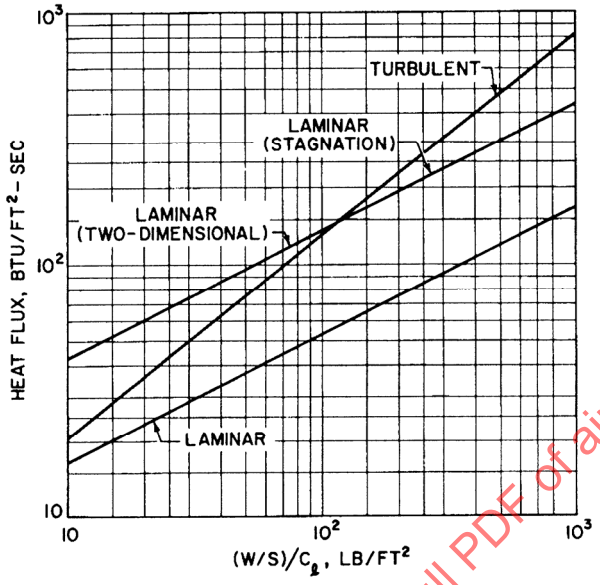

FIGURE 60 - Maximum Laminar and Turbulent Heat Fluxes (Glide), Polar Entry

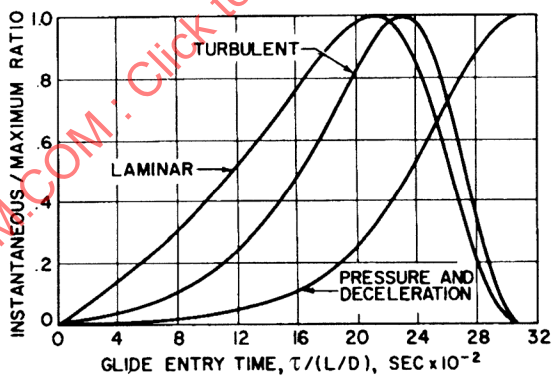

FIGURE 61 - Heat Flux, Pressure, and Deceleration Ratios for Glide Entry Versus Time, Polar Entry

1.3.5 Aerodynamic Heating - Preliminary Design: For the preliminary design of entry vehicles it is usually sufficiently accurate to assume that the hypersonic heat transfer distribution over the vehicle is a function only of vehicle attitude. This distribution may be obtained either analytically or experimentally. Analytical methods are described in Paragraphs 5 and 6. Once the heat transfer distribution has been obtained, it is necessary to consider only the variation of the reference heating rate with altitude and velocity. The normalized heating curves show this variation when flying ballistic or equilibrium glide paths. The reference heat flux is usually the heating rate at some location on a simple geometric shape, for example, a stagnation point or 10 ft location on a flat plate. Thus, to completely describe the time history of cold wall convective heating at any location on the vehicle, only the maximum value of the reference heating must be evaluated. For glide vehicles, the parameter $W/SC_l \cos \phi$ determines the maximum value of the reference heating rate, whereas $(L/D) \cos \phi$ determines the total entry time.

1.4 Entry Heat Protection Techniques:

Several approaches may be taken for protection of hypervelocity vehicles from the thermally induced effects of their environment, each having advantages for particular applications. This section presents heat protection concepts that employ the reradiative capability of a high-temperature surface, the sensible and latent heat capacities of materials, and the effect of mass injection into the boundary layer. The influence of heating as well as pressure and enthalpy levels on the various heat protection concepts are described for the purpose of preliminary heat protection subsystem selection. Zones of environmental applicability for thermal protection concepts and materials are presented in Figure 62. Although discrete zones of applicability exist for certain concepts, where these zones join or overlap, specific detailed trade-off or parametric studies are required to select the most appropriate concept or material.

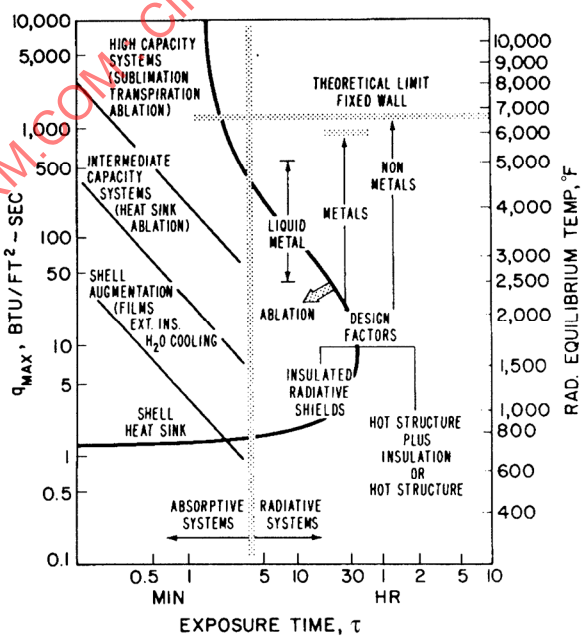

FIGURE 62 - Zones of Environmental Applicability for Thermal Protection Systems

1.4.1 Thermodynamic Systems: One of the simplest heat protection systems that can be formulated thermodynamically is a high-temperature surface to reradiate the heat transferred to the vehicle. This concept can be applied for heat fluxes as high as the low hundreds of Btu/ft^2-s, depending on the structural design. Material strength drops off rapidly above 2000 °F; however, from data given in Figure 63 for design purposes, the operation of load-carrying structures is limited in radiative heat flux to approximately 20 Btu/ft^2-s.

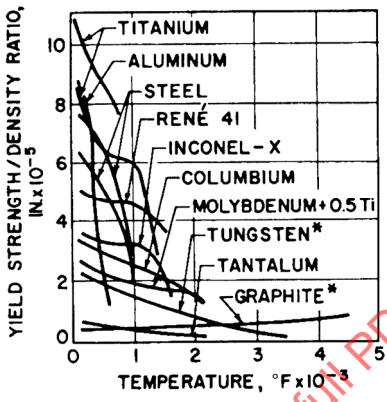

FIGURE 63A - Structural Efficiency of Some Representative Materials as a Function of Temperature (From Reference 5)

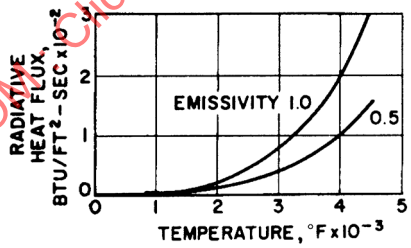

FIGURE 63B - Radiative Heat Transfer as a Function of Temperature

1.4.1 (Continued):

In addition to the loss in strength, oxidation is a serious problem for materials such as molybdenum and its alloys. Coatings, while presenting a general solution to oxidation, are susceptible to local failures, which can propagate through the base metal beneath the surface. Also, the large-scale use of coated structures present logistic handling problems because of their low-temperature brittleness. Columbium, which forms a stable oxide, is not subject to catastrophic failures, and therefore is more useful as a high-temperature structural material. Columbium is also superior to molybdenum from a fabrication standpoint, although the ultimate capability of molybdenum is better above 2000 °F. The refractory metals such as tungsten and tantalum find application in less critical structural areas, where their high densities will not impose a weight penalty. Graphite can also be used for similar applications, particularly in view of the rapid progress now being made in graphite applications technology.

The use of a high-temperature structure appears to be limited to the nonlifting surfaces of large L/D glide vehicles. Ballistic satellites and other lifting entry bodies might use it as an alternate approach in ablation areas where laminar boundary layer flow (aerodynamic heating rate less than 30 Btu/ft^2-s) can be assured. For glide vehicle design, the following considerations are also of importance:

(1) Surface temperatures may be reduced 10 to 15% by providing an efficient heat path such as internal radiation to a highly cooled surface, as in Figure 64.

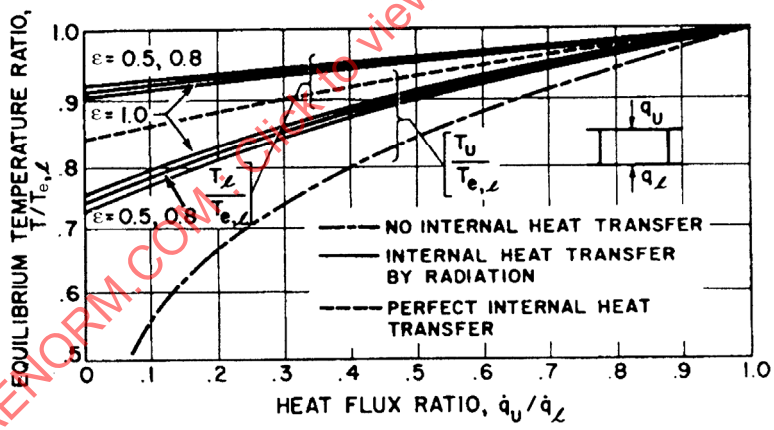

FIGURE 64 - Effect of Internal Heat Transfer on Wing Skin Temperatures

(2) During the maximum heating portions of the trajectory, the aerodynamic loads will be normally less than 1 g. Therefore thermally induced stresses and aerothermoelastic effects may predominate in high-temperature design.

(3) Axial loads during boost will be the highest to which a glide vehicle will be subjected in the overall trajectory.

(4) Maximum lateral loads will normally occur in the terminal phases of flight and in landing, after the structure has been subjected to its maximum temperature.

1.4.1 (Continued):

The leading edge of a glide vehicle is an area where reradiation is desirable, particularly from the standpoint of shape stability and aerodynamics. For this application, the use of a refractory metal such as tungsten or graphite is practical. Over the major portion of its surface, the high-temperature reradiation metallic structure finds severe competition weightwise from charring ablatives, even for L/D > 2 glide vehicles.

The determination of the effectiveness with which heat is dissipated per pound of the reradiation structure is difficult to assess on an aerothermodynamic basis, since the heat protection system weight is an integral part of the structural weight. To obtain a measure of the reradiating structure as a heat protection concept, it is necessary to analyze the structural weight of representative designs as a function of material structural efficiency. The weight of the heat protection system may then be considered to be the difference between the structural weight of the high-temperature design and one using a representative low-temperature structural efficiency. Note, however, that reliability will probably outweigh any other design criteria in an application where the thermostructure may be used; hence the effectiveness of this concept is somewhat academic.

1.4.2 Absorptive Systems - Heat Sink: A second type of heat protection system is one that makes use of the sensible heat capacity of a material to absorb energy, thereby providing a shield for the vehicle from its environment. Solutions for the thermal response of a finite-thickness, insulated slab subjected to a triangular heat pulse idealized for a ballistic entry have shown that the response of the slab varies gradually from the "thin skin" at zero thickness up to a value of approximately 1 for the thickness parameter, and then departs rapidly to the infinite thickness solution (Reference 3). Results from Figure 65 show that for a value of the thickness parameter of 1, the heat flux parameter $\dot{q}_{max}\sqrt{\alpha\tau}\,/\,k\Delta T_{max}$ is 1.508 as compared with 1.575 for the infinite slab. Considering the stagnation point of a ballistic entry body as representative, the following relation between material properties, vehicle parameters, and entry velocity may be obtained:

$$\frac{(\Delta T)_{max}\,k}{\alpha^{0.5}} = 3.40 \times 10^{-10} \cdot \left[\frac{W / C_D A}{r_n}\right]^{0.5} V_e^{2.7} \qquad \text{(Eq.124)}$$

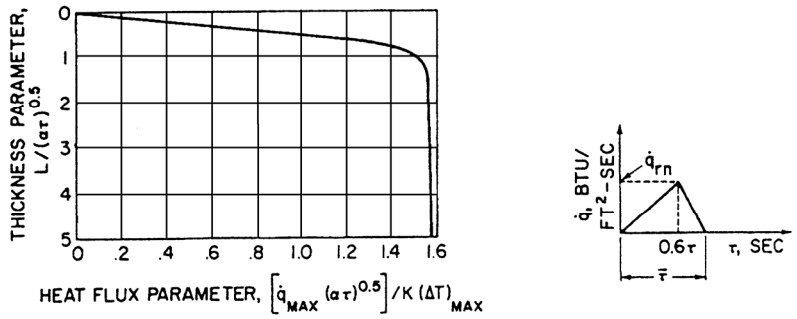

FIGURE 65 - Variation of Heat Flux Parameter with Thickness Parameter for Triangular Heat Pulse $\dot{q}_{max}$ at $\tau = 0.6\ \bar{\tau}$

1.4.2 (Continued):

Values of $(\Delta T)_{max}k/\alpha^{0.5}$ for representative materials up to their melting points are presented in Table 2 and results from Equation 124 are presented in Figure 66. From this combination it is possible to determine the limitations of a material for a ballistic entry without regard to its effectiveness and excluding surface reradiation.

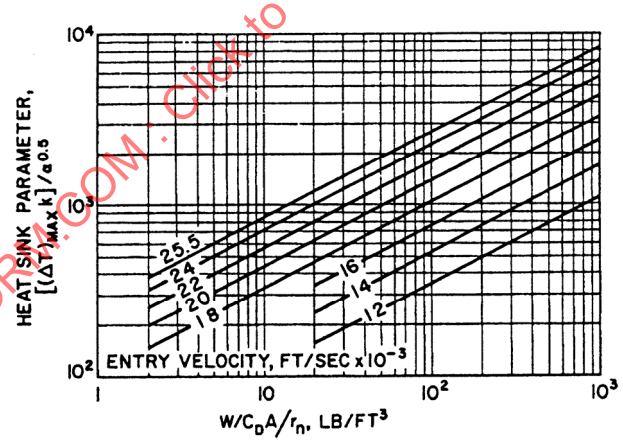

FIGURE 66 - Stagnation Point Heat Sink Requirements for Ballistic Entry

TABLE 2 - Thermal Properties of Materials

Material	Melting Point, °R	Density lb/ft^3	Specific Heat Btu/lb-°R	Thermal Conductivity, Btu/ft-s-°R	Thermal Diffusivity, ft^2/s	$(\Delta T_w)_{max}$	$k(\Delta T_w)_{max}$	$\alpha^{0.5}$	$\frac{k(\Delta T)_{max}}{\alpha^{0.5}}$	$C_p(\Delta T)_{max}$	ΔH_{max}
Aluminum	1680.1	168.7	0.215	3.66^{-2}	1.01^{-3}	1180.1	43.19	3.175^{-2}	1.36^{3}	255	170
Beryllium	2800	113.7	0.52	2.55^{-2}	4.315^{-4}	2300	58.65	2.075^{-2}	2.83^{3}	1150	470
Carbon	7160	132.5	0.165	3.83^{-3}	1.752^{-4}	6660	25.51	1.322^{-2}	1.93^{3}	1100	
Columbium	4840	535	0.065	8.39^{-3}	2.415^{-4}	4380	36.75	1.552^{-2}	2.37^{3}	285	
Copper	2441.1	559	0.092	6.32^{-2}	1.23^{-3}	1941.1	122.68	3.53^{-2}	3.475^{3}	180	91.1
Iron	3262	492	0.11	1.21^{-2}	2.235^{-4}	2762	33.42	1.494^{-2}	2.305^{3}	305	117
Magnesium	1662	108.8	0.25	2.55^{-2}	9.37^{-4}	1162	29.63	3.06^{-2}	9.68^{2}	290	160
Molybdenum	5220	637	0.061	2.35^{-2}	6.05^{-4}	4720	110.92	2.46^{-2}	4.51^{3}	290	126
Nickel	3110	556	0.105	1.48^{-2}	2.535^{-4}	2610	38.63	1.591^{-2}	2.43^{3}	275	133
Rhenium	6215	1312	0.033	1.142^{-2}	2.635^{-4}	5715	65.27	1.622^{-2}	4.025^{3}	190	
Silicon	3065	145.6	0.162	1.35^{-2}	5.72^{-4}	2565	34.63	2.39^{-2}	1.45^{3}	415	607
Silver	2210.6	655	0.056	6.72^{-2}	1.833^{-3}	1710.6	114.95	4.28^{-2}	2.685^{3}	95	45
Tantalum	5885	1038	0.036	8.73^{-3}	2.338^{-4}	5385	47.01	1.529^{-2}	3.075^{3}	195	
Titanium	3760	284	0.126	8.73^{-3}	2.442^{-4}	3260	28.46	1.561^{-2}	1.825^{3}	410	
Tungsten	6630	1206	0.032	3.23^{-2}	8.37^{-4}	6130	198.00	2.892^{-2}	6.85^{3}	195	79
Alumina, 99%, Bonded	4120	170	0.33	5.56^{-4}	9.91^{-6}	3620	2.012	3.15^{-3}	6.38^{2}	1195	
Beryllia	5117.4	180	0.26	1.80^{-2}	3.845^{-4}	4617.4	83.0	1.962^{-2}	4.23^{3}	1200	
Chrome	4000	180	0.21	2.78^{-4}	7.35^{-6}	3500	0.973	2.713^{-3}	3.586^{2}	735	
Fosterite	3921	153	0.25	2.38^{-4}	6.22^{-6}	3421	0.814	2.493^{-3}	3.267^{2}	855	
Graphite	6790	137	0.39	5.09^{-3}	9.53^{-5}	6290	32.05	0.78^{-3}	3.275^{3}	2450	
Magnesia	5530	175	0.283	4.17^{-4}	8.42^{-6}	5032	2.095	2.905^{-3}	7.22^{2}	1425	
Magnesite	5530	168	0.27	4.63^{-4}	1.02^{-5}	5030	2.332	3.20^{-3}	7.29^{2}		
Mullite	3777	152	0.23	3.47^{-4}	9.93^{-6}	3277	1.138	3.153^{-3}	3.61^{2}		
Mullite, Conv.	3710	145	0.23	3.24^{-4}	9.72^{-6}	3210	1.041	3.12^{-3}	3.335^{2}	870	
Silica	3600	105	0.28	3.31^{-4}	1.13^{-5}	3100	1.027	3.367^{-3}	3.05^{2}	1165	
Silicon Carbide	4542	158	0.288	2.52^{-3}	5.54^{-5}	4042	10.2	7.47^{-3}	1.366^{3}		
Silicon Nitride Bonded SiC	4002	173	0.288	2.63^{-3}	5.28^{-5}	3502	9.2	7.28^{-3}	1.265^{3}		
Zircon	4850	205	0.15	5.09^{-4}	1.66^{-5}	4350	2.213	4.08^{-3}	5.42^{2}		
Zirconia, Stabilized	5170	275	0.20	1.62^{-4}	2.95^{-6}	4670	0.756	1.719^{-3}	4.40^{2}	935	

NOTE: Exponent indicates power of 10. $(\Delta T_w)_{max}$ is melting temperature minus 500 °R.

1.4.2 (Continued):

For the heat sink concept the effectiveness may be defined as the total heat pulse per unit area divided by the weight of material per unit area. The effectiveness may be expressed as

$$Q_H^* = \nu C_p (\Delta T)_{max} \qquad \text{(Eq.125)}$$

where:

ν = Heat sink efficiency as measured by the ratio of mean to surface temperature, plotted in Figure 67 as a function of the heat flux parameter

Table 2 gives the ultimate heat capacities of potential heat sink materials up to their melting points. From Table 2 and Figure 66 their maximum effectiveness may be determined. In general, as seen in Table 2, metals can be utilized in more severe entry conditions than can the inorganic compounds, based on the parameter $k(\Delta T)_{max}/\alpha^{0.5}$; exceptions are beryllium, beryllia, and graphite, which combine high thermal effectiveness with sufficient conductivity to permit their use on relatively low W/C_DA ballistic entry bodies. Surface reradiation is of little significance to the performance of low melting point materials, but is significant to the performance of high-temperature ceramic oxides by as much as 20%. For extremely high-temperature materials such as tungsten and graphite, the reradiation can amount to as much as 40% for tungsten and 100% for graphite, dependent upon the specific temperature attained during entry.

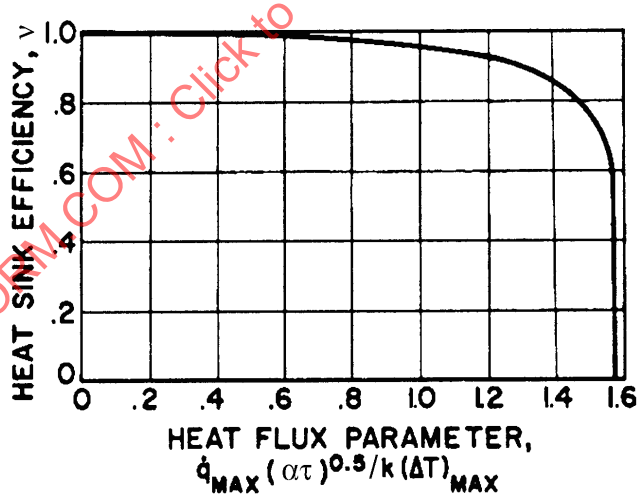

FIGURE 67 - Heat Sink Efficiency as a Function of Heat Flux Parameter

1.4.2 (Continued):

The use of the sensible heat of a material, including the effects of surface reradiation as a heat protection system, is limited to moderate W/C_DA ballistic entry bodies. The effectiveness of the heat sink concept is in the low hundreds of Btu/lb for most metals, with the notable exception of beryllium, which is of the order of 1000 Btu/lb. Ceramics have effectivenesses of the order of 1000 Btu/lb, but their low conductivities limit their use to low W/C_DA entry bodies. Graphite is an effective heat sink material, with an effectiveness of up to 4000 Btu/lb. In addition to the thermodynamic considerations, chemical reactions with the environment and structural ramifications will limit the use of high-temperature heat sinks to less than the theoretical performance presented above.

The heat sink thermal protection technique is extended by allowing the material to change phase, thereby removing the heat flux limitation of the sensible heat concept as well as gaining the latent heat effect of the phase change. The limitation of heat flux that must be imposed on a system employing only its sensible heat capacity may be removed by permitting the material to change phase, with vaporization generally necessary for a high effectiveness heat protection system. In addition to the latent heat of vaporization, the injection of gaseous species into the boundary layer results in a further decrease in heat transfer to the surface (Reference 4). This blocking action in the boundary layer may be expressed in units of effectiveness and is primarily a function of the total enthalpy of the environment, and hence of the vehicle velocity, as shown in Figure 68.

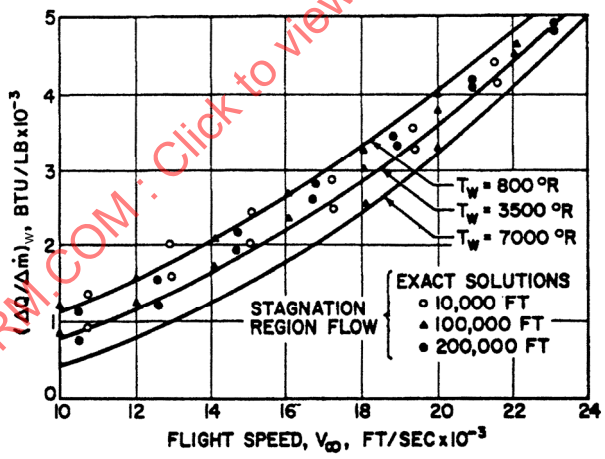

FIGURE 68 - Effectiveness Quotient Versus Flight Speed

The means of achieving vaporization when melting occurs and a liquid phase is present is the most general problem associated with the use of this heat protection concept, since very few materials exhibit sufficient vapor pressure in the solid phase to sustain a significant rate of sublimation, as shown in Figure 69. In order to achieve the theoretical effectiveness of a vaporization system, including gas injection into the boundary layer, it is necessary to restrain the liquid phase from flowing.

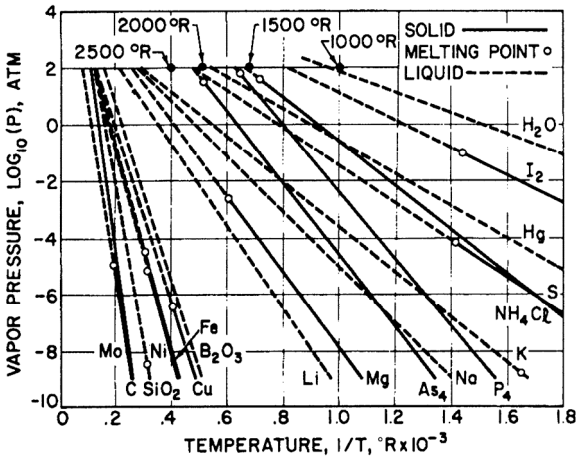

FIGURE 69 - Vapor Pressures of Various Materials

1.4.2 (Continued):

For a material capable of melting as well as vaporizing when subjected to a hypervelocity environment, the effectiveness of this concept is expressed as (Reference 4)

$$Q_v^* = \Gamma\left[\left(\frac{\Delta Q}{\Delta \dot{m}}\right) + (h_i - h_w) + \frac{1-\Gamma}{\Gamma}(h_e - h_w)\right] \qquad \text{(Eq.126)}$$

where:

Γ = Ratio of vaporization to melting $(\Delta Q / \Delta \dot{m})$, taken from Figure 68

h_i = Enthalpy of gaseous mixture, including vaporized species at gas-liquid interface

Q_v^* = Heat of vaporization based on material melted

$\Delta Q / \Delta \dot{m}$ = Taken from Figure 68

The effectiveness of this type of system is strongly dependent on the ratio of vaporization to melting and on the interrelation between the flow of a molten material and its vaporization.

Theoretically, a heat protection system employing vaporization as an energy absorbing mechanism could achieve an effectiveness, including the mass transfer effect, in the range 5000 to 10,000 Btu/lb; however, the presence of a liquid phase will considerably lower its performance. In addition, when melting occurs, such a system will vary in effectiveness both by virtue of the velocity effect on mass transfer and through the influence of pressure on the vaporization-to-melting ratio. A further disadvantage to a melting system is the tendency for molten material to flow from high to low heat flux regions, adding heat that otherwise might be avoided.

1.4.3 Absorptive Systems - Mass Injection: The injection of gas through a porous surface into the boundary layer, using either an active or passive reservoir for coolant, represents another absorptive heat protection concept. An active system, while yielding a positive control over the coolant flow rate, has the disadvantage of requiring a control system. In addition to the reliability problems of an active system, the range of flow rates required in the short time of a ballistic entry introduces certain complex design problems.

Passive reservoir systems, using both the equilibrium vapor pressure and the decomposition of a polymer as the driving force for the mass flow, afford the better approach on the basis of ease of handling and fabrication. Also, the depolymerization of a plastic is governed energetically by the heat flux to the system and not by the pressure, as is the case with vaporization. In addition, significant mass flow rates may be achieved from thermoplastic materials at relatively low temperatures (Figure 70). A system of this type is capable of sustaining heat fluxes in the low thousands of Btu/ft^2-s with an effectiveness of 3000 to 5000 Btu/lb. The surface heat flux and temperature of a representative system are included in Figure 71, where the intimacy of contact between the plastic and the porous surface is immediately apparent.

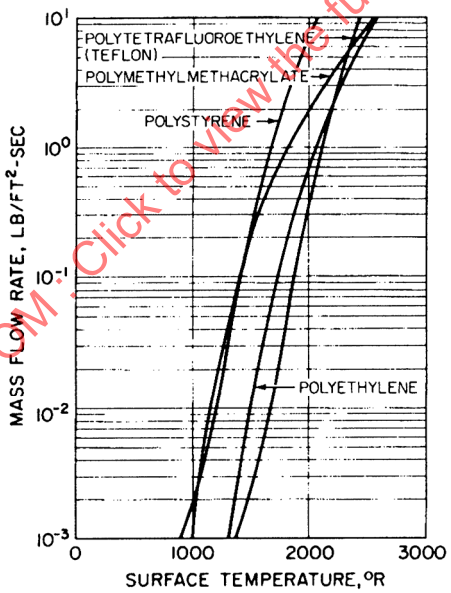

FIGURE 70 - Ablation Rates of Polymers

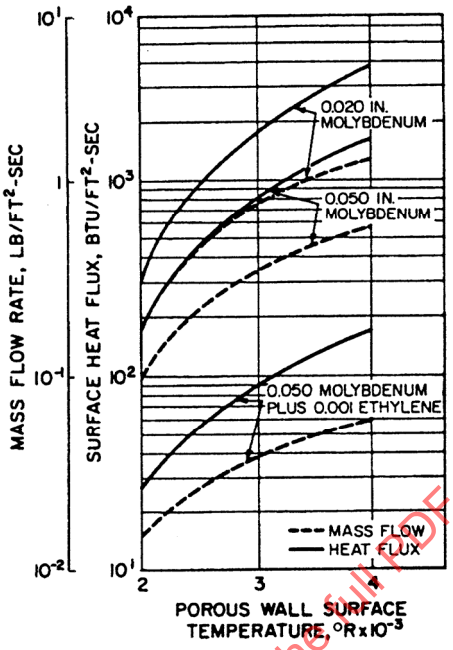

FIGURE 71 - Performance of Polyethylene (Transpiration Cooling System)

1.4.3 (Continued):

This type of system could be utilized on those portions of the vehicle, such as control surfaces, where dimensional change may not be tolerable. The porous-wall cooling system is basically the same as the ablation of thermosetting plastics, which form a porous char upon decomposition (Figure 72). Although this heat protection concept allows physical change of the outer surface, it is applicable where variations in shape are a secondary consideration or where shape change control can be accomplished. This type of heat protection system is capable of sustaining unlimited aerodynamic heating with effectiveness in the range 3000 to 5000 Btu/lb. It is the most widely used of heat protection system concepts. Its zone of applicability is shown in Figure 62.

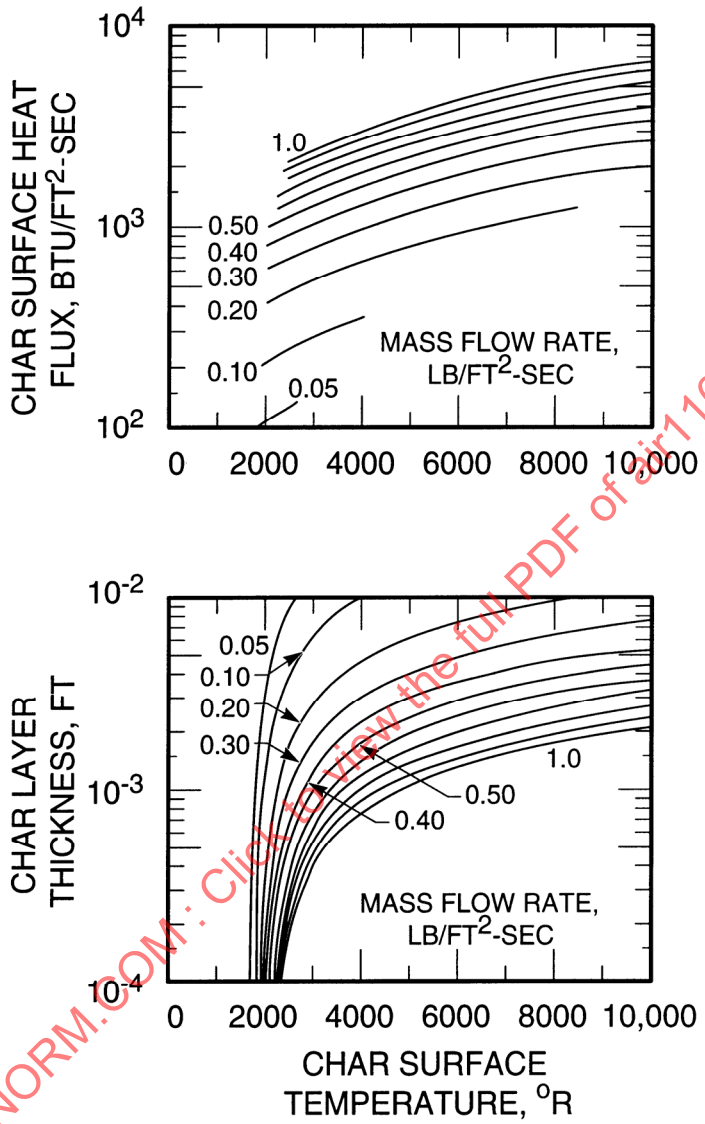

FIGURE 72 - Thermosetting Plastic Decomposition (Flow Through Porous Char)

1.4.3 (Continued):

The final consideration in the formulation of a successful and efficient heat protection system lies in providing sufficient insulation for the internal environments from the surface heating of the vehicle. The operating temperature of the surface heat protection scheme will have a significant influence on the insulation requirements and hence on the overall system effectiveness. Approaches to providing internal environmental control include high-temperature structures backed with nonstructural insulation and the use of water cooling at low pressures (also useful for environment control). Consideration must also be given to the energy balance during the orbiting phase of vehicles, as well as during entry, in synthesizing systems requiring significant insulation capability. The design engineer must be aware that the insulating qualities of a heat protection system are at least as important as the surface heat protection scheme in formulating overall heat protection systems.

It should be emphasized that the approximate range of applicability of the heat protection systems defined above are shown in Figure 62. The approximate material efficiency in heat absorption capability in Btu/lb is given in Table 2. These values are highly approximate and dependent upon the details of the entry vehicle configuration, trajectory, and emergency requirements. Further, an entry vehicle heat protection system may be made up of several types of materials or material systems in order to provide an optimum design.

1.5 Entry Heat Transfer and Heat Protection Analysis Procedure:

Entry heat transfer analysis proceeds by an investigation of the response of the spacecraft system from the initiation of entry at an Earth atmospheric altitude of approximately 400,000 ft to impact or touchdown. The process is initiated by definition of the spacecraft geometry. Its trajectory is defined, either by approximate methods which may neglect gravitational forces or by multidegree of freedom motion analysis, which accounts for vehicle mass asymmetries, mass loss, roll, and other factors.

In detail analyses, the motion of the vehicle in roll, pitch, and yaw may be the thermal design limiting case. For other than approximate thermal analyses, a detailed pressure distribution is required. The magnitude of the thermal environment is then investigated along the trajectory, encompassing the gas dynamics regimes of low density flow, continuing flow, and (for all systems) some degree of flow which is not in thermal equilibrium. At velocities somewhat in excess of Earth orbital velocity, the radiation from the high-temperature gas enclosed within the spacecraft induced shock system becomes a significant portion of the total thermal load. From considerations of vehicle thermal environment level, time of application, and weight considerations, the class of heat protection subsystem is selected.

These steps are indicated in flow diagram form in Figure 73. Figure 74 gives the primary regimes of the entry system which are to be investigated and correlated with the flow diagrams of Figure 73. With the flow diagram as a “check list,” the approximate magnitude of the thermal environment may be obtained by cross reference to a detailed altitude-velocity heat transfer map (Figure 75).

The thermal environment history and variation with flow over the spacecraft surface (laminar-turbulent flow) are given in Paragraph 6.

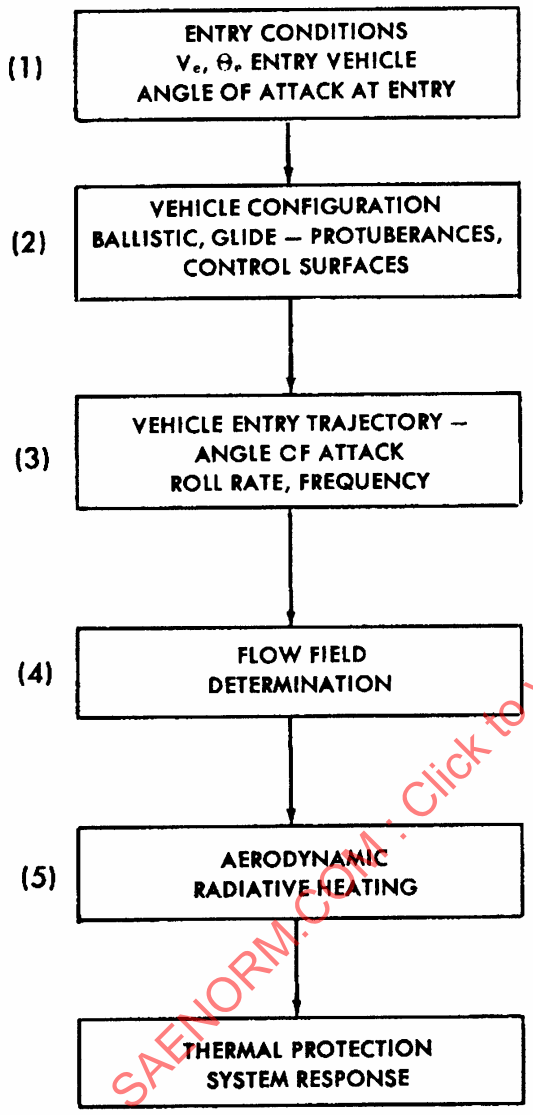

FOR BALLISTIC, ASSUME $\alpha = 0$ AT ENTRY. CORRECT FOR α EFFECTS AFTER ESTIMATING THERMAL ENVIRONMENT. FOR ESTIMATION PURPOSES, ASSUME CONTINUUM FLOW – CORRECT TO LOW DENSITY CONDITIONS

FOR BALLISTIC AND GLIDE, EXAMINE CONTOUR OF VEHICLE FOR FLOW INTERFERENCE EFFECTS. GENERALLY, ESTIMATE THERMAL ENVIRONMENT FOR SMOOTH BODY, CORRECT FOR INTERFERENCE EFFECTS

FOR BALLISTIC ENTRY, ANGLE OF ATTACK IN REGIONS OF HIGH HEAT TRANSFER ARE NORMALLY LOW $0 \leq \alpha \leq 5°$. INTEGRATED EFFORT SHOULD BE ASSESSED BY EXAMINING ANGLE OF ATTACK AS FUNCTION OF TIME OF REPRESENTATIVE VEHICLE LOCATIONS. SAME APPROACH FOR GLIDE VEHICLES WHICH NORMALLY FLY AT $(L/D)_{MAX} \leq \alpha \leq (C_l)_{MAX}$

FOR BALLISTIC VEHICLES DETERMINE IF VORTICITY EFFECTS ARE IMPORTANT, i.e., $X/r_n > 10$. EXPERIMENTAL PRESSURE DISTRIBUTION NORMALLY REQUIRED FOR GLIDE VEHICLE CONFIGURATIONS

ESTIMATE HEAT TRANSFER (CONVECTIVE) ON BASIS OF EQUILIBRIUM, CONTINUUM FLOW. UTILIZE TURBULENT FLOW RELATIONS FOR CONSERVATIVE THERMAL SHIELD DESIGN (PARTICULARLY FOR GLIDE VEHICLES). EXAMINE BASE HEAT TRANSFER AND EFFECTS OF ANGLE OF ATTACK, LOW DENSITY FLOW

FIGURE 73 - Entry Heat Transfer Flow Chart

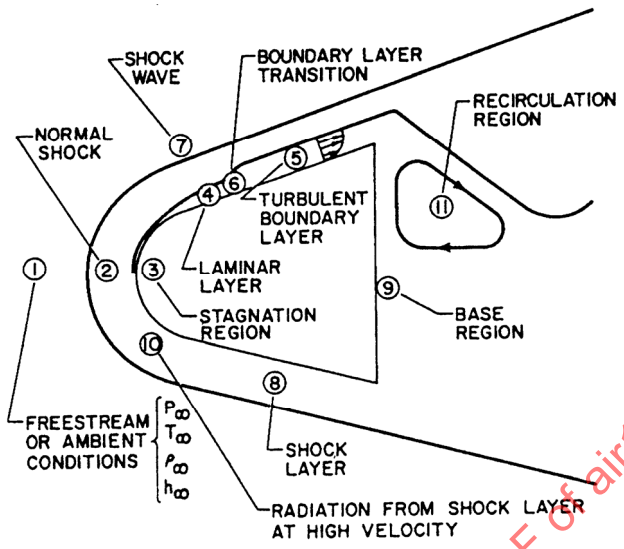

FIGURE 74 - Schematic of Typical Entry System Flow Field Structure and Heat Transfer Regions (Not to Scale)
Note: At the Stagnation Point, Conservation of Energy Gives Complete Conversion of Kinetic Energy to Air and Total Enthalpy:
$h_t = h_\infty + (U_\infty^2/2gJ)$

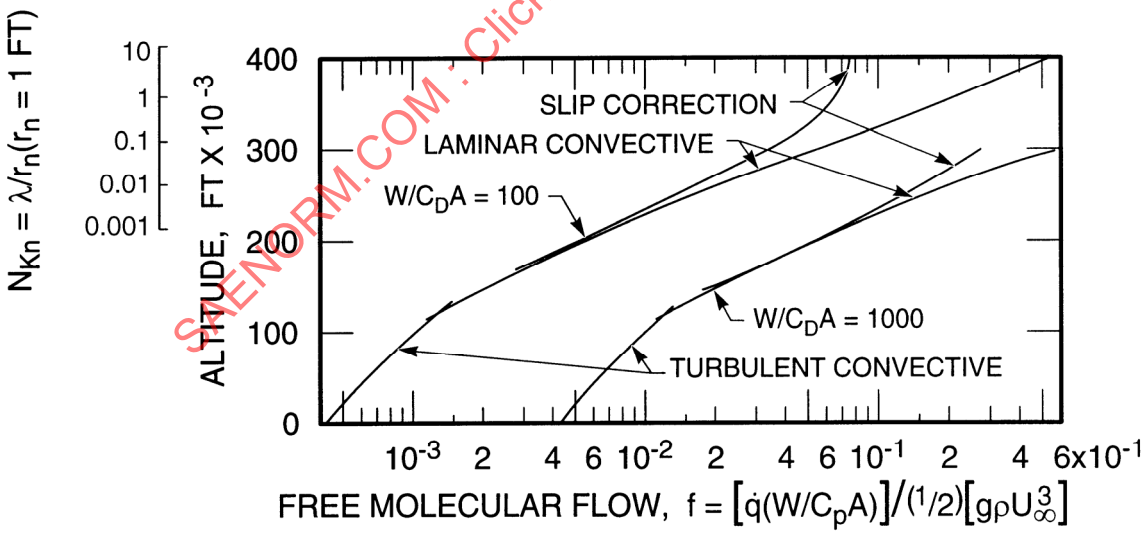

FIGURE 75 - Entry Heat Transfer Flow Regimes

2. ENTRY VEHICLE CHARACTERISTICS:

Ballistic entry vehicles encompass systems utilized for intermediate and intercontinental ballistic missile purposes as well as those utilized for entry satellites. Although widely varying in configuration and size, they are axisymmetric bodies. For more advanced entry spacecraft, such as manned entry vehicles, some lift and range control is obtained by use of an offset center of gravity, which permits the vehicle to fly at an angle of attack. Lift-to-drag ratios on the order of 0.25 to 0.6 may be obtained by such techniques.

The configurations of lifting entry vehicles are normally asymmetric with elliptical or half-cone cross sections. Control is provided by use of combinations of fins and flaps, and in certain cases by fluid injection.

2.1 Ballistic Entry Vehicles:

Representative ballistic configurations and a summary of their design characteristics are presented in Figure 76. For all vehicles, particular attention must be given to the allowable gaps between panels, antenna windows, yield joints, and major heat shield subassemblies.

2.2 Lifting Entry Vehicles:

Representative lifting entry configurations and a summary of their design characteristics are presented in Figure 77. Analysis of the aerothermodynamic environment of lifting vehicles, because of their asymmetric geometry, requires considerable judgment and pieceworking of techniques and methods used for axisymmetric or simple geometry analysis. In many cases, experimental pressure and heat transfer data must be obtained.

3. PROPERTIES OF THE ENTRY ATMOSPHERE:

The size of a planet and the structure and composition of its atmosphere govern the dynamic behavior and flight environment of a planetary entry vehicle. Whereas engineering estimates of the size and physical constants of the major planets are available, the uncertainties in the temperature levels and composition of the atmospheres are significant, even for Earth at higher altitudes. Consequently, any analysis of planetary entry must consider a range of atmospheric parameters. For preliminary design purposes, reference atmospheres are needed to initiate the entry heat transfer analysis. Representative atmospheres are given in Section 2A, AIR1168/9.

The designer should be alert to the need for a wide variation in vehicle design for entry into the atmospheres of the neighboring planets. Representative planet characteristics are given in this section. (Also see Table 3.)

CONFIGURATION		DESIGN CHARACTERISTICS
BLUNT, EARLY GENERATION ENTRY VEHICLE		$100 \leq W/C_DA \leq 150$; AFTERBODY IN SEPARATED FLOW. FOR FOREBODY SEMIVERTEX ANGLES $> 45°$, FLOW OVER FOREBODY IS SUBSONIC; SONIC LINE AT SHORT CYLINDER SECTION CORNER. CONFIGURATIONS COMPARATIVELY INSENSITVE TO ANGLE OF ATTACK EFFECTS (HEATING)
ADVANCED ENTRY VEHICLES	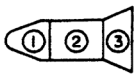	$500 \leq W/C_DA \leq 1500$, NEWTONIAN IMPACT THEORY NORMALLY ADEQUATE FOR SECTION (1) PRESSURE DISTRIBUTION. FLOW FIELD CHARACTERISTICS SOLUTIONS FOR PRESSURES ON (2) PRESSURE ON (3) OBTAINED FROM REF. 14. WEDGE AND CONE COMPRESSION AT LEADING AND TRAILING EDGE OF (3). BOUNDARY LAYER EDGE PROPERTIES AT TRAILING EDGE OF (2) REQUIRED FOR EXPANSION. ASSUMPTION OF ISENTROPIC FLOW FOR BOUNDARY LAYER PROPERTY DETERMINATION ADEQUATE. SECTION (3) FLARE ANGLE SHOULD BE $\sim 24°$ OR LESS TO AVOID BOUNDARY LAYER SEPARATION
	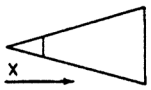	$1000 \leq W/C_DA \leq 10{,}000$; CONICAL FLOW PRESSURE AND HEAT TRANSFER RELATIONS ADEQUATE FOR $X/r_n > 40$. ASSUMPTION OF ISENTROPIC FLOW ADEQUATE ONLY FOR $0 \leq X/r_n \leq 10$–15. ENTROPY GRADIENT EFFECTS ANALYSIS REQUIRED IN INTERMEDIATE REGION. STRONG ANGLE OF ATTACK HEAT TRANSFER EFFECTS
ENTRY SATELLITE OR BALLISTIC ENTRY VEHICLE	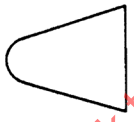	60–$100 \leq W/C_DA \leq 500$–700. LOWER VALUES FOR ENTRY SATELLITE. BLUNT BODY, ISENTROPIC EXPANSION ADEQUATE. ANGLE OF ATTACK EFFECTS SHOULD ALSO BE CONSIDERED. FOR LARGE NOSE RADII, SHOCK LAYER THERMAL RADIATION SHOULD BE CONSIDERED
TYPICAL MANNED VEHICLE CONFIGURATION		$50 \leq W/C_DA \leq 100$; AT SUPERORBITAL VELOCITIES RADIATIVE HEAT TRANSFER MUST BE EVALUATED. FOREBODY IN SUBSONIC FLOW. AFTERBODY NORMALLY DESIGNED FOR SEPARATION EXCEPT WHEN FLOWN AT ANGLE OF ATTACK

FIGURE 76 - Representative Ballistic Entry Configurations

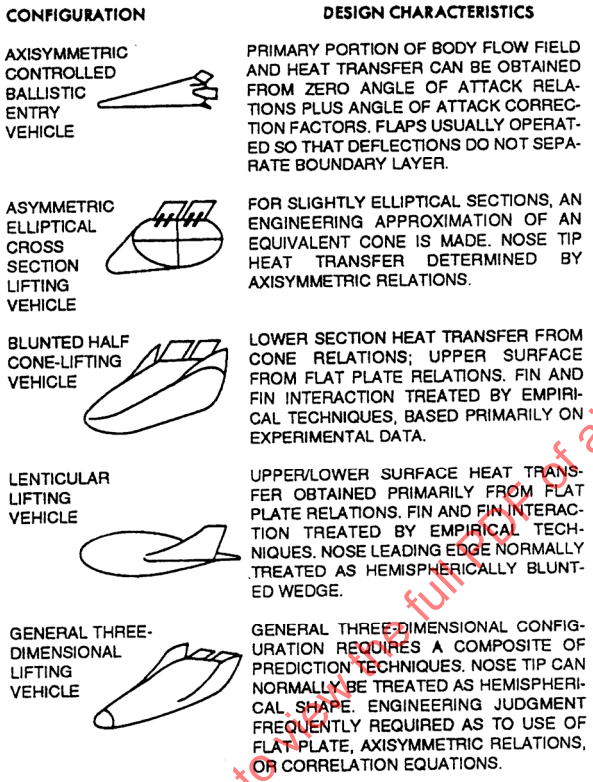

FIGURE 77 - Representative Lifting Entry Configurations

TABLE 3 - Reference Atmospheric Constants

Parameter	Earth	Mars	Venus
Sea Level Temperature, K	288	240	600
Stratosphere Temperature, K	240	190	250
Troposphere Temperature Gradient, K/ft	-1.66×10^{-3}	-1.17×10^{-3}	-2.62×10^{-3}
Thermosphere Temperature Gradient, K/ft	0.37×10^{-2}	0.155×10^{-2}	0.74×10^{-2}
Height of Stratosphere, ft	3×10^{5}	3×10^{5}	2×10^{5}
Composition	$0.79N_2$ $0.21O_2$	$0.98N_2$ $0.02CO_2$	$0.85N_2$ $0.15CO_2$
Sea Level Density, lb/ft^3	0.0762	0.00644	0.306
Acceleration of Gravity, ft/s^2	32.17	12.5	27.6
Radius of Planet, ft	20.98×10^{6}	11.1×10^{6}	20.0×10^{6}

3.1 Earth:

A scale height of 23,500 ft has been successfully used for approximate analyses of lifting and ballistic Earth entries. This scale height corresponds to a stratosphere temperature of 240 K. The resultant temperature profile for Earth is shown in Section 2A, AIR1168/9. Standard sea level conditions are assumed, and the density variation with altitude is found by hydrostatic equilibrium considerations.

For atmosphere entry predictions (400,000 ft and below), the ARDC 1962 atmosphere is recommended for design purposes. For higher altitudes, the density, pressure, and temperature variations presented in Figures 78 to 80 are suggested for preliminary design.

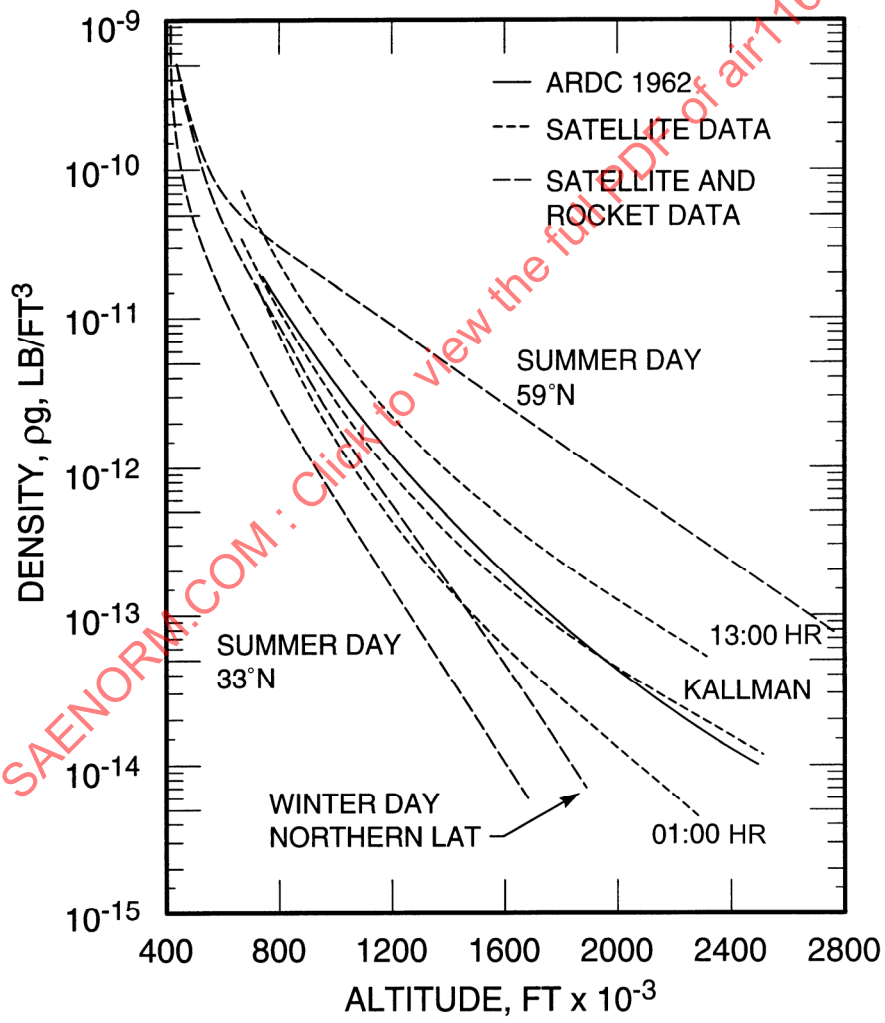

FIGURE 78 - Density Variation with Altitude

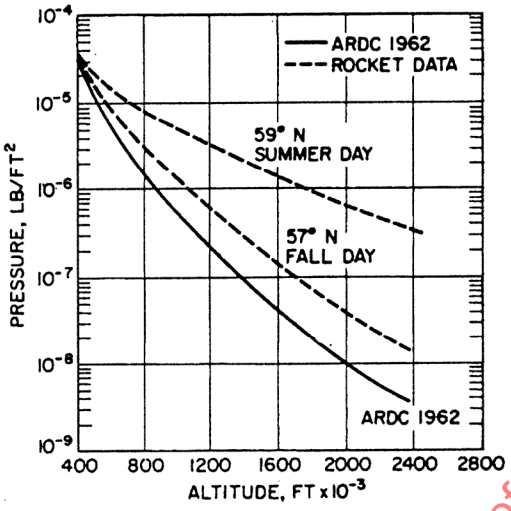

FIGURE 79 - Pressure Variation with Altitude

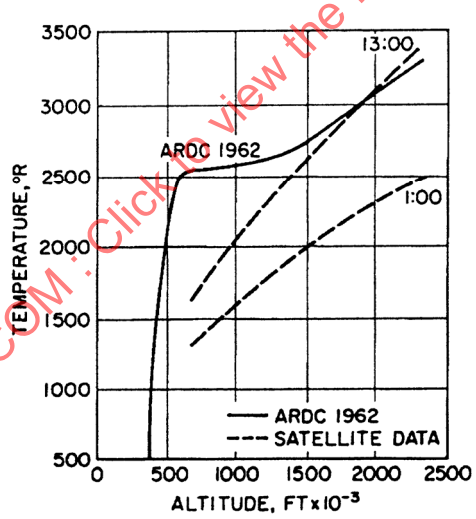

FIGURE 80 - Temperature Variation with Altitude

3.2 Venus, Mars:

"Standard" and extreme model atmospheres of the planets Venus and Mars have been calculated and presented by NASA. Pressure, temperature, and density are given as functions of height. The models are to be considered as preliminary.

4. ENTRY TRAJECTORY CHARACTERISTICS:

Typical ballistic and lifting entry vehicle trajectory characteristics were presented in Paragraph 1. However, the designer should be cognizant of the effect of entry with angle of attack oscillations and (simultaneously with angle of attack motion) varied spin rates which result in an elliptical or conning motion.

4.1 Ballistic:

In the absence of roll control systems or other specific methods of active entry vehicle position control prior to and during atmospheric flight, the angle of attack amplitude and frequency on aerodynamic heating rate and total aerodynamic heating load must be considered. Typical curves of angle of attack and frequency are shown in Figures 81 and 82. It should be noted that the angle of attack is normally minimal (and frequency greatest) at peak dynamic pressure.

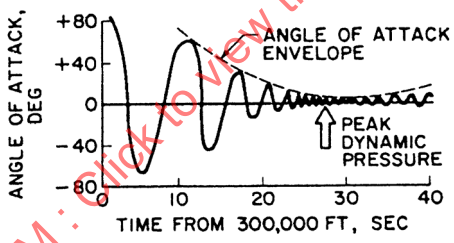

FIGURE 81 - Entry Vehicle Angle of Attack Characteristics

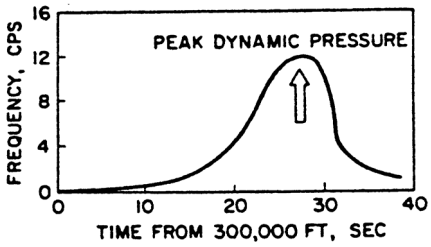

FIGURE 82 - Entry Angle of Attack Frequency

The comparison of the summer-day rocket flights at 59° N and 33° N indicates that the warmer and more dense atmosphere is found at higher latitudes, since during the summer the solar photon and corpuscular radiations heat the upper atmosphere 24 h each day.

4.1 (Continued):

At an altitude of 722,000 ft the density of the atmosphere is equal to 1.3 to 3.1 x 10^{-11} lb/ft^3. By changing the period of revolution of the Sputniks around the Earth, and by changing the position of the perigee, it was found that the density of the atmosphere at this altitude was greater in the day than at night and greater in the polar than in the equatorial regions, which agrees with La Gow.

The satellite results do not show the strong latitude dependence which appears in the rocket data. Satellite measurements always give the density at the position of perigee, and a satellite therefore automatically samples a broad range of latitudes during the course of the rotation of its perigee in the plane of the orbit. Rocket pressure data from the Fort Churchill firings have been analyzed for summer and fall days, up to an altitude of 660,000 ft.

Day-night variations of temperature have been compared to the ARDC Standard and are shown in Figure 80. Unlike the density data, which compare rather favorably, the day-night effects are lower than ARDC, though the temperature values were calculated from the density. According to Priester, there is relative uncertainty about the validity of the temperature values because of insufficient knowledge of the molecular weight.

4.2 Lifting Entry Vehicle Trajectory Characteristics:

Although lifting vehicle entry characteristics are frequently estimated on the basis of equilibrium glide paths (see Paragraph 1) for which a constant L/D is assumed (and a specific angle of attack), practical entry path management considerations may require a wide variation in the angle of attack. (See Figure 83.)

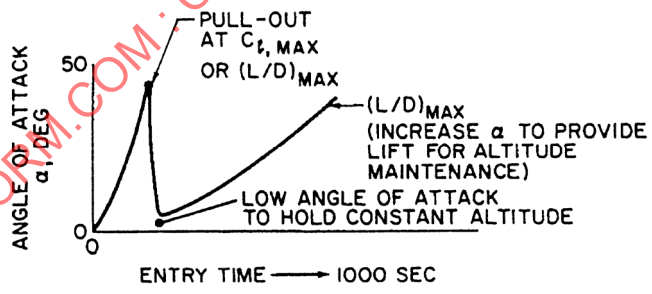

FIGURE 83 - Lifting Entry Angle of Attack Modulation (Pull Out and Constant Altitude Flight)

The designer is cautioned to examine the mission and configuration to ensure that upper surface heat transfer rates are compatible with the heat protection system material selection.

5. ENTRY VEHICLE FLOW FIELD CHARACTERISTICS:

A requirement for entry vehicle aerodynamic and thermodynamic design is entry vehicle static pressure level and distribution and flow field gas state property information. For aerodynamic design these quantities are needed for predicting vehicle pressure loads as well as force and moment characteristics. Within the past 10 years, numerical solutions have been developed for predicting the aerodynamic flow field about sharp and blunt nosed axisymmetric entry vehicles at zero and small angles of attack, and about sharp and blunted wedges. Similar development efforts have been under way for general three-dimensional flow fields.

Results from the numerical solution of the flow field have been used extensively in the aerothermodynamic design of entry vehicles. In the process of predicting surface pressures and pressure distributions, the flow field technique generates the entire inviscid shock layer structure, including the thermodynamic quantities, temperature, and density. This permits the determination of gas composition throughout the shock layer and the resulting gas radiation once the gas emissive and absorptive characteristics are known. From the pressure distribution alone the flow properties at the upper edge of the boundary layer, velocity, density and temperature, and subsequently the aerodynamic heating analyses and viscous drag can be determined. The flow field shock geometry information also provides a means for including vorticity effects on the viscous heating and skin friction and indicates regions of shock-wave/control-surface interaction.

The numerical techniques available are primarily those which solve the equations of motion for steady flow of an inviscid, nonheat-conducting, compressible gas in chemical equilibrium at hypersonic speeds. In order to solve these equations for the blunt body problem, it is usually necessary to consider the shock layers as being divided into a subsonic region at the nose of the body and a supersonic region downstream from the sonic line. The mixed flow field is separated in this way because the mathematical nature of the basic equations are different in each region; in the subsonic region they are of the elliptic type and in the supersonic region they are of the hyperbolic type.

Stable numerical solutions of the hyperbolic equations may be obtained by the method of characteristics, which requires only the specification of initial conditions along a boundary in the supersonic flow field and the given body shape. A solution of the elliptic equations is more difficult to obtain because numerical processes in the subsonic region are unstable unless conditions are specified around a complete boundary. In practice, only the freestream conditions and the body shape are known for the blunt body problem. Consequently, most investigators have utilized forward integration techniques which are numerically suitable in the subsonic region. For a detailed review of numerical solutions of the entry flow field problem, refer to Reference 6.

The purpose of this section is to present to the designer a series of approximate methods and charts summarizing results from exact numerical solutions so that rapid estimates of the pressure and pressure distribution and flow field properties may be made. Body surface pressure and shock shapes are emphasized.

5.1 Equilibrium Air Properties:

The development of entry vehicle flow field and pressure distribution, as well as the analysis of aerodynamic heat transfer characteristics of an entry system exposed to a high-temperature gas environment, requires a set of high-temperature gas state properties, including air density, temperature as a function of entropy, enthalpy, or pressure. Extensive tables and charts of the properties of air in thermochemical equilibrium are available (References 7 and 8). A summary of these air properties are given in Figures 84 through 92 for temperatures associated with flight velocities up to and including orbital velocity. From the references cited above, similar curves may be prepared for velocities greater than orbital velocity; for precise calculations, the designer should always resort to the detailed tables and charts. Normally, the two most readily determined state properties are pressure and enthalpy. Once these are determined, the remainder of the air properties can be obtained by reference to the charts or to the referenced tables. The determination of pressure and enthalpy is given in the subsequent sections. Although air properties are normally presented as equilibrium values (Figures 84 through 92), the dynamic and chemical phenomena resulting from high-speed flow frequently result in conditions of nonequilibrium.

Chemical nonequilibrium occurs when finite time is required for the chemical reactions in the gas to take place following large changes in energy levels, as when passing through a strong shock wave. At low flight velocities the chemical reactions are considered instantaneous and the gas is in “chemical equilibrium.” As satellite velocities are approached, the time required for the chemical reaction relaxation time becomes appreciable; in fact, the gas may pass through the shock wave and over the nose without chemical reaction occurring. This flow condition is termed “chemically frozen” (Reference 9). Qualitatively,

Chemical Equilibrium:

$$\frac{\text{Chemical relaxation time}}{\text{Characteristic flow time}} << 1 \qquad \text{(Eq.127)}$$

Chemically Frozen:

$$\frac{\text{Chemical relaxation time}}{\text{Characteristic flow time}} >> 1 \qquad \text{(Eq.128)}$$

For relaxation a particle passing through a shock front requires several collisions before the various forms of energy are excited. The approximate number of atomic collisions required for the various modes is shown in Table 4.

Although the exact number of collisions required to complete dissociation and recombination is still undetermined, the number may be several times greater than indicated above. The time required for the collisions to occur increases with decreasing number density. Thus at high altitudes the relaxation times become appreciable when compared with the large flight velocities, and nonequilibrium flow conditions can exist.

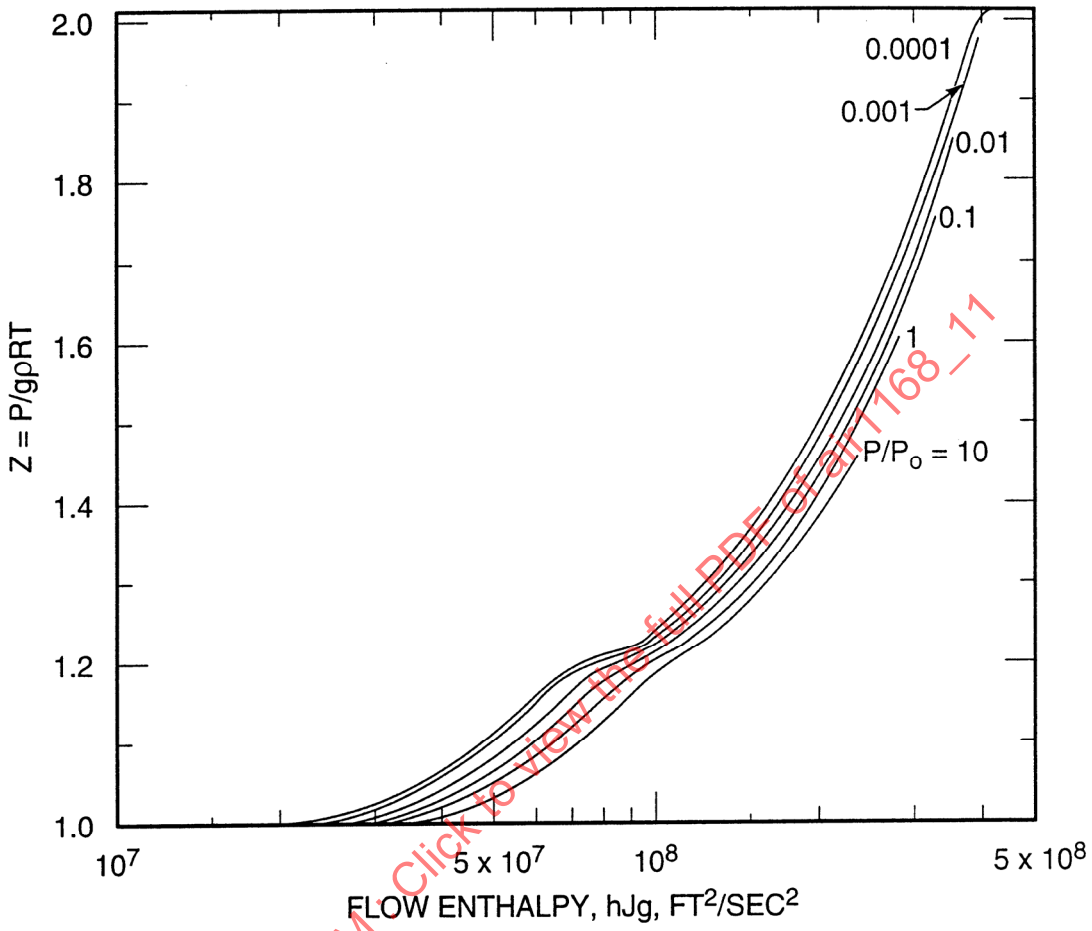

FIGURE 84 - Characteristics of Real Gases as a Function of Flow Enthalpy for Various Pressure Ratios; Compressibility Factor Z

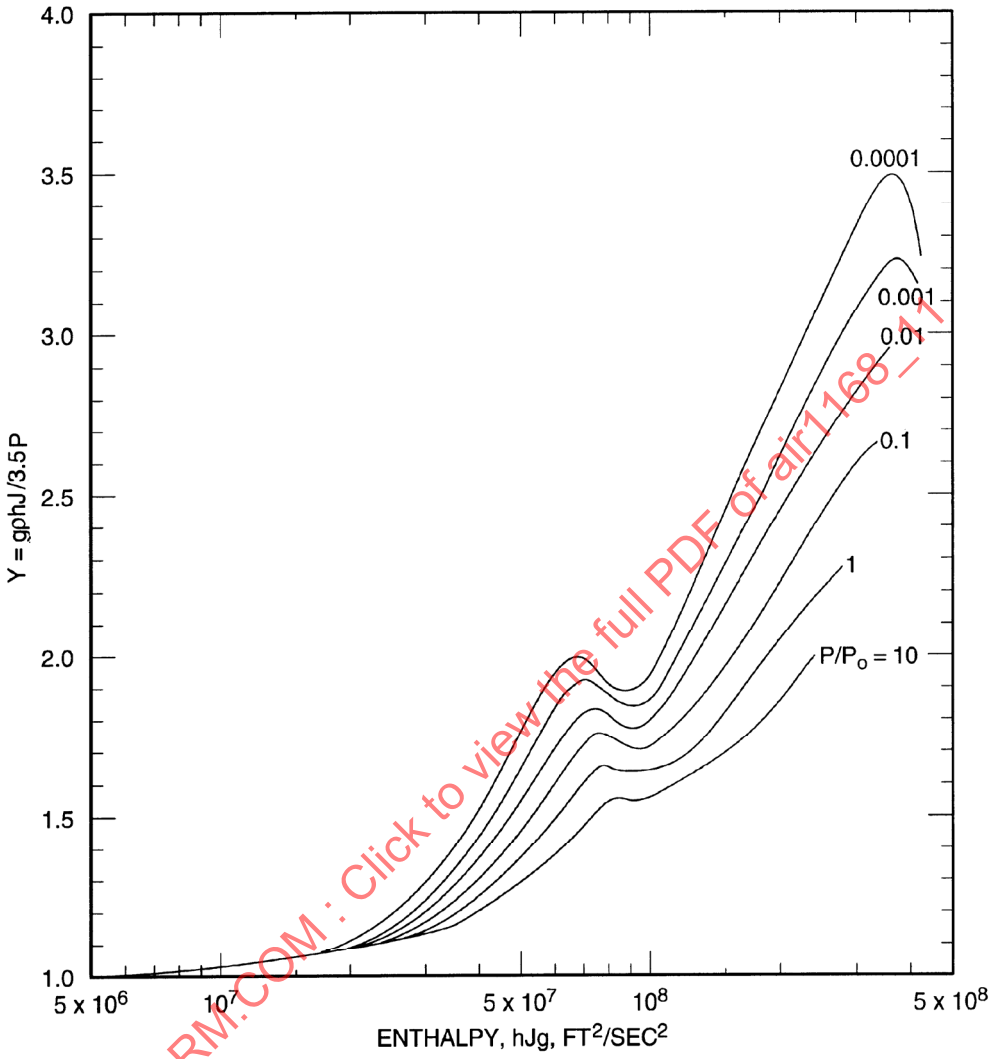

FIGURE 85 - Characteristics of Real Gases as a Function of Flow Enthalpy for Various Pressure Ratios; Compressibility Factor Y

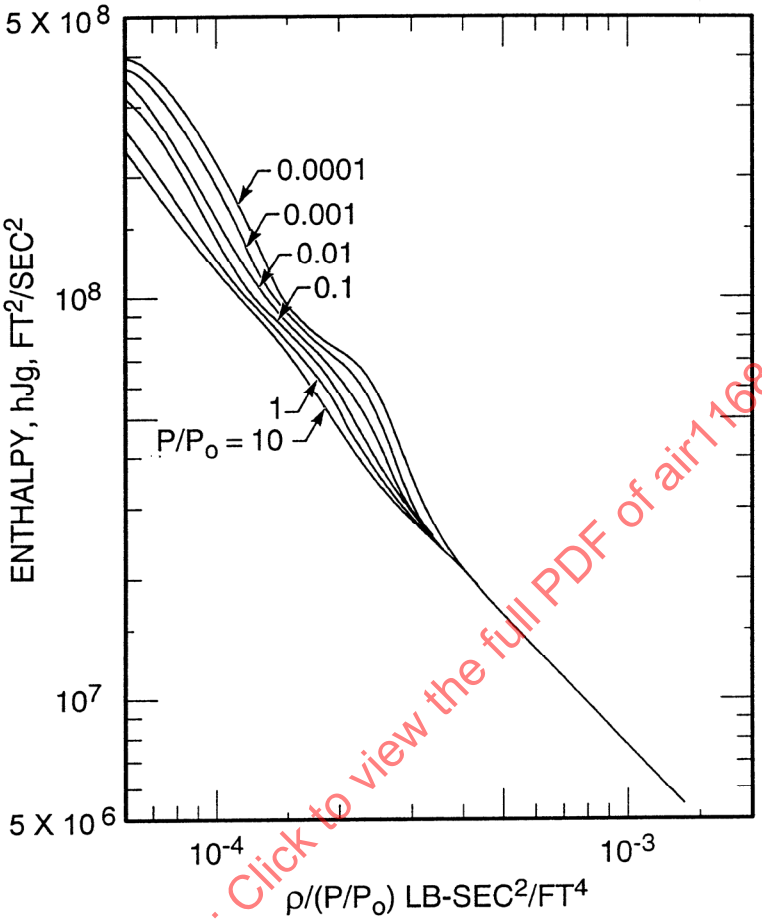

FIGURE 86 - Characteristics of Real Gases as a Function of Flow for Various Pressure Ratios; Density

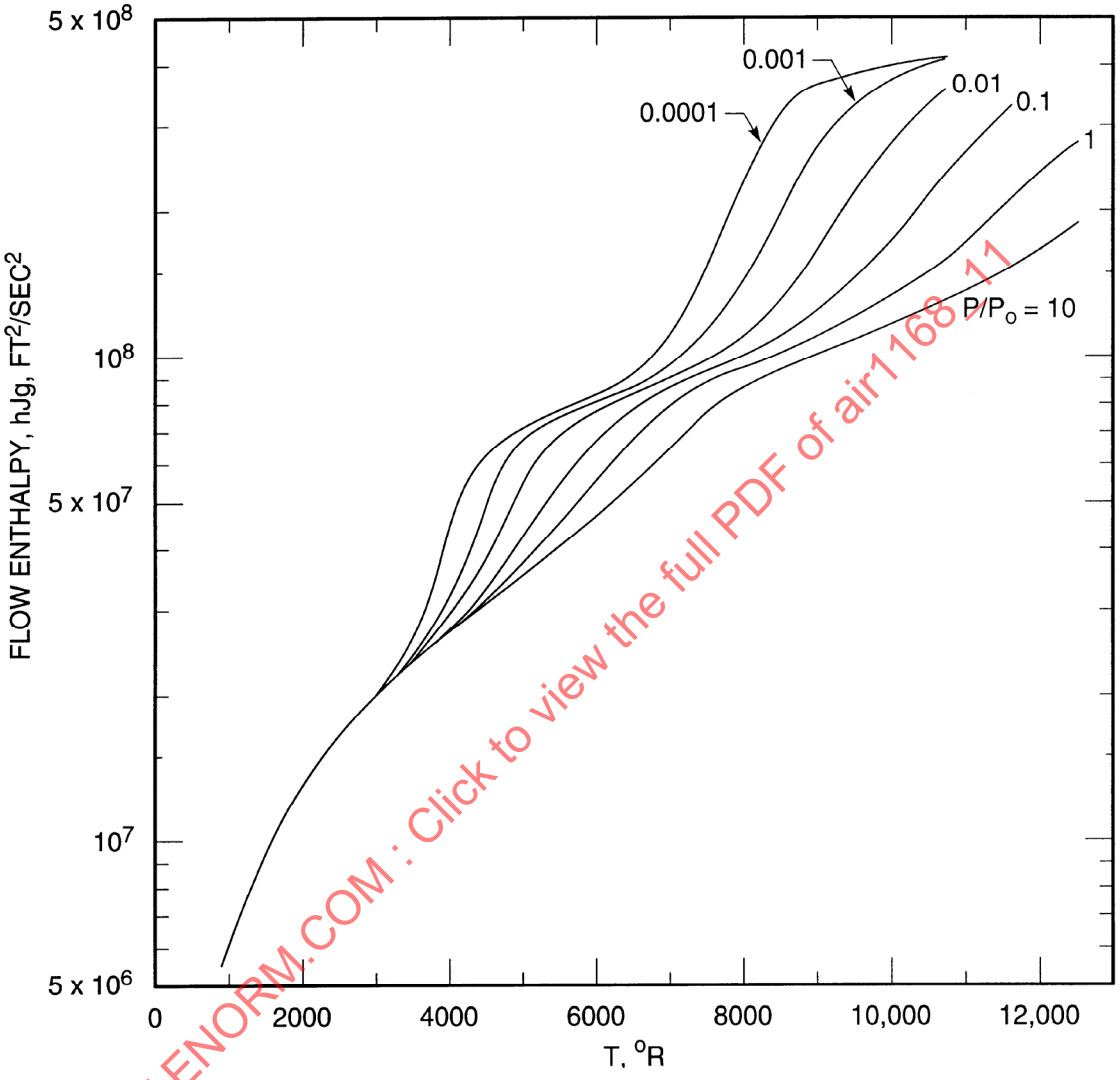

FIGURE 87 - Characteristics of Real Gases as a Function of Flow Enthalpy for Various Pressure Ratios; Temperature

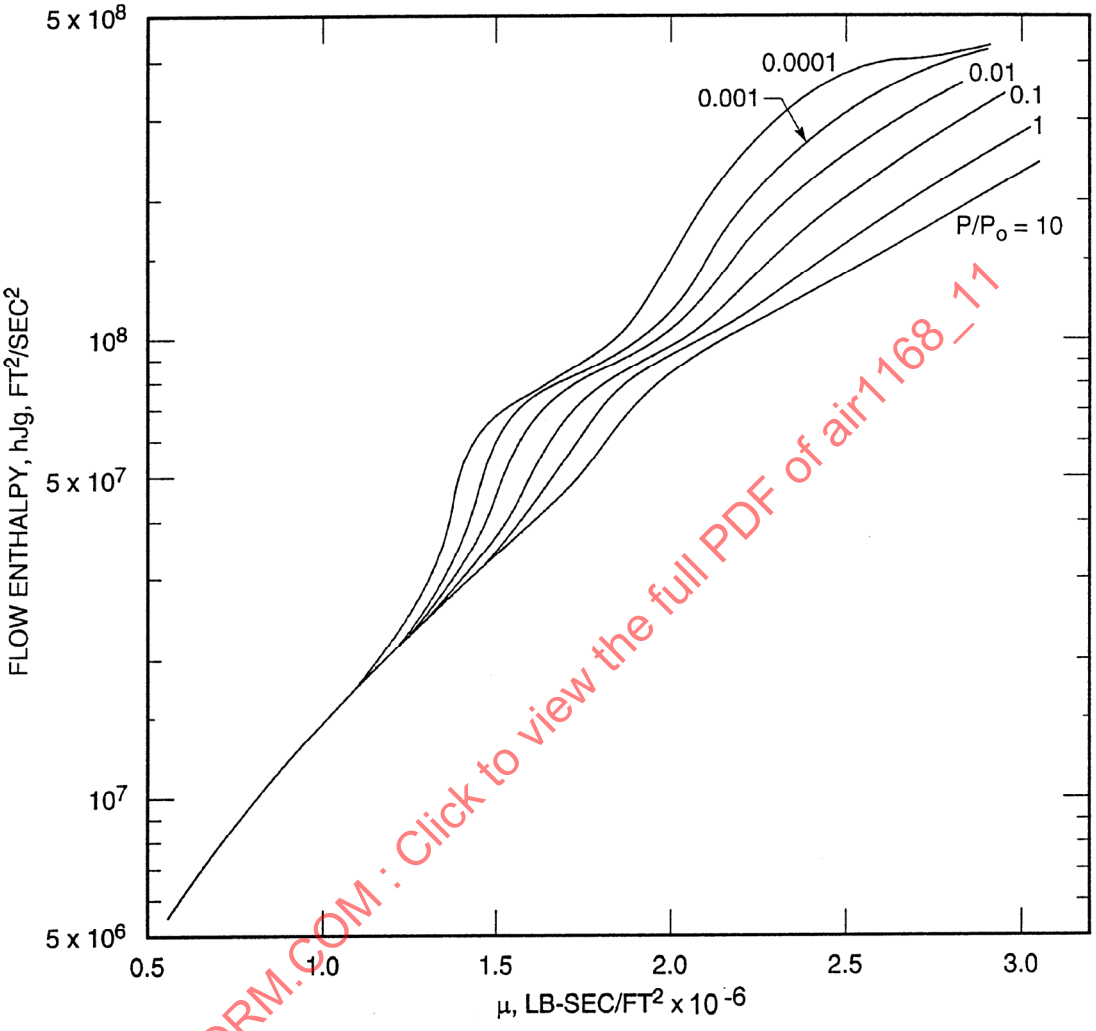

FIGURE 88 - Characteristics of Real Gases as a Function of Flow Enthalpy for Various Pressure Ratios; Viscosity

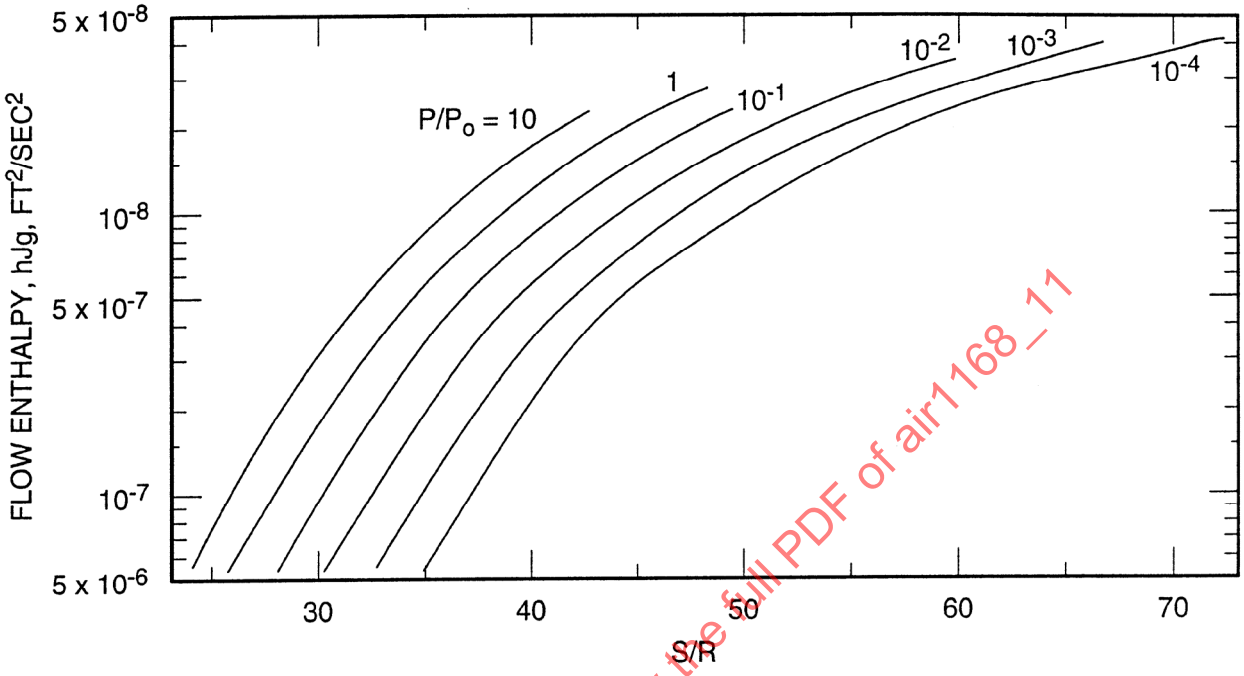

FIGURE 89 - Characteristics of Real Gases as a Function of Flow Enthalpy for Various Pressure Ratios; Entropy, Where S, R Have the Units of Btu/mole-°R

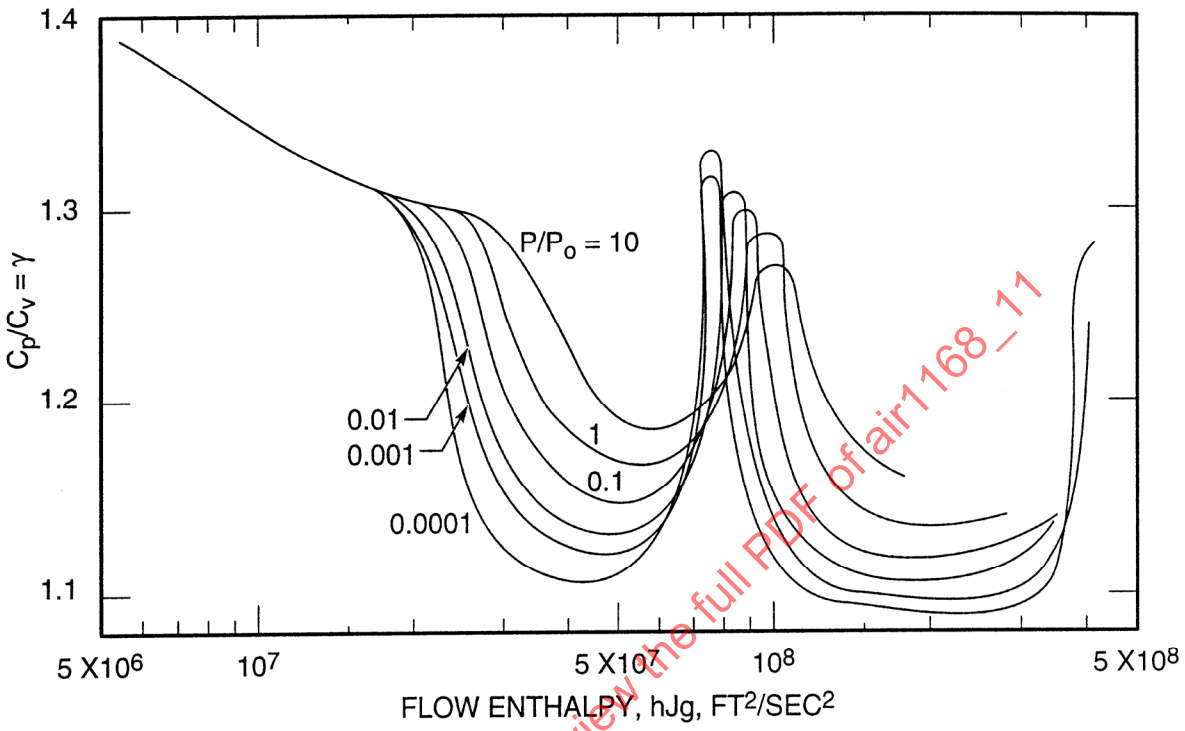

FIGURE 90 - Characteristics of Real Gases as a Function of Flow Enthalpy for Various Pressure Ratios; Effective Ratio of Specific Heats

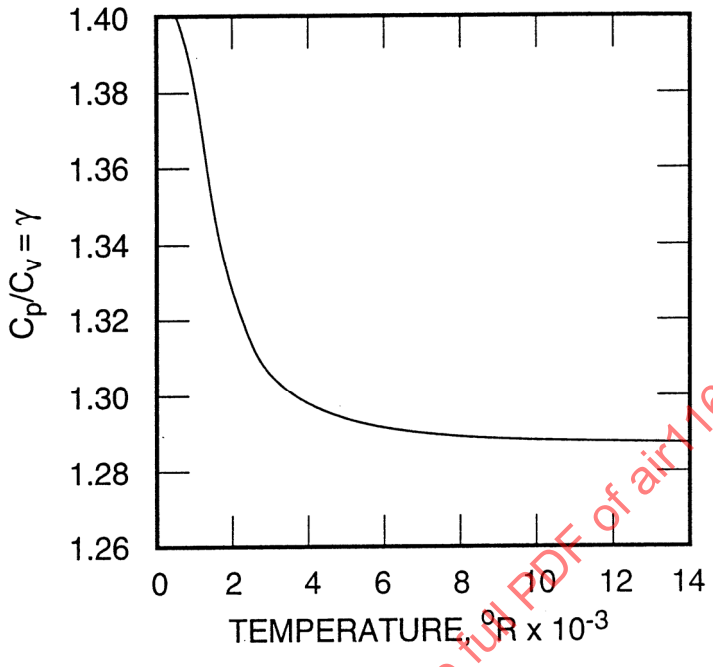

FIGURE 91 - Characteristics of Thermally Perfect Gases; Variation of Ratio of Specific Heats with Temperature

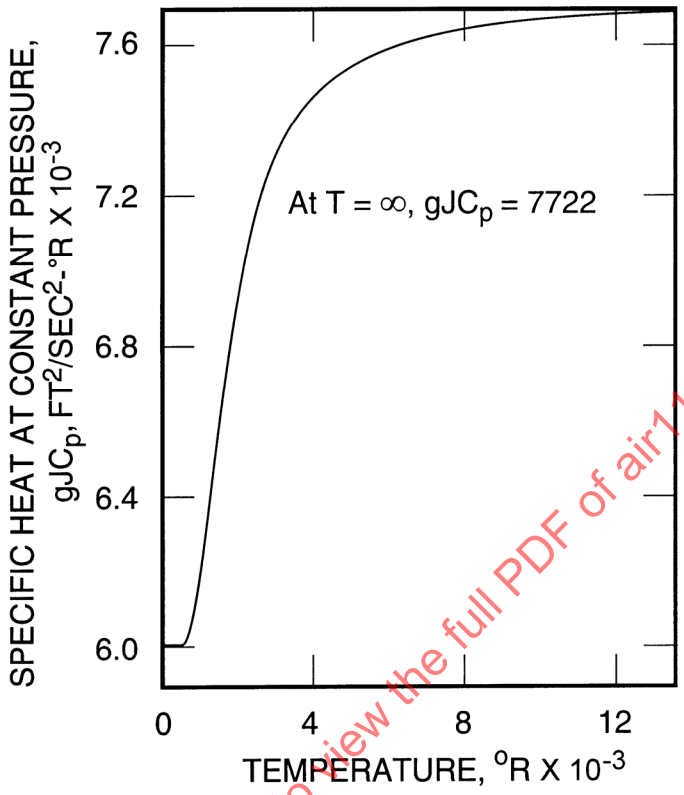

FIGURE 92 - Characteristics of Thermally Perfect Gases; Variation of Specific Heat at Constant Pressure with Temperature

TABLE 4 - Atomic Collisions Per Mode

Mode	Collisions
Translation	2
Rotation	>10
Vibration	10^5

5.2 Normal Shock Relations:

By use of the air properties presented in the previous section, the conditions of pressure, density, and temperature change across a normal shock may be computed. Further, the total conditions existing at the stagnation point of an entry system may be readily evaluated and are normally the most useful quantities for aerodynamic heat transfer purposes. Representative curves of pressure, temperature, and density change across a normal shock are given in Figures 93 to 97. From these curves and the air properties presented in Figures 84 to 92, the stagnation flow conditions may be readily determined. For convenience, the stagnation point pressure may be obtained from the following correlations of the Rankine-Hugoniot normal shock relations as

$$\frac{P_t}{P_\infty} = (1 + 0.2M_\infty^2)^{3.5} \qquad (M_\infty < 1) \qquad \text{(Eq.129)}$$

$$\frac{P_t}{P_\infty} = (1.2M_\infty^2)^{3.5}\left(\frac{6}{7M_\infty^2 - 1}\right)^{2.5} \qquad (1 \le M_\infty \le 5) \qquad \text{(Eq.130)}$$

$$\frac{P_t}{P_\infty} = 1.155M_\infty^{2.075} \qquad (5 \le M_\infty \le 8) \qquad \text{(Eq.131)}$$

$$\frac{P_t}{P_\infty} = 1.35M_\infty^2 \qquad (8 \le M_\infty \le \infty) \qquad \text{(Eq.132)}$$

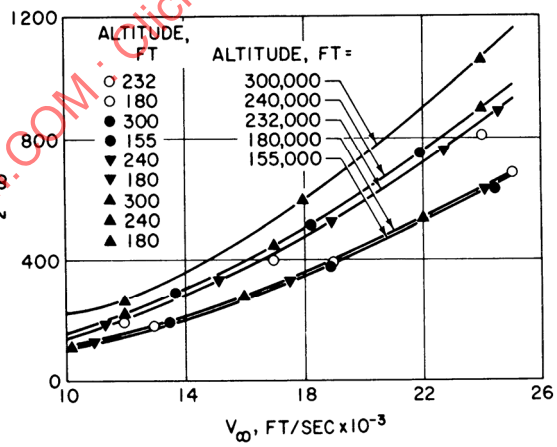

FIGURE 93 - Normal Shock Wave-to-Freestream
Pressure Ratio Versus Flight Speed for Constant Altitude

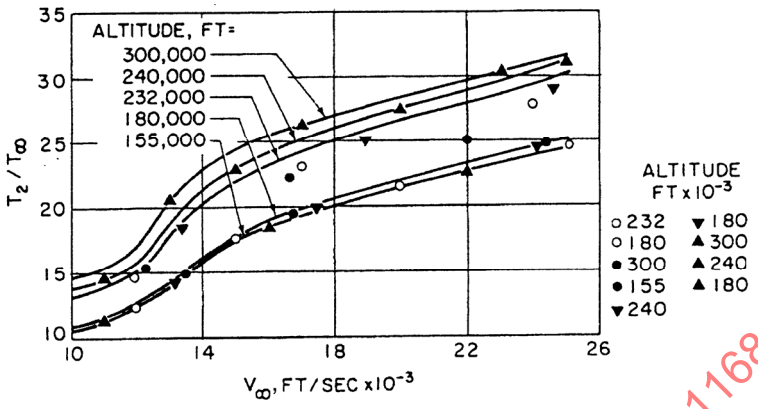

FIGURE 94 - Normal Shock Wave-to-Freestream Temperature Ratio Versus Flight Speed for Constant Altitude

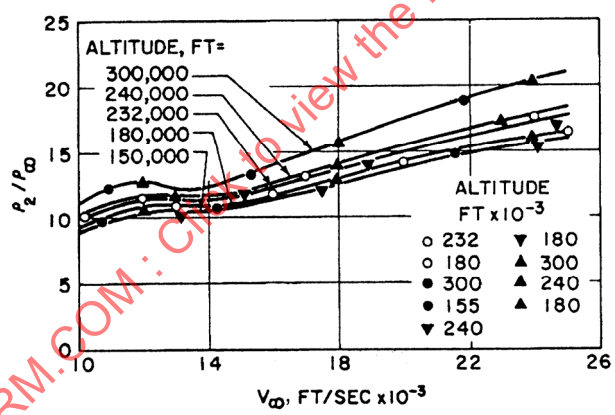

FIGURE 95 - Normal Shock Wave-to-Freestream Density Ratio Versus Flight Speed for Constant Altitude

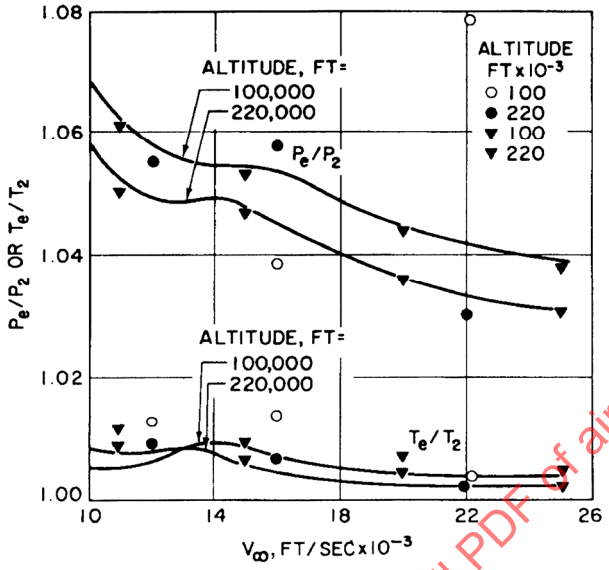

FIGURE 96 - Stagnation-to-Normal Shock Wave Pressure and Temperature Ratios Versus Flight Speed for Constant Altitude

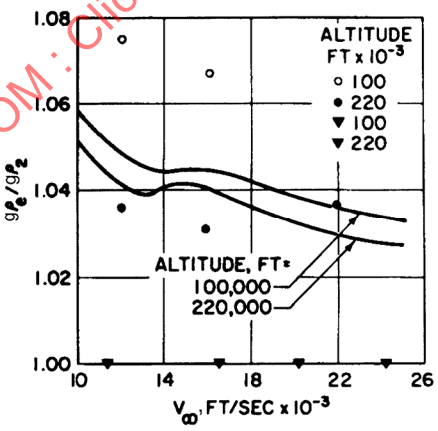

FIGURE 97 - Stagnation-to-Normal Shock Wave Density Ratio Versus Flight Speed for Constant Altitude

5.2 (Continued):

Total enthalpy is conserved; consequently,

$$h = h_\infty + \frac{U_\infty^2}{2gJ} \qquad \text{(Eq.133)}$$

Similar pressure ratio curves are available for oblique shocks. A curve of speed of sound is given in Figure 98 for convenience in computing Mach number.

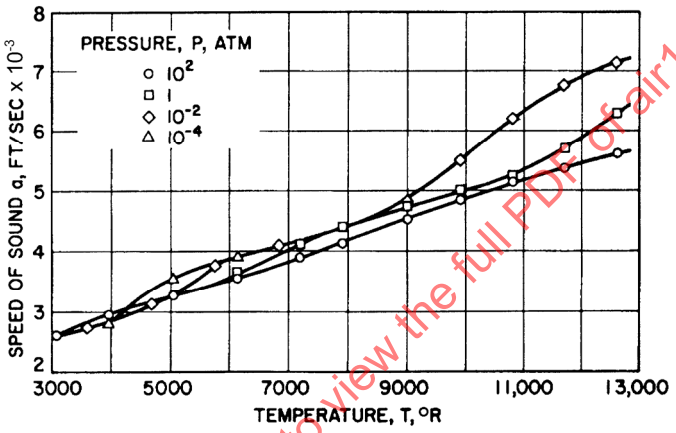

FIGURE 98 - Speed of Sound in Air Versus Temperature

5.3 Surface Pressure Distributions:

As the initial step in the determination of the shock layer characteristics, the pressures at the inner boundary, the centerbody surface, must be determined.

The pressure distributions for the spherical portion of the sphere-cone configuration may be approximated reasonably well by modified Newtonian theory plus a Prandtl-Meyer expansion. Far downstream, the pressure approaches the pointed cone value predicted by the Taylor-Maccoll theory or by the theory of Chernyi; however, in the vicinity of the sphere-cone junction, none of the simple methods (such as the modified Newtonian or blast wave theory) gives satisfactory predictions of the inviscid pressure distributions over a large range of cone angles and free-stream conditions. For the limiting case of a hemispherical nose tip followed by a cone of semivortex angle greater than 20 deg, Newtonian theory gives a good approximation to the pressure and pressure distribution.

5.3.1 Newtonian and Modified Newtonian Theory: Newtonian theory gives the pressure coefficient on the surface of a body as

$$C_P = 2 \sin^2 \theta \qquad \text{(Eq.134)}$$

where:

θ = Body surface angle

This relation is obtained from compressible flow theory for the limits $M \rightarrow \infty$ and $\gamma \rightarrow 1$ and by neglect of the centrifugal effect of the flow about the body. In Newtonian theory the shock wave is assumed to coincide with the body surface, and consequently there is an infinitesimally thin layer of fluid of infinite density following the contours of the body surface; the centrifugal effect of this flow must be taken into account.

Modified Newtonian theory replaces Equation 134 by

$$\frac{C_P}{C_{P,max}} = \sin^2 \theta \qquad \text{(Eq.135)}$$

where:

$C_{P,max} = 4\gamma/(\gamma+1)$

Equation 135 is the pressure coefficient ratio immediately behind a shock wave of shock angle θ_s for $M \rightarrow \infty$. Since γ is not unity, this shock wave does not coincide with the body surface and the actual shock angle is not equal to the body angle θ. Therefore, modified Newtonian theory approximates the shock angle by the body angle and assumes that the pressure on the body surface is equal to that immediately behind the shock, thereby assuming that there is no velocity component perpendicular to the body surface, as well as neglecting the centrifugal effect.

Newtonian theory may also be written in the following form, which is more practical for aerothermodynamic design use.

$$\frac{P_w}{P_t} = \sin^2 \theta + \cos^2 \left(\frac{P_\infty}{P_t} \right) \qquad \text{(Eq.136)}$$

where:

P_∞ represents the freestream atmospheric pressure

5.3.2 Prandtl-Meyer Theory: Newtonian theory is inaccurate at local surface angles less than 20 deg. For surface angles less than 20 deg, Prandtl-Meyer expansion is recommended where the expansion is begun at the sonic line (θ = 45 deg) to the local surface angle. The local pressure ratio may be found by use of Reference 14.

5.3.3 Pure and Blunted Cone Theory and Methods: A correlation of available equilibrium real gas inviscid surface pressures and shock wave angles for pointed cones at hypersonic speeds is presented in Figures 99 and 100. These results are compared with theoretical results (Reference 10) for perfect gas conditions (γ = 1.405). The differences due to the type of gas, real or ideal, for air in chemical equilibrium are small.

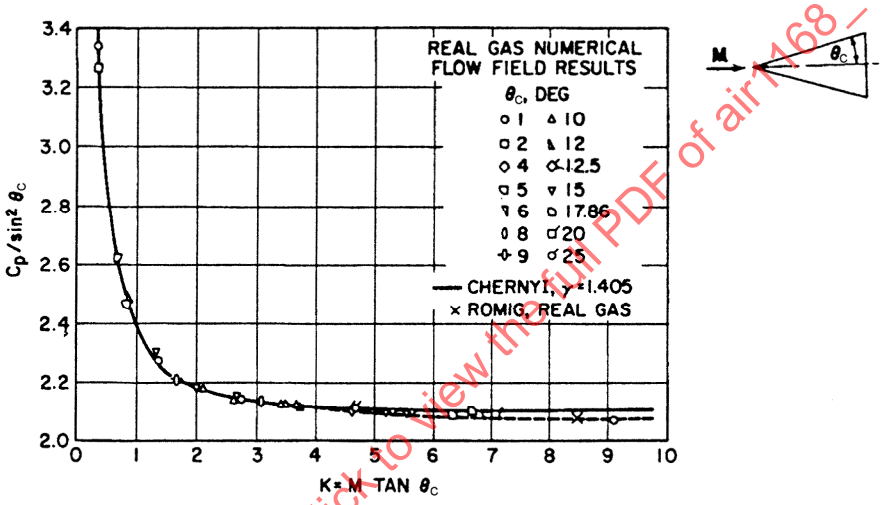

FIGURE 99 - Hypersonic Similarity Correlation of Surface Pressure for Pointed Cones

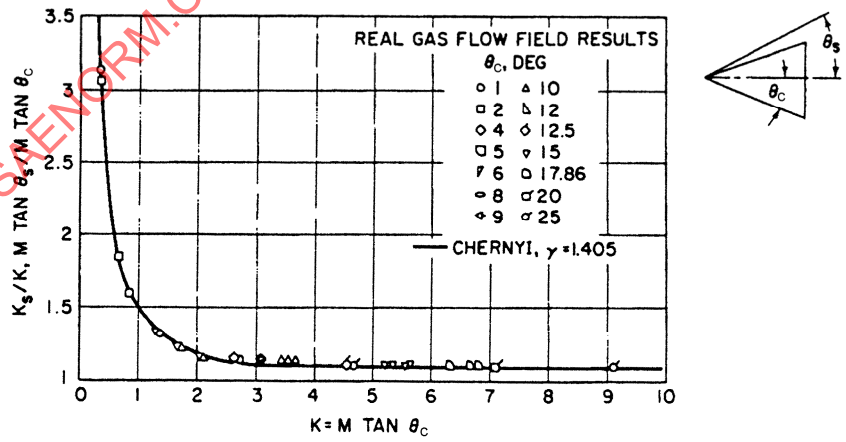

FIGURE 100 - Hypersonic Similarity Correlation of Shock Wave Angle for Pointed Cones

5.3.3 (Continued):

Figure 99 shows the pressure coefficients for real gas conditions on pointed cones with different apex angles θ_c and at different Mach numbers M plotted as a function of the hypersonic similarity parameter K = M (tan θ_c). The data shown were obtained from the exact solution for flow past a right circular cone (Reference 11) and the solid curve is the result of the numerical solutions obtained using the equivalence principle for perfect gas (γ = 1.405), given in Reference 10. For values of K ≥ 3, the real gas effects upon the pressure coefficients are small, and for K ≤ 3, real and ideal gas values are nearly identical. The differences at large values of K were cross checked by comparison to calculations for real gas conical flow (Reference 12). These are in good agreement as shown in Figure 99.

The correlation of shock wave parameter K is shown in Figure 100. The solid curve in this figure corresponds to the dependence found using the equivalence principle for perfect gas (γ = 1.405). This dependence is well approximated by the following relation:

$$\frac{K_s}{K} = \frac{\gamma + 1}{2} + \frac{1}{K^2} \qquad \text{(Eq.137)}$$

where:

K_s = M tan θ_s
K = M tan θ_c
θ_s = Shock angle measured relative to the cone axis

To provide design information for the effect of nose bluntness and entropy gradient on local pressure distribution, the local pressure on the cone surface is normalized by the theoretical pointed cone value, and the longitudinal coordinate is stretched by the ratio of the densities for real to ideal gas properties in the shock layer at the nose of the body. An example is shown in Figure 101 for a 9 deg sphere cone over a wide range of Mach numbers and altitudes. The abscissa is expressed in terms of the effective gamma approximation to the density behind the normal shock multiplied by the axial station, x/r_n, minus the value at the sphere cone tangency point, x_T/r_n. Using correlations of the type shown in Figure 101, median correlation curves are obtained which can be used for design purposes. These correlations for Mach numbers greater than 10 are presented in Figure 102. Additional pressure distributions, suitable for design purposes, are given in Figure 103.

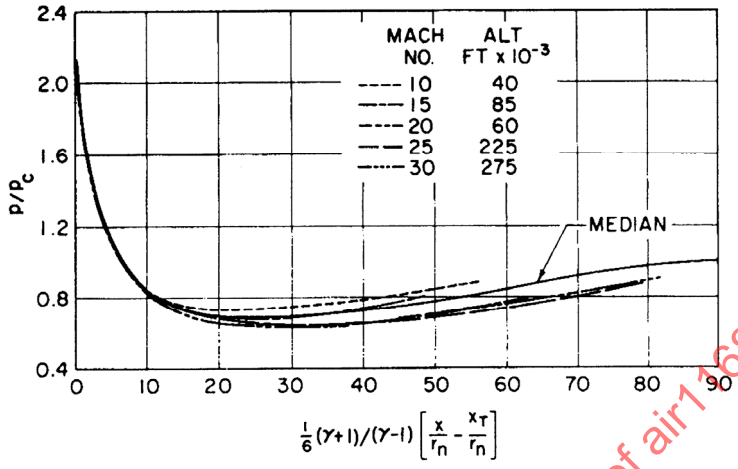

FIGURE 101 - Examples of Pressure Correlation, Flow Fields, 9 deg Sphere Cone

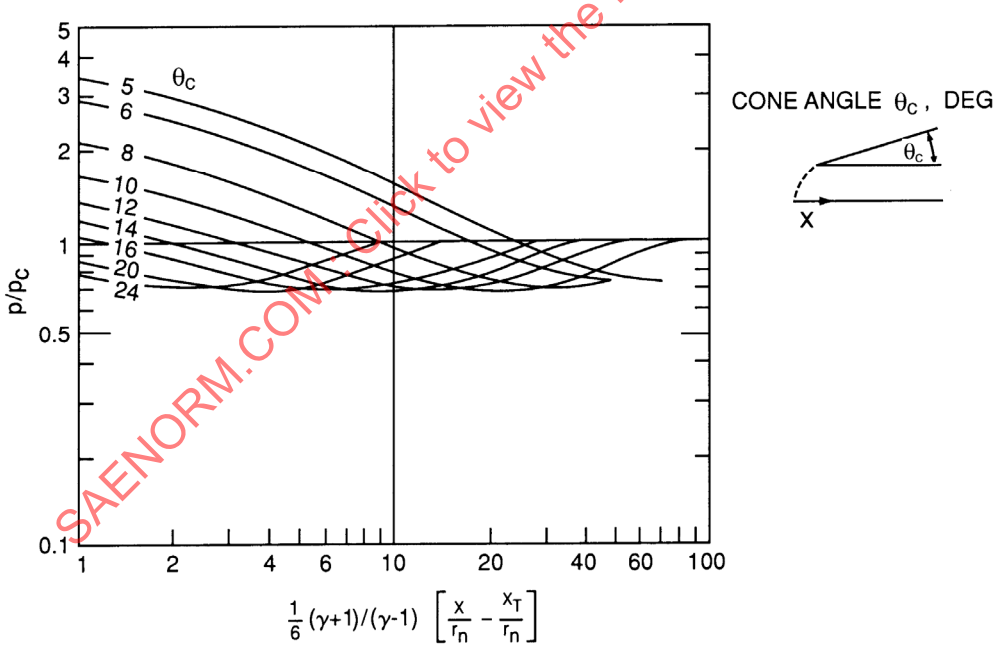

FIGURE 102 - Median Pressure Distribution, Mach Number ≥ 10

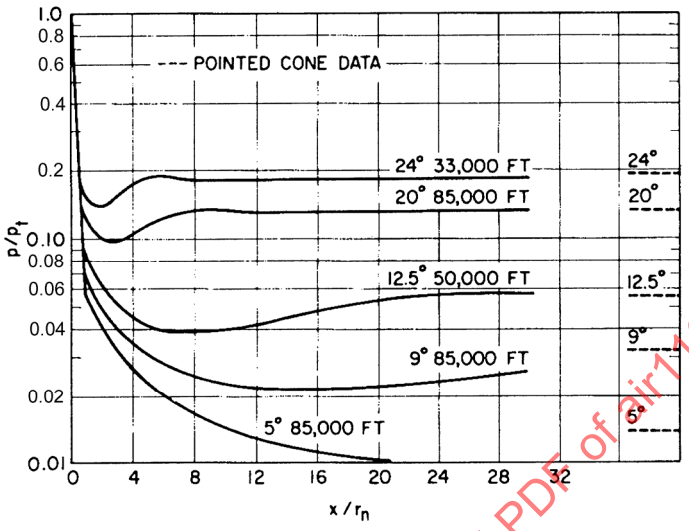

FIGURE 103 - Typical Pressure Distributions, Flow Fields, Sphere Cones, Mach Number = 15

5.3.4 Axisymmetric Entry Vehicle Base Regions: No adequate methods exist for the prediction of entry vehicle base region flow fields, including base pressure. Consequently, empirical or experimental data must be utilized to provide a means of predicting wake pressure, flow field, and subsequently base region heat transfer. For slender, low bluntness ratio vehicles, the base pressure is a function of the boundary layer flow, either laminar or turbulent flow. Figures 104 and 105 give the variation of wake closure angle with boundary layer flow and configuration, and also the ratio of base to local pressure as a function of entry vehicle Mach number. From the air property information in Paragraph 5.1 and the methods for determining surface pressure distribution in Paragraphs 5.3.1, 5.3.2, and 5.3.3, local flow Mach number and pressure can be determined. Quantitative base pressure results can be taken directly from Figure 105. The results presented in this figure permit the determination of flow field properties in the base region, primarily by the assumption of isentropic expansion described in Paragraph 5.6.1.

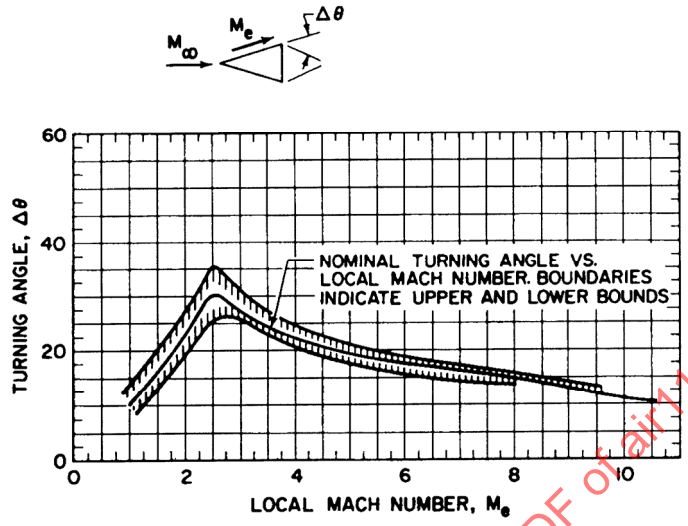

FIGURE 104 - Flow Turning Angle Versus Local Mach Number

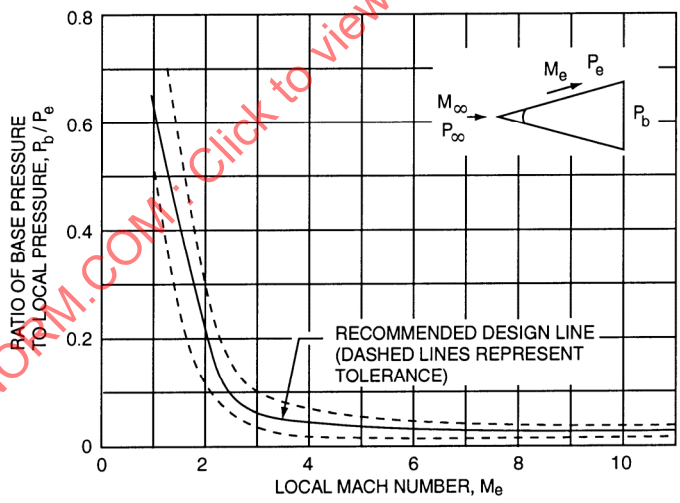

FIGURE 105 - Base Pressure Correlation from Firing Range Data; Pressure Ratio Versus Local Mach Number

5.3.5 Asymmetric Entry Vehicle Methods: The prediction of primary body pressure on lifting vehicle configuration is normally a composite of methods, that is, combinations of Newtonian theory, axisymmetric body flow field correlations (Paragraph 5.3.3), two-dimensional flow field correlations and approximate techniques. The methods described in Paragraphs 5.3.1, 5.3.2, 5.3.3, and in this section should allow the designer to obtain values of pressure from which engineering estimates of heat transfer may be made. Also, see Paragraph 2 for regions of applicability.

This section presents design charts together with analytical expressions for pressure distributions on blunted two-dimensional sections for the hypersonic speed regime. The design charts are based on a variation of the blast wave analogy and account for the effects of nose bluntness on the afterbody pressures. The design charts for pressures on the cylindrical nose and the downstream sections are presented in Figures 106 and 115 through 118. The use of these charts is illustrated by sample calculations. Also presented are methods for predicting pressures on expansion surfaces for attached flow and pressures for blunted plates with swept leading edges.

5.3.5.1 Blunted Leading Edges: The engineering method which most realistically predicts the pressures on a cylindrically blunted leading edge is a combination of modified Newtonian together with a Prandtl-Meyer expansion initiated from the point on the cylinder at which the pressure slopes of modified Newtonian theory and Prandtl-Meyer expression are equal; that is,

$$\left(\frac{dp}{ds}\right)_{Newtonian} \equiv \left(\frac{dp}{ds}\right)_{P-M} \qquad \text{(Eq.138)}$$

(Also see Paragraph 5.3.2.) The pressure ratio of freestream pressure to total pressure behind a normal shock, Table II of Reference 14, is used in the Prandtl-Meyer expression. It is this theoretical expression that is recommended. The results are presented in Figure 106 for the chord parameters x/r_n and s/r_n.

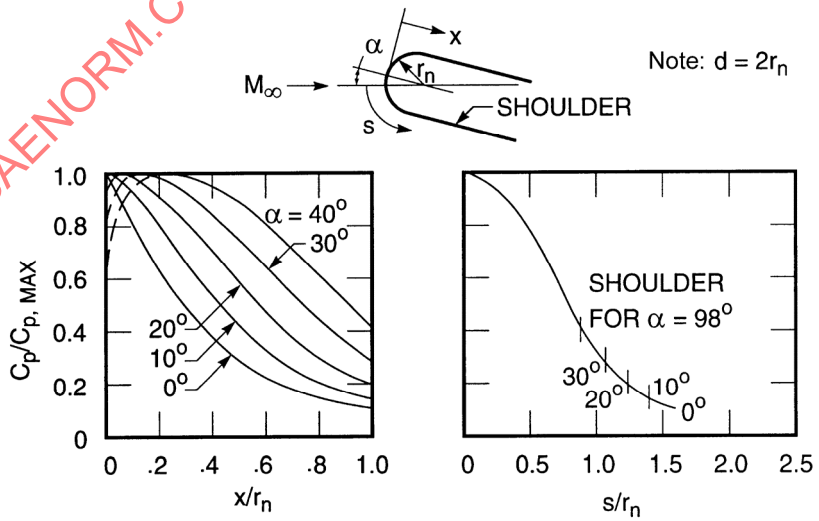

FIGURE 106 - Pressure Distributions, Two-Dimensional Blunt Bodies, Leading Edge

5.3.5.2 Downstream Sections: Four major areas in downstream sections are discussed in the following paragraphs.

(1) Compressive Surfaces: Comparisons of available experimental pressure data for two-dimensional blunted sections with various theoretical methods indicate that the correlation parameters (Reference 15) yield consistently good agreement with experimental data for compressive angles of deflection and Mach numbers of 4 to 12. These parameters,

$$\frac{\Delta P / P_\infty}{\frac{\gamma(\gamma+1)}{2} M_\infty^2 \alpha^2} \qquad \text{(Eq.139)}$$

and

$$\frac{(M_\infty^3 K d/x)^{2/3}}{M_\infty^2 \alpha^2} \qquad \text{(Eq.140)}$$

are modified forms of the blast wave parameters. The plot of these correlation parameters for available experimental data is presented in Figure 107. The equation of the curve faired through these data points is expressed as:

$$\frac{\Delta P}{P_\infty} = 0.36\left[\gamma(\gamma+1)M_\infty^2\alpha^2\right] + 0.0383\left[\gamma(\gamma+1)(M_\infty^3 K d/x)^{2/3}\right] \qquad \text{(Eq.141)}$$

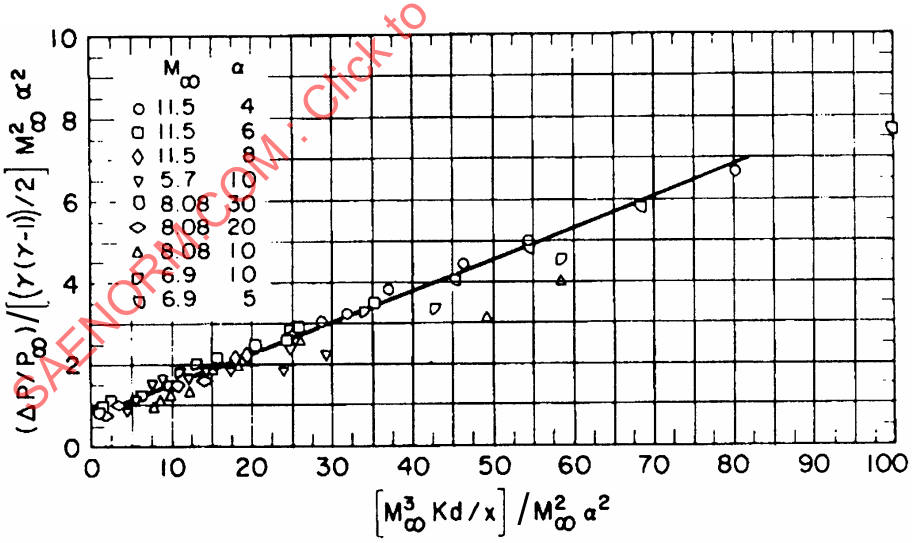

FIGURE 107 - Correlation of Experimental Pressure Data, Blunt Flat Plate

5.3.5.2 (Continued):

The agreement between the experimental data and Equation 141 is adequate for design purposes. Those data that are not in good agreement with Equation 141 are usually data obtained near the leading edge and afterbody tangency point. This is emphasized from results presented in Figures 108 through 110, which show the comparisons in physical coordinates. An additional indication that the theory overestimates the pressure in this region is shown in Figure 111, which presents a comparison of numerical flow field results with that of Equation 141. Although the flow field data are limited to a distance a few nose radii from the leading edge, it appears that better agreement is obtained downstream from this location.

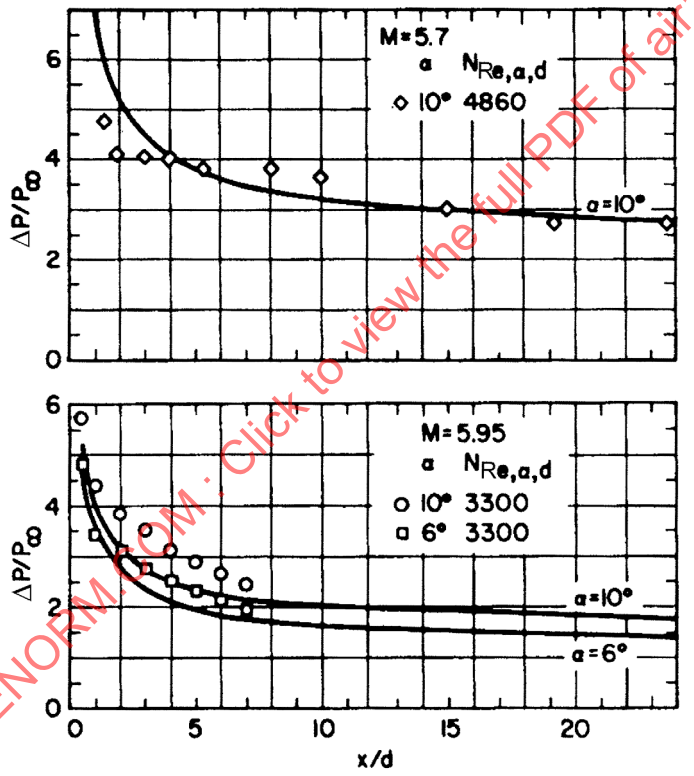

FIGURE 108 - Comparison of Experimental and Predicted Pressure Distributions, Two-Dimensional Blunt Bodies

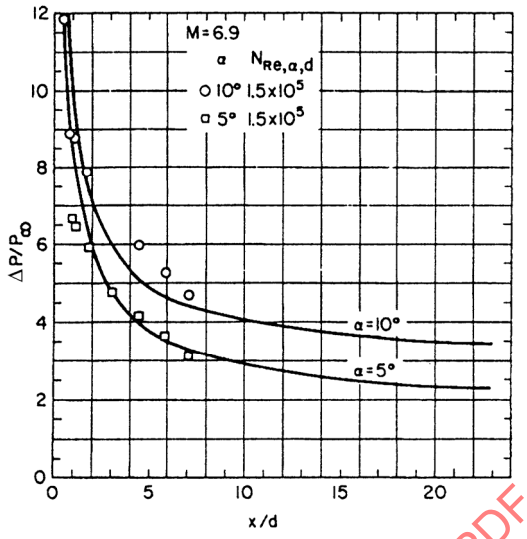

FIGURE 109 - Comparison of Experimental and Predicted Pressure Distributions, Two-Dimensional Blunt Bodies

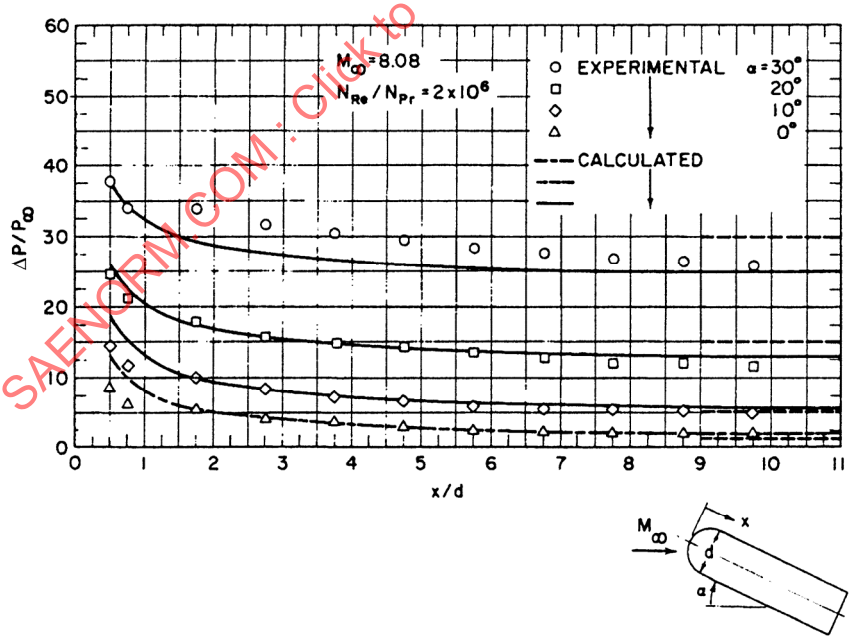

FIGURE 110 - Comparison of Experimental and Calculated Pressure Data, Two-Dimensional Blunt Bodies

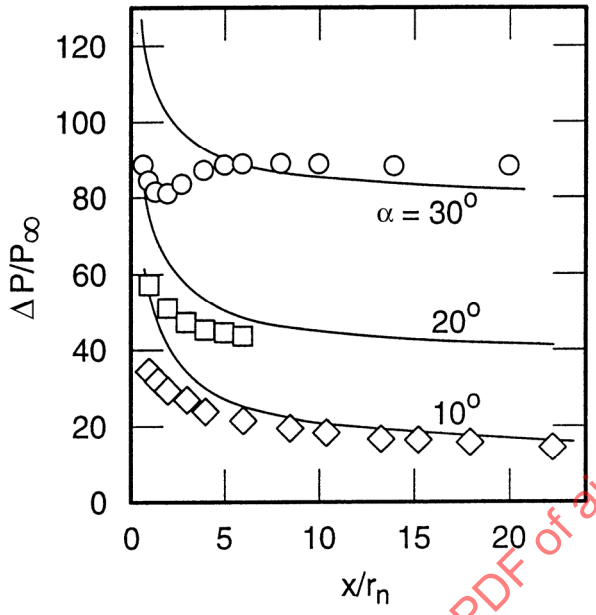

FIGURE 111 - Pressure Distribution, Two-Dimensional Blunt Bodies
(M = 15, Altitude = 100,000 ft)

5.3.5.2 (Continued):

Equation 141 does not correlate with experimental data well at zero angles of deflection (see Figures 112 and 113); therefore, blast wave theory (Reference 16) is used in the design charts for the zero deflection angle condition:

$$\frac{\Delta P}{P_\infty} = 0.187\,\varepsilon\left[\sqrt{\gamma}\,(\gamma-1)\,\frac{M_\infty^2 K}{x/d}\right]^{2/3} - 0.26 \qquad \text{(Eq.142)}$$

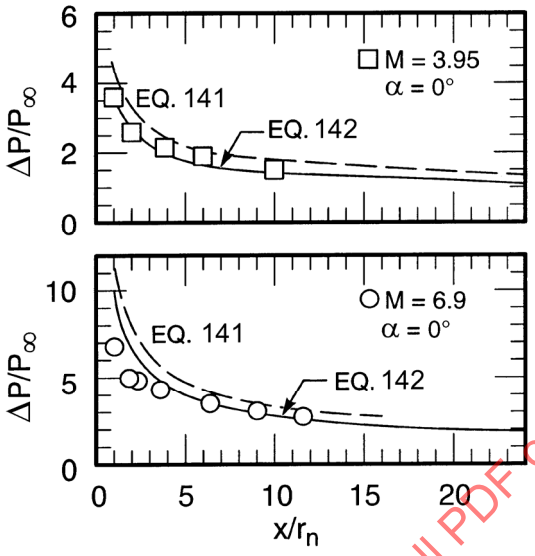

FIGURE 112 - Comparison of Experimental and Calculated Pressure Distributions, Two-Dimensional Blunt Bodies

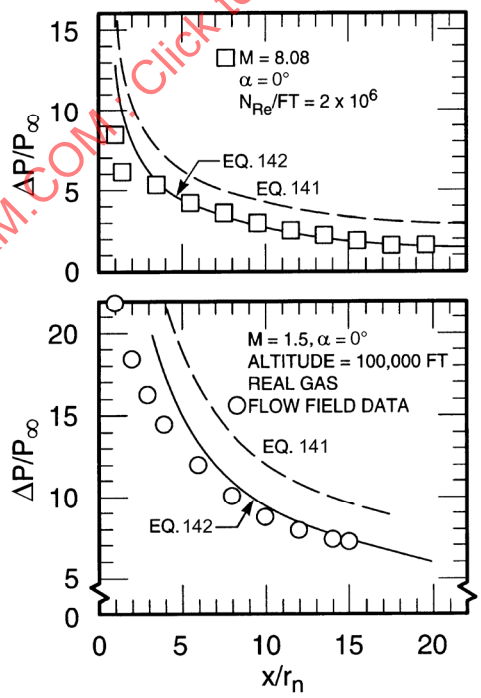

FIGURE 113 - Comparison of Experimental and Calculated Pressure Data

5.3.5.2 (Continued):

The ε factor is obtained from Reference 16. Equation 142 agrees with available experimental data, as shown in Figures 112 and 113. Equation 142 may be expanded to take account of slight local flow angles less than 10 deg by addition of inviscid wedge values, as follows:

$$\left(\frac{P}{P_\infty}\right)_{\alpha\neq 0} = \left(\frac{P}{P_\infty}\right)_{\text{inviscid wedge}} + \left(\frac{\Delta P}{P_\infty}\right)_{\text{Eq. 142}} \qquad \text{(Eq. 143)}$$

(The last term is determined using Equation 142.) Equation 143 is not used in the design charts; however, a comparison of predicted values obtained by use of Equations 141 and 143 is presented in Figure 114 for angles of attack of 0, 5, and 10 deg.

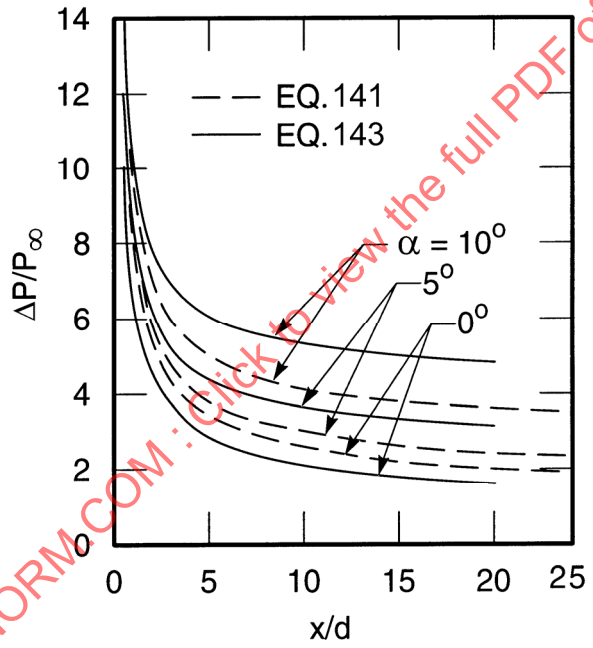

FIGURE 114 - Pressure Distribution on Blunted Flat Plate (M = 6.9)
All Solid Lines from Equation 143; All Dashed Lines from Equation 141

Although the above equations are derived primarily for a blunted plate at angle of attack, they may also be used for blunted wedges if care is exercised in determining the correct axis system and the correct chord parameter to be used. In order to predict pressures for both blunted flat plates and wedges, a wetted length parameter (measured from the stagnation point) is used, s/r_n. Consequently Equation 141 may be rewritten as

5.3.5.2 (Continued):

$$\frac{\Delta P}{P_\infty} = 0.36\left[\gamma(\gamma+1)M_\infty^2\theta^2\right] + 0.0383\left\{\gamma(\gamma+1)\left[\frac{M_\infty^2 K}{(1/2)\left(1+\frac{s}{r_n}-\frac{90-\theta}{57.3}\right)}\right]^{2/3}\right\} \qquad \text{(Eq.144)}$$

where:

θ = Local flow angle or body angle on the surface

Design charts for pressure distributions on blunted slab afterbodies are presented in Figures 115 and 116 for the chord parameter x/r_n and in Figures 117 and 118 for the chord parameter s/r_n. These charts cover the Mach number range 5.0 to 20.0 and local flow angles of 0 to 30 deg.

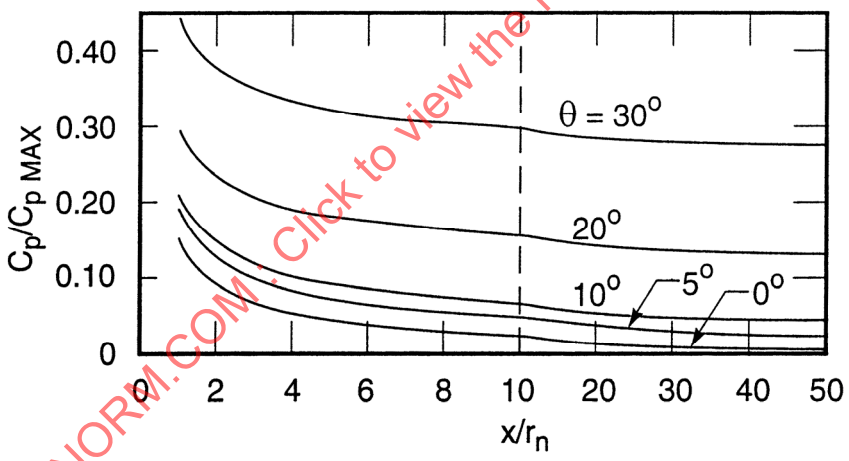

FIGURE 115 - Pressure Distributions, Two-Dimensional Blunt Bodies, M = 5

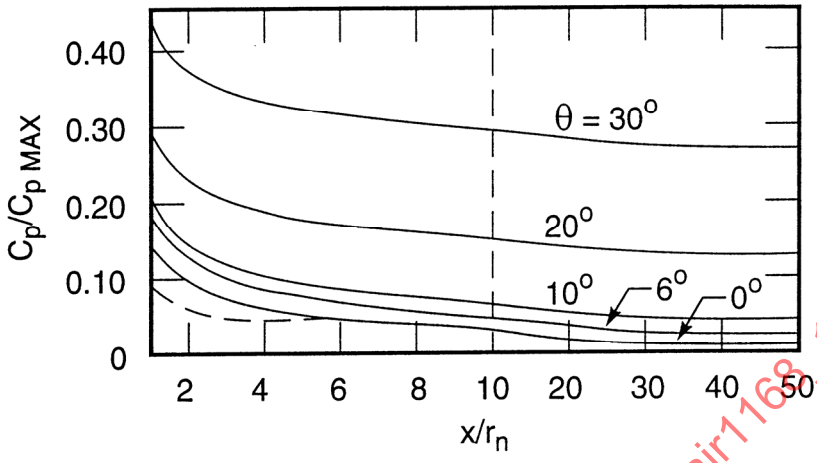

FIGURE 116 - Pressure Distributions, Two-Dimensional Blunt Bodies, M = 10-20

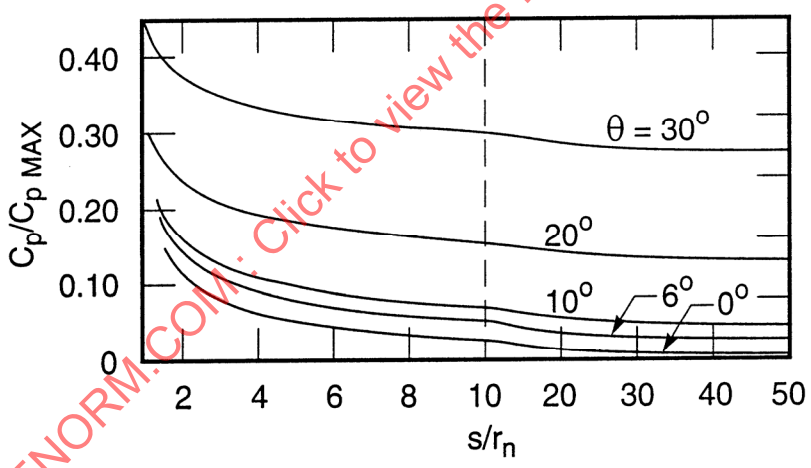

FIGURE 117 - Pressure Distributions, Two-Dimensional Blunt Bodies, M = 5

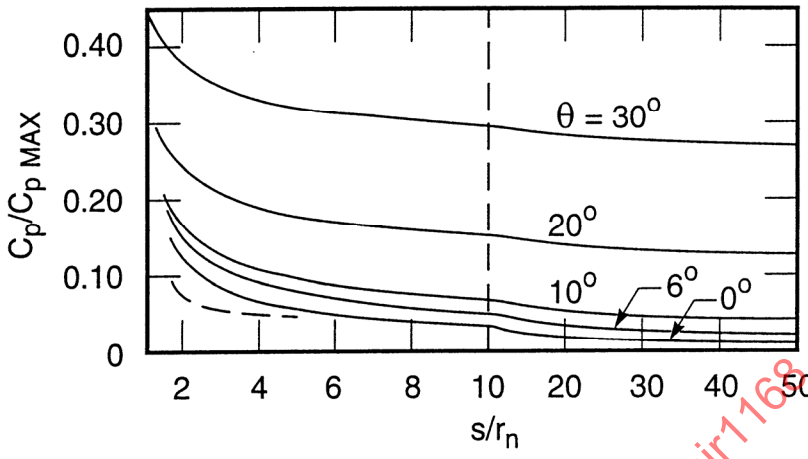

FIGURE 118 - Pressure Distributions, Two-Dimensional Blunt Bodies, M = 10-20

5.3.5.2 (Continued):

(2) Leading Edge-Afterbody Tangency Region for Compressive Surfaces: The largest deficiency of the aforementioned methods is the tendency to overpredict the pressures in the cylinder-afterbody tangency region. An expression for predicting pressures in this region, for a blunted plate at zero angle of attack, is given in Reference 17 as

$$\frac{P}{P_{max}} = \left[\frac{1}{1+\left(\frac{x-r_n}{d}\right)^{2/3}}\right]^{P_t/P_{max}} + \left[\frac{1}{1+\left(\frac{x-r_n}{d}\right)^{-2/3}}\right]^{P_t/P_\infty}\left[\frac{P_\infty}{P_{max}}\right] \qquad \text{(Eq.145)}$$

The ratios P_t/P_{max} and P_t/P_∞ (from $C_p/C_{p,max}$) may be obtained from Figure 106 together with Reference 14 for air. One of the assumptions made in deriving Equation 145 is that the maximum pressure coefficient $C_{P,max}$ is essentially constant; thus the use of Equation 145 is limited to Mach numbers greater than 5.0.

Comparisons of the method of Reference 17 with experimental data are given in Figures 112 and 113. While the pressures in the leading edge-afterbody tangency region predicted very well, the pressures a few nose radii back are underpredicted. A more representative prediction of pressure distribution can be obtained by using Equation 145 for values in the shoulder region and then fairing the curve into the basic blast wave expression at two or three nose diameters back. These fairings are presented as dashed curves for Mach numbers greater than 5.0 in Figures 116 and 118.

5.3.5.2 (Continued):

At angles of attack, there is also a tendency of the theoretical methods for the afterbody to overpredict pressures at the tangency point. Since Equation 145 does not give satisfactory results for local flows other than zero, a pressure discontinuity due to the method will likely occur in the transition region. Furthermore, at high angles of local flow, a type of overexpansion is evident in the data (Figures 110 and 111), which is not compatible with the theoretical expressions given for design application. Consequently, the pressure data from Figures 115 to 118 must be faired in this transition region, as illustrated in the example presented.

(3) Expansion Surfaces: Limited available experimental data for the expansion side of a blunt flat plate are presented in Figure 119 along with the theoretical results of Reference 15. Due to lack of available experimental data and this inconclusive comparison with the data, the use of an approximate method is necessary. Until additional experimental data become available to allow a more comprehensive correlation of pressures on an expansion surface, it is recommended that a simple Prandtl-Meyer expansion be used. Results of this expansion are also presented in Figure 119 for design use.

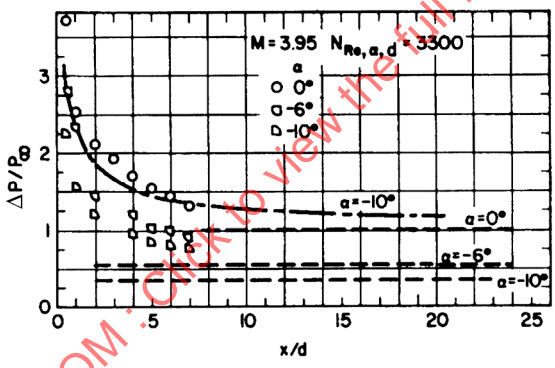

FIGURE 119 - Expansion Side Pressures

(4) Swept Surfaces: As with expansion surfaces, there are limited experimental data showing the effects of sweep on the pressure distributions of two-dimensional blunt bodies. Sweep effects can be estimated by multiplying the nose bluntness term by the square of the cosine of the sweep angle (Reference 18). Modification of Equation 141 by this procedure yields

$$\frac{\Delta P}{P_\infty} = 0.36\left[\gamma(\gamma+1)M_\infty^2\alpha^2\right] + 0.0383\left[\gamma(\gamma+1)\left(\frac{M_\infty^3\,Kd}{x}\right)^{2/3}\right]\cos^2\Lambda \qquad \text{(Eq.146)}$$

The results of Equation 146 together with experimental data, presented in Figure 120, indicate that this modification gives representative pressure values for sweep effects and should be used to predict pressures on bodies with swept leading edges.

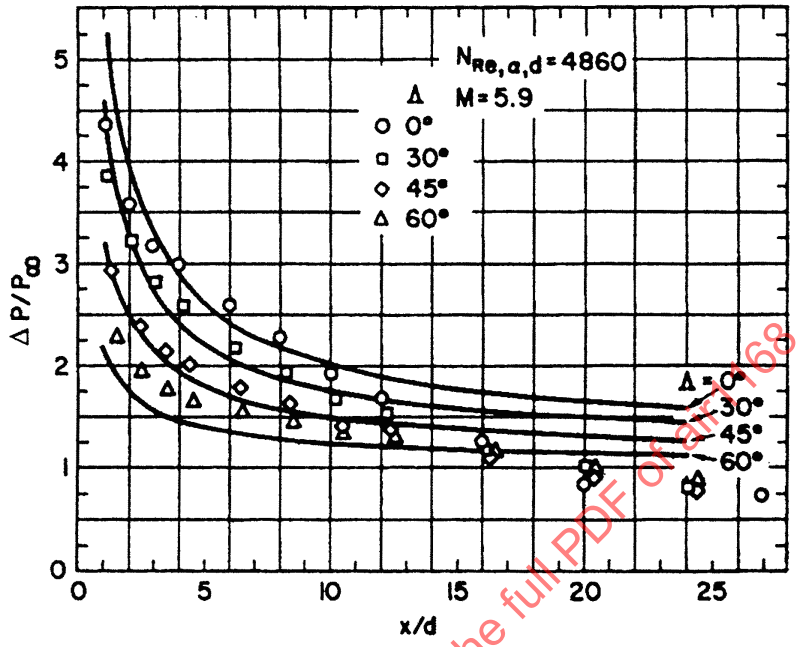

FIGURE 120 - Effect of Sweep on Pressure Distribution

5.3.5.2 (Continued):

Example: Figures 106 and 115 to 118 are used to determine pressure distributions on blunted flat plates and blunted wedges. Two sample problems and their solutions are presented to illustrate the use of the charts.

Problem 1: Determine the windward pressure distribution on a flat plate section with a hemicylindrical leading edge at a Mach number of 10 and an angle of attack of 10 deg.

Solution: For a flat plate, either x/r_n or s/r_n may be used. For this example, x/r_n will be used.

(a) The ordinate of Figure 106 indicates that the maximum pressure point is located at $x/r_n = 0.013$ for an angle of attack of 10 deg.

Pressure ratios for the various chord stations to the leading edge-afterbody tangency point (Figure 106) are given in Table 5.

TABLE 5 - Pressure Ratios (Figure 106)

x/r_n	$C_P/C_{P,max}$
0	0.970
0.013	1.000
0.1	0.926
0.2	0.797
0.4	0.535
0.6	0.323
0.8	0.208
1.0	0.141

5.3.5.2 (Continued):

(b) Figure 116, with θ equal to 10 deg, is used for the pressures on the afterbody. These are given in Table 6.

TABLE 6 - Pressure Ratios

x/r_n	$C_P/C_{P,max}$
1.0	0.209
2.0	0.142
4.0	0.100
6.0	0.0830
10.0	0.0650
20.0	0.0530
30.0	0.0460
50.0	0.0430

(c) These calculated points are plotted in Figure 121. As noted previously, there is a pressure discontinuity in the method at the leading edge-afterbody tangency point ($x/r_n = 1$). Based on the comparisons of experimental and theoretical pressure values (Figures 108 through 111) the pressure at the shoulder obtained from Figure 106 is faired into the afterbody pressures at x/r_n equal to approximately 7.

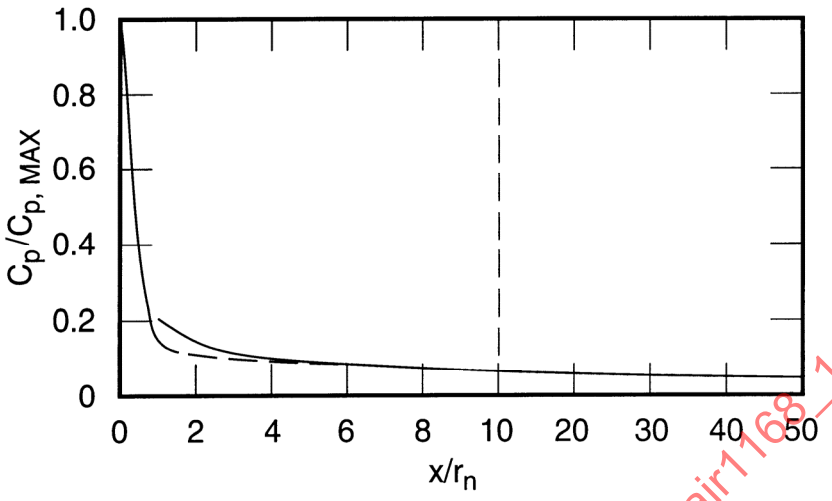

FIGURE 121 - Sample Problem 1: Pressure Distribution on a Blunted Flat Plate M = 10, α = 10 deg

5.3.5.2 (Continued):

Problem 2: This is the same as Problem 1 except that the section is a blunted, 10 deg, half-angle wedge at angles of attack equal to -10, 0, 10, and 20 deg.

Solution:

(a) For a wedge, the chord parameter s/r_n is used in Figure 106. The deflection angles θ are equal to 0, 10, 20, and 30 deg, respectively, that is, the angle of attack plus the wedge half angle. See Table 7.

TABLE 7 - Chord Parameters (Figure 106)

s/r_n	$C_P/C_{P,max}$
0.0	1.000
0.2	0.958
0.4	0.856
0.6	0.684
0.8	0.487
1.045	0.283, α = 20 deg
1.220	0.197, α = 10 deg
1.392	0.143, α = 0 deg
1.57	0.100, α = -10 deg

5.3.5.2 (Continued):

(b) Figure 118 is used for the afterbody pressures. θ is equal to 0, 6, 10, 20, and 30 deg. See Table 8.

TABLE 8 - Afterbody Pressures (Figure 118)

s/r_n	$C_P/C_{P,max}$ (α =) (θ =)	$C_P/C_{P,max}$ -10 0	$C_P/C_{P,max}$ 0 10	$C_P/C_{P,max}$ 10 20	$C_P/C_{P,max}$ 20 30
1.045		--	--	--	0.438
1.220		--	--	0.295	0.417
1.392		--	0.208	0.272	0.403
1.57		0.100	0.185	0.257	0.392
2.0		0.066	0.158	0.235	0.373
4.0		0.047	0.105	0.188	0.330
6.0		0.045	0.086	0.170	0.312
10.0		0.033	0.068	0.154	0.295
20.0		0.019	0.053	0.139	0.282
30.0		0.013	0.047	0.133	0.276
50.0		0.010	0.042	0.127	0.271

(c) These data are plotted in Figure 122. Again, the pressures in the shoulder region are faired. Note that the zero local flow angle condition has previously been faired in the design charts, using Equation 146. To obtain pressures in the tangency region for local flow angles greater than 20 deg, the pressures will have to be faired, using experimental and numerical flow field data (Figures 110 and 111) as guides.

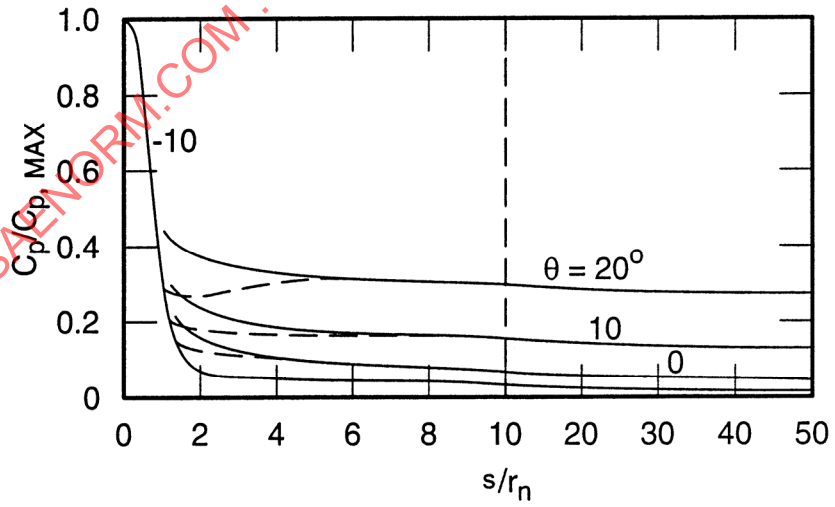

FIGURE 122 - Sample Problem 2: Pressure Distribution on a Blunted Wedge, Half-Angle = 10 deg, M = 10

5.4 Shock Shapes:

As the second step in the determination of the shock layer characteristics (the outer boundary), the bow shock wave location must be predicted. Two phases are considered: the shock location in the vicinity of the nose of the reentry vehicle, and the shock location as it extends downstream.

5.4.1 Downstream Region: Design considerations relative to bow shock wave location in the downstream region are discussed below.

5.4.1.1 Correlations: Flow field solutions for bow shock wave shapes about a sphere-cone show that as the Mach number increases the shock wave lies closer to the body; also, that as the cone angle increases, the shock moves in closer to the body and then moves away again. Consequently, cone angle and Mach number must be considered as important correlation parameters. The analytic method of Cheng (Reference 13) is used as a correlation method. The results from Cheng's theory in terms of the parameters

$$\left(\frac{\theta}{\sqrt{\varepsilon K}}\,\frac{r_s}{2r_n}\right) \qquad \text{(Eq.147)}$$

and

$$\left(\frac{\theta^2}{\sqrt{\varepsilon K}}\,\frac{x}{2r_n}\right) \qquad \text{(Eq.148)}$$

are given in Figure 123, where ε is given by

$$\varepsilon = \frac{\gamma - 1}{\gamma + 1} \qquad \text{(Eq.149)}$$

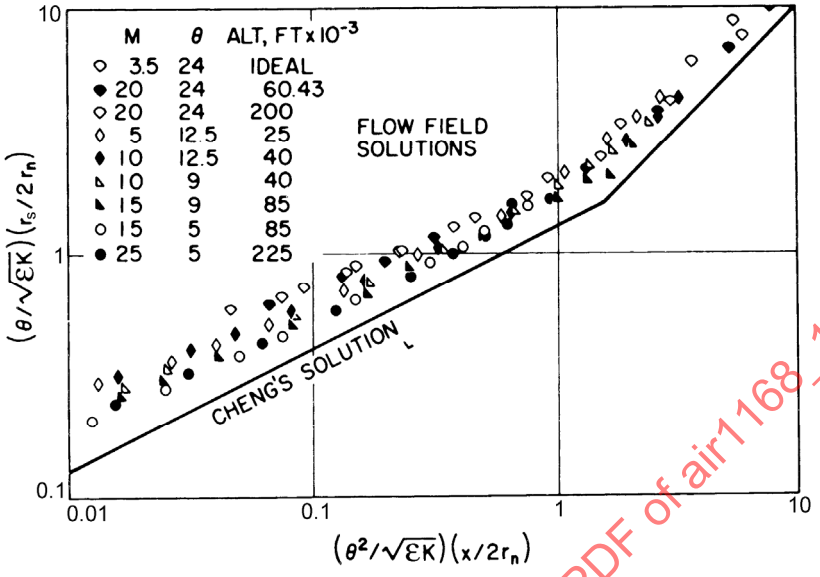

FIGURE 123 - Comparison of Flow Field Shock Shape Data (Cheng's Correlation Parameters), (Reference 13), Where Body Angle θ is in Radians

5.4.1.1 (Continued):

Also presented are the results of available numerical flow field solutions. Comparison of these data indicates that the agreement is qualitatively good, but agreement between specific values is lacking. The "dogleg" in Cheng's theoretical result is due to the fact that the shock is influenced rather abruptly by the presence of the conical afterbody. In terms of flow field results, the "dogleg" arises because the conical portion of the body cannot influence the flow upstream from the last left-hand characteristic emanating from the cone-sphere tangency point. This implies that the correlation prior to the "dogleg" $[(\theta^2 / \sqrt{\varepsilon K})(x / 2r_n)]$ (less than approximately 1.0) is independent of the afterbody cone angle. Since both coordinates derived from Cheng's solution are functions of θ, a single line will correlate all values of cone angle in this region only if the slope of the line is equal to 0.5. Cheng's solution satisfies this condition; however, as evidenced in Figure 123, the results of the exact numerical solutions indicate that the slope for specific freestream conditions and afterbody cone angles is not necessarily equal to 0.5. Also, there is a definite variation with cone angle in the flow field results.

In order to improve this difference, the correlation parameters for the region prior to the "dogleg" have been modified and the functions of cone angle eliminated. This modified correlation of the flow field data prior to the "dogleg" is presented in Figure 124. The modified parameters correlate all cone angle effects in the region prior to the dogleg in Cheng's theory.

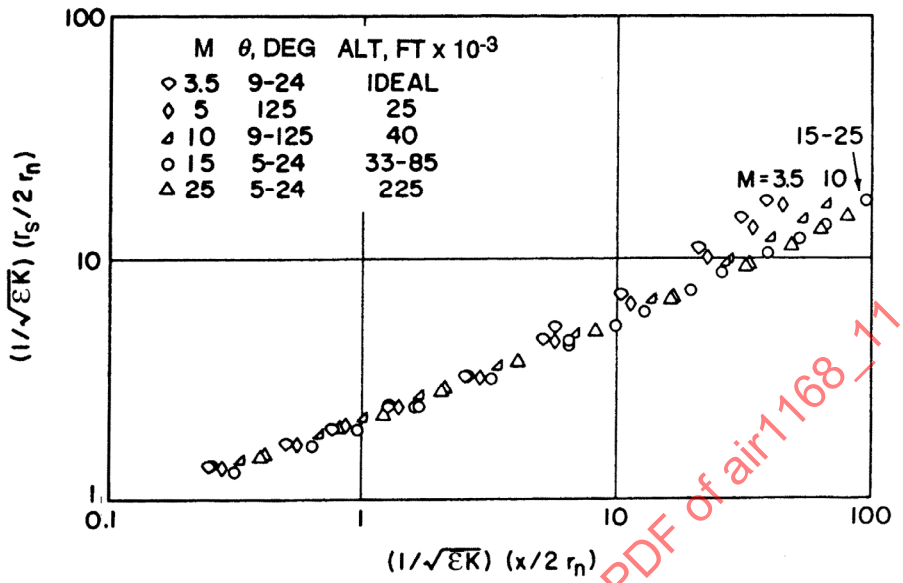

FIGURE 124 - Comparison of Flow Field Shock Shape Data
(Modified Correlation Parameters)

5.4.1.1 (Continued):

In Figure 123 there is still a dependence of the flow field shock wave results on Mach number. Over the left-hand side of the correlation, this Mach number effect is slight; however, over the right-hand side of the correlation, the Mach number effect is quite pronounced.

On the basis of these correlations, a design method is recommended which considers the correlation in three separate regions. These regions are the three regions shown in Figure 125, where:

I. The correlation is independent of afterbody shape and only slightly dependent on freestream Mach number.

II. The correlation is independent of afterbody shape but dependent on freestream Mach number.

III. Cheng's correlation parameters are used, since the results are dependent upon both the afterbody shape and Mach number.

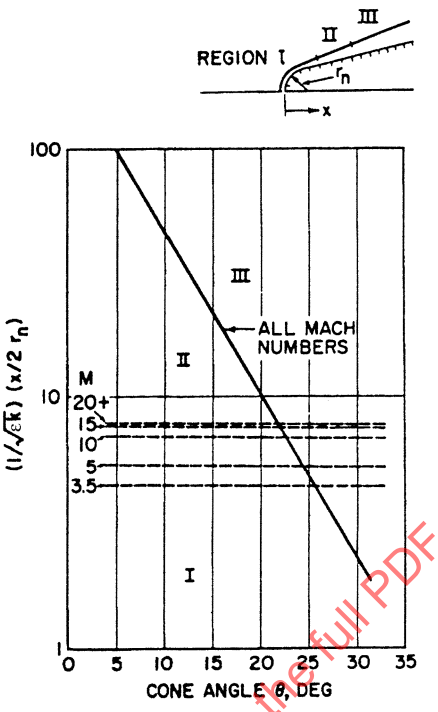

FIGURE 125 - Boundaries of Applicability for Bow Shock Shape Configuration

5.4.1.1 (Continued):

The three regions are illustrated in Figure 125 and are shown to be functions of Mach number, cone angle θ, and the parameter $[(1/\sqrt{\varepsilon K})(x/2r_n)]$.

5.4.1.2 Design Method: Analytic expressions have been written to fit the exact flow field results for the three regions just indicated. These expressions all have the form:

$$\frac{r_s}{2r_n} = K_1\theta^{K_2}(\varepsilon K)^{K_3}(x/2r_n)^{K_4} \qquad \text{(Eq.150)}$$

where:

K = $(C_A/C_{ps})(C_{ps})\cos^2\theta$
C_A = Nose drag coefficient, dimensionless
C_{ps} = Maximum pressure coefficient, dimensionless

where the constants K are functions of the applicable region and Mach number; the calculated values of these constants are presented in Figure 126.

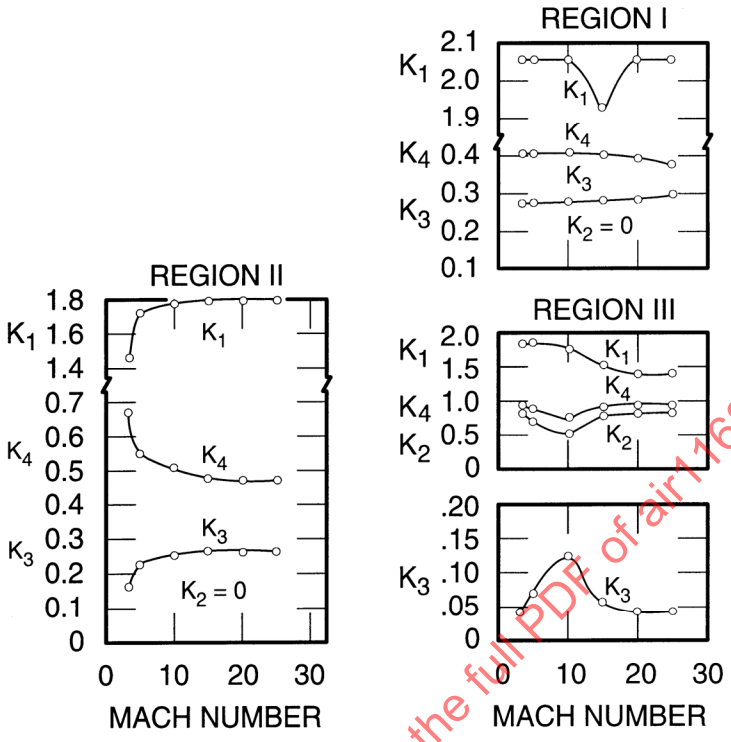

FIGURE 126 - Constants for Shock Shape Determination; Sphere-Cone Body

5.4.1.2 (Continued):

This correlation technique is developed for a sphere-cone body at zero angle of attack; however, it is applicable with little modification for the prediction of the bow shock shape along the windward ray of the body at angle of attack (Reference 19). The method involves the use of the tangent-cone approach, that is, the shock shape for a 9 deg sphere-cone at an angle of attack of 10 deg is determined by using a shock shape for an equivalent 19 deg cone at zero angle of attack. In this application the method prescribed for zero angle of attack calculations of the shock location are utilized with a modification in the calculation of the nose drag term k and in the boundaries of applicability of the correlation constants K.

For the shock shape corresponding to the leeward meridian, experimental data have shown that the leeside shock shape remains fixed in space for a large range of angles of attack (up to approximately 60 deg). Consequently the shock shape calculated for zero angle of attack may be used for the leeward values over a wide range of angles of attack.

Figure 127 gives comparisons of this analytical method of predicting windward and leeward meridional shock shapes at angle of attack with experimental data. Good agreement is shown (note that the leeside shock shape is fixed in space for angles of attack at least as great as 60 deg).

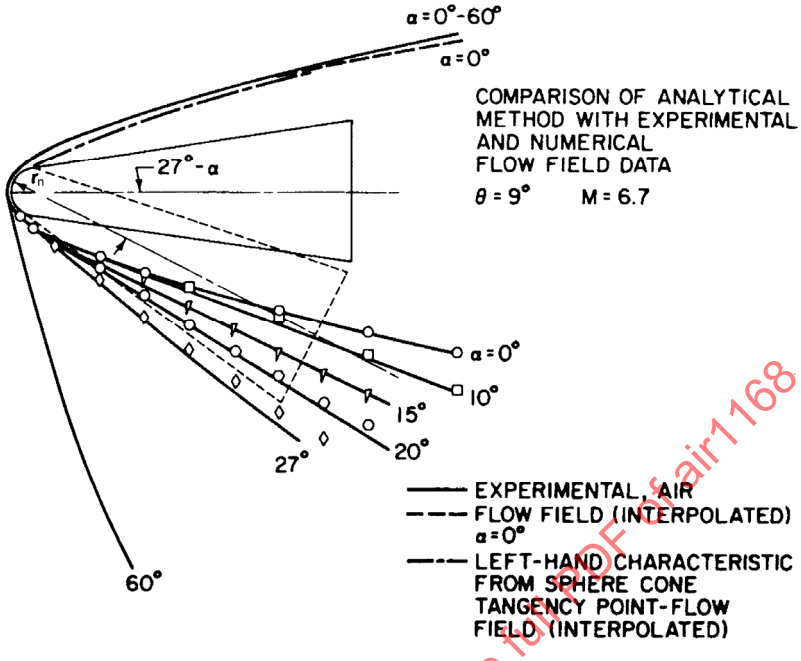

FIGURE 127 - Shock Shape About Sphere-Cone Body at Angle of Attack; Symbols Present Analytical Method

5.4.2 Nose Region: An accurate method for predicting the bow shock shape is obtained by correlating available numerical flow field results, using the equation for conic sections utilized by Van Dyke and Gordon.

$$r_s = 2R_s x_s - B_s x_s^2 \qquad \text{(Eq.151)}$$

where:

r_s, x_s = Cylindrical coordinates of the shock shape
R_s = Radius of curvature of the shock at the axis ($r_s = 0$)
B_s = Measure of the eccentricity of the conic section

To facilitate the use of Equation 151, the origin of the coordinates is translated to the nose of the body by substituting $x_s = \Delta x + x$, where Δx is the stagnation point shock stand-off distance. Then, normalizing by the body nose radius r_n yields

$$\left(\frac{r_s}{r_n}\right) = 2\left(\frac{x_s}{r_n}\right)\left(\frac{x}{r_n}+\frac{\Delta x}{r_n}\right) - B_s\left(\frac{x}{r_n}+\frac{\Delta x}{r_n}\right)^2 \qquad \text{(Eq.152)}$$

5.4.2 (Continued):

The introduction of the stagnation point shock stand-off distance, Δx, is obtained from a correlation of values of Δx flow field solutions (Reference 6). These results for Mach numbers greater than 5 are presented in Figure 128. This correlation is obtained by use of the density ratio across a normal shock:

$$\frac{g\rho_\infty}{g\rho_t} \qquad \text{(Eq.153)}$$

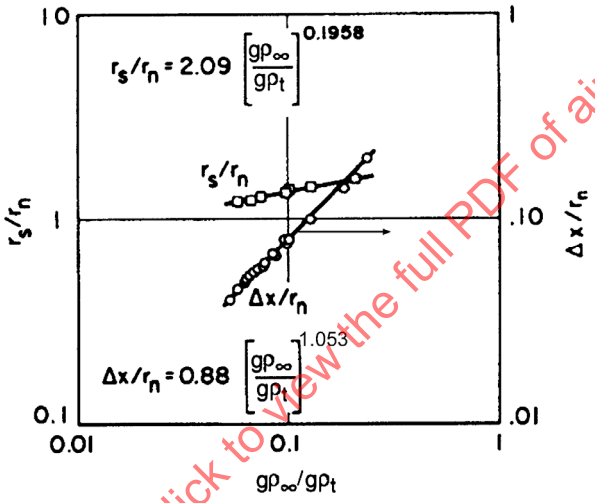

FIGURE 128 - Correlation of Shock to Body Radius Ratio and Shock Stand-Off Distance with Density Ratio

Because of its applicability to the correlation of Δx, the density ratio is also used to correlate the ratio of the radius of curvature of the shock and the body r_s/r_n measured at the axis.

By use of Equation 152 and numerical flow field results, the bluntness or eccentricity factor B_s is determined. These values, shown in Figure 129, indicate a dependence on the density ratio and on the axial distance. Further, for any given axial station, the factor B_s is nonlinear with density ratio and reaches a maximum at approximately $g\rho_\infty/g\rho_t = 0.095$.

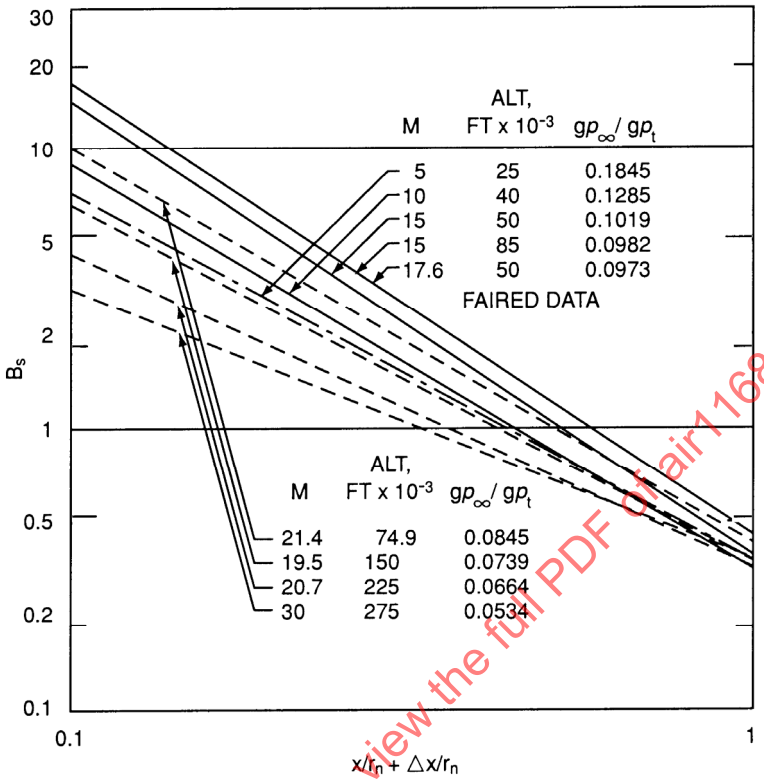

FIGURE 129 - Shock Shape Bluntness Factor

5.4.2.1 Design Method: Equation 151 may be used to obtain r_s as a function of x for various combinations of Mach number and altitude [$0.05 \leq (g\rho_\infty/g\rho_t) \leq 0.25$]. Figures 128 and 129, together with values of the density ratio across the normal shock obtained from normal shock charts, such as those published in Reference 20, are used in conjunction with Equation 151 for these calculations.

A simplified expression for the bow shock wave determination has been obtained by approximating the eccentricity data in Figure 129 with a single analytical expression (straight line), by determining the analytic relations for the curves of x/r_n and r_s/r_n in Figure 130, and by substituting these expressions into Equation 151 to obtain the following results:

$$\frac{r_s}{r_n} = \left\{ 4.18 \left(\frac{g\rho_\infty}{g\rho_t} \right)^{0.1958} \cdot \left[\frac{x}{r_n} + 0.88 \left(\frac{\rho_\infty g}{\rho_t g} \right)^{1.053} \right] - 0.646 \left[\frac{x}{r_n} + 0.88 \left(\frac{\rho_\infty g}{\rho_t g} \right)^{1.053} \right]^{1.467} \right\}^{0.5} \qquad \text{(Eq.154)}$$

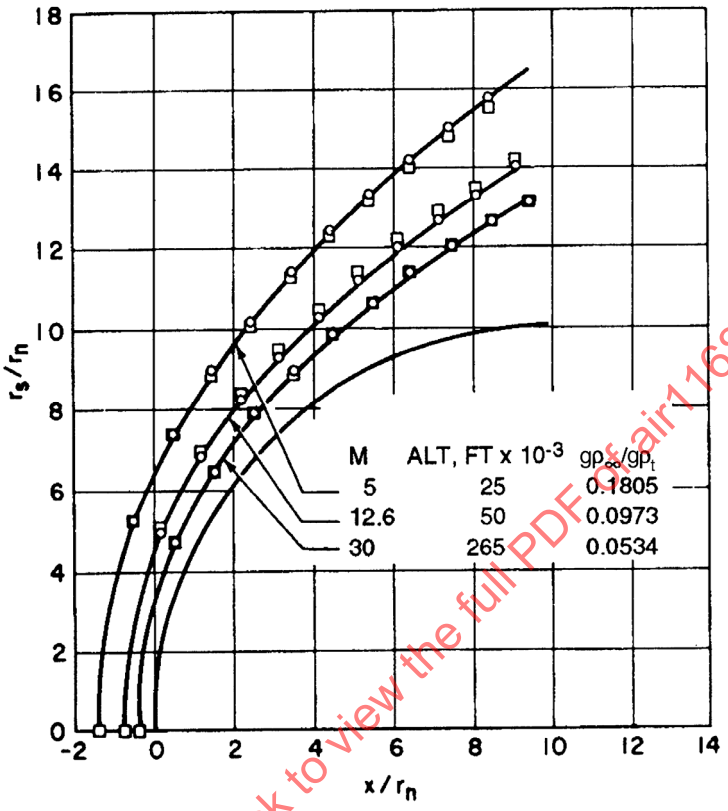

FIGURE 130 - Comparison of Bow Shock Shapes; Data From General Electric Co., Missiles and Space Div.

5.5 Shock Layer Characteristics:

5.5.1 Correlation: Shock layer profile correlations are obtained from the surface pressure and shock wave shape and the nondimensional pressure correlation of Reference 21. This is presented in Figure 131. In this figure the ratio of the local to body surface pressure (P/P_w) is correlated as a function of body station in the form

$$\left(\frac{r_n}{x}\right)^{0.35} \frac{r - r_s}{r_s - r_b} \qquad \text{(Eq.155)}$$

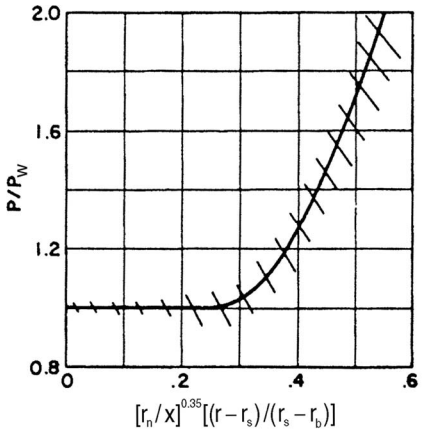

FIGURE 131 - Correlation of Shock Layer Pressure Distributions;
Crosshatching Indicates the Spread in the Data

5.5.1 (Continued):

The crosshatching indicates the scatter in the flow field results. By use of this figure the local pressure in the flow field can be obtained.

5.5.2 Design Method: The local pressure is obtained by using the expression

$$\frac{P}{P_\infty} = \left(\frac{P}{P_w}\right)\left(1+\frac{P_w - P_\infty}{P_\infty}\right) \qquad \text{(Eq.156)}$$

where:

(P/P_w) is obtained from Figure 131 for a given body station
P_w is obtained from the correlation procedure discussed previously

5.6 Boundary Layer Flow Property Determination:

In order to determine the local flow conditions existing at the edge of the boundary layer (which are necessary for the determination of Reynolds number, boundary layer dimensional parameters such as boundary layer velocity thickness δ, boundary layer displacement thickness δ^*, boundary layer momentum thickness θ, and local aerodynamic heating $\dot{q}$), an assumption of isentropic expansion from total conditions existing at the stagnation point is normally made. For entry system geometrical parameters describing bluntness, that is, $(x/r_n) < 10$, the assumption of isentropic expansion is valid; for x/r_n values between 10 and 40, this assumption is no longer valid, and vorticity or entropy effects on boundary layer edge conditions must be considered. For x/r_n values greater than 40, the pure cone relations presented in Paragraph 5.3.3 are valid.

5.6.1 Isentropic Expansion: For regions of x/r_n where the assumption of isentropic flow is valid, the local boundary layer edge properties are independent of boundary layer velocity thickness δ and may be determined from the initial conditions of stagnation (total) point pressure and enthalpy (P_t and h_t) and from the local value of static pressure P_e. The value of entropy at the P_t and h_t conditions at the stagnation point are determined from Figures 84 through 90 or tables of high-temperature air properties. Expansion of the flow at constant entropy is made to the local static pressure at the edge of the boundary layers. Local density, temperature, and compressibility factors are then obtained by reference to the tables or figures at the local enthalpy or pressure. Local velocity (at the edge of the boundary layer) is obtained from the following relation:

$$u_e = \sqrt{2gJ(h_s - h_e)} \qquad \text{(Eq.157)}$$

Local flow conditions at the edge of the boundary layer such as Reynolds number may then be determined; that is,

$$N_{Re,s} = \frac{g\rho_e u_e s}{\mu_e} \qquad \text{(Eq.158)}$$

as well as the aerodynamic heating (see Paragraph 6).

5.6.2 Vorticity/Entropy Gradient Effects: Specifically, for $x/r_n \geq 0.6$ and, in general application, for $x/r_n \geq 10$, the assumption of an isentropic expansion of the flow from the stagnation point to entry vehicle location i is no longer valid. For increasing values of x/r_n the flow entering the boundary layer crosses the entry vehicle bow shock at increasing angles of obliquity (see Figure 132) rather than through the stagnation region where the shock angle is approximately 90 deg. At very large values of x/r_n at position i, the flow entering the boundary layer is that crossing the conical shock wave defined for pure cone configurations. The method for determining the local flow properties is based on the conservation of mass flow through the boundary layer at each position which crossed the entry vehicle bow shock at the position of a common streamline. The mechanics of this procedure are defined as follows: An isentropic expansion is taken from a point immediately behind the oblique shock location through which the freestream passes to yield the local pressure P_e at a body point. The oblique shock angle θ_s used in this example is determined by an iterative procedure. For the first iteration, assume that the shock angle θ_s is known.

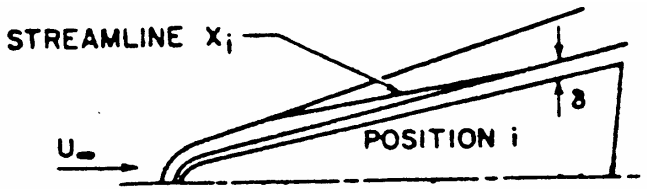

FIGURE 132 - Flow Entering the Boundary Layer

5.6.2 (Continued):

The pressure and enthalpy immediately behind the oblique shock where the angle is θ_s is:

When $M_\infty \sin\theta_s > 4$:

$$P_s = P_\infty \left[1 + 1.4M_\infty^2 \sin^2\theta_s \left(1 - \frac{u_2}{u_1}\right)\right] \quad \text{(Eq.159)}$$

and

$$h_s = h_\infty \left[1 + 0.2M_\infty^2 \sin^2\theta_s \left(1 - \left(\frac{u_2}{u_1}\right)^2\right)\right] \quad \text{(Eq.160)}$$

When $M_\infty \sin\theta_s \le 4$:

$$P_s = \frac{P_\infty (7M_\infty^2 \sin^2\theta_s - 1)}{6} \quad \text{(Eq.161)}$$

and

$$h_s = h_\infty \frac{(7M_\infty^2 \sin^2\theta_s)(M_\infty^2 \sin^2\theta_s + 5)}{36M_\infty^2 \sin^2\theta_s} \quad \text{(Eq.162)}$$

The velocity ratio u_2/u_1 is obtained from linear interpolation of values given in Table 9. The following properties are then obtained from tables of high-temperature air properties for subsequent calculations:

$$g\rho_s,\ S_s = f(h_s, P_s) \quad \text{(Eq.163)}$$

$$h_e,\ T_e,\ g\rho_e = f(S_s, P_e) \quad \text{(Eq.164)}$$

TABLE 9 - $u_2/u_1 = f(h, M \sin \theta_s)$

Altitude[1]	M sin θ_s 4	M sin θ_s 6	M sin θ_s 8	M sin θ_s 10	M sin θ_s 12	M sin θ_s 14	M sin θ_s 16	M sin θ_s 20	M sin θ_s 24	M sin θ_s 28	M sin θ_s 36
0	0.207	0.161	0.139	0.121	0.111	0.105	0.102	0.090	0.082	0.082	0.085
50	0.212	0.171	0.147	0.128	0.111	0.104	0.101	0.090	0.078	0.076	0.080
100	0.211	0.168	0.142	0.118	0.102	0.097	0.094	0.080	0.071	0.067	0.077
150	0.208	0.177	0.129	0.103	0.093	0.091	0.083	0.072	0.063	0.062	0.067
200	0.206	0.164	0.129	0.101	0.087	0.080	0.078	0.065	0.059	0.058	0.068
250	0.216	0.175	0.145	0.114	0.093	0.083	0.086	0.070	0.060	0.054	0.059
300	0.212	0.172	0.147	0.106	0.089	0.082	0.072	0.067	0.056	0.049	0.041

[1] In thousands of feet.

5.6.2 (Continued):

Parameters u_e, h_w, μ_e, $N_{Re,s}$ are determined by procedures previously described. T_e^*, $g\rho_e^*$, and μ_e^* are evaluated at the local pressure and entropy and h_e^* values.

To perform the mass balance needed to locate the entering stream, the following boundary layer parameters are needed:

$$\delta_L = \frac{5.3 x N_{Pr}^{2/3}}{g\rho_e u_e (h_e^*/h_e)^{0.18}} \left[\frac{\dot{q}}{(h_r - h_w)}\right] \quad \text{(Eq.165)}$$

The displacement boundary layer thickness is

$$\delta_L^* = \left(\frac{\delta_L^*}{\delta_L}\right)\delta_L \quad \text{(Eq.166)}$$

where:

$$\frac{\delta_L^*}{\delta_L} = \frac{(h_t/h_e) + 3.36(h_w/h_e) - 1.376}{(h_t/h_e) + 3.36(h_w/h_e) + 4.79} \quad \text{(Eq.167)}$$

$$\theta_L = \frac{0.663 x \dot{q} N_{Pr}^{2/3}}{g\rho_e u_e (h_r - h_w)} \quad \text{(Eq.168)}$$

$$N_{Re,\theta} = \frac{g\rho_e u_e \theta_L}{\mu_e} \quad \text{(Eq.169)}$$

5.6.2 (Continued):

For any assumed shock angle θ_s, all the above calculations can be performed. A mass balance residual is then computed:

$$\Delta M = r_s^{2/(2-k)} g\rho_\infty U_\infty - g\rho_e u_e (\delta - \delta^*)(2r_e)^k \qquad \text{(Eq.170)}$$

where:

δ and δ^* are the velocity and displacement boundary layer thickness for either laminar or turbulent flow

The first term on the right-hand side represents the mass crossing the shock at radius r_s when the shock angle is measured. The functional relationship between r_s and θ_s for a given freestream Mach number can be determined from the shock shapes given in Paragraph 5.4. The second term on the right-hand side represents the mass flow through the boundary layer at the point.

During the iteration process, the mass balance residual, ΔM, is used as the dependent variable, and r_s as the independent variable.

5.6.2.1 Turbulent Flow, Zero Mass Addition Option: For turbulent flow, the momentum thickness θ enters into the calculations:

$$\theta_T = \frac{0.037}{g\rho_e u_e^{[2+(\delta_T^*/\theta_T)]}} \cdot \left\{ \int_0^o g\rho_e u_e^{[2.25+1.25(\delta_T^*/\theta_T)]} \cdot \mu_e^{0.25} (\varepsilon y^k)^{1.25}\, dS \right\}^{0.8} \qquad \text{(Eq.171)}$$

where:

$$\varepsilon = \left(\frac{g\rho_e^*}{g\rho_e}\right)^{0.8} \left(\frac{\mu_e^*}{\mu_e}\right)^{0.2} \qquad \text{(Eq.172)}$$

For $(h_t/h_e) \leq 6$:

$$\frac{\delta_T}{\theta_T} = 8 + \left(1.29\frac{h_w}{h_r} + 1\right)\left(1.51\frac{h_t}{h_e} - 0.51\right) \qquad \text{(Eq.173)}$$

$$\frac{\delta_T^*}{\theta_T} = -1 + \left(1.29\frac{h_w}{h_r} + 1\right) \cdot \left(1.04\frac{h_t}{h_e} - 0.04\right) \qquad \text{(Eq.174)}$$

5.6.2.1 (Continued):

For $(h_t/h_e) > 6$:

$$\frac{\delta_T}{\theta_T} = 8 + \left(1.29\frac{h_w}{h_r} + 1\right)\cdot\left(1 + 3.02\sqrt{\frac{h_t}{h_e}} - 1\right) \quad \text{(Eq.175)}$$

$$\frac{\delta_T^*}{\theta_T} = -1 + \left(1.29\frac{h_w}{h_r} + 1\right)\cdot\left(1 + 2.08\sqrt{\frac{h_t}{h_e}} - 1\right) \quad \text{(Eq.176)}$$

θ_T is obtained by integrating from the stagnation point to the point, even though the flow along the body preceding the point may have been laminar.

Velocity and displacement boundary layer thicknesses are

$$\delta_T = \left(\frac{\delta_T}{\theta_T}\right)\theta_T \quad \text{(Eq.177)}$$

$$\delta_T^* = \left(\frac{\delta_T^*}{\theta_T}\right)\theta_T \quad \text{(Eq.178)}$$

5.7 Boundary Layer Transition:

The boundary layer during certain critical portions of the entry trajectory will become or begin to become turbulent. With transition from laminar to turbulent flow, large increases occur in skin friction, heat transfer rate, and surface shear forces. Unfortunately, present-day (circa 1968) understanding of transition in a hypersonic boundary layer is far from adequate. Literature surveys reveal the massive effort, both theoretical and experimental, that has been exerted to solve the transition problem. However, the majority of this work has been confined to areas not considered applicable for hypersonic entry vehicles. The theoretical work has concerned itself with the stability of the laminar boundary layer. This work has produced, for low supersonic flows, critical Reynolds numbers below which disturbances would be dissipated by viscous forces. However, the usefulness of the analytical results is very questionable, especially with respect to high Mach numbers (about 20).

Regardless of the Mach number restraint, further practical arguments demonstrate the difficulty in using a theoretical approach to the transition problem. Even a nebulous difference between critical Reynolds number appears to be significant.

5.7 (Continued):

A correlation, which appears to collapse the available test data as well as any other that is examined, is based on using $N_{Re,\theta}/M$ as the dependent variable and $(h_w/h_{adw})^{1/2}$ as the entry argument. The following equation was used to determine the Reynolds number based on momentum thickness:

$$N_{Re,\theta} = \frac{0.664}{(1+2k)^{1/2}} (N_{Re,s})^{1/2} \left(\frac{h}{h^*}\right)^{0.19} \quad \text{(Eq.179)}$$

Figures 133 and 134 show a successful correlation useful for design application. Figure 133 plots the data against $(h_w/h_{adw})^{1/2}$, whereas Figure 134 plots the same data against (h_w/h_{adw}). It appears that the compressed enthalpy parameter yields slightly less scatter than Figure 134. The line through the data was determined by a least squares fit. Both curves show increasing Reynolds number of transition with increasing local Mach number, an observation made by numerous experimenters. Further, the correlation presented is for nonmass injection conditions and for very low angles of attack. A reduction by a factor of 2 in the values presented have been observed. In all cases, extreme caution must be taken against the universal use of the data in Figures 133 and 134.

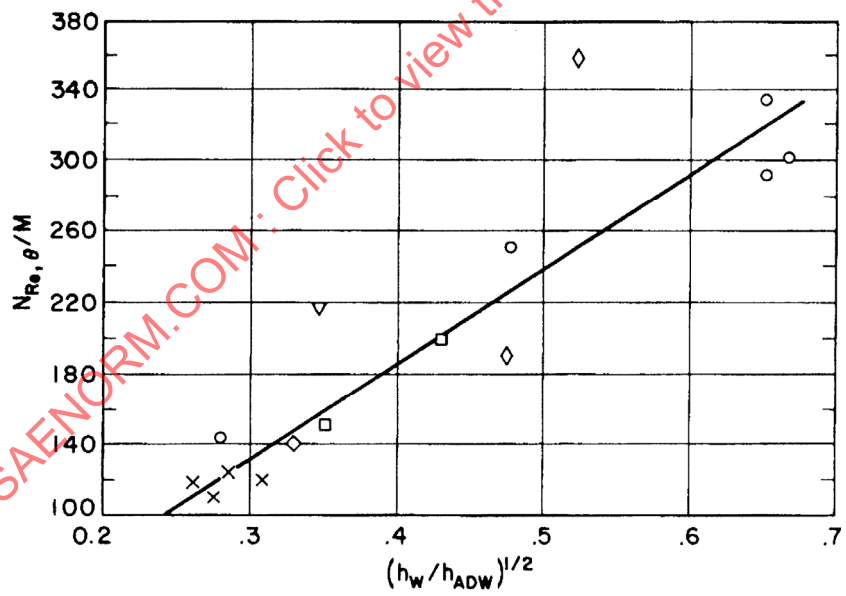

FIGURE 133 - Transition Reynolds Number as a Function of Mach Number and Wall Cooling
(Subscript ADW Means Adiabatic Wall)

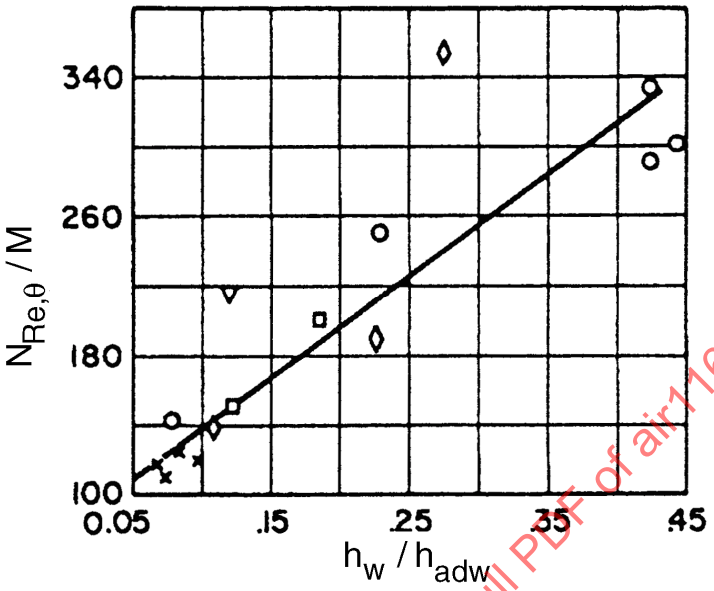

FIGURE 134 - Transition Reynolds Number as a Function of Mach Number and Wall Cooling

5.8 Stagnation Region Velocity Gradient:

The velocity field in the vicinity of the stagnation point of an axisymmetric or two-dimensional configuration is normally defined as the velocity gradient. It is a necessary parameter for the evaluation of stagnation point (region) heat transfer. It is defined as

$$\left(\frac{du_e}{ds}\right)_{s=0} = \frac{U_\infty}{r_n}\left[\frac{g\rho_\infty}{g\rho_t}\left(2 - \frac{g\rho_\infty}{g\rho_t}\right)\right]^{1/2} \qquad M \geq 1 \qquad \text{(Eq.180)}$$

$$\left(\frac{du_e}{ds}\right)_{s=0} = 1.5\frac{U_\infty}{r_n} \qquad M < 1 \qquad \text{(Eq.181)}$$

The preceding relations and Figure 135 are for hemispherical configurations only. For cut hemispheres, the velocity gradient values presented in Figure 136 should be used. For cut hemispheres and radius hemispheres, velocity gradient values from Figures 136 and 137 should be used. For cylindrical configurations, divide the above relations by a factor of 2.

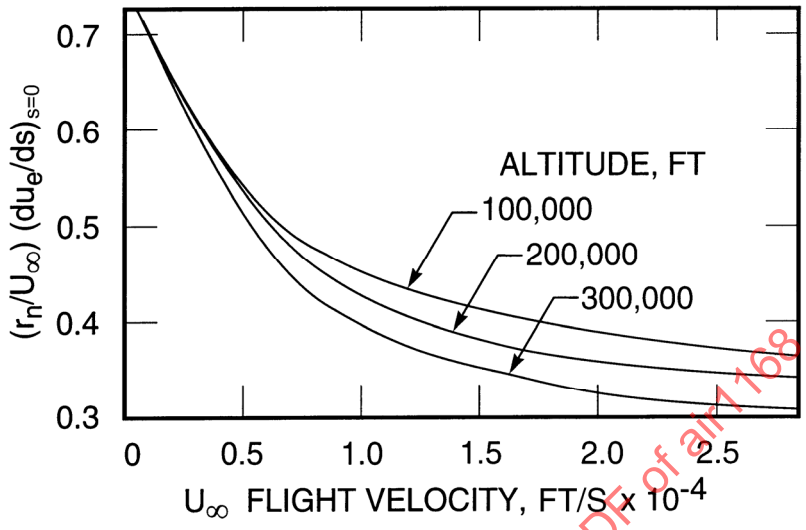

FIGURE 135 - Stagnation Point Velocity Gradients (From General Electric Data)

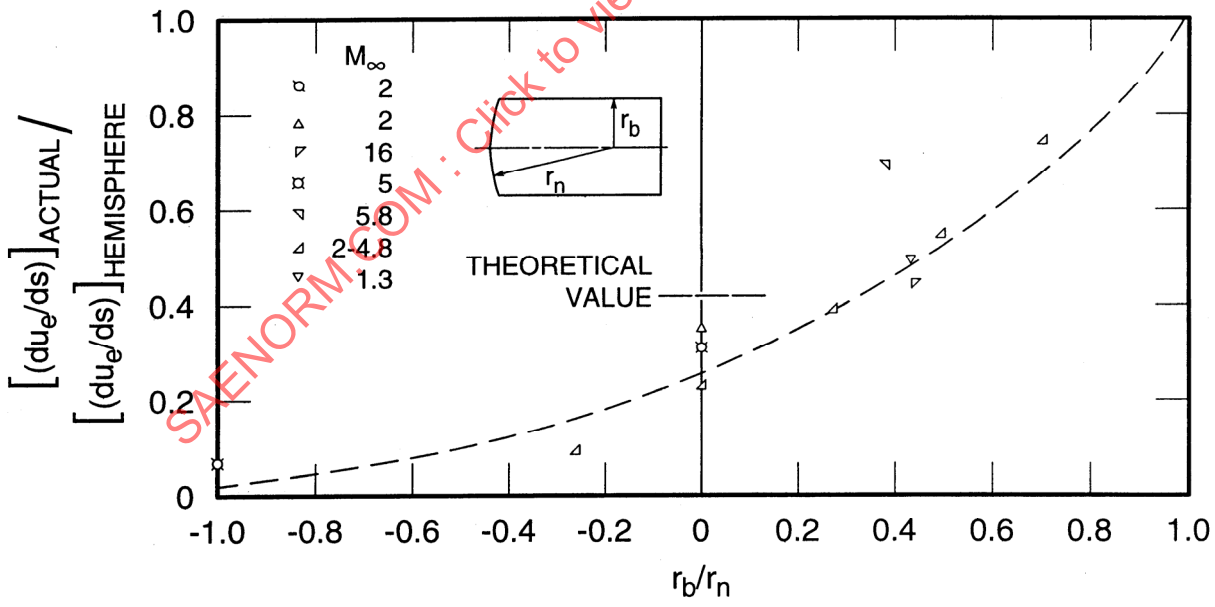

FIGURE 136 - Stagnation Point Velocity Gradient for Cut Hemisphere Family

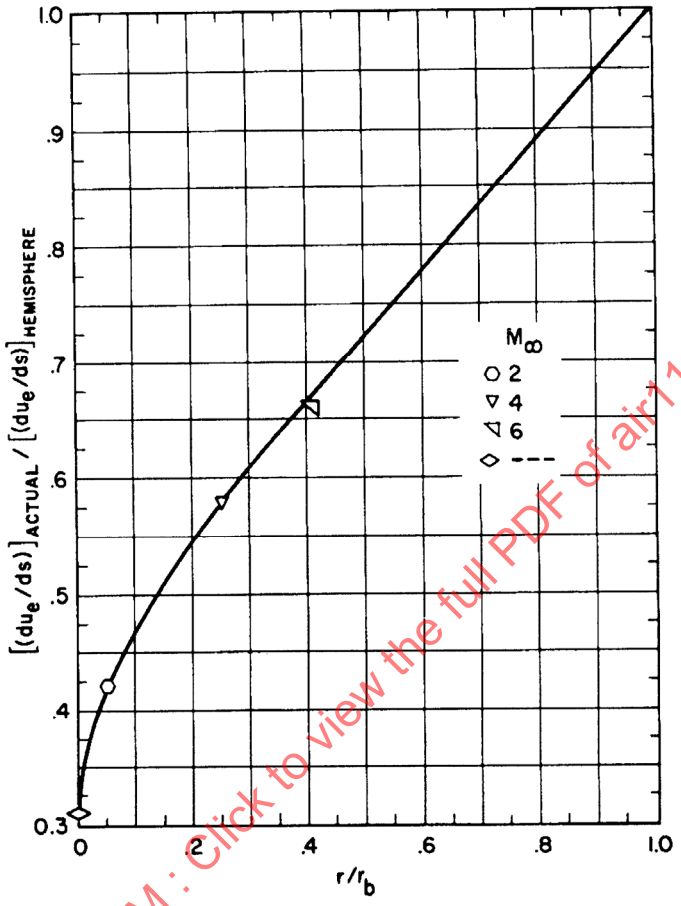

FIGURE 137 - Effect of Corner Radius on Stagnation Point Velocity Gradient for Flat Faced Cylinders

5.8 (Continued):

Another convenient parameter for the evaluation of shock layer thermal radiation is stagnation region shock detachment distance Δx. At hypersonic Mach numbers, Δx may be approximated as $\Delta x \cong 0.1 r_n$ (for hemispherical configurations). It was given in Figure 128 as a function of density ratio $g\rho_\infty/g\rho_i$. For cut hemispherical noses, utilize Figure 138.

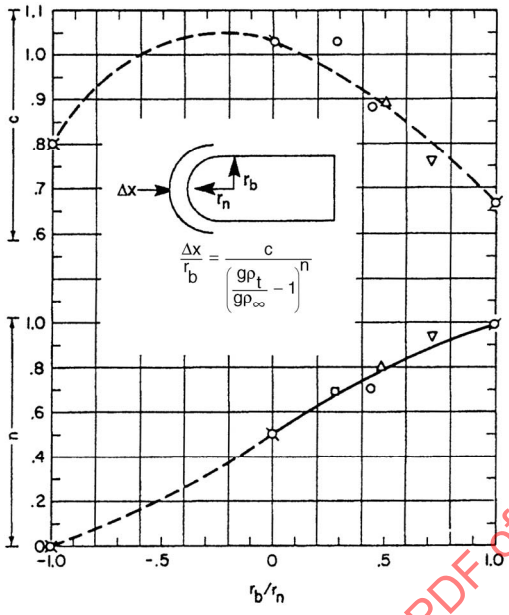

FIGURE 138 - Correlation for Shock Detachment Distance for Blunt-Nosed Axisymmetric Forebodies of Cut Hemisphere Family

6. ENTRY HEAT TRANSFER PREDICTIVE METHODS:

This section provides methods and techniques for defining the convective and the shock layer thermal radiation environment of ballistic and lifting entry systems. In several cases, simplifications of analytical expressions for aerodynamic heating are made to provide the designer with the degree of simplification or approximation useful for estimation purposes. This section does not provide a step by step procedure for the solution of all aerodynamic heat transfer problems. However, it provides methods and techniques for a large number of contemporary problems.

6.1 Entry Convective Heat Transfer/Continuum Flow:

For most entry vehicle systems, the thermal protection subsystem is primarily designed by the aerothermodynamic environment of forced convection in the continuum flow regime. For entry vehicle velocities less than 26,000 ft/s, shock layer thermal radiation is normally negligible and needs to be checked only approximately for each design and its intended trajectory. For velocities in excess of 26,000 ft/s, shock layer thermal radiation should always be carefully estimated and included with the convective heat transfer. For lifting entry vehicles or for entry satellites, low-density flow corrections to continuum flow aerodynamic heat transfer results should be checked to determine their potential significant contribution to the continuum thermal pulse. The problems of heat transfer at angle of attack for both ballistic and glide entry vehicles should be estimated to ensure that a condition of entry vehicle pitch or yaw motion is not in frequency with spin rate so that one side of the vehicle is exposed at high angle of attack and high heating rates for extended periods of time.

6.1.1 Stagnation Point Heat Transfer: For stagnation point heat transfer predictions the method of Lees (Reference 22) for air in thermodynamic equilibrium, modified by evaluation of the local thermodynamic air properties at a reference enthalpy rather than at the edge of the boundary layer, is valid for velocities equal to or less than 26,000 ft/s. The Lees method with a coefficient change is recommended for rapid design evaluation because of its simplicity. The stagnation point heat rate according to the modified Lees solution is given by

$$\dot{q} = \frac{0.5\sqrt{2}}{N_{Pr}^{2/3}} \sqrt{g\rho_t\mu_t \left(\frac{du_e}{ds}\right)_{s=0}} \cdot \sqrt{\frac{\rho^* g}{\rho_t g}\frac{\mu^*}{\mu_t}} (h_t - h_w) \qquad \text{(Eq.182)}$$

A Prandtl number of 0.72 is used. Thermodynamic properties are obtained from tables for air in chemical equilibrium for the predicted stagnation pressure and enthalpy. A curve fit to the National Bureau of Standards (NBS) calculations is used to describe the variation of viscosity with temperature, presented in Reference 22 as

$$\mu = 2.49 \times 10^{-7} (T)^{0.630} \qquad \text{(Eq.183)}$$

The starred quantities of Equation 182 are evaluated at the values of the predicted pressure and the reference enthalpy, where for any point on the surface

$$\frac{h^*}{h_e} = 0.5 + 0.5\frac{h_w}{h_e} + 0.22r\frac{u_e^2}{2Jgh_e} \qquad \text{(Eq.184)}$$

At the stagnation point, Equation 184 is reduced to

$$\frac{h^*}{h_e^0} = 0.5 + 0.5\frac{h_w}{h_e^0} \qquad \text{(Eq.185)}$$

where:

h_e^0 = Boundary edge enthalpy at the stagnation point

The velocity gradient is determined according to the procedures in Paragraph 5.8.

A comparison with results from the theories of Fay and Riddell (Reference 23) and Scala (Reference 24) to determine both the level and the trend of predicted to observed heat transfer with increasing velocity with these theories shows less than a ±10% deviation for velocities up to 26,000 ft/s. (See Appendix, Paragraph 6.3.1.)

A simplification of the modified Lees relation suitable for design purposes is given in the Appendix, Paragraph 6.3.2, as (Equation 286)

$$\dot{q} = f_L (g\rho_\infty)^{0.5} \mu_\infty^{3.0} \qquad \text{(Eq.186)}$$

6.1.1 (Continued):

where, for $h_w = 0$,

$$f_L \equiv \frac{1.85 \times 10^{-5}}{N_{Pr}^{2/3}} \left(\frac{\gamma_\infty - 1}{\gamma_\infty}\right)^{0.25} \cdot \left(\frac{\gamma + 1}{\gamma - 1}\right)^{0.25} \left(\frac{\mu_\infty}{a_\infty}\right)^{0.5} \sqrt{\frac{1}{r_n}} \qquad \text{(Eq.187)}$$

For constant values of $\gamma_\infty = 1.4$, $\gamma = 1.2$, $N_{Pr} = 0.72$, and $T_\infty = 500$ °R, Equation 186 becomes

$$\dot{q}\sqrt{r_n} = 3.16 \times 10^{-9} (g\rho_\infty)^{0.5} u_\infty^{3.0} \qquad \text{(Eq.188)}$$

Equation 188 has been evaluated and the results presented in Figure 139 for a range of altitudes from 35,000 to 300,000 ft and a range of freestream velocities from 6000 to 26,000 ft/s.

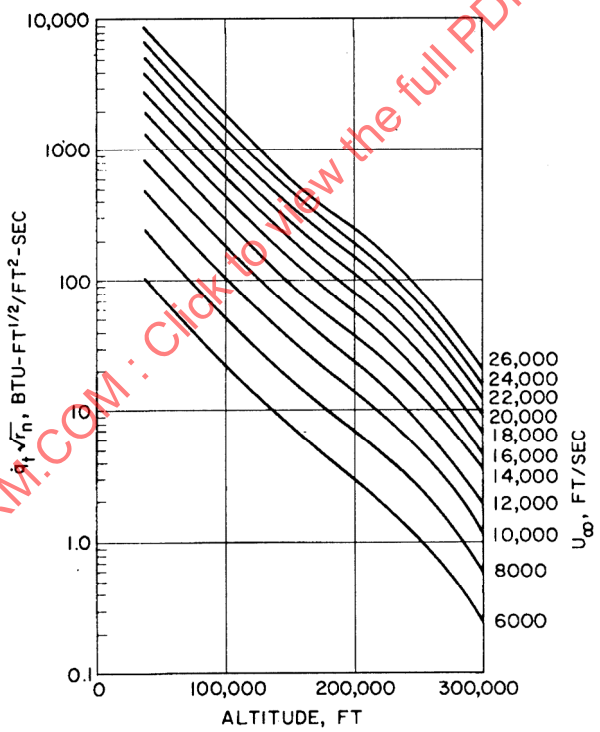

FIGURE 139 - Approximate Stagnation Point Heat Flux, $T_w = 0$ °R

The effects of nonzero wall temperature on the stagnation point (and turbulent) heat flux is given in Figure 140 (Reference 25).

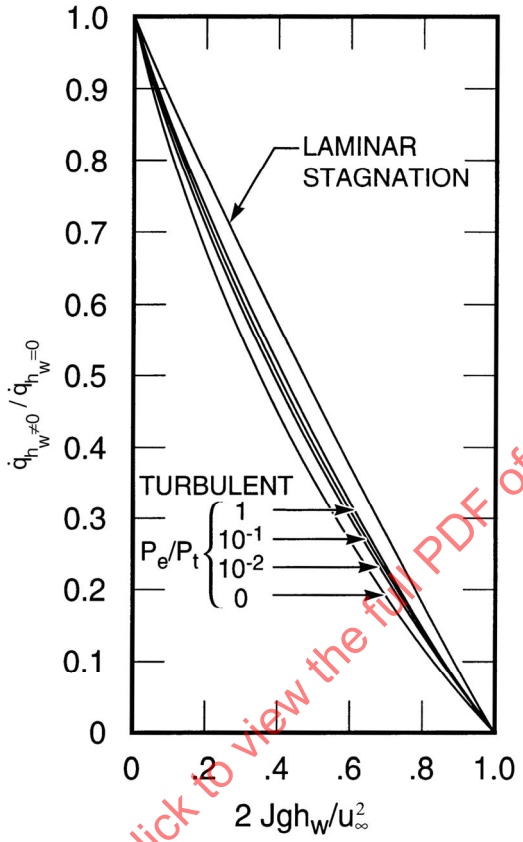

FIGURE 140 - Nonzero Wall Temperature Correction (γ = 1.2)

6.1.1.1 Stagnation Point Heat Transfer for Blunt Axisymmetric Configurations: In the preceding section, relatively simple analytical methods were presented for determining convective heat transfer for hemispherical forebodies in hypersonic flow. For data on blunt forebodies of shapes other than hemispherical, empirical correlations are based on experimental data for the "cut hemisphere" family of blunt forebody shapes, including concave and hemispherical nose extremes. These correlations are first approximations, pending more exact determination by flow field computer program or experiment for the particular configuration.

The correlations are limited to forebody shapes of the "cut hemisphere" family in which the forebody surface is a section cut from a hemisphere. The logical dimensionless shape parameter is r_b/r_n, where r_b and r_n are defined in Figure 141.

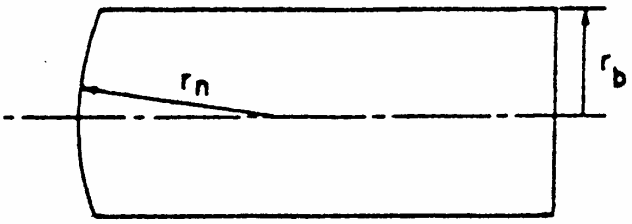

FIGURE 141 - Forebody Surface as a Section Cut from a Hemisphere

6.1.1.1 (Continued):

Three special cases and their corresponding values of r_b/r_n are illustrated in Figure 142. A negative value of r_b/r_n indicates a concave nose.

FIGURE 142 - Three Special Cases

A convenient way of representing the effects of bluntness on the dependent parameters such as heat flux or velocity gradient is to present dimensionless ratios in which the results are normalized with respect to the corresponding values for a hemispherical nose of the same gross outer dimension. For example, stagnation point heat flux can be given as $\dot{q}_t / (\dot{q}_t)_{hemi}$, where $(\dot{q}_t)_{hemi}$ is based on a nose radius of r_b. This form of presentation minimizes Mach and Reynolds number effects which might otherwise be significant if the actual dimensional dependent variables were correlated.

A correlation of stagnation point heat flux for blunt asymmetric forebodies of the cut hemisphere family is given in Figure 143. The value of $\dot{q}_t$ is the experimentally determined value of stagnation point heat flux for the particular forebody geometry as defined by r_b/r_n. The value of $(\dot{q}_t)_{hemi}$ is the theoretical value of stagnation point heat flux of a hemispherical forebody whose nose radius r_n equals the body radius r_b of the model being tested, and was computed at the test conditions from the modification of the Lees expression, Equation 182.

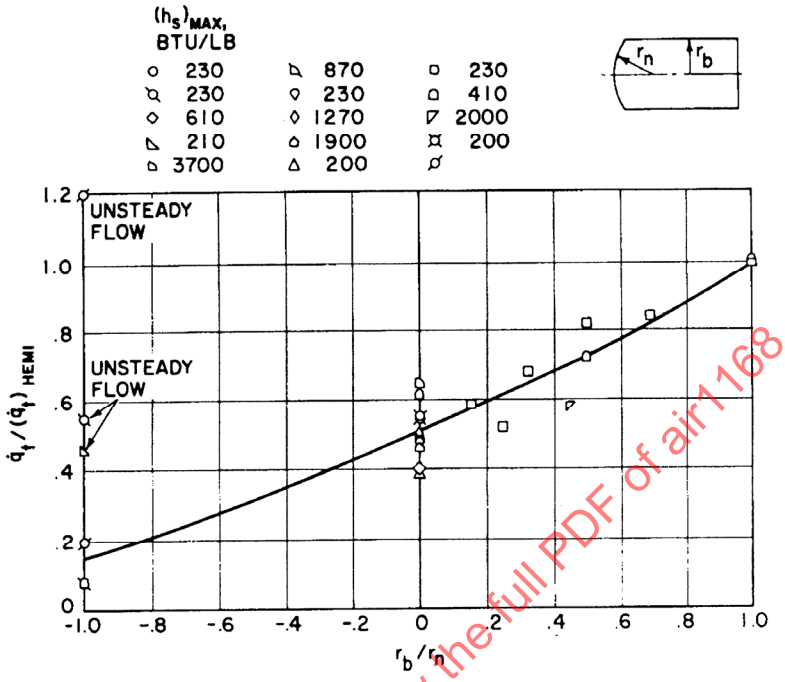

FIGURE 143 - Stagnation Point Heat Flux for Cut-Hemisphere Family

6.1.1.1 (Continued):

Each datum point plotted on Figure 143 (Reference 26) is the average of several points of different Mach and Reynolds numbers. For example, the h_s point of 2000 Btu/lb in Figure 143 (Reference 26), which is plotted as $(\dot{q}_t / \dot{q}_t)_{hemi} = 0.59$ is actually the average of five points whose values range from 0.42 to 0.73. Cross plots of $\dot{q}_t / (\dot{q}_t)_{hemi}$ versus M_∞ and $N_{Re,\infty}$ show no discernible Mach or Reynolds number effects within the scatter of data.

The large values of $\dot{q}_t / (\dot{q}_t)_{hemi}$ for the concave nose marked “unsteady flow” are due to a flow instability phenomenon which is characteristic of concave noses.

6.1.1.2 Stagnation Heat Transfer at Velocities > 26,000 ft/s: Although radiative heating increases rapidly with flight speed and can become a serious problem at speeds much in excess of 26,000 ft/s, depending upon body configuration and size and nose bluntness, convective heating is, for many practical flight cases, the dominant heat transfer mechanism. Methods for determining aerodynamic heat transfer at lower speeds, particularly for simple hemispherical shapes, were given in the preceding section. At higher speeds the primary concern is adequacy of the extrapolation of lower-speed theory and whether new phenomena enter whose effects are sufficiently in doubt to make extrapolation uncertain. At these higher speeds, air ionization in addition to air dissociation is significant.

6.1.1.2 (Continued):

Convective heat transfer in partially ionized air has been examined by several investigators (References 27-36). Adams (Reference 27) estimated the heat transfer increase due to ionization in a frozen boundary layer, using a Lewis number of unity for the atoms and 2 for the ion-electron pairs, with a thermal conductivity proportional to the one-half power of the temperature up to 8000 K, and the five-halves power above that. He found that up to 45,000 ft/s, there was a maximum increase of 30% above the extrapolation of lower-speed theories. Three other investigations (References 28-30) have dealt with the equilibrium boundary layer, using the transport properties of Hansen (Reference 31). These are "equilibrium" transport properties in which the contributions of dissociation and ionization are included in the specific heat and thermal conductivity. The results indicate heat transfer rates somewhat less then those found by Adams (Reference 27).

Heat transfer in ionized nitrogen has been studied by Scala and Warren (Reference 32) and by Pallone and Van Tassell (Reference 33), also for thermodynamic equilibrium. Scala uses his computed values of nitrogen transport properties as described in Reference 34, whereas Pallone and Van Tassell use transport properties developed by Yos (Reference 35). Scala found a very rapid rise in heat transfer above 30,000 ft/s, leading to values larger (by a factor of 2.5) than the other theories at 35,000 ft/s. Pallone and Van Tassell (Reference 33) found no such effect, and attributed the differences to different transport properties. Scala used a charge-exchange cross section for N - N^+ collisions which is two orders of magnitude smaller than the one used by Yos, and a N_2 - N^+ cross section one order of magnitude smaller. This had a major effect on the equilibrium thermal conductivity, resulting in Scala's value being one to two orders of magnitude above Yos' value in the range 10,000 to 20,000 K.

Experimental data included in References 28 to 30 agree generally with the respective theories. The results of several investigations for air and for typical CO_2 and N_2 gas mixtures are presented in graphical form in Figures 144 and 145. A summary of various experimental data, compared with theory, are also presented in these two figures. From these data a somewhat simplified form of the heat transfer parameter $\dot{q}\sqrt{r_n p_t}$ is obtained which is an extrapolation of lower-speed theory. From the experimental data scatter, it would appear that the results of Figure 145 are adequate for engineering purposes in the excess orbital velocity regime and for the entry heating analyses of planets Mars and Venus. They are consequently recommended for design purposes.

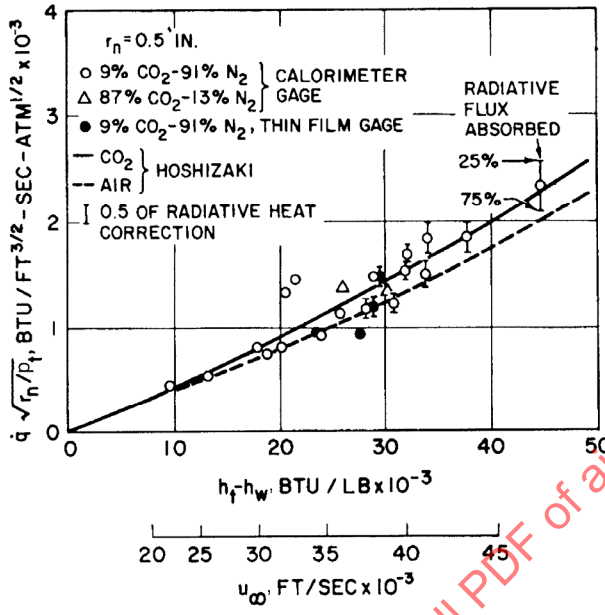

FIGURE 144 - Hypervelocity Stagnation Point Heat Transfer in Simulated Planetary Atmospheres in a Shock Tube

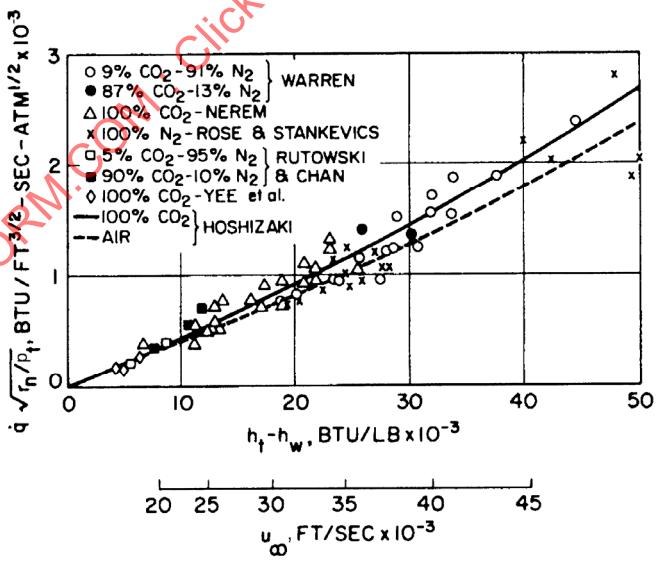

FIGURE 145 - Comparison of Stagnation Point Heat Transfer Results in Carbon Dioxide, Carbon Dioxide-Nitrogen Mixtures and Nitrogen Obtained by Several Experimenters

6.1.2 Local Laminar Heat Transfer: Methods for predicting aerodynamic heating level and distribution for an axisymmetric configuration are those of Lees (Reference 22) and Kemp and Detra (Reference 36). These were developed by applying local similarity methods, that is, by neglecting the effect of the tangential pressure gradients on the velocity profiles.

A modification of Lees method is given by

$$N_{Nu} = \frac{0.5 N_{Pr}^{1/3}}{\sqrt{2}} \cdot \left[\frac{(g\rho_e)^2 u_e^{\,2} r^2 s^2 \left(\frac{g\rho^* \mu^*}{g\rho_e \mu_e} \right)^2}{\int_0^s g\rho_e u_e \mu_e r^2 \left(\frac{g\rho^* \mu^*}{g\rho_e \mu_e} \right) ds} \right]^{0.5} \qquad \text{(Eq.189)}$$

where:

$$N_{Nu} = \frac{qsN_{Pr}}{\mu_e (h_r - h_w)} \qquad \text{(Eq.190)}$$

It is convenient to define

$$N^*_{Re,s} = \frac{(g\rho_e)^2 u_e^2 r^2 s^2 \left(\frac{g\rho^* \mu^*}{g\rho_e \mu_e} \right)^2}{\int_s^0 g\rho_e u_e \mu_e r^2 \left(\frac{g\rho^* \mu^*}{g\rho_e \mu_e} \right) ds} \qquad \text{(Eq.191)}$$

Combining Equations 189 and 191 gives

$$N_{Nu} = \frac{0.5 N_{Pr}^{\,1/3}}{\sqrt{2}} \sqrt{N^*_{Re,s}} \qquad \text{(Eq.192)}$$

The accuracy of the results of Equation 192 is strongly dependent upon the accurate definition of the local flow parameters u_e, h_3, and $g\rho_e$. As shown in Paragraph 5, it is important on long laminar runs or on slender cones, where x/r_n exceeds 10 to 15, to account for the external inviscid flow field entropy layer, rather than to assume isentropic expansion, to obtain the local flow quantities.

6.1.2 (Continued):

An evaluation of aerothermodynamic heat transfer requires a knowledge of the inviscid flow field, particularly a knowledge of the pressure distribution impressed on the surface of the body. For purposes of preliminary design this pressure distribution must frequently be assumed and initial estimates of aerodynamic heat transfer made. In evaluations of test data it is often inconvenient to measure the pressure in addition to the heat transfer (temperature) and therefore the pressure distribution again must be assumed. When a great many values are involved in the evaluation of test data (flight test data, for example), although the pressure may have been measured, it is often convenient to use an assumed pressure distribution for the calculation of theoretical heat transfer and then correct the initial values. For the conditions described above the possibility exists of obtaining the theoretical heat transfer by using one pressure distribution while preferring to obtain it by using another different pressure distribution.

A readily applied pressure variation correction to the heat transfer calculation has been developed by Walker (Reference 25). Results for laminar flow are given in Figures 146 and 147.

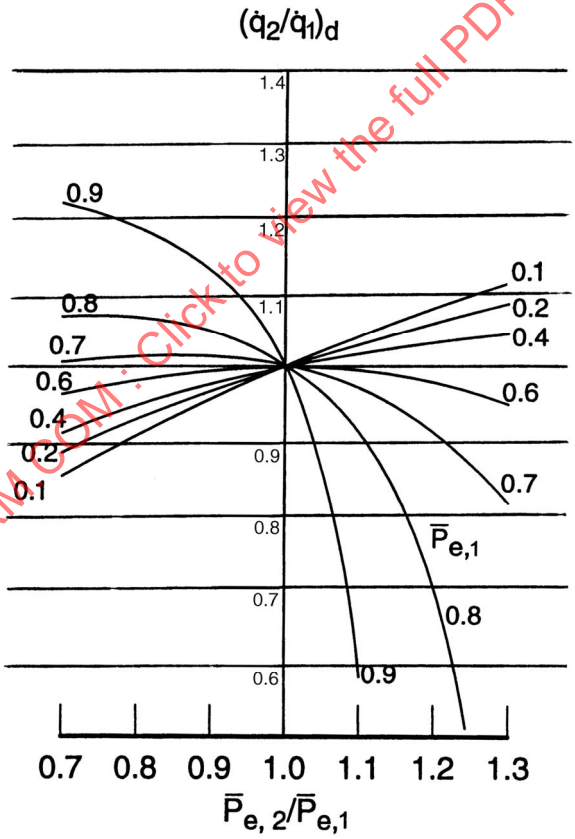

FIGURE 146 - Effects of Moderate Pressure Variations on Laminar Heat Transfer; $\gamma = 1.2$, $\bar{P}_e = P_e/P_t$

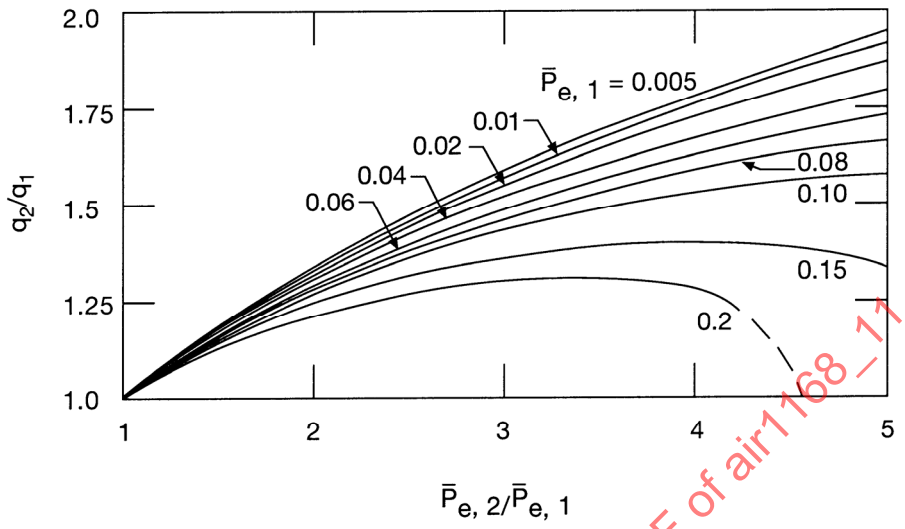

FIGURE 147 - Large Pressure Effects on Laminar Heat Transfer;
$\gamma = 1.2$, $\bar{P}_e = P_e/P_t$

6.1.2 (Continued):

The distribution of local laminar heat transfer over a hemisphere is adequately predicted by the modified method of Lees (Reference 22). For a hemisphere, the heat flux is maximum at the stagnation point and drops monotonically as expansion occurs around the body.

It has been shown by several experimental investigations that blunting the forebody decreases the stagnation point heat flux, as shown in Figure 143. However, this advantage is offset by the increase in heat flux as expansion occurs around the body (see Figures 148 through 150).

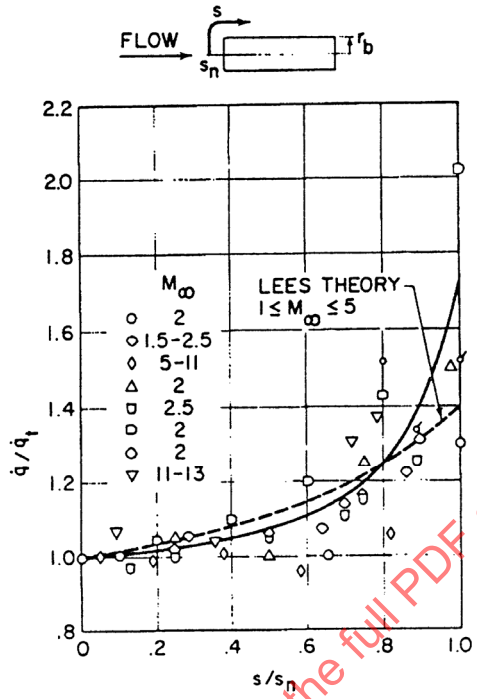

FIGURE 148 - Distribution of Laminar Heat Flux on a Flat Nosed Body;
Symbols Denote Experimental Data
(s_n is the Distance from the Center of the Cylinder to the Corner; for a Flat Face Cylinder, $s_n = r_b$)

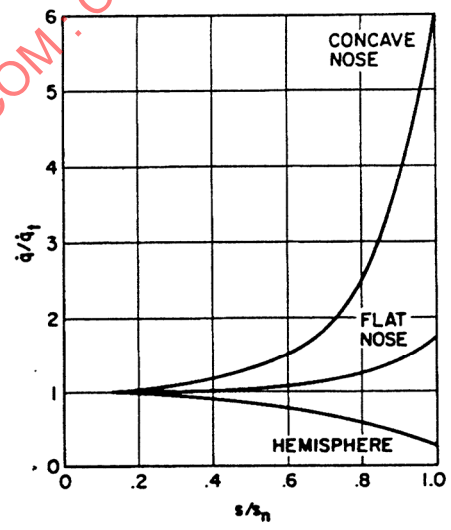

FIGURE 149 - Comparison of Laminar Heat Flux Distribution
for Hemisphere, Flat Nose, and Concave Nose

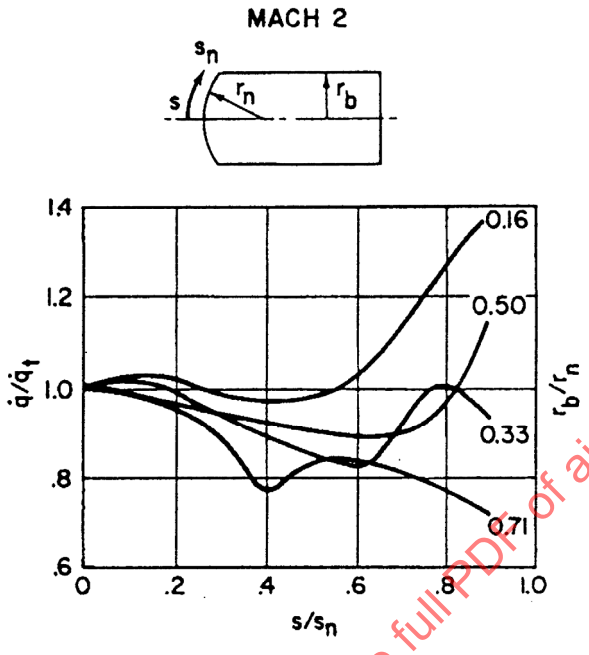

FIGURE 150 - Distribution of Laminar Heat Flux for Several Blunt-Nose Bodies

6.1.2 (Continued):

Most of the available data are for low supersonic Mach numbers. In Figure 148, somewhat conflicting effects of increasing Mach number are apparent in the data for M_∞ in the region between 7 and 12 for a flat nose. Each datum point in these figures for free flight tests is the average of several points obtained in the higher Mach number range of flight. Crossplots of $\dot{q}/\dot{q}_t$ versus M_∞ from the free flight tests show no discernible Mach number effect within the large scatter of data.

The theoretical values of $\dot{q}/\dot{q}_t$ obtained by the Lees method are given in Figures 149 and 150 (from Reference 37), based on experimental pressure distributions. The Lees method can be used for a reasonable first approximation of the laminar heat flux distribution on blunt forebodies, provided the appropriate pressure distribution is used for the particular nose shape. Precise calculations require a detailed and accurate pressure distribution. For design purposes the results in Figures 148 to 150 are adequate.

6.1.3 Turbulent Heat Transfer: The simplest method of predicting the turbulent heat transfer rate to a blunt body in hypersonic flow is provided by the flat plate reference enthalpy (FPRE) method (see Reference 38). This method, derived for a flat plate with a zero pressure gradient, combines the Blasius turbulent skin friction relation, Eckert's reference enthalpy compressibility concept, and Colburn's Reynolds analogy. In terms of a Nusselt number and Reynolds number, the FPRE method is given by

$$N_{Nu} = 0.0296(N_{Pr})^{1/3}(N_{Re,s})^{0.8} \quad \text{(Eq.193)}$$

where the Nusselt number is defined as

$$N_{Nu} \equiv \frac{\dot{q}_t N_{Pr} s}{\mu_e (h_r - h_w)} \quad \text{(Eq.194)}$$

and where the Reynolds number is defined as

$$N_{Re,s} = \frac{g\rho_e u_e s}{\mu_e}\varepsilon^{1.25} \quad \text{(Eq.195)}$$

where:

$$\varepsilon \equiv \left(\frac{\mu^*}{\mu_e}\right)^{0.2}\left(\frac{g\rho^*}{g\rho_e}\right)^{0.8} \quad \text{(Eq.196)}$$

The starred quantities are evaluated with the local value of pressure and the local value of the reference enthalpy

$$\frac{h^*}{h_e} = 0.5 + 0.5\left(\frac{h_w}{h_e}\right) + 0.22r\frac{u_e^2}{2Jgh_e} \quad \text{(Eq.197)}$$

where r is assumed to be 0.896. The FPRE relation for turbulent heat transfer may be simplified; for maximum heat transfer rate see Appendix, Paragraph 6.3.3. A method of predicting the turbulent heat transfer rate for an axially symmetric body with finite pressure gradient is given in Reference 39. In this derivation the Blasius flat plate skin friction relation and a modified Reynolds analogy have been used. The momentum and energy integral equations have been solved without resorting to explicit assumptions for boundary layer velocity distribution, the enthalpy-velocity relation, or the value of the Prandtl number. This solution yields:

$$\dot{q}_T = \frac{0.0296 g\rho_e u_e (\mu_e r^k)^{0.25}\varepsilon(h_r - h_w)}{N_{Pr}^{2/3}\left[\int_0^s g\rho_e u_e \mu_e^{0.25} r^{1.25k} ds\right]^{0.2}} \quad \text{(Eq.198)}$$

6.1.3 (Continued):

where:

k = 0 for a two-dimensional body
k = 1 for an axisymmetric body

To consider the altitude and freestream velocity effects when $\dot{q}_T s^{0.2}$ is maximum with respect to pressure P_e/P_t it is convenient to use the approximate turbulent flat plate reference enthalpy equation. For constant values $\gamma_\infty = 1.4$, $\gamma = 1.2$, $N_{Pr} = 0.72$, $T_\infty = 500$ °R, and $T_w = 0$ °R. This equation becomes

$$(\dot{q}_T s^{0.2})_{max} = 4.26 \times 10^{-8} (g\rho_\infty)^{0.8} U_\infty^{3.0} \qquad \text{(Eq.199)}$$

Figures 151A and 151B show this equation for rapid prediction purposes. As in the case of local laminar heat transfer distribution, it is convenient for the designer to have a rapid method of evaluating the effect of another pressure distribution on the local turbulent heat transfer. Figures 152 to 154 provide corrections to the local pressure ratio. Pressure effects on heat transfer are given in Figure 153 for small variations in pressure ratio and in Figure 154 for large variations in pressure ratio. Note that in the previous approximations for local laminar flow and turbulent flow, local flow properties were determined by assuming isentropic expansion from the stagnation point to the local pressure.

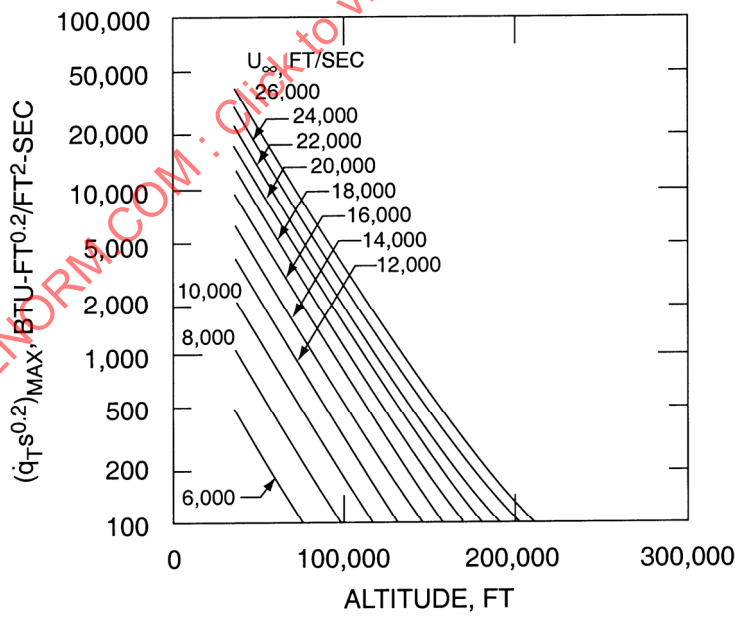

FIGURE 151A - Approximate Turbulent Heat Flux, $T_w = 0$

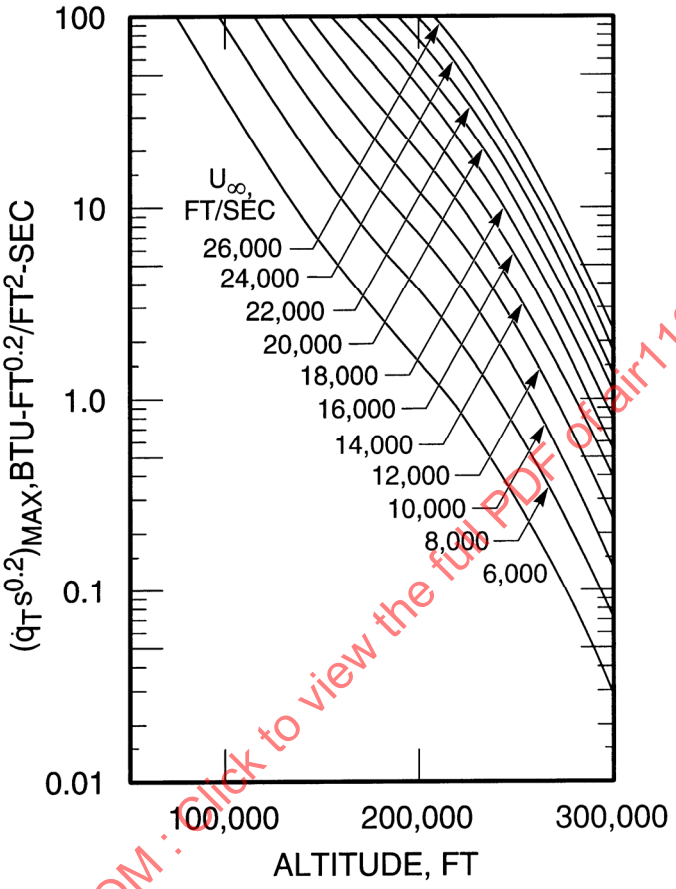

FIGURE 151B - Approximate Turbulent Heat Flux (Continued from Figure 151A)

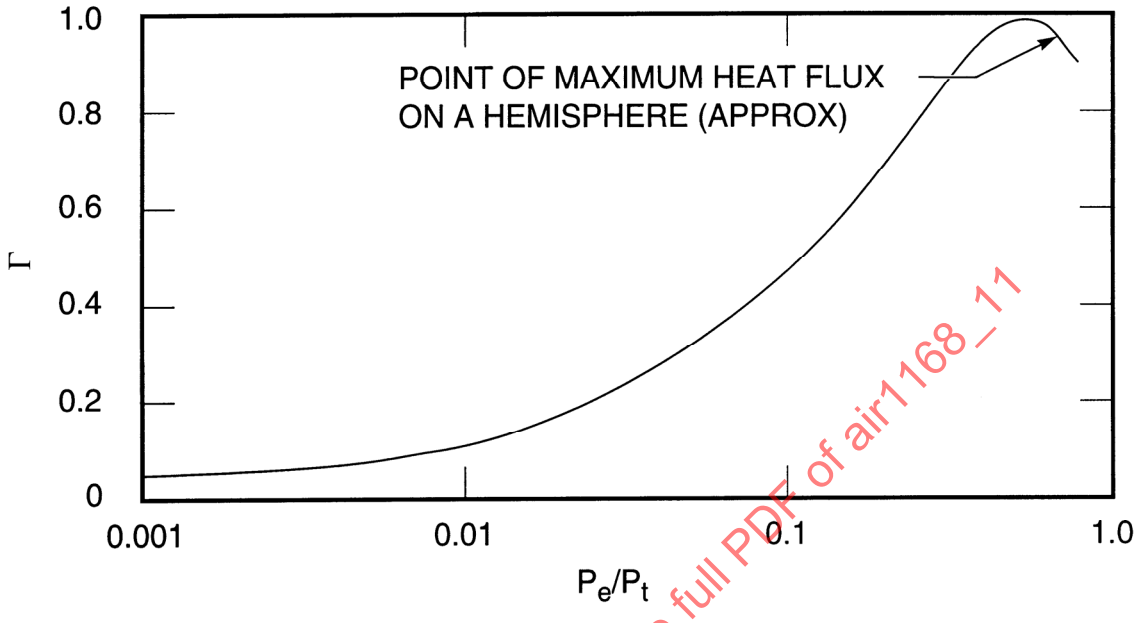

FIGURE 152 - Pressure-Function Ratio for Approximate Turbulent Heat Flux, T_w = 0 °R

$$\Gamma = \left[\dot{q}_T s^{0.2} / (\dot{q}_T s^{0.2})_{max}\right] = \frac{1}{0.17}\left(\frac{P_e}{P_t}\right)^{0.76}\left[1-\left(\frac{P_e}{P_t}\right)^{0.167}\right]^{0.4} \Bigg/ \left[1+1.272\left(\frac{P_e}{P_t}\right)^{0.167}\right]^{0.46}$$

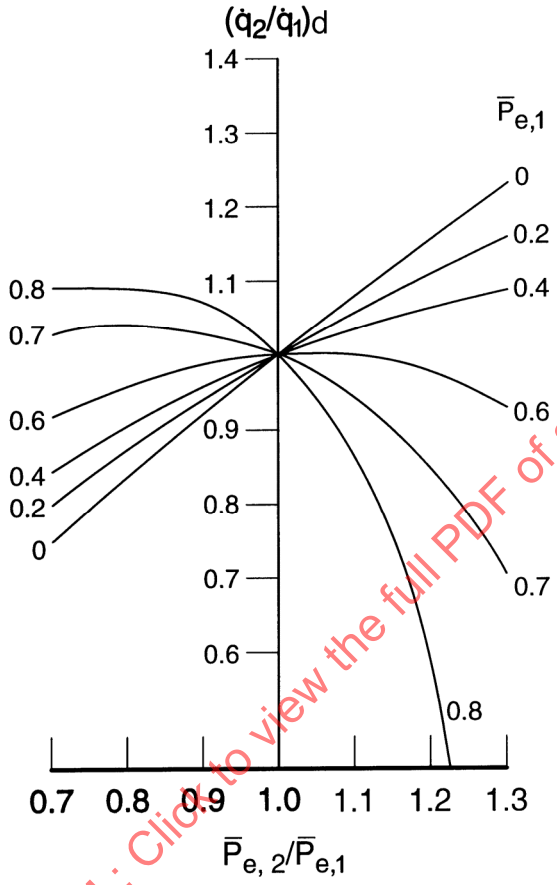

FIGURE 153 - Effects of Moderate Pressure Variations on Turbulent Heat Transfer; $\bar{P}_e = P_e/P_t$,$\gamma = 1.2$

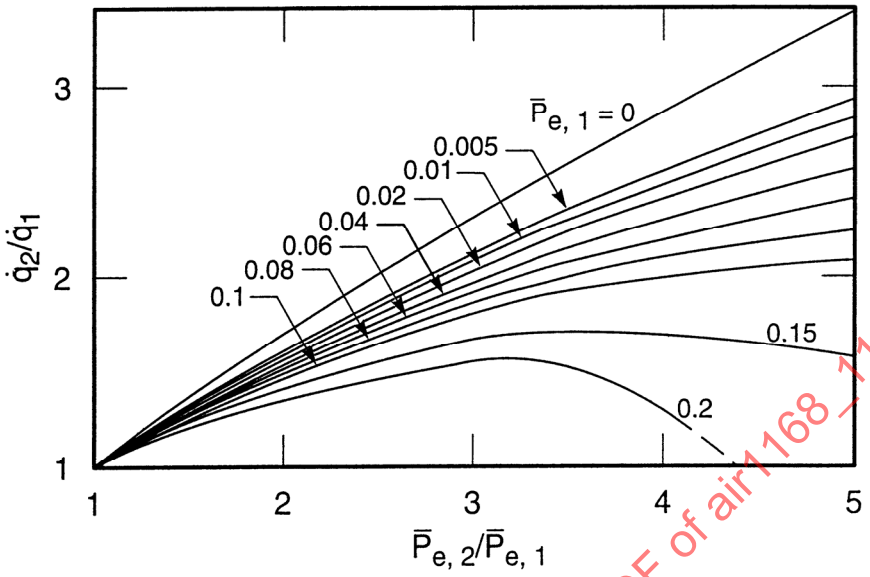

FIGURE 154 - Large Pressure Effects on Turbulent Heat Transfer, $\bar{P}_e = P_e/P_t$,$\gamma = 1.2$

6.1.3.1 Turbulent Boundary Layer Correction at High Reynolds Numbers: In most analyses of turbulent flow a modified form of the Blasius flat plate skin friction coefficient is employed because of its algebraic simplicity. For the range of Reynolds numbers from 10^5 to 10^7, the Blasius equation is in good agreement with the incompressible skin friction data (Reference 40). However, for Reynolds numbers greater than 10^7, the Blasius equation lies below the data. Good agreement with the data over the entire range of Reynolds numbers is given by the Schultz-Grunow relation (Reference 41). However, the algebraic form of the latter equation is rather unwieldly for most applications. Therefore its use has usually been restricted to flat plate conditions.

In the past, local Reynolds numbers occurring on blunt-nosed entry vehicles have not exceeded a value of the order of 10^7. Recently, however, missions have been defined for relatively sharp conical configurations on which the Reynolds number reaches the order of 10^8 and higher. Therefore, although the current turbulent heat transfer method used in design programs is valid for blunt-nosed vehicles, the range of validity may be exceeded for sharp conical configurations.

The Schultz-Grunow equation can be approximated, for Reynolds numbers greater than 10^7, by an equation of a relatively simple algebraic form. With this simplification, a correction is derived which can be applied to the current heat transfer calculation to account for the invalidity of the Blasius equation in turbulent flow at high Reynolds numbers. The simplification is given in the Appendix, Paragraph 6.3.4.

The change of skin friction coefficient with Reynolds number is given, for design purposes, in Figure 155. The high Reynolds number correction becomes significant for $\varepsilon_H N_{Re,s} > 10^7$, where ε_H is defined by Equation 312.

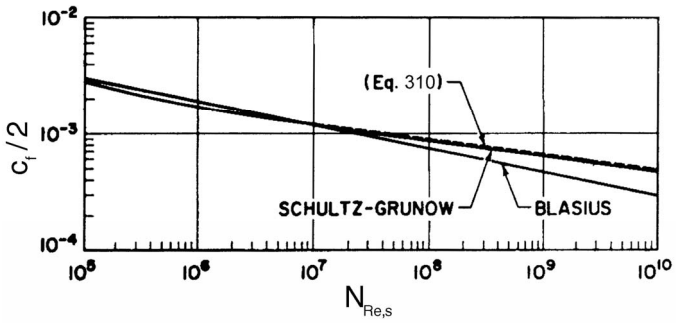

FIGURE 155 - Incompressible Flat Plate Skin Friction Coefficients, Turbulent Flow

6.1.3.1 (Continued):

To estimate the value of ε_H (for example, for conditions characteristic of the conical portion of a relatively pointed configuration, it is found that $h_w/h_e \cong 4$ and $V \cong 20$. From these values, ε_H is estimated to be about 1/10. Consequently the high Reynolds number correction becomes significant for compressible flow at a value of $N_{Re,s}$ that is an order of magnitude higher than that obtained for incompressible flow. On the conical portion of the vehicle, the high Reynolds number correction is not expected to be significant for $N_{Re,s} < 10^8$. On the blunt portion of the vehicle, ε_H has a value of about unity, so that the high Reynolds number correction is not significant for $N_{Re,s} < 10^7$. The value of s on the blunt portion is usually so small that in most cases $N_{Re,s}$ will not reach 10^7.

6.1.3.2 Pressure-Gradient and Varying Geometry Effects: A method of determining the turbulent skin friction and heat transfer for the case of finite pressure gradient and varying geometry has been derived only with the fundamental assumption that the momentum form of the Blasius compressible flat plate skin friction coefficient equation is invariant for finite pressure gradient and varying geometry (Reference 39). A similar method has been derived for the compressible Schultz-Grunow equation as given in the more convenient approximate form of Equation 60 in Reference 41.

Since the method of Reference 38 is frequently used for design estimates of turbulent heat transfer, it is more convenient for the engineer to use the ratios of Reference 38 rather than those of Reference 39. For the case of zero pressure gradient, the results are

$$\frac{\dot{q}}{\dot{q}_B} = (0.94)^k K \qquad \text{(Eq.200)}$$

where:

K is given by Equation 319 in Paragraph 6.3.4
k = 0 for a two-dimensional body
k = 1 for an axisymmetric body

6.1.3.2 (Continued):

Also,

$$\frac{c_f}{c_{f,B}} = (0.94)^k K \qquad \text{(Eq.201)}$$

and

$$\frac{\theta}{\theta_B} = (0.985)^k (0.921) K \qquad \text{(Eq.202)}$$

For the case of finite pressure gradient and varying geometry, the results of the present analysis yield trends that are similar to those of Reference 39. For engineering purposes, the engineer may assume that the ratios given in Equations 200 to 202 are approximately correct for the general case of finite pressure gradient and varying geometry.

6.1.3.3 Procedure: The flat plate turbulent heat transfer relation used for design estimates will significantly underestimate the correct heat transfer rate prediction when the product $\varepsilon_H N_{Re,s} > 10^7$. The value of ε_H has been estimated to be about 1/10 on the conical portions of relatively sharp vehicles, and about unity for spherical portions of vehicles. Therefore the high Reynolds number correction should be applied at a Reynolds number, $N_{Re,s}$ of about 10^8 on conical sections and about 10^7 on spherical sections. For example, a 20% increase in heat transfer rate is predicted on a conical section for $N_{Re,s} = 4 \times 10^9$, and on a spherical section for $N_{Re,s} = 4 \times 10^8$.

It is recommended that the high Reynolds number correction for turbulent heat transfer rate, skin friction, and momentum thickness be calculated for the approximate equations given by Equations 200 to 202, respectively. In these equations, k = 1 for axisymmetric bodies and k = 0 for two-dimensional bodies. The function K is given by Equation 319, Paragraph 6.3.4. The term ε_H is defined in Equation 312, Paragraph 6.3.4.

These corrections should be applied (to the method of Reference 39) when the appropriate value of $\varepsilon_H N_{Re,s}$ is exceeded. For a two-dimensional body, the skin friction and heat transfer corrections should be applied when $\varepsilon_H N_{Re,s} > 10^7$, whereas the momentum thickness correction should be applied when $\varepsilon_H N_{Re,s} > 3.26 \times 10^7$. For an axisymmetric body, the corrections for skin friction and heat transfer should be applied when $\varepsilon_H N_{Re,s} > 2.52 \times 10^7$, whereas the correction for momentum thickness should be applied when $\varepsilon_H N_{Re,s} > 4.10 \times 10^7$.

For hand calculations, ε_H can be approximated by assuming $g\rho^*/g\rho_e \cong (h^*/h_e)^{-0.7}$ and $\mu^*/\mu_e \cong (h^*/h_e)^{0.5}$, so that $\varepsilon_H \cong (h^*/h_e)^{-1.2}$.

The boundary layer thickness ratios δ/θ and δ^*/θ are relatively insensitive to the particular velocity distribution law which applies. Therefore the results determined in Reference 40 for δ/θ are considered to be independent of $N_{Re,s}$ and consequently remain unchanged.

6.1.4 Entropy Gradient Factors for Sphere Cones: Results in Figures 156 and 157 give an approximate indication as to where transition occurs from blunt to conical body heat transfer, that is, the region over which the assumption of isentropic expansion to obtain local flow parameters is no longer valid. Isentropic expansion of the flow from the stagnation region to locations downstream (to obtain local flow properties) is an inaccurate technique in the presence of a strong vorticity layer. A method for evaluating entropy gradient effects on heat transfer is provided in Paragraph 5.6.2.

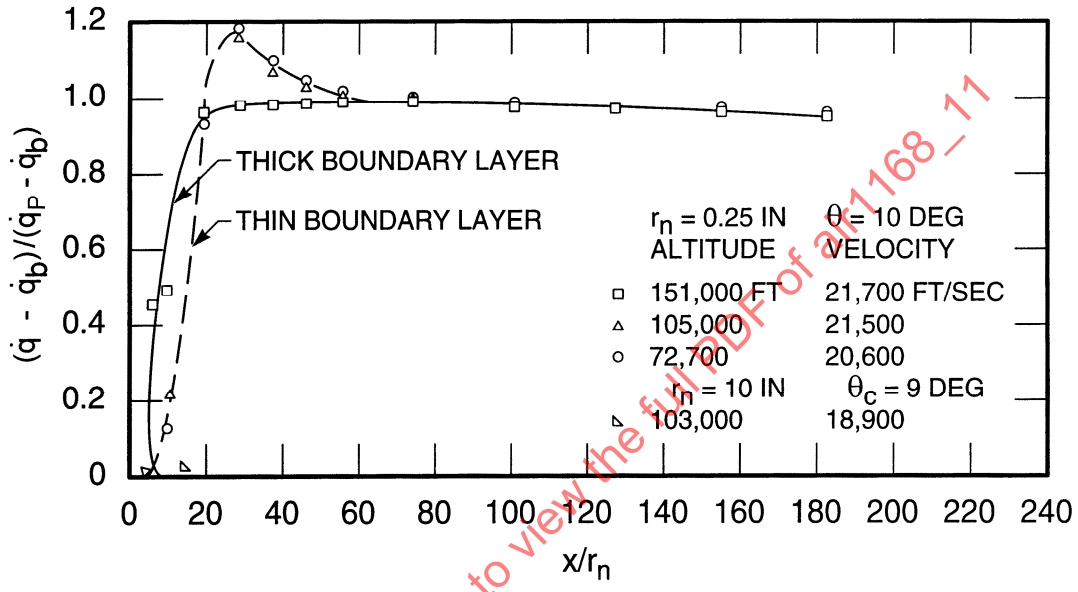

FIGURE 156 - Entropy Gradient Effect on Convective Heat Transfer Over Sphere Cones

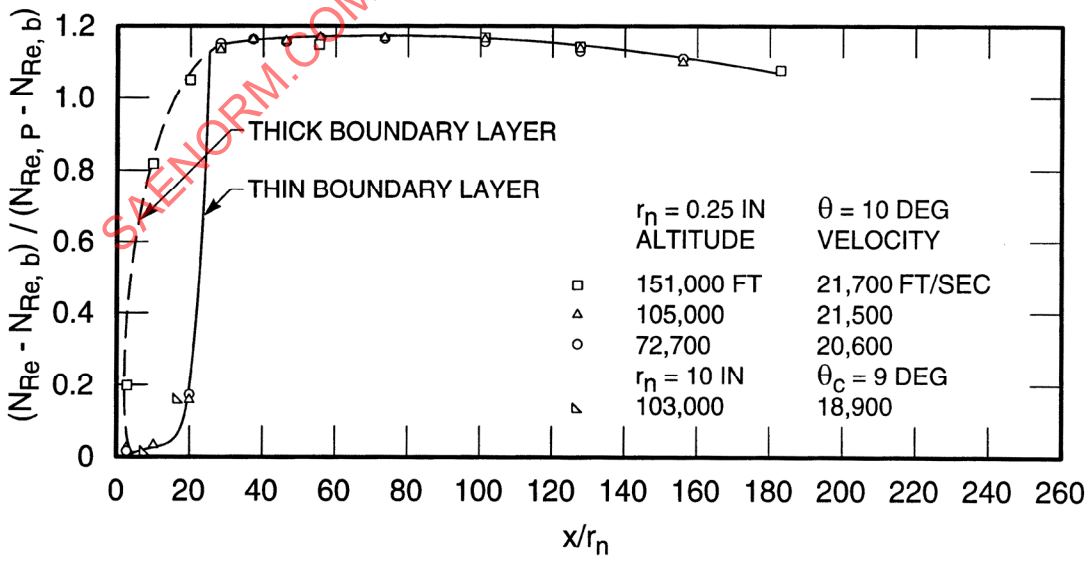

FIGURE 157 - Entropy Gradient Effect on Edge Reynolds Numbers Over Sphere Cones

6.1.4 (Continued):

Figure 156 presents the convective turbulent heat flux parameter over the surface of a sphere cone for various altitudes at a velocity which is almost constant. The heat flux parameter $(\dot{q} - \dot{q}_b)/(\dot{q}_p - \dot{q}_b)$ was used for correlating the results over the body because normal shock heat transfer becomes important at low values of x/r_n and negligible at high values of x/r_n.

Figure 157 is a similar comparison of Reynolds number at the edge of the boundary layer over the surface of the cone. The effect of altitude becomes evident at $0 < x/r_n < 25$. This effect is attributed to a thickening of the boundary layer along with maintaining the same shock shape. The dashed line in the figure is for a boundary layer thickness of the order of the shock wave thickness; the solid line is for a boundary layer thickness equal to about 1/10 the shock layer thickness.

6.1.5 Heat Transfer at Angle of Attack: Hypersonic entry configurations experience varying heat transfer rates due not only to the nature of a reentry trajectory, but also due to the gyrations by the body itself, typified by any combinations of motions such as spinning, wobbling, or tumbling (motions about each of the three body axes). Body motions caused by any number of parameters, such as varying center of gravity, coning, and separation, increases the need to consider not only the trajectory variation of the heat transfer rates, but also the effects of angle of attack and circumferential variations (at angle of attack) on the heat transfer rates.

Engineering methods are presented to predict the effect of angle of attack on the convective heating for both laminar and turbulent flow and the circumferential variations for sharp and blunt conical bodies. These methods are based on the analyses of References 42, 43, and 44.

6.1.5.1 Laminar Regime, Windward Ray: A parameter which correlates the available convective heat transfer data within ±15% for the laminar regime, windward ray is:

$$\frac{(\dot{q}_L)_\alpha}{(\dot{q}_L)_{\alpha=0}} = \sqrt{\frac{(2k+1)}{3}\frac{(g\rho^*\mu^* u_e)_\alpha}{(g\rho^*\mu^* u_e)_{\alpha=0}}} \cdot \frac{(h_r - h_w)_\alpha}{(h_r - h_w)_{\alpha=0}} \qquad \text{(Eq.203)}$$

In these angle of attack correlations, the local properties employed are based on an isentropic expansion from the stagnation conditions on the aft side of a normal shock to the local surface pressure.

In Figure 158, heat transfer experimental data available are compared with the correlation (Equation 203). Agreement is within approximately ±15%.

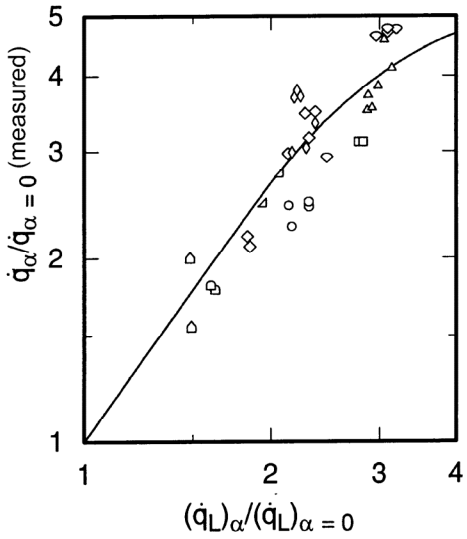

α, DEG	θ, DEG	r_n/r_b	CONFIG	M_∞
○ 8	7.1	} 0.0003	SHARP	10.16
□ 12				
◇ 8		} 0.105	SLIGHTLY BLUNT	
△ 12				
◇ 8		} 0.368	BLUNT	
◇ 12				
⌂ 5	10	} 0.015	SHARP	8.09
◿ 10				
⌂ 10	10	} 0	THEORY	4.95
○ 20	10		NASA TND 179	

FIGURE 158 - Heat Transfer Data Correlation at Angle of Attack for Windward Meridian, Laminar Region

6.1.5.2 Laminar Regime, Leeward Ray: A parameter that correlates the available data (with more scatter than the windward ray) is (Reference 44)

$$\frac{(\dot{q}_L)_\alpha}{(\dot{q}_L)_{\alpha=0}} = \sqrt{\frac{(\cos\alpha)(g\rho^*\mu^*u_e)}{(g\rho^*\mu^*u_e)_{\alpha=0}}} \cdot \frac{(h_r - h_w)_\alpha}{(h_r - h_w)_{\alpha=0}} \qquad \text{(Eq.204)}$$

The leeward data show considerable scatter relative to the correlation developed in Reference 44. The correlation employed represents a recommended engineering method for limited usage. Further investigations and additional data are required for this case (laminar-leeward) in order to develop a more suitable correlation (Figure 159).

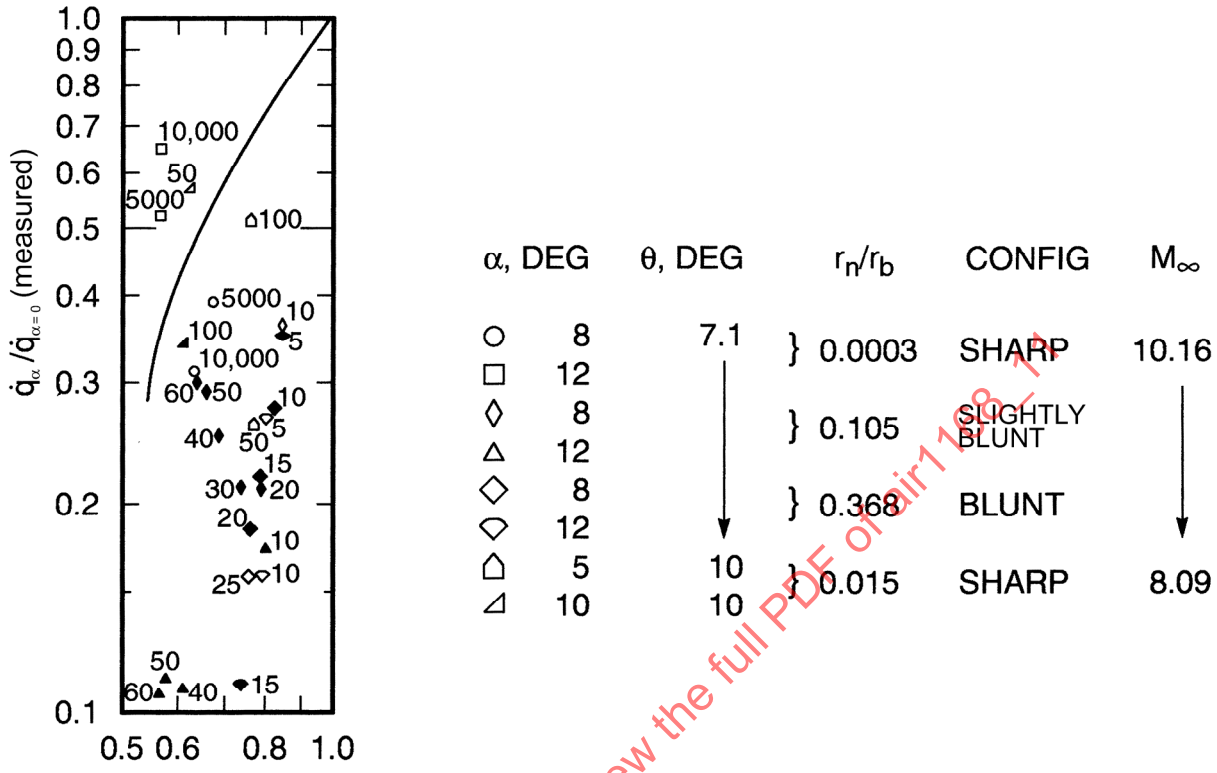

FIGURE 159 - Heat Transfer Data Correlation at Angle of Attack for Leeward Meridian, Laminar Region (Note: Numbers Beside Symbols Denote X/r_n Values; Solid Symbols Denote Extrapolated Data)

6.1.5.3 Turbulent Regime, Windward Ray: A turbulent windward parameter correlation which correlates the experimental data within approximately ±15% is (see References 42 and 45)

$$\frac{(\dot{q}_T)_\alpha}{(\dot{q}_T)_{\alpha=0}} = \frac{[(g\rho^* u_e)^{0.8}(\mu^*)^{0.2}]_\alpha}{[(g\rho^* u_e)^{0.8}(\mu^*)^{0.2}]_{\alpha=0}} \cdot \left(\frac{1.25K+1}{2.25}\right) \frac{(h_r - h_w)_\alpha}{(h_r - h_w)_{\alpha=0}} \quad \text{(Eq.205)}$$

where:

$$K = 1 + \frac{\sin\alpha \cot\theta_c}{\cos(\alpha + \theta_c)} \text{ (for windward side)} \quad \text{(Eq.206)}$$

$$K = \frac{3\cos(\alpha - 1)}{2} \text{ (for leeward side)} \quad \text{(Eq.207)}$$

6.1.5.3 (Continued):

This correlation is presented in Figure 160.

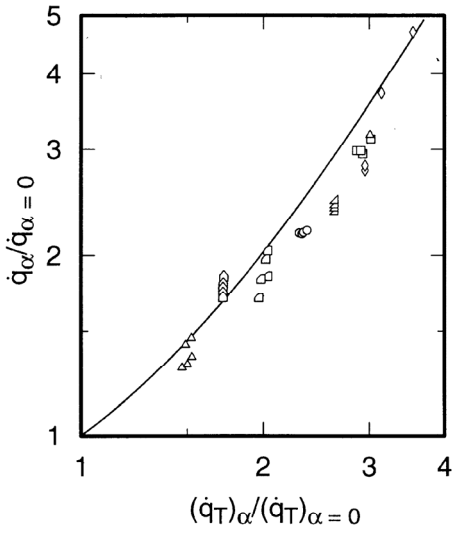

(As defined by Eq. 205)

	α, DEG	θ, DEG	r_n/r_b	CONFIG	M_∞
○	8	7.1	0.0003	SHARP	10.16
□	12	↓	0.0003	SHARP	
◇	12		0.105	SL BLUNT	
△	5	10	0.015	SHARP	8.09
▱	10	10	0.015	SHARP	
⬠	10	10	0	NASA TND 179	4.95
◿	20	10	0		

FIGURE 160 - Heat Transfer Data Correlation at Angle of Attack for Windward Meridian, Turbulent Regime

6.1.5.4 Turbulent Regime, Leeward Ray. The leeward correlation is of the same form as the (turbulent) windward (Reference 44). Test data are compared with the correlation in Figure 161. The data generated fall substantially below the mean curve of Reference 44; it is recommended that the upper limit curve be used as an engineering correlation curve. The lower curve represents a reasonable value estimated by assuming the approximate separated region criteria (approximately 60% of the attached flow value). However, the data plotted as on the leeward side laminar regime also incorporate boundary layer transition effects as well as possible separation effects. Since the separation and transition effects obscure the interpretation of these data, a mean line is constructed which provides data agreement within approximately ±20%, representing a suitable engineering solution. (Further investigation, including additional reliable data for the turbulent leeward regime, is required.)

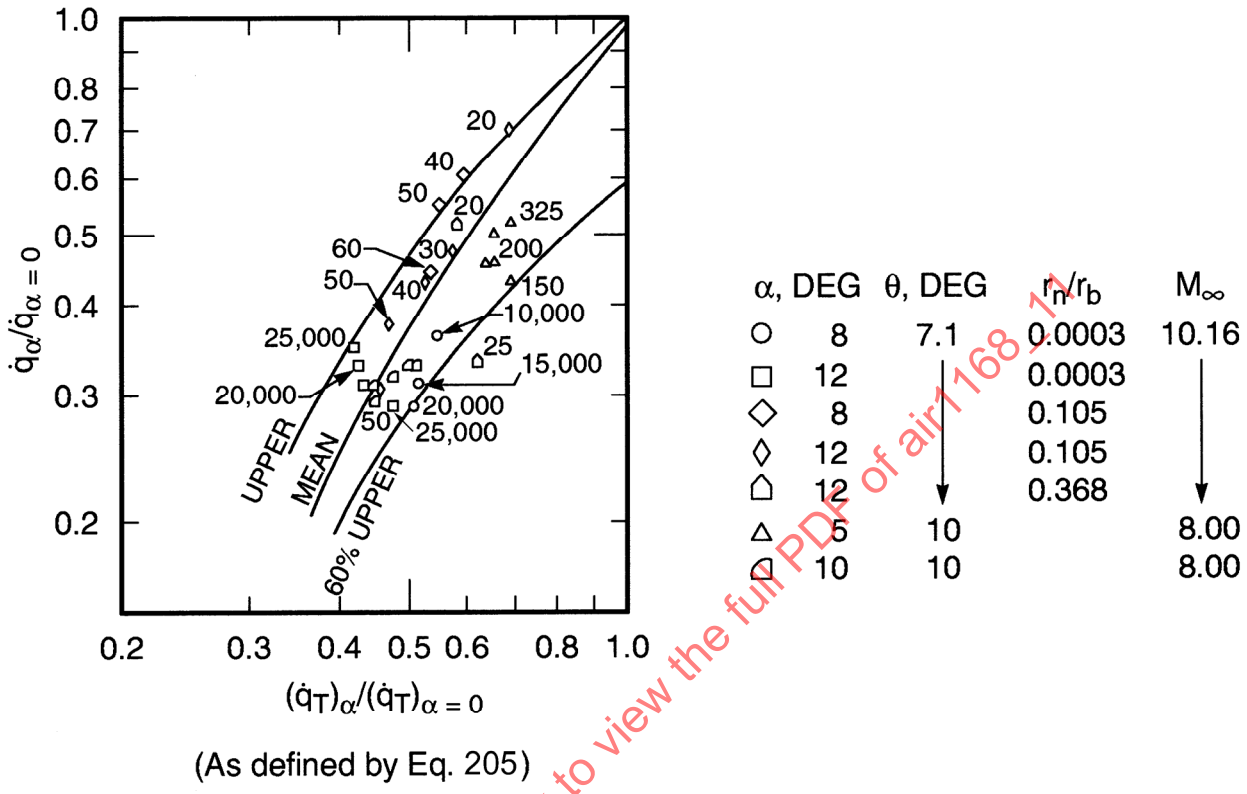

FIGURE 161 - Heat Transfer Data Correlation at Angle of Attack for Leeward Meridian, Turbulent Regime (Note: Numbers Beside Symbols Denote x/r_n Values)

6.1.5.5 Angle of Attack, Circumferential Variation: An expression for circumferential heat flux variation is (see Reference 44)

$$\frac{(\dot{q})_\alpha}{(\dot{q})_{\alpha=0}} = \frac{W_q - L_q}{2}\cos\phi + \frac{W_q + L_q - 2}{4}\cos 2\phi + \frac{W_q + L_q + 2}{4} \qquad \text{(Eq.208)}$$

A comparison of the results of Equation 208 with experimental data, References 42 and 45, is given in Figures 162 and 163.

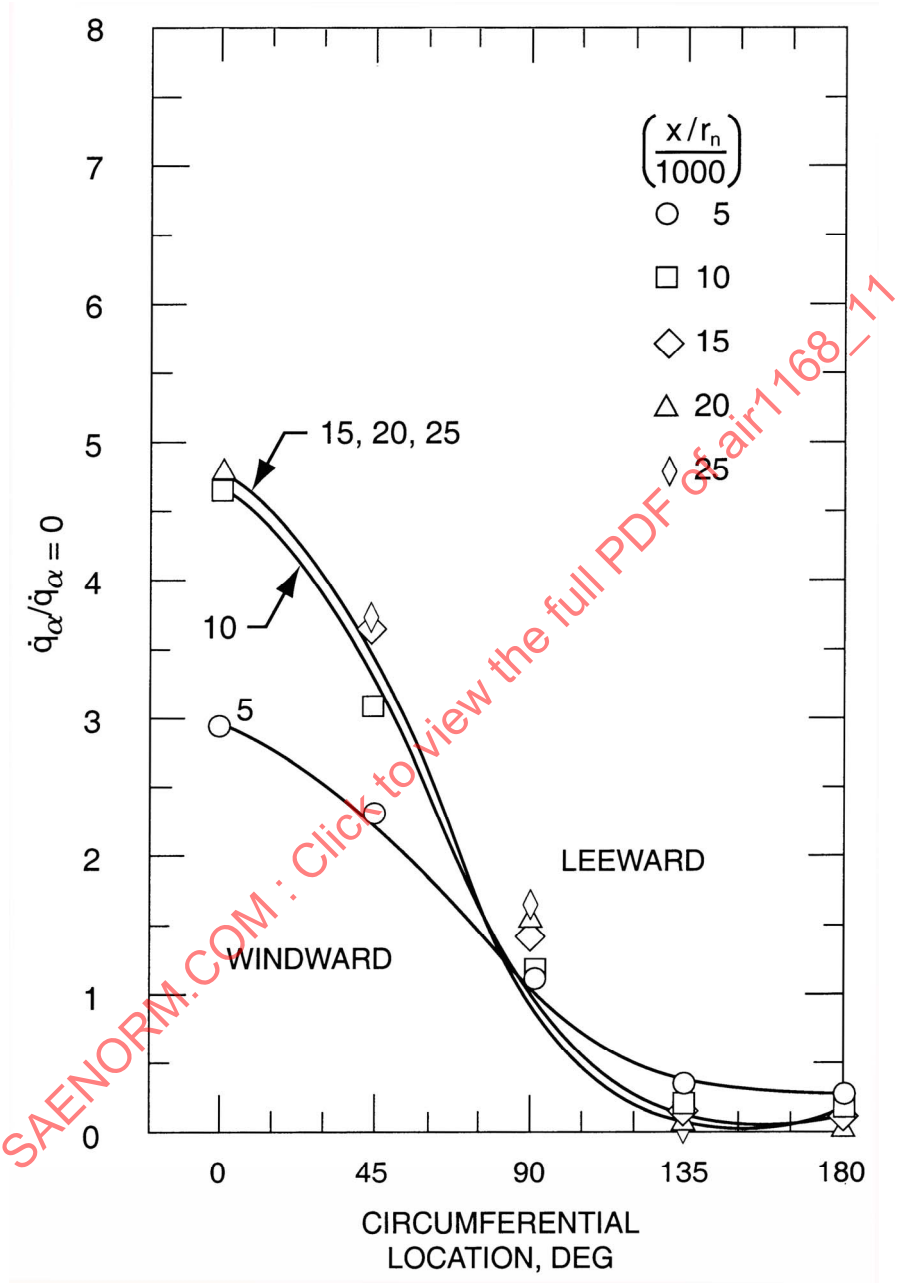

FIGURE 162 - Variation of Heat Flux Ratio Circumferentially

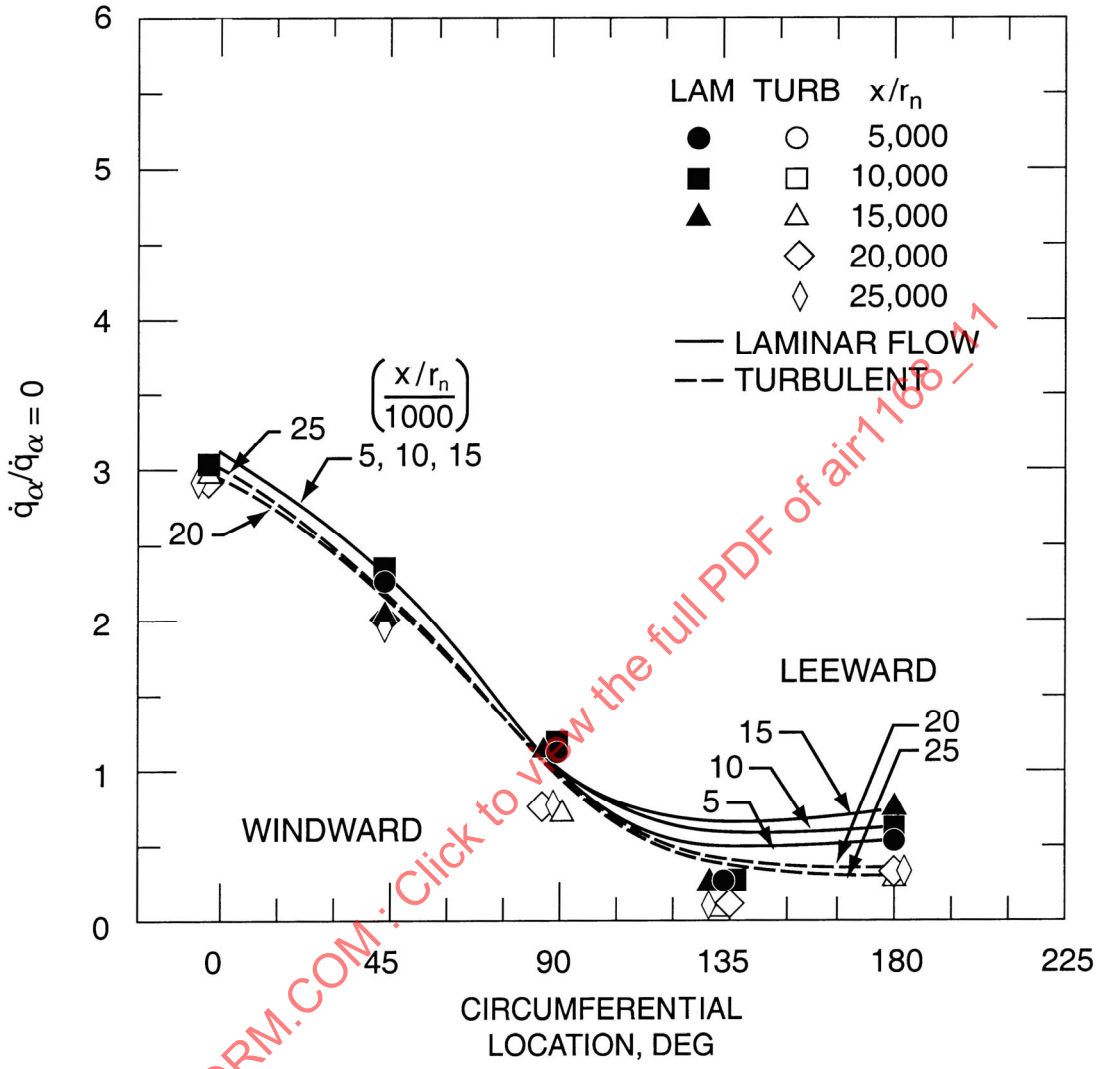

FIGURE 163 - Variation of Heat Flux Ratio Circumferentially

6.1.5.5 (Continued):

A length effect (x/r_n) is apparent in the data. The data, excluding the side ray, is found to be within approximately ±20% of the zero angle of attack value when correlated by Equation 208. Since the circumferential expression utilized, Equation 208, does not adequately reflect the length effect on the side ray, correction factors are required. Approximate expressions for the side ray (ϕ = 90 deg) ratioed to that at α = 0 deg are as follows:

6.1.5.5 (Continued):

For $10 \le x/r_n \le 50$:

$$(S_{\dot{q}})_L = \frac{(\dot{q}_L)_\alpha}{(\dot{q}_L)_{\alpha=0}} = 1 + \left[\sin\left(\frac{x/r_n}{60}\right)\right](0.05\alpha) \qquad \text{(Eq.209)}$$

For $x/r_n > 50$ (laminar flow):

$$(S_{\dot{q}})_L = \frac{(\dot{q}_L)_\alpha}{(\dot{q}_L)_{\alpha=0}} = 1 + 0.01\alpha \qquad \text{(Eq.210)}$$

For $x/r_n > 50$ (turbulent flow):

$$(S_{\dot{q}})_T = \frac{(\dot{q}_T)_\alpha}{(\dot{q}_T)_{\alpha=0}} = 1 - 0.015\alpha \qquad \text{(Eq.211)}$$

Incorporation of the above expressions for the side ray length effect improves the circumferential variation for all rays within the ±20% of the zero angle of attack value.

Incorporating the length effect of Equations 209 through 211 into Equation 208 gives the following engineering relation:

$$\frac{\dot{q}_\alpha}{\dot{q}_{\alpha=0}} = \frac{W_q - L_q}{2}\cos\phi + \frac{W_q - L_q + 2S_{\dot{q}}}{4}\cos 2\phi + \frac{W_q + L_q + 2S_{\dot{q}}}{4} \qquad \text{(Eq.212)}$$

6.1.5.6 Application of Method: The heat flux on cones and the conical section of blunt cones can be determined for any meridian in terms of the heat flux at zero angle of attack for the particular station under consideration.

First the heat flux at zero angle of attack is determined by the best method available, that is, incorporating entropy gradient effects and other pertinent considerations as previously presented. Then the heating on the windward and leeward meridians can be found by utilizing Figures 158 through 161; however, the local properties used may be considered fictitious, since for all cases (including sharp cones) the local conditions are evaluated based on the normal shock type of solution. Next, the heating can be evaluated on any other meridian by utilizing Equations 209 through 212. The resultant step is illustrated by

$$(\dot{q}_\alpha)_\phi = \left(\frac{\dot{q}_\alpha}{\dot{q}_{\alpha=0}}\right)_\phi \cdot \dot{q}_{\alpha=0} \qquad \text{(Eq.213)}$$

6.1.5.6 (Continued):

The angle of attack heat transfer ratio as given by the correlation parameters of Figures 158 through 161 are based on experimental data, and therefore include the angle of attack effects on entropy gradient on the heating rate. The heat transfer at zero angle of attack should be determined as accurately as possible.

Figures 164 and 165 permit rapid determination of the properties needed for the laminar correlating parameter. Figure 166 presents the equivalent curve for the turbulent case.

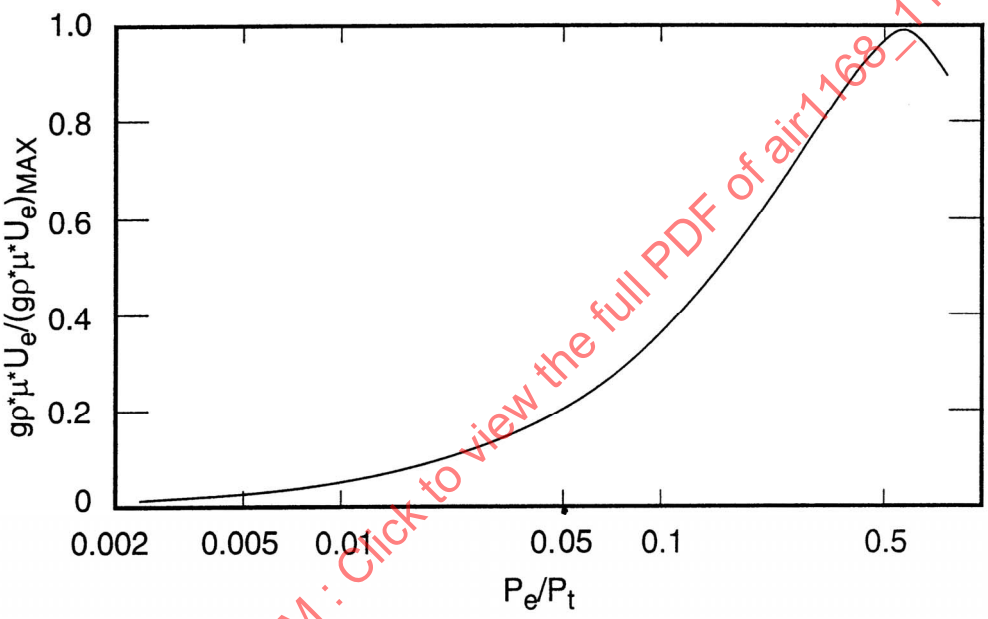

FIGURE 164 - $g\rho^*\mu^*U_e/(g\rho^*\mu^*U_e)_{max}$ versus P_e/P_t for T_w = 0°R for Isentropic Expansion from P_e^*

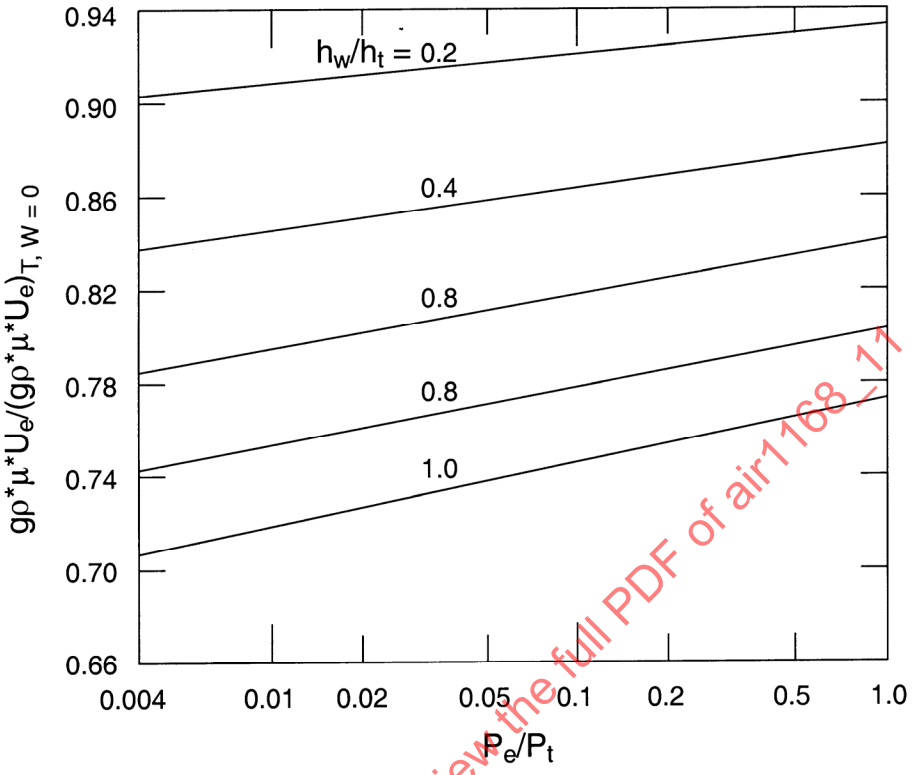

FIGURE 165 - Nonzero Wall Temperature Correction on $g\rho^*\mu^*U_e$

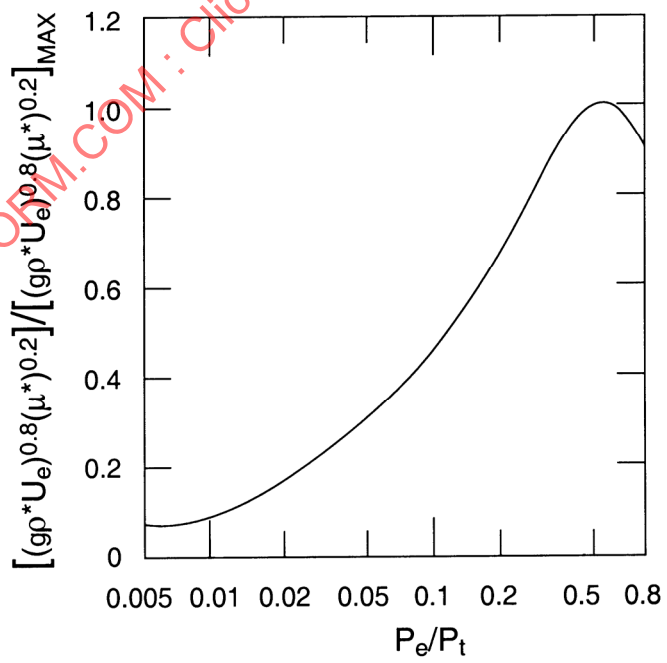

FIGURE 166 - Pressure Function for Approximate Turbulent Heat Flux

6.1.6 Protuberance Heat Transfer: Whenever the designer requires a probe or control surface on an entry vehicle, he is confronted with the problem of thermally protecting the probe or protuberance and protecting the localized surface area adjacent to the probe. Test data have shown a strong interaction effect to occur in the neighborhood of these protuberances as a result of the highly nonlinear vorticity, pressure, and flow field quantities.

The cause of the high heating zone on the body surfaces in the region adjacent to a protuberance appears to be the formation of a high-pressure three-dimensional separation region surrounding the obstacle. In the case of locally supersonic approach flow, an additional pressure increase is caused by the shock wave which forms around the protuberance. Subsonic flow studies (Reference 46) have shown the existence of strong reverse flow in the separated region (see Figure 167) which causes a high shear area ahead of the protuberance.

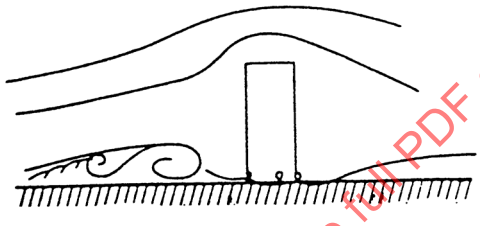

FIGURE 167 - Reverse Flow in Separated Region in Subsonic Flow

The merging of this reverse flow with the approach flow causes the formation of high-energy vortices which flow around the obstacle. A wake forms behind the obstacle, with a region of high shear at the wake centerline. Pressure surveys behind a cylinder (Reference 47) indicate the existence of a vortex on each side of the cylinder as far as 48 diameters downstream.

Local flow and heat transfer effects in the interaction zone are divided into at least two general classes:

Class 1 (see Figure 168):

$$(L/\delta) > 1, \quad \frac{L}{D} > 1 \qquad \text{(Eq.214)}$$

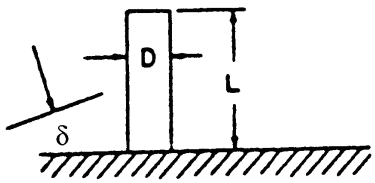

FIGURE 168 - Class 1 Obstacle

6.1.6 (Continued):

Class 2 (see Figure 169):

$$(L / \delta) \leq 1, \quad \frac{L}{D} \leq 1 \qquad \text{(Eq.215)}$$

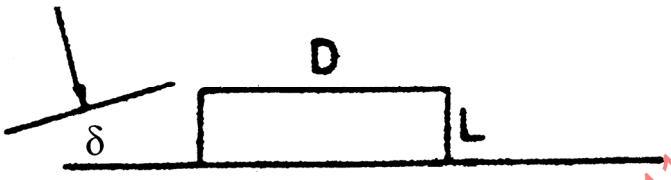

FIGURE 169 - Class 2 Obstacle

In most tests the protuberances are an example of Class 1. Interaction heating data in the vicinity of cylindrical protuberances of the Class 1 variety are available from References 48 and 49. In tests reported in Reference 48, the undisturbed boundary layer was turbulent and in Reference 49 the flow was laminar. Cylinder diameters were also significantly different (larger). Typical results are given in Figures 170 and 171. In order to provide design information in a usable form, it is convenient to take the ratio of the local body heat transfer coefficient in the protuberance region to the undisturbed local body heat transfer coefficient with no protuberance present. For example, divide the measured local values of C_H by the theoretical turbulent value of $C_{H,T,t}$ which would exist at the same location on a body with no probe present. The choice of a turbulent reference value of C_H rather than the measured laminar values of the probeless body is motivated by two reasons: the probe normally causes transition of the separated flow to a turbulent shear layer, followed by turbulent boundary layer upon reattachment; and most investigators use a turbulent reference value, even when the undisturbed flow is laminar.

Nondimensional maps are given in terms of x/D and y/D for both diameters tested. These figures show general agreement of results, which indicates that the interaction zone scales as the cross-sectional area of the cylinder.

The interaction heating factors from Reference 49 are compared with the results of Burbank (Figure 170) in Figure 172. Although somewhat higher levels of interaction heating factors resulted from the data of Reference 49, especially upstream of the protuberance, the general pattern is similar and agrees well 4 diameters downstream. Hence it can be concluded for design purposes that the interaction heating pattern is similar for a wide range of $N_{Re,s}$ and cylinder diameter.

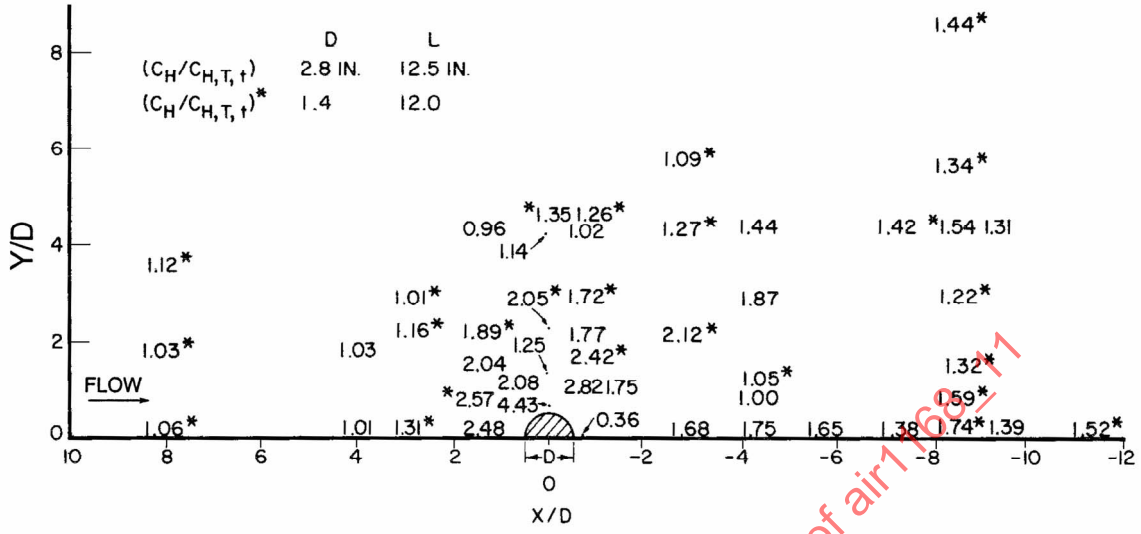

FIGURE 170 - Effect of Cylinder Diameter on Interaction Heating Factors
Note: M_e = 2.65; $N_{Re,s}$ = 5 x 10^6; Λ = 0 deg; δ = 0.70 in
Decimal Points Locate Data Point $C_H/C_{H,T,t}$ Values Given.
Y is the Distance Measured Normal from the Flow Streamline that Would Pass Through the Center of the Obstacle; "*" Indicates $(C_H/C_{H,T,t})$ for D = 1.4 in, L = 12.0 in

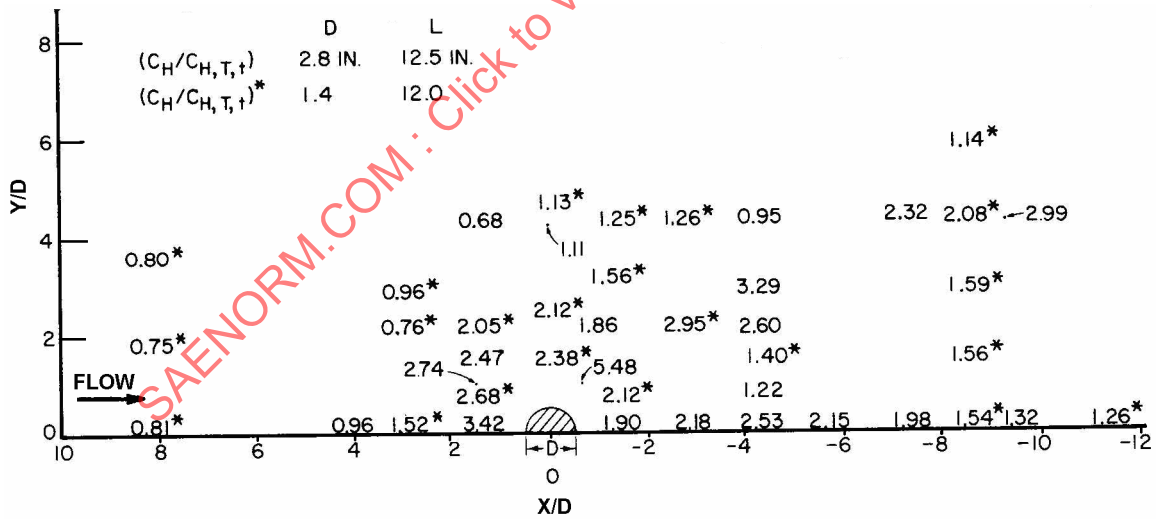

FIGURE 171 - Effect of Cylinder Diameter on Interaction Heating Factors
Note: M_e = 4.44; $N_{Re,s}$ = 8 x 10^6; Λ = 0 deg; δ = 0.70 in
Decimal Points Locate Data Point $C_H/C_{H,T,t}$ Values Given.
Y is the Distance Measured Normal from the Flow Streamline that Would Pass Through the Center of the Obstacle; "*" Indicates $(C_H/C_{H,T,t})$ for D = 1.4 in, L = 12.0 in

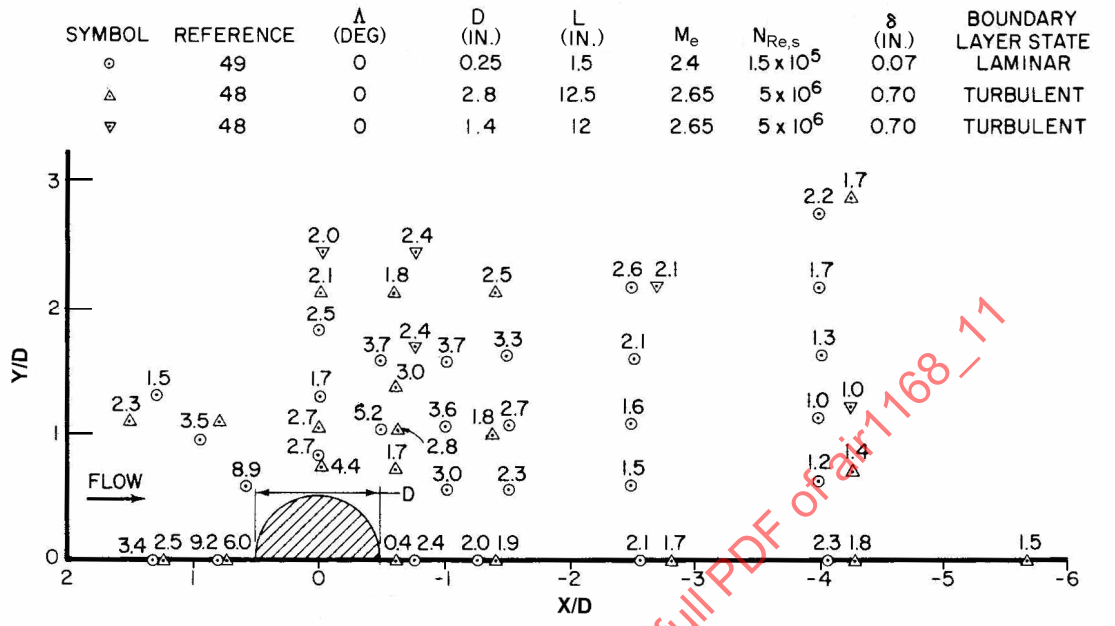

FIGURE 172 - Comparison of Interaction Heating Factors for Cylinders with L/D > 4

6.1.6 (Continued):

The effect of local Mach number M_e and local Reynolds number $N_{Re,s}$ on maximum interaction heating factor $C_H/C_{H,T,t}$ is given in Figure 173. Despite the data scatter, the results of References 48 and 49 show a significant increase in $C_H/C_{H,T,t}$ with increasing M_e and decreasing $N_{Re,s}$. The $C_H/C_{H,T,t}$ results are correlated by the following empirical equation to within 20%:

$$\frac{C_H}{C_{H,T,t}} = \frac{22\,M_e}{N_{Re,s}^{0.15}} \qquad \text{(Eq.216)}$$

This correlation is shown in Figure 174.

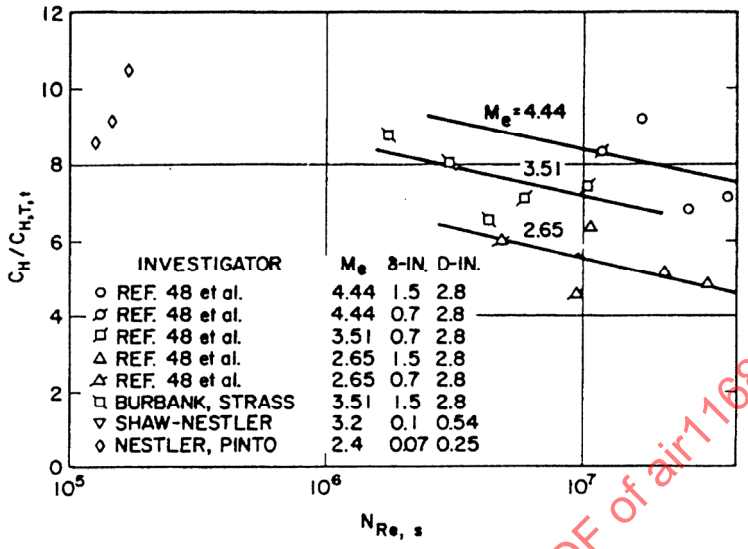

FIGURE 173 - Effect of Local Mach and Reynolds Numbers on Maximum Heating Factors for Unswept Cylinders

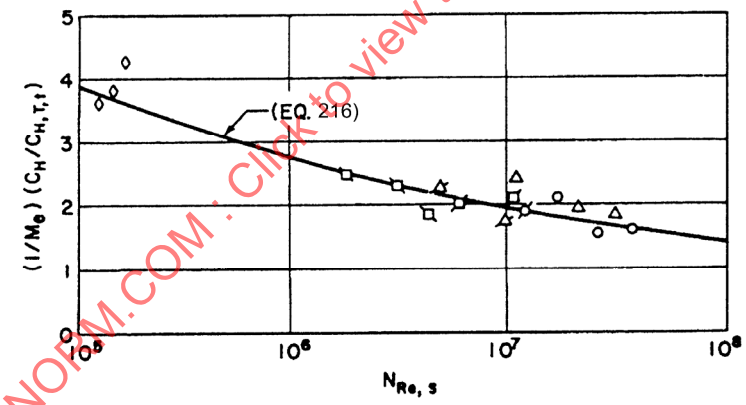

FIGURE 174 - Correlation of Maximum Interaction Heating Factors for Unswept Cylinders (For Key, see Figure 173)

6.1.6 (Continued):

The effect of sweepback of the probes on the interaction heating factors is given in Figure 175. In this figure, values of $C_H/C_{H,T,t}$ are plotted versus dimensionless distance parameters for three meridian angles ϕ and for sweep angles Λ from 0 to 45 deg. Sweepback causes large reductions in interaction heating, particularly upstream of the probe. A sweep angle of only 15 deg causes approximately 50% reduction in maximum local heat transfer rate. The effects of sweep downstream of the probe are less significant, having little effect for x/D > 3.

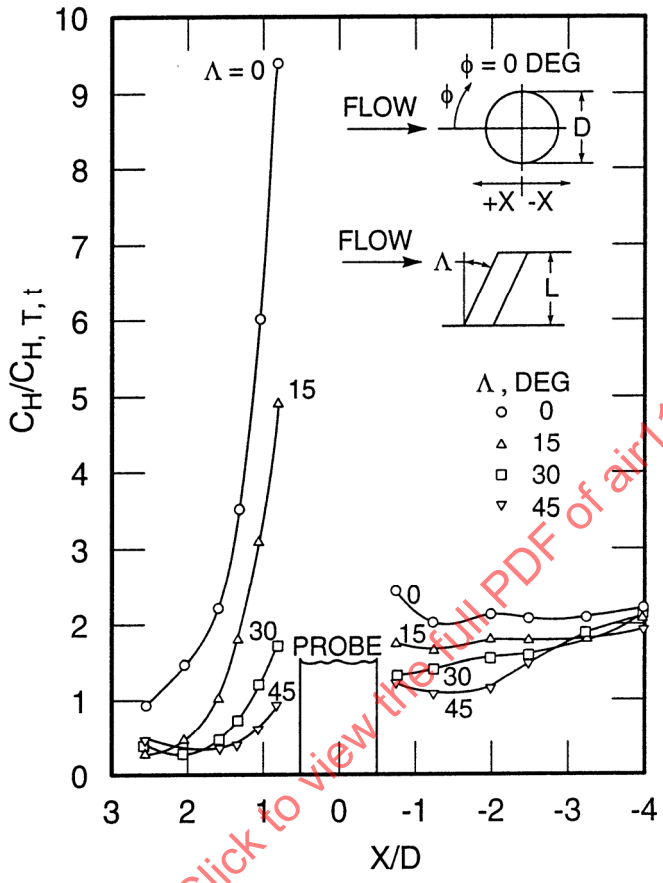

FIGURE 175 - Effect of Probe Sweep Angle on Interaction Heating Factors

6.1.6 (Continued):

The effects of sweep on maximum interaction heating are summarized in Figure 176, which is taken from test data in Reference 48. Sweep is somewhat more effective for laminar undisturbed boundary layers than for the turbulent case. The assumption of turbulent flow is the conservative design procedure.

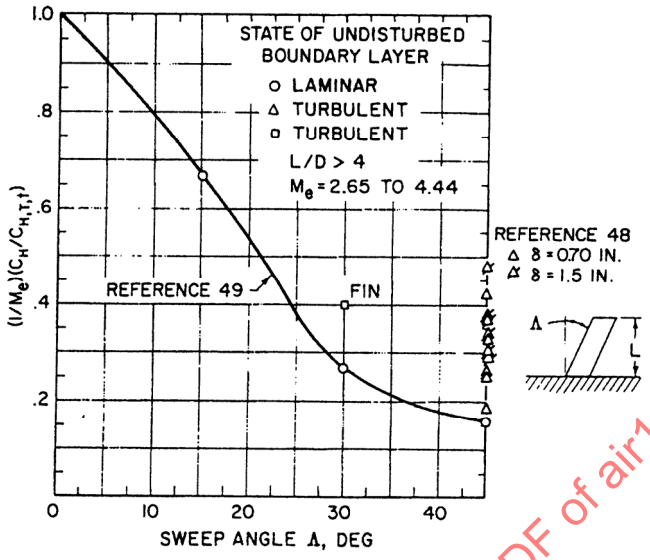

FIGURE 176 - Effect of Sweep Angle on Maximum Body Interaction Heating

6.1.6 (Continued):

Experimental data on steps ($L < \delta$) reveal the existence of a pronounced maximum in heat transfer away from the window or step centerline meridian, downstream of the window. This maximum occurs at y/D of 0.25, and is indicative of the presence of vortices. (This vortex effect has been noted in previous ablation tests of small protuberances as well as cavities.) No evidence of such a maximum of the centerline meridian was noted in the probe results, indicating that the sources of the vortex may be the interaction of the top plane and lateral surface of the window. Probe interaction heating appears to include at least two general classes of protuberance effects:

Class 1:

$$L/\delta > 1,\ L/D > 1 \qquad \text{(Eq.217)}$$

Class 2:

$$L/\delta \sim 1,\ L/D \sim 1 \qquad \text{(Eq.218)}$$

In Class 2, the boundary layer thickness approaches the same order of magnitude as the protuberance height.

The “short cylinder” or probe class of protuberance has been reported in investigations of undisturbed turbulent boundary layers (References 50 and 51). Reference 51 did not measure heat transfer in the high heating area upstream of the protuberance; hence the results are primarily useful for downstream effects.

6.1.6 (Continued):

Figure 177 summarizes these results. It indicates little reduction in heating until the cylinder height is reduced to 0.5 in, to give an L/δ of 0.36 and an L/D of 1.33. Sweepback does not appear to have significant effect in reducing the maximum heating levels downstream of the cylinder.

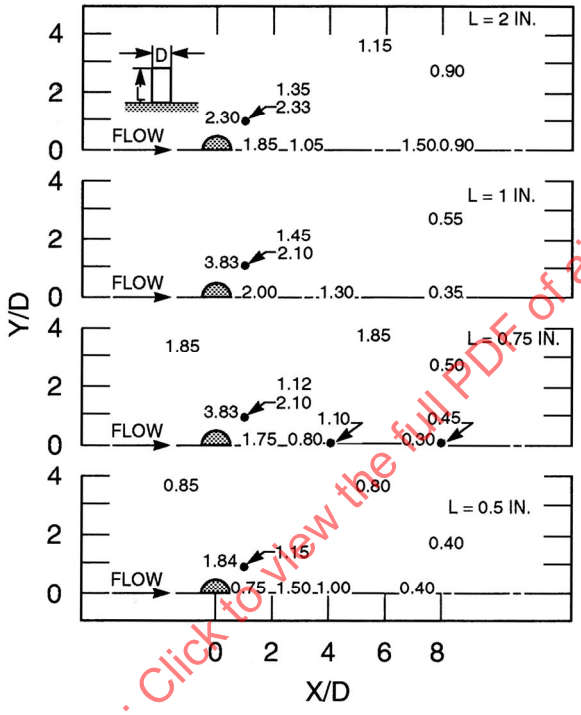

FIGURE 177 - Interaction Heating on Body Due to Cylinders
δ = 1.4 in, Turbulent Boundary Layer Λ = 0 deg
(Bloom and Pallone, M_c = 6, D = 0.375 in); Values Plotted are $C_H/C_{H,T,t}$
(NOTE: Decimal Points are Locations of Readings)

A drastic increase in heating near the cylinder was observed from these data when it was swept forward. Scaling of the interaction region with cylinder cross-sectional area was investigated in Reference 48. The results are somewhat inconclusive and may support the conclusion of Reference 51 that interaction heating does not scale with cylinder size. More detailed studies are needed to resolve this question.

The designer must recognize that the results presented in this section should be used with caution when applied to design analysis for geometries and local flow conditions much different from those which existed during these tests. There are not sufficient data available to determine a generalized correlation of the effects of M_e, $N_{Re,s}$, L/D, and L/δ on interaction heating factors due to “short cylinders” of windows.

6.1.6.1 Heat Transfer Rates on Probes: Representative measured heat transfer coefficient ratios are given in Table 10. The theoretical freestream stagnation line heat transfer coefficient is computed from the relation

$$\frac{(C_{H,\infty,t})_{cyl}}{(C_{H,t})_{body}} = \left[\frac{(r_n)_{body}}{D_{cyl}}\right]^{1/2} \qquad \text{(Eq.219)}$$

TABLE 10 - Summary of Maximum Values of $C_{H,t}/C_{H,t,\infty}$

Ref.	M_∞	$N_{Re,\infty,D}$ x 10^{-6}	$C_{H,t}/C_{H,t,\infty}$
48	2.65	0.7	1.4
	3.51	0.7	2.3
	4.44	0.7	2.0
52	2.25	1.0	1.0
	2.64	1.13	1.4
	2.97	1.22	2.0
	3.23	1.28	1.0
	3.89	1.41	1.2
	4.92	1.71	1.6
	5.5	1.87	1.3
53	2.65	0.7	1.8
	3.51	0.7	2.1
	4.44	0.7	3.0
49	10	0.04	0.8

Previous measurements of stagnation line heating rates to protuberances in supersonic and hypersonic flow have been reported in References 48, 52, and 53. A summary of the maximum values of $C_{H,t}/C_{H,t,\infty}$ from tests reported in these references is given in Table 10.

Further investigation is required to determine whether the low values of $C_{H,t}/C_{H,t,\infty}$ for the last investigation listed above are due to the low freestream Reynolds number or higher freestream Mach number. The present result of $C_{H,t}/C_{H,t,\infty} = 0.8$ should be used only for similar flow conditions, pending further results at higher $N_{Re,\infty,D}$ and M_∞.

6.1.7 Entry Vehicle Wake Heat Transfer: A method of correlating the heating rates in the separated flow field behind a rearward-facing step is provided by Donaldson (Reference 54). This correlation of data obtained from wind tunnel and shock tube tests can be expressed in terms of the Stanton number and Reynolds number:

Laminar:

$$N_{St} = \frac{0.0097}{N_{Re,\Delta b}^{0.5}} \quad \text{(Eq.220)}$$

Turbulent:

$$N_{St} = \frac{0.018}{N_{Re,\Delta b}^{0.25}} \quad \text{(Eq.221)}$$

where the Stanton number is defined as

$$N_{St} \equiv \frac{\dot{q}}{g\rho_b u_b (h_t - h_w)} \quad \text{(Eq.222)}$$

(Donaldson actually reduced the data in terms of $(h_r - h_w)$ instead of $(h_t - h_w)$. However, in view of the overall scatter observed in wake heat transfer data this difference is usually insignificant.) The Reynolds number is defined as

$$N_{Re,\Delta b} \equiv \frac{g\rho_b u_b (\Delta b)}{\mu_b} \quad \text{(Eq.223)}$$

where the length Δb is the distance between the dividing streamline and the afterbody surface, measured normal to the axis of symmetry (see Figure 178).

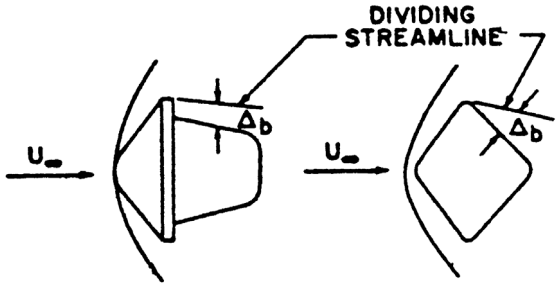

FIGURE 178 - Entry Vehicle Geometry

6.1.7 (Continued):

The thermodynamic properties denoted by the subscript b have been determined along the dividing streamline (this assumes that pressure across the separated flow region is constant and equal to the value at the afterbody surface of the entry vehicle). The length Δb has been determined by assuming that the flow along the dividing streamline expands isentropically, with $\gamma = 1.4$ (Prandtl-Meyer flow), from the sonic point on the body. The sonic point has been assumed to occur at a local body angle of 45 deg.

For flat based configuration, the Δb parameter is as shown in Figure 179. In the limit, Δb reduces to the boundary layer thickness δ. The designer should be cautioned that the above procedure is approximate and is used to estimate the magnitude of the heat transfer rate in the wake area.

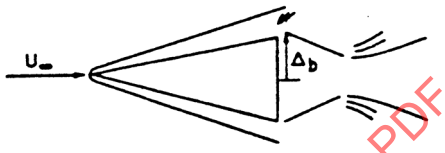

FIGURE 179 - Flat Based Configuration for Entry Vehicle

6.1.8 Asymmetric Entry Vehicle Heat Transfer: Lifting entry vehicle configurations are normally asymmetric; this, coupled with high angle of attack flight attitudes results in complex three-dimensional flow fields, flow separation, and reattachment in the control surface section of the vehicle. Present winged configurations are relatively simple shapes: swept wings and blunt leading edges and noses, elliptical body cross sections, or various combinations of rectangular and conical cross sections. Generally, these comparatively simple geometries facilitate the heating analysis of this class of vehicles; however, as the capability of high-temperature structural materials and cooling techniques improve, more sophisticated designs and configurations will require more detailed analyses and/or extensive ground facility heat transfer tests.

Detailed analysis of lifting entry vehicle aerodynamic heating can be performed by judicious approximations of various portions of the lifting vehicle by geometries such as blunted cones, wedges, or flat plates, which may then be treated by the methods of predicting flow fields, pressure distributions, and heat transfer given in Paragraphs 5 and 6.1.1 to 6.1.7. Approximate relations for glide entry vehicle environmental parameters were presented in Paragraph 1.3. This section presents additional approximate relations which may be used to supplement the methods given in the sections referenced above. The stagnation region usually experiences the highest heating rate on a hypersonic lifting entry vehicle, thereby requiring detailed analyses.

Wing leading edge heating is the next most important area to be considered. Approximate methods for the effects of wing geometry (both section and planform), heating rate distribution, and the effects of angle of attack are given. Analysis of the region aft of the leading edge then follows, treating this region as a flat plate.

6.1.8 (Continued):

Throughout this section, heating on the lower surface is emphasized. Hypersonically, the upper surface will be in a region of extremely low pressure and normally in separated flow. It has been shown that separated flows reduce heating, with only the reattachment creating increased heating. For preliminary design, convective heating on the upper surface may be estimated conservatively by assuming pressure levels equal to ambient pressure for upper surface angles of inclination greater than 10 to 15 deg referenced to the vehicle velocity vector.

6.1.8.1 Stagnation Point Heat Transfer - Hemicylinder Nose: The Lees method previously presented may be written in terms of lifting vehicle velocity, atmospheric density and entry vehicle hemispherical nose radius as

$$\frac{\dot{q}_t\sqrt{r_n}}{1-(h_w/h_t)} = 3.16 \times 10^{-9} (g\rho_\infty)^{0.5} V_\infty^3 \qquad \text{(Eq.224)}$$

and for a hemicylinder nose,

$$\frac{\dot{q}_t\sqrt{r_n}}{1-(h_w/h_t)} = 3.16\times10^{-9}(g\rho_\infty)^{0.5}V_\infty^3/\sqrt{2} \qquad \text{(Eq.225)}$$

The local laminar heat transfer distribution, up to included angles of 70 deg, can be simplified to

$$\frac{\dot{q}(r_n)^{0.5}}{(g\rho_\infty)^{0.5}(V_\infty/1000)^3\,[1-(h_w/h_t)]} = \left(3.16/\sqrt{2}\right)\cos^n\theta \qquad \text{(Eq.226)}$$

where the pressure distribution according to Newtonian theory is valid; that is,

$$\frac{P}{P_t} = \cos^2\theta \qquad \text{(Eq.227)}$$

The local-to-stagnation heating rate may be further simplified up to 70 deg as

$$\frac{\dot{q}}{\dot{q}_t} \approx \cos^n\theta \qquad \text{(Eq.228)}$$

where:

n = 1 for $M_\infty \simeq 2$
= 1.5 for $M_\infty \geq 5$

6.1.8.1 (Continued):

Figure 180 is a design chart for the surface heating rate distribution for a two-dimensional body with a hemicylinder leading edge. The heating rate $(\dot{q}/\dot{q}_t)$ is presented as a function of the surface distance from the stagnation point (s/r_n), for various values of the effective angle of attack. This distribution is valid for only a short portion aft of the leading edge, $(s/r_n) < 5$. For hemispherical nose regions the stagnation heat transfer rate to a hemicylinder is multiplied by $\sqrt{2}$.

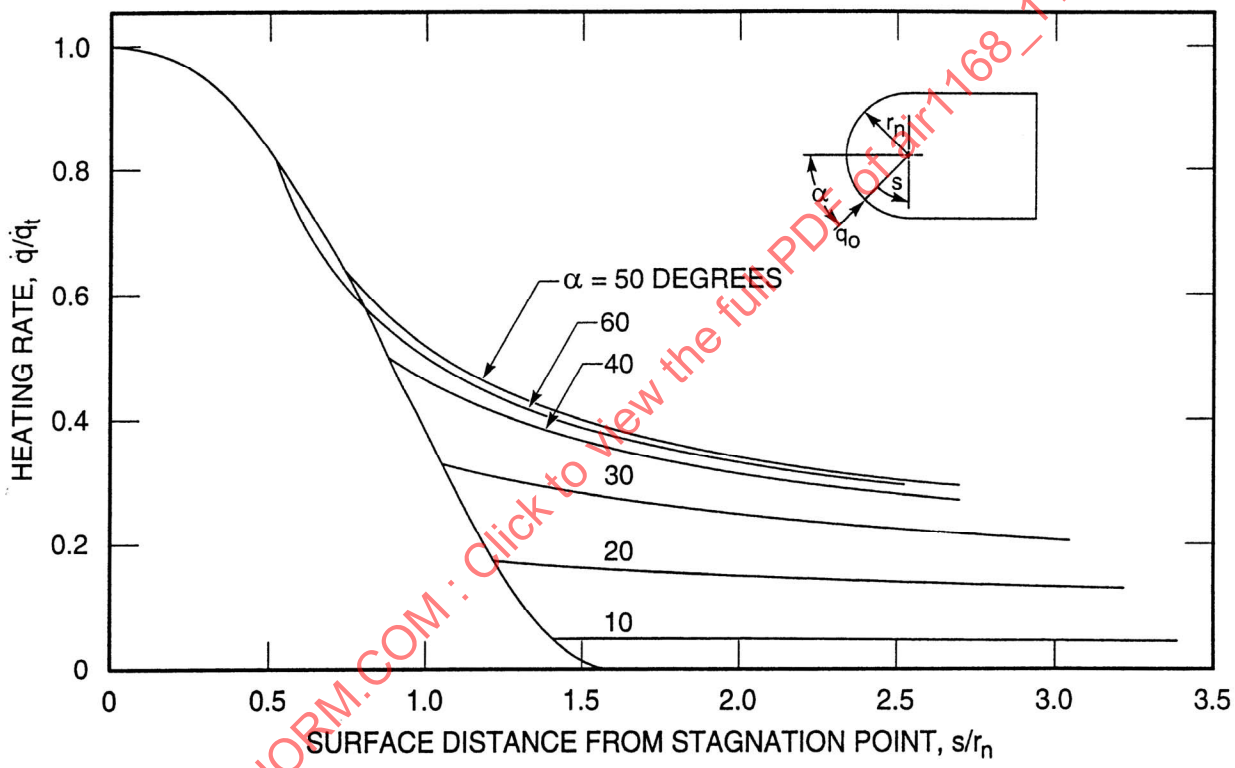

FIGURE 180 - Surface Heating Rate Distribution for a Two-Dimensional Hemicylindrical Leading Edge

6.1.8.1 (Continued):

Local turbulent heating on the hemicylinder leading edge may be similarly simplified; that is,

$$\frac{\dot{q} r_n^{0.2}}{(g\rho)^{0.8}(V_\infty / 1000)^3[1-(h_w / h_t)]} = \frac{5}{2^{0.2}}\left[\frac{\theta^{0.6}\cos^{1.6}\theta}{0.54\,(1-\beta^2\theta^2)^{0.7}}\right]\left(\frac{0.408}{\beta}\right)^{0.6} \quad \text{(Eq.229)}$$

For $\gamma = 1.2$ ($\beta = 0.408$), maximum heating occurs at θ equal to approximately 35 deg.

6.1.8.2 Wing Leading Edge Heating: The next most severe condition to be considered in lifting entry vehicle heat transfer is wing or control surface leading edge heating for conditions exterior to the vehicle shock layer system. The laminar stagnation point heating rate to a cylinder normal to the flow may be obtained by a coordinate transformation of a sphere in three dimensions to a two-dimensional system by multiplying the former value by $1/\sqrt{2}$. Wing or fin control surfaces are not usually normal to the flow, however, and geometric considerations for wing sweep and angle of attack must be applied. Sweeping a wing or fin leading edge of a hypervelocity vehicle will generally result in a reduction of the convective heat input to the wing. The reduction may be expressed in the form of a correction to the heating rate of an unswept wing.

FOR LAMINAR FLOW:

(1) Sweep Only:

$$\dot{q}_\Lambda = \frac{3.16}{\sqrt{2}}\left(\frac{\rho_\infty g}{r_n}\right)^{0.5}\left(\frac{V_\infty}{1000}\right)^3 \cos\Lambda \quad \text{(Eq.230)}$$

By normalizing this equation to the zero sweep heating rate, a sweep correction factor for laminar flow is obtained:

$$\frac{\dot{q}_\Lambda}{\dot{q}_{\Lambda=0}} = \cos\Lambda \quad \text{(Eq.231)}$$

The preceding simplified analysis is intended to indicate trends only. Experimental data have shown that the sweep correction factor can best be expressed in the form

$$\frac{\dot{q}_\Lambda}{\dot{q}_{\Lambda=0}} = \cos^n\Lambda \quad \text{(Eq.232)}$$

A value of n = 1.5 is recommended for 0 deg $\le \Lambda \le$ 60 deg; however, lower values of n from $1.0 \le n \le 1.5$ are possible at higher angles.

6.1.8.2 (Continued):

(2) Sweep and Angle of Attack: When a delta wing is pitched to an angle of attack the effective sweep is decreased and the local angle of attack to the leading edge or effective angle of attack is increased. The following relationships are applicable to delta wing configurations:

$$\alpha_e = \tan^{-1}\left(\frac{\tan\alpha}{\cos\Lambda}\right) = \text{effective angle of attack} \qquad \text{(Eq.233)}$$

$$\Lambda_e = \sin^{-1}(\sin\Lambda\cos\alpha) = \text{effective angle of sweep} \qquad \text{(Eq.234)}$$

For laminar flow, from the above, the sweep correction equation for an angle of attack becomes

$$\frac{\dot{q}_\Lambda}{\dot{q}_{\Lambda=0}} = \cos^n\Lambda_e = \left[1-\sin^2\Lambda\cos^2\alpha\right]^n \qquad \text{(Eq.235)}$$

FOR TURBULENT FLOW:

$$\frac{\dot{q}_\Lambda r_n^{0.2}}{(g\rho)^{0.8}(V/1000)^3(1-h_w/h_t)} \simeq \frac{5\theta^{0.6}\cos^{1.6}\theta}{2^{0.2}(0.542)}\cos^{2.4}\Lambda \qquad \text{(Eq.236)}$$

The sweep correction for turbulent flow is reduced to

$$\left(\frac{\dot{q}_\Lambda}{\dot{q}_{nose}}\right)_{max.\ turb.} = \frac{\cos^{2.4}\Lambda}{1.1} \qquad \text{(Eq.237)}$$

6.1.8.3 Heat Transfer in the Blunt Nose Induced Pressure Field: The stagnation point and local stagnation region distributions presented in this section apply only in the immediate vicinity of the nose ($s/r_n < 5.0$). Far downstream from the blunt nose ($s/r_n > 10$), flat plate values may be successfully used. In the intermediate region, an overpressure exists for several diameters rearward because of the blunt-nose induced pressure field. In this region the pressure must be determined from the methods presented in Paragraph 5.3.5, and the heat transfer rate evaluated from the equations given in Paragraphs 6.1.2 and 6.1.3 or by pressure corrections to the flat plate relationships below.

6.1.8.4 Flat Plate Relationships: Summarizing, equations for laminar and turbulent flow are as follows:

$$\frac{\dot{q}x^{0.5}}{(g\rho)^{0.5}(V_\infty/1000)^3[1-(h_w/h_t)]} = 0.0312\alpha^{2/3} \text{ (laminar flow)} \qquad \text{(Eq.238)}$$

$$\frac{\dot{q}x^{0.2}}{(g\rho)^{0.8}(V_\infty/1000)^3[1-(h_w/h_t)]} = \frac{\alpha}{3[1+(11/3)(h_w/h_t)]} \text{ (turbulent flow)} \qquad \text{(Eq.239)}$$

where:

α = Angle of attack, deg

Table 11 summarizes pertinent heating relations.

TABLE 11 - Resume of Laminar and Turbulent Heating Equations for Lifting Entry

Location	Laminar Parameter	Turbulent Parameter
	$\frac{\dot{q}r_n^{0.5}}{(g\rho_\infty)^{0.5}(V_\infty/1000)^3[1-(h_w/h_t)]} =$	$\frac{\dot{q}r_n^{0.2}}{(g\rho_\infty)^{0.8}(V_\infty/1000)^3[1-(h_w/h_t)]} =$
Hemicylinder Nose	$\left(3.16/\sqrt{2}\right)\cos^n\theta$ where: n = 1 for M ≃ 2 n = 1.5 for M ≥ 5	$\frac{5}{2^{0.2}}\left(\frac{\theta^{0.6}\cos^{1.6}\theta}{0.542(1-0.166\theta^2)^{0.7}}\right)$
Leading Edge	$\frac{3.16}{2^{0.5}}\cos\Lambda_e\cos^n\theta$ where: $\Lambda_e = \sin^{-1}(\sin\Lambda\cos\alpha)$	$\left[\frac{5}{2^{0.2}}\cos^{2.4}\Lambda_e\right]\left[\frac{\theta^{0.6}\cos^{1.6}\theta}{0.542}\right]$ where: $\Lambda_e = \sin^{-1}(\sin\Lambda\cos\alpha)$
Flat Plate	$0.0312\left(\frac{r_n}{x}\right)^{0.5}\alpha^{2/3}$	$\frac{0.333(r_n/x)^{0.2}\alpha}{1+(11/3)(h_w/h_t)}$

6.1.9 Low-Density Effects: At superorbital entry speeds and for flight missions where maximum heat rates occur at high altitudes, other phenomena have a significant effect on the heat transfer. Among these are nonequilibrium flow chemistry in both the shock layer and the boundary layer; radiation from the high-temperature gas behind the shock, which can be intensified by nonequilibrium effects; and release of electrons in ionization which, because of their high degree of mobility, may tend to increase convective heating.

Figure 181 identifies the primary hypersonic entry problems. In this figure, velocity-altitude curves for selected typical entry trajectories are given. Also shown in the figure are boundaries indicating certain important domains where the chemical or physical processes previously mentioned may occur and where the designer must check his vehicle system to ensure that he has examined its performance in these regions. Boundaries as shown are somewhat arbitrary in nature, since they depend largely on the configuration and size of the body, the model atmosphere, and other factors. Information presented in the figure was made for the stagnation region of a body with a 1 ft nose radius, using a 1962 ARDC model atmosphere. The boundary line (A), which gives the maximum altitude for thermodynamic equilibrium in the shock layer, is based on the relaxation distance for the temperature to reach its equilibrium value behind a normal shock, similar to the estimates given previously in Reference 55. Curve (B) represents the upper altitude limit for an equilibrium boundary layer and is related to a recombination-rate parameter similar to that in Fay and Riddell's theory of the stagnation point boundary layer (Reference 23).

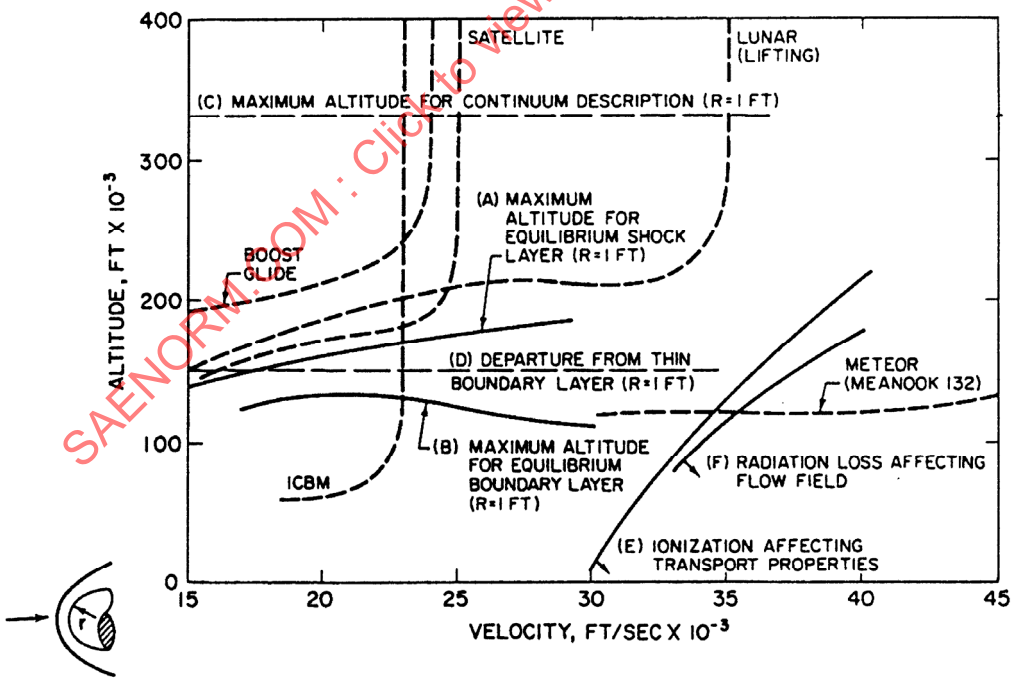

FIGURE 181 - Typical Flight Trajectories and Boundaries Delimiting Some of the Important Domains

6.1.9 (Continued):

Except in the case of deep penetration typified by the ICBM trajectory, the critical portion of most entry flight paths (where maximum deceleration and heating occur) lies above both boundaries (A) and (B). The nonequilibrium chemistry of the shock layer is particularly critical for listing entry from superorbital speed because chemical nonequilibrium tends to increase the temperature behind the shock and thus the radiative heat transfer. From curve (C) it is seen that the assumption of a continuum flow for predicting the critical motion and heating of entry vehicles may be largely valid. On the other hand, departure from the classical, thin boundary-layer concept, curve (D), as a result of external vorticity and other rarefaction effects can be significant even at relatively low altitude. The boundaries (E) and (F) are related to the electronic heat conduction and radiation loss effects, inferred, respectively, from the results of References 27 and 56.

By use of Figure 182, the designer can rapidly estimate the magnitudes of the aerodynamic and radiative heating according to his systems mission. The results in the figure represent predictions for continuum flow, and by means of approximate methods for the lower-density regimes, the designer can rapidly estimate the critical portions of the entry trajectory with respect to vehicle loading and heating.

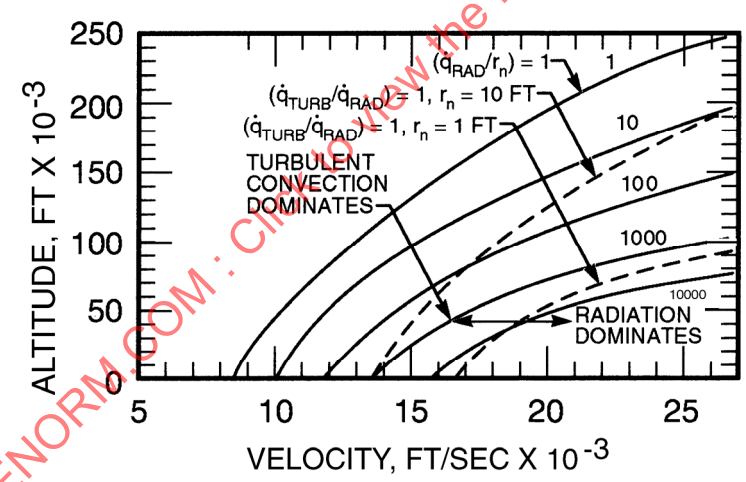

FIGURE 182 - Altitude-Velocity Heat Transfer Map, Ballistic Entry
(NOTE: The parameters 1, 10, 100, 1000, and 10,000 have the units of Btu/ft^3-s)

In Figure 183, the high-altitude hypersonic flight regime is shown divided into subregimes. Typical ballistic and lifting entry trajectories of hypersonic vehicles are superimposed. Figure 183 is typical for a nominal nose radius equal to 0.1 ft. For smaller nose radii, all low-density effects are shifted to lower altitudes. Descriptive stagnation region velocity profiles are shown to the right of the respective flight regimes.

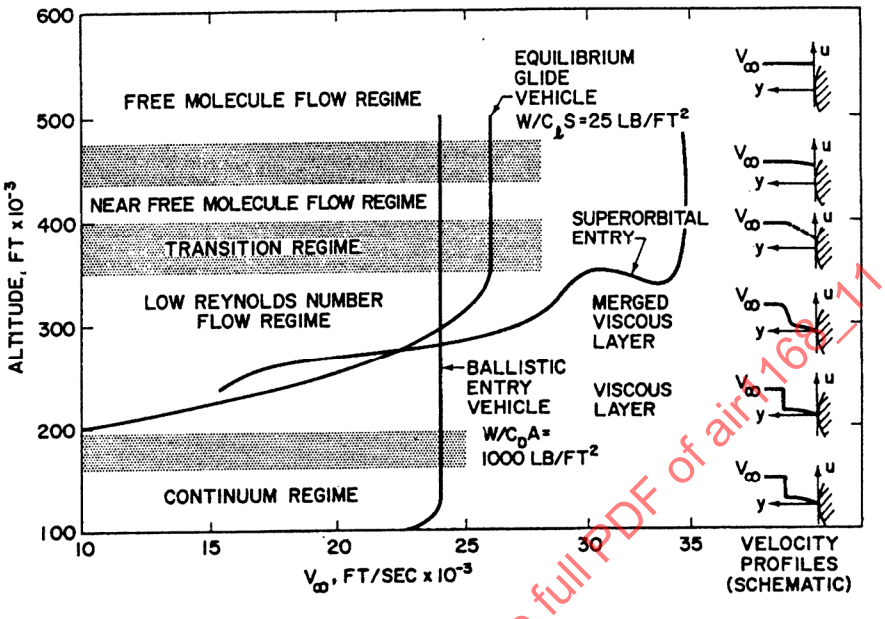

FIGURE 183 - High Altitude Hypersonic Flight Regimes, r_b = 0.1 ft

6.1.9 (Continued):

The first significant low-density effect to appear is the interaction of the boundary layer displacement thickness or streamline deflection:

$$\text{Streamline deflection} \sim \frac{M_\infty^2}{\sqrt{N_{Re}}} \qquad \text{(Eq.240)}$$

At higher altitudes the boundary layer merges with the inviscid flow field, and a viscous region exists from the body surface to the shock wave. As the gas stream becomes more rarefied, the effect of slip at a body surface becomes significant. When the mean free path of the fluid is much larger than a characteristic body length, the boundary layer and shock wave disappear and free molecule flow exists. Added complications at low densities, which require consideration by the designer, are the transverse curvature, transition, entropy gradient, and nonequilibrium flow effects.

The various flow regimes can be classified on the basis of the Knudsen number:

$$N_{Kn} = \frac{\lambda}{L} = \frac{\text{Mean free path}}{\text{Characteristic body length}} \qquad \text{(Eq.241)}$$

6.1.9 (Continued):

The following arbitrary definition (Reference 64) of the flow regimes should be utilized:

$$\text{Continuum flow} = N_{Kn} < 0.01 \quad \text{(Eq.242)}$$

$$\text{Merged continuum flow} = 0.01 < N_{Kn} < 0.1 \quad \text{(Eq.243)}$$

$$\text{Slip flow} = 0.1 < N_{Kn} < 1 \quad \text{(Eq.244)}$$

$$\text{Transition flow} = 1 < N_{Kn} < 10 \quad \text{(Eq.245)}$$

$$\text{Free molecule flow} = N_{Kn} > 10 \quad \text{(Eq.246)}$$

Figure 184 describes the regimes for which the freestream mean free path (as in Figure 183) was used to compute N_{Kn}.

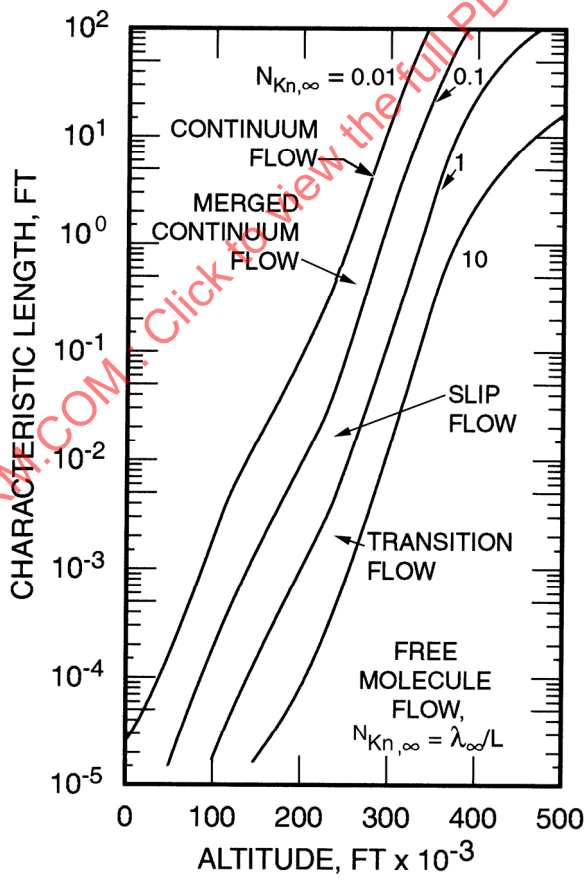

FIGURE 184 - Flow Regimes of Entry Aerodynamics

6.1.9.1 Viscous-Inviscid Interaction: The pressure on a blunt body in hypersonic flow is significantly higher than freestream pressure because of two effects: the inviscid or bluntness effect and the viscous or displacement effect. Pure viscous effects can be closely approximated by assuming an infinitesimally thin body. Since an infinitesimally thin body is impossible to obtain in practice, the viscous and inviscid contributions to the surface pressure occur simultaneously as shown in Figure 185.

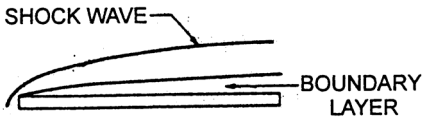

FIGURE 185 - Thin Body Geometry

The strength of the viscous interaction is directly proportional to the boundary layer displacement thickness of streamline deflection, and $\delta^* \sim M^2 / \sqrt{N_{Re}}$. The induced pressure is proportional to the product of streamline deflection and freestream Mach number:

$$P \sim \delta^* M \qquad \text{(Eq.247)}$$

$$P \sim \psi \sim M^3 \sqrt{N_{Re}} \qquad \text{(Eq.248)}$$

At hypersonic speeds the boundary layer at a given Reynolds number is thicker than that at lower speeds. The thicker boundary layer effectively distorts the body contours and thereby causes higher pressure distributions than those predicted by inviscid flow theories. The increased pressure also causes higher heating rates, which are of significance to the design of heat protection systems.

An approximate engineering method applicable to the prediction of the surface heat transfer on a flat plate with pressure gradient, caused by nose bluntness and viscous interaction effects, is given below (Reference 57). The method provides correction for the effect of sweep and angle of attack on the surface heat transfer. The method is also a linear addition of the two limits of the zero order theory (Reference 58) which corresponds to limit cases in which displacement and bluntness dominate (Reference 59).

The engineering relations are listed below.

(1) Unswept Plate at Zero Angle of Attack:

$$M_\infty^3 C_{H,\infty} = 0.219 \left[\frac{\gamma - 1}{\gamma + 1} \cdot \left(0.664 + 1.73 \frac{T_w}{T_t} \right) \right]^{1/2} \cdot (\bar{x}_\infty)^{3/2} \sqrt{\gamma_\infty} + 0.119 \bar{x}_\infty \sqrt{\gamma_\infty} \cdot \left[M_\infty^3 C_D \left(\frac{\gamma - 1}{\gamma + 1} \right) \frac{t}{X} \right]^{1/3} \qquad \text{(Eq.249)}$$

6.1.9.1 (Continued):

where:

$\bar{x}_\infty = M_\infty^3 \sqrt{C_w} / \sqrt{N_{Re,\infty,x}}$ is based on undisturbed freestream conditions

(2) Unswept Plate at Angle of Attack: All quantities are based on sharp wedge inviscid flow conditions.

$$\bar{x}_\alpha = \frac{M_\alpha^3 \sqrt{C_w}}{\sqrt{N_{Re,\alpha,x}}} \quad \text{(Eq.250)}$$

$$N_{Re,\alpha,x} = \frac{g\rho_\alpha u_\alpha x}{\mu_\alpha} \quad \text{(Eq.251)}$$

$$N_{Re,\alpha,x} = \left(\frac{T_\infty}{T_\alpha}\right)^{0.147} \left(\frac{g\rho_\alpha}{g\rho_\infty}\right) \left(\frac{M_\alpha}{M_\infty}\right) \frac{x}{t} \cdot N_{Re,t} \quad \text{(Eq.252)}$$

$$\mu = T^{0.647} \quad \text{(Eq.253)}$$

$$M_\alpha^3 C_{H,\alpha} = 0.219 \left[\frac{\gamma-1}{\gamma+1} \cdot \left(0.664 + 1.73 \frac{T_w}{T_t}\right)\right]^{1/2} (\bar{x}_\alpha)^{3/2} \sqrt{\gamma_\infty} + 0.119 \bar{x}_\alpha \sqrt{\gamma_\infty} \cdot \left[M_\alpha^3 C_D \left(\frac{\gamma-1}{\gamma+1}\right) \frac{t}{x}\right]^{1/3} \quad \text{(Eq.254)}$$

(3) Swept Plate at Zero Angle of Attack:

$$M_\infty^3 C_{H,\infty} = 0.219 \left[\frac{\gamma-1}{\gamma+1} \cdot \left(0.664 + 1.73 \frac{T_w}{T_t}\right)\right]^{1/2} (\bar{x}_\infty)^{3/2} \sqrt{\gamma_\infty} + 0.119 \bar{x}_\infty \sqrt{\gamma_\infty} \cdot \left[M_\infty^3 \left(\frac{\gamma-1}{\gamma+1}\right) C_D \left(\frac{t}{x}\right) \cos^3 \Lambda\right]^{1/3} \quad \text{(Eq.255)}$$

6.1.9.1 (Continued):

(4) Swept Plate at Angle of Attack:

$$M_\alpha^3 C_{H,\alpha} = 0.219 \left[\frac{\gamma - 1}{\gamma + 1} \cdot \left(0.664 + 1.73 \frac{T_w}{T_t} \right) \right]^{1/2} (\bar{x}_\alpha)^{3/2} \sqrt{\gamma_\infty} + 0.119 \bar{x}_\alpha \sqrt{\gamma_\infty} \cdot \left[M_\alpha^3 \left(\frac{\gamma - 1}{\gamma + 1} \right) C_D \left(\frac{t}{x} \right) \cos^3 \Lambda \right]^{1/3} \quad \text{(Eq.256)}$$

Equations 254 through 256 give acceptable agreement with available experimental results, when pressure gradient occurs (±20%). For negligible pressure gradient the zero pressure gradient method of Reference 38 gives good agreement with the experimental values (M^3C_H). For design purposes, when $\bar{x}_\alpha \geq 3.0$, the method (with pressure gradient) should be used, and for $\bar{x}_\alpha \leq 3.0$, the zero pressure gradient method should be used.

6.1.9.2 Merged Viscous Layer: With increased altitude the boundary layer merges with the shock layer, and from the body surface to the shock a viscous region exists. Figure 186 gives a criterion which determines when the technique of dividing the flow field into a viscous and inviscid layer must be abandoned (Reference 60). At this point the complete Navier-Stokes equations must be applied from the body surface to the shock wave. This merged layer parameter is defined as the ratio of the nominal boundary layer thickness to shock detachment distance, multiplied by the square root of the vehicle nose radius, and evaluated at the forward stagnation point of the body. The abandonment of the viscous interaction solution occurs when the magnitude of $\delta/\Delta x$ approaches unity.

The hypersonic shock wave in the merged viscous layer regime is curved, and the originally irrotational flow becomes rotational as the result of passing through this curved shock. When the vorticities generated by the shock and wall are of the same order of magnitude, the increase in heat transfer becomes significant.

The effect of shock-generated vorticity (merged viscous layer flow) on stagnation point heat transfer rates on a hemisphere is presented in engineering form in Figures 187 through 189 (Reference 61). In these figures, $\dot{q}/\dot{q}_t$ is the ratio of the heat transfer rate determined by solutions to the Navier-Stokes equations and the heat transfer rate determined by conventional continuum theory.

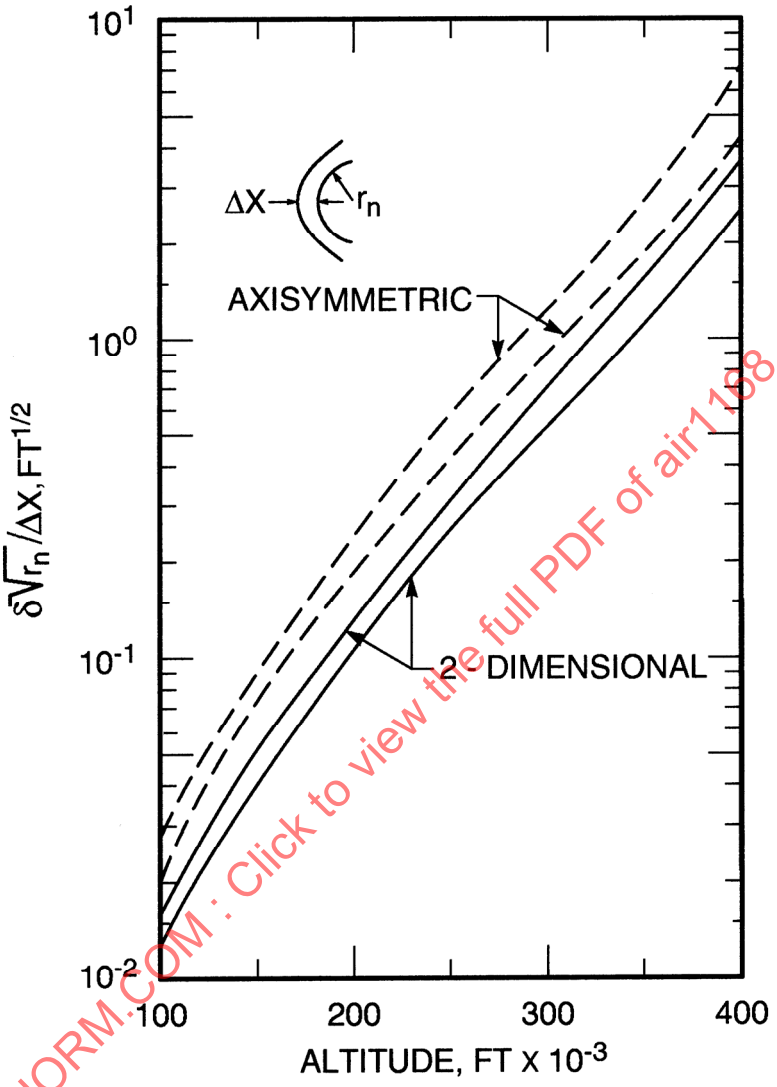

FIGURE 186 - Merged Layer Parameter (Stagnation Point), $1000 \leq T_w \leq 3000$ °R, $16 \leq$ Mach No. ≤ 24

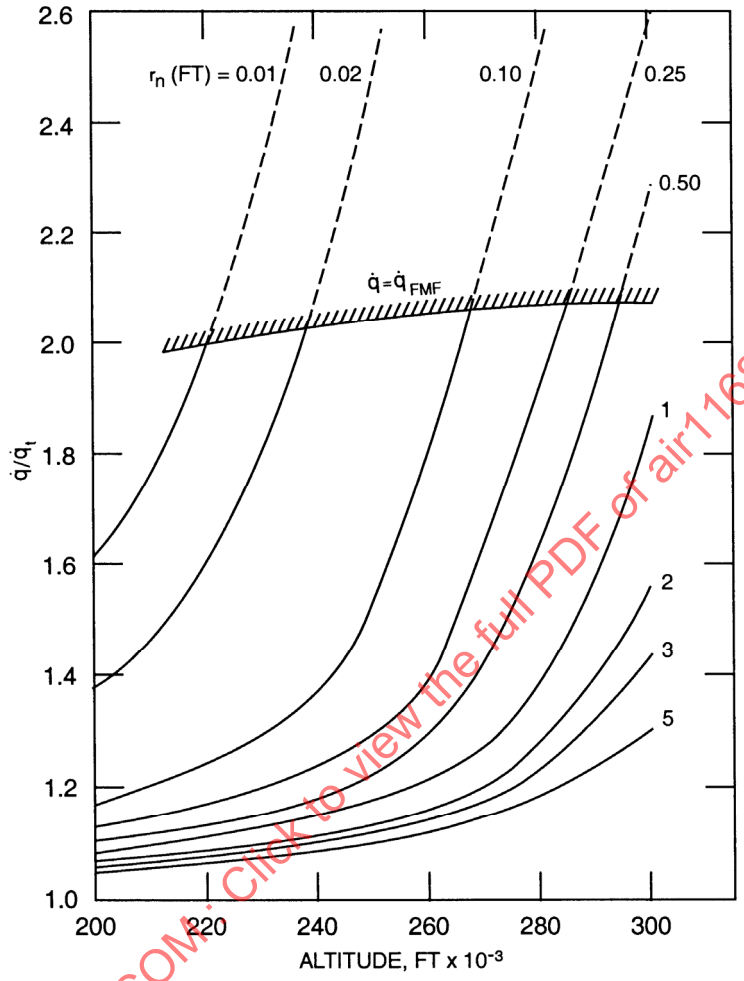

FIGURE 187 - Design Charts for Estimating Transverse Curvature Effects
(U_∞ = 35,000 ft/s)
($\dot{q}_{FMF}$ is the Heat Transfer at Free Molecule Flow)

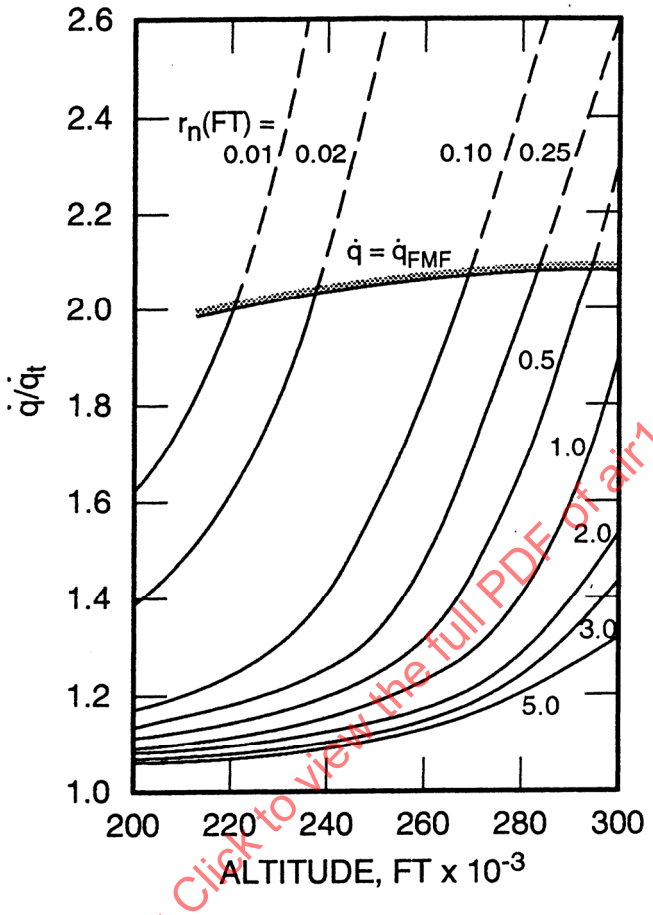

FIGURE 188 - Design Charts for Estimating Transverse Curvature Effects
(U_∞ = 25,000 ft/s)